Rapid Drawdown Analysis using the Finite Element Method

Daniel Roy VandenBerge

Dissertation submitted to the faculty of the Virginia Polytechnic Institute and State University
in partial fulfillment of the requirements for the degree of

Doctor of Philosophy
In
Civil Engineering

J. Michael Duncan, Chair
Thomas L. Brandon, Co-Chair
George M. Filz
Joseph E. Dove

March 27, 2014
Blacksburg, VA

Keywords: rapid drawdown, finite element analysis, undrained strength, compacted clay, reliability analysis

Rapid Drawdown Analysis using the Finite Element Method

Daniel Roy VandenBerge

ABSTRACT

Rapid drawdown (RDD) occurs when the water level adjacent to a slope or embankment is lowered quickly after a long period of being elevated either at the normal operating level for a dam or in the case of levees, during a prolonged flood. The current state of practice for RDD analysis is a multi-stage undrained strength method based on limit equilibrium.

The primary objective of this research was to develop a new method for rapid drawdown based on the finite element method. The new method estimates undrained strengths based on effective consolidation stresses from finite element analysis and the results of isotropically consolidated undrained triaxial compression (ICU-TC) tests. The field strengths appropriate for use with this rapid drawdown method were found to be on average 70% of the strength measured in ICU-TC tests based on back analysis of rapid drawdown failures. For rapid drawdown, anisotropic consolidation, plane strain deformation, and principal stress rotation were shown to produce field undrained strengths in the range of 60 to 80% of the strengths measured in isotropically consolidated undrained (ICU) triaxial compression. The current limit equilibrium method for rapid drawdown was shown to produce a similar reduction in ICU-TC strength.

This study also investigated other issues related to RDD. Effective stress analysis of RDD, especially using uncoupled transient seepage analysis, was shown to be inappropriate because important aspects of soil behavior are ignored. Consolidated-undrained strength tests on compacted clay specimens highlighted the importance of relative compaction on undrained strength. Anisotropic consolidation was shown to produce lower undrained strengths in triaxial compression than isotropic consolidation, especially at higher consolidation stresses. The behavior of compacted specimens under principal stress rotation was investigated using triaxial and direct simple shear tests. Finally probabilistic methods were applied to RDD to assess the probability that the factor of safety is less than one, assuming RDD occurs.

Acknowledgements

I am grateful for the support of all the people in my life who inspired me to pursue doctoral studies and have made this dissertation possible. I would especially like to thank:

- Dr. J. Michael Duncan and Dr. Thomas Brandon for their creative input, constructive criticism, and faithful advising;
- Dr. George Filz and Dr. Joseph Dove for serving on my committee;
- The students of the VT GSO, especially Bernardo Castellanos who helped with many of the laboratory tests and Abeera Batool for many inspiring geotechnical discussions;
- Dr. Stan Vitton at MTU for his continued support and advice;
- Alan Esser, Joe Petraus, John Dingeldein, and Tony Jarem for teaching me so much about geotechnical engineering and writing well;
- Our many friends at Grace Covenant Presbyterian Church for their invaluable encouragement;
- My wife, Carolyn, and kids, Sam and Janna, for loving and supporting me over the last four years and encouraging me to keep going; and
- My faithful Savior, Jesus Christ, for giving me strength and purpose for each day.

Financial support for this work was provided by the Virginia Tech Institute for Critical Technology and Applied Science, the Center for Geotechnical Practice and Research, the Charles Edward Via Department of Civil and Environmental Engineering, and the United States Army Corps of Engineers. I also would like to thank Rocscience Inc. for the research licenses of Slide and Phase^2 used to perform the limit equilibrium and finite element analyses, and Schnabel Engineering for permission to use their data from the Cobbs Creek Dam project.

Table of Contents

List of Tables

Table of Figures

1. Introduction

Rapid drawdown (RDD) has long been recognized as one of the critical design conditions for the upstream or riverside slope of dams and levees. The rapid drawdown condition occurs when the water level adjacent to a slope or embankment is lowered quickly after a long period of being elevated either at the normal operating level for a dam or in the case of levees, during a prolonged flood. Rapid removal of the supporting water load from the upstream face of the embankment, combined with changes in pore pressure, results in an undrained unloading condition in which total stresses decrease, but shear stresses within the embankment increase.

The rapid drawdown problem combines a number of complex soil mechanics problems. First the problem is rapid or undrained, meaning that excess pore pressures which develop due to the change in loading are not dissipated quickly relative to the timescale of the problem. Unlike the undrained end-of-construction case, the soil is typically assumed to be consolidated under the steady state conditions. Thus the void ratio of the compacted fill has reached equilibrium under the steady state effective stresses. Strengths must be determined from saturated, consolidated, undrained laboratory tests rather than unconsolidated tests.

In order to determine the consolidated strengths applicable to the field conditions, the distribution of stresses must be known within the embankment due to its self-weight and any imposed loads. A closed form method of analyzing these stresses is not available. Historically this led to approximate methods of estimating stresses, such as those proposed by Lowe and Karafiath (1960) and Goodman and Brown (1963). With modern computers and advances in finite element analysis (FEA), stresses can now be calculated throughout an embankment with relative ease by numerical analysis. While its accuracy depends on the input parameters and the sophistication of the constitutive model, FEA is a better tool for stress analysis than other more

approximate methods. FEA also allows the orientation of the principal stresses to be calculated throughout the soil mass.

Undrained strengths must be related to the calculated consolidation stresses in order to evaluate embankment stability. For rapid drawdown, undrained strength has historically been determined using isotropically consolidated undrained (ICU) triaxial compression tests. In contrast to the ICU test, soil in the field is consolidated anisotropically, failure occurs in plane strain, and the stresses are able to rotate during loading. These conditions, labeled stress system effects herein, must be considered if ICU tests are to be used for rapid drawdown.

Intellectual Merit

Rapid drawdown analysis remains one of the most misunderstood design cases in slope stability (France and Winckler 2008). The method of interpreting undrained strength in the current limit equilibrium method (Duncan et al. 1990) differs from traditional methods of undrained stability analysis, which tend to relate undrained strength directly to the major effective consolidation stress. A total stress rapid drawdown method that more closely follows conventional undrained analysis methods would benefit the state of practice.

Lowe and Karafiath's (1960a) assumptions result in a consolidation stress state that is not rigorously correct. At a given point in the embankment, the consolidation stress state varies with the inclination of the trial failure surface passing through that point. A unique stress state is not predicted at any point in the embankment. While Lowe and Karafiath's use of limit equilibrium analysis to estimate consolidation stresses was ingenious for the technology at their disposal, the accessibility of computational methods such as finite element analysis has made their method outdated. A total stress rapid drawdown method that takes advantage of the ease of finite element stress analysis is needed.

Significant amounts of research have been done on the volume change behavior of compacted clays and many aspects of their strength. However, the effects of anisotropic consolidation on the undrained strength of saturated compacted clays has not been studied in detail, especially in the range of consolidation stresses applicable to rapid drawdown. In addition, no prior research was found on the effects of principal stress rotation on the undrained strength of compacted clay. Parts of this study provide valuable insight into compacted clay behavior in these areas.

Broader impacts

Operational policy changes within the USACE are likely to require that rapid drawdown analyses be performed in much greater number for levees in the near future. The use of a finite element based procedure has the potential to make these evaluations more accurate. The use of a more conventional relationship between consolidation stress and undrained strength will hopefully improve understanding of rapid drawdown analysis by practitioners.

Improvement of methods for rapid drawdown analysis may help to make our dams and levees safer. At the same time, better design procedures for dams and levees can prevent unnecessary conservatism and can reduce repair costs associated with rapid drawdown failures. Both of these improvements can lower the overall cost to society for these critical pieces of infrastructure.

An improved understanding of the strength of compacted clay may result in a better understanding of all types of undrained slope failure in compacted clays. The design of other types of embankments, not just dams and levees, may be impacted by this improved knowledge.

Overview

Chapter 2 will review the available effective stress methods for rapid drawdown, establishing the importance of undrained strength methods. In particular, the difficulties associated with uncoupled transient seepage analysis are highlighted, and exacting guidelines are presented for numerical analyses that attempt to determine pore pressures in embankments following changes in hydraulic and total stress boundary conditions.

Chapter 3 explores stress system effects on the undrained strength of clays, developing adjustment factors to facilitate the relation of strengths measured in ICU triaxial compression tests to those appropriate for the field. This information provides a theoretical and empirical basis for the need to adjust undrained strengths for rapid drawdown.

Chapter 4 presents guidelines for performing high quality finite element stress analyses, focused on non-linear analysis using the Duncan-Chang hyperbolic model. Stress analyses of the embankments for the two well-documented rapid drawdown failures, Pilarcitos and Walter Bouldin Dams, are presented. In Chapter 5, FEA stress analyses are used to evaluate the assumptions made by Lowe and Karafiath (1960), which are inherent in the total stress limit equilibrium procedures for RDD.

Chapters 6 and 7 present the results of a laboratory testing program on compacted specimens of Oak Harbor clay. The effects of anisotropic consolidation on compacted clay are explored by comparing strengths from ICU and anisotropically consolidated (ACU) triaxial compression tests. The effects of principal stress rotation on undrained strength are investigated using triaxial and direct simple shear tests. The importance of the compaction conditions on undrained strength is observed in the triaxial tests.

Chapter 8 presents two methods for total stress rapid drawdown analysis based on the finite element method. The Rational FEA Method relates effective consolidation stresses from linear elastic FEA to undrained strengths from ICU-TC tests. The ICU-TC strengths are adjusted to account for stress system effects using a constant factor. A detailed FEA Method is also presented, which begins with an effective consolidation stress state determined by non-linear FEA. The ICU-TC strengths are adjusted differently throughout the embankment depending on the consolidation stresses and orientation. These strengths are then imported into limit equilibrium to evaluate embankment stability.

Chapter 9 considers the application of reliability analysis to rapid drawdown, particularly Duncan et al.'s (1990) limit equilibrium method and the Rational FEA Method. The Taylor series approximation, the Hasofer-Lind method, and Monte Carlo analysis are used to calculate the probability that the factor of safety is less than one for an example dam. The probability that RDD occurs is shown to have an important influence on the interpretation of the results of both deterministic and probabilistic RDD analyses.

2. Appropriate Use of Transient Seepage for Effective Stress Stability Analysis

Introduction

The water impounded by an earth dam or levee imposes boundary conditions that affect the total stresses and the pore pressures within the structure. The boundary loads and hydraulic boundary conditions on the embankment both change with the water level (Figure 2-1).

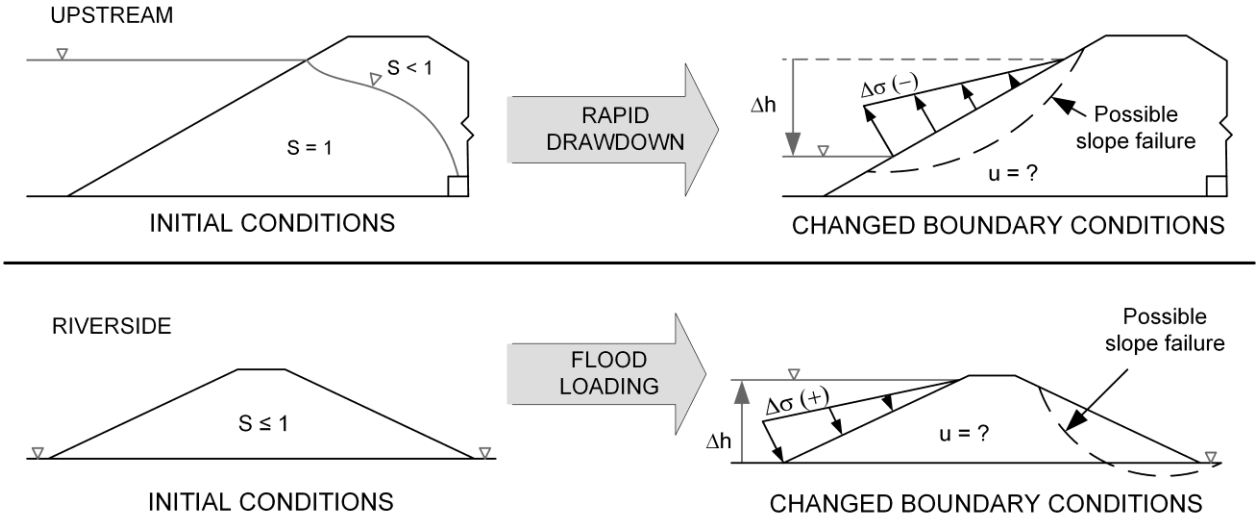

Figure 2-1. Changes in embankment boundary conditions due to water level fluctuations

Critical stability conditions can develop as stresses and pore pressures in the embankment respond to the changes in boundary conditions. For example, rapid drawdown (RDD) reduces the total stress on the upstream face and lowers the head driving seepage through the embankment. The shear stresses increase within the slope, which may lead to instability. Similarly, flood loading on a levee increases the riverside total stress and the head differential across the levee.

In principle, the stability of a slope can be evaluated using either total stress (undrained) or effective stress (drained) strength parameters. Effective stress analysis uses drained strengths

which are often easier to measure and tend to be less dependent on the direction of loading or loading stress path. For these reasons, effective stress analyses are attractive for embankments experiencing changing water levels, such as RDD or flood loading. However, pore water pressures in the embankment must be known or predicted accurately for effective stress analysis. The use of transient seepage analyses have been proposed by some for this purpose (e.g. Li and Desai 1983, Lam et al. 1987).

This chapter considers the methods available to predict pore pressures due to transient water levels and the modeling requirements for accurate prediction of these pressures. Examples are provided which illustrate the shortcomings of using uncoupled transient seepage analysis to obtain pore pressures for stability analyses.

Methods of Predicting Pore Pressure Changes

Pore pressures within an embankment will respond to total stress and head boundary condition changes. In the rapid drawdown case, pore pressures will drop as a function of the reduced total stress acting against the slope as well as the lowered upstream head. Coupled analyses are those that consider the link between changes in stress and changes in pore pressure. Uncoupled analyses only consider changes in pore pressure caused by the hydraulic boundary conditions. Methods of predicting pore water pressures due to water level changes can be simplified into three groups:

- $\overline{B}$ methods
- Uncoupled transient seepage analysis
- Fully coupled transient seepage / stress analysis

$\overline{B}$ Methods

In 1954, Bishop applied Skempton's (1954) pore pressure parameter concept to RDD analysis using a parameter labeled $\overline{B}$, which is the ratio of the change in pore pressure, Δu, to the change in major principal stress, $\Delta\sigma_1$. $\overline{B}$ is coupled to changes in the total major principal stress through the pore pressure parameters, *A* and *B*. Changes in the hydraulic boundary conditions do not directly affect the predicted pore pressures and no time-dependency is considered. Bishop conservatively assumed that *A* equals 1.0, which results in $\overline{B}$ equal to 1.0 for saturated soil. This assumption considers all embankment fill materials to be as contractive as a normally consolidated soil. Both Bishop (1954) and Morgenstern (1963) further assumed that $\Delta\sigma_1$ is equal to the change in vertical total stress due to the change in the height of water above the point in question.

Barrett and Moore (1975) observed that $\Delta\sigma_1$ in finite element analyses was typically less than the change in overburden pressure due to the lowered water level. They recommended the use of the parameter $\overline{B}_h$, which was defined as the change in pore pressure at a given point in the embankment divided by the change in total vertical stress at that point. Values of $\overline{B}_h$ were shown to be in the range of 0.7 to 0.9. Values of $\overline{B}_h$ less than 1.0 lead to lower Δu and higher pore pressures after drawdown.

Because of their inherently conservative assumptions, the pore pressures predicted by the $\overline{B}$ or $\overline{B}_h$ method, are a conservative upper bound to the pore pressures that develop after drawdown in a compacted soil. These methods provide a simple, easily calculated check for other more complex methods of predicting pore pressures.

Uncoupled Transient Seepage Analysis

Transient seepage analysis is another method that has been suggested for predicting pore pressures in embankments after changing the impounded water level. In the 1960s, researchers (e.g. Browzin 1961, Brahma and Harr 1963) used transient seepage principles to predict pore pressures after drawdown. Desai (1972, 1977) used transient seepage analyses to predict pore pressures due to rising water or drawdown, using numerical analyses. The soil was assumed to be rigid, and Dupuit-Forchheimer horizontal flow approximation was assumed to be valid. Through the 1980s, uncoupled transient seepage analysis by the finite element method was further refined for use along with stability analysis (e.g. Li and Desai 1983, Lam et al. 1987).

Uncoupled transient seepage analysis has been applied to case studies of rapid drawdown (e.g. Whiteside 1976, Pauls et al. 1999). More recently, researchers including Xu et al. (2009) and Fredlund et al. (2011) analyzed slope stability following RDD using pore pressures from uncoupled transient seepage analysis. These latter studies report the saturated hydraulic conductivity, k_s, used in the analyses while the values of soil compressibility are not reported. Where reasonable factors of safety are reported, the values of k_s are typically orders of magnitude higher than reasonable for the soils considered. A variety of parametric studies (e.g. Huang and Jia 2009, Nian et al. 2011) on hypothetical slopes have been performed to examine different aspects of effective stress rapid drawdown analysis, using uncoupled transient seepage analysis. These studies invariability ignore soil compressibility or assume incompressibility.

Many modern slope stability and seepage analysis software packages, such as SEEP/W (GEO-SLOPE 2012) and Slide (Rocscience 2012), present methods for using uncoupled transient seepage analysis along with limit equilibrium to evaluate the stability of slopes affected by changing hydraulic boundary conditions. The latest version of the USBR Embankment Dam

design standards (2011) recommends using the effective stress approach with pore pressures from uncoupled transient seepage analysis to analyze stability following rapid drawdown. The following review of the formulation of the transient seepage equation is provided to help illustrate the shortcomings of uncoupled transient analysis.

Review of the Transient Seepage Equation

The transient seepage analyses performed by commercial finite element analysis (FEA) programs are uncoupled from changes in total stress. The changes in pore pressures predicted by these programs result only from changes in the hydraulic boundary conditions, and changes in the total stress boundary loads do not affect the pore pressures.

The importance of this effect can be examined by reviewing the governing equation for transient flow in soil. Continuity of mass requires that the mass of water which flows into or out of a reference volume of soil be equal to the change in water mass within the reference volume. Shrinking to an infinitesimal reference volume (Bear 1979), the mass balance equation becomes

$$\nabla\left[\rho_w\left(\mathbf{k}\nabla h\right)\right]=\frac{D}{Dt}\left(\rho_w Sn\right) \tag{2-1}$$

where:

∇ = the gradient operator,

ρ_w = unit weight of water,

$\boldsymbol{k}$ = hydraulic conductivity tensor for the soil,

h = total head,

D/Dt = Lagrangian (material) derivative associated with the soil volume,

S = saturation, and

n = porosity.

Expanding the right-hand side using the chain rule yields

$$\nabla\left[\rho_w\left(\mathbf{k}\nabla h\right)\right] = Sn\frac{D\rho_w}{Dt} + \rho_w n\frac{DS}{Dt} + \rho_w S\frac{Dn}{Dt} \tag{2-2}$$

At any time, *t*, the values of head and corresponding pore pressures can be determined throughout the embankment by solving Eq. (2-2). For constant ρ_w in saturated, rigid soil, all of the terms on the right hand side equal zero, and the equation reduces to the Laplace equation for steady state flow.

In order to solve Eq. (2-2), transient seepage analysis treats the derivatives in the three right-hand terms in the following ways:

1. *Change in the Density of Water*

Water compressibility is much smaller than the soil structure compressibility so ρ_w is effectively constant, and the first term drops from the analysis. This is a reasonable assumption for problems involving water level changes and soil slopes.

2. *Change in Saturation*

The second term is addressed by the relationships between saturation, suction, and hydraulic conductivity through the soil-water characteristic curve (SWCC) and the hydraulic conductivity function (HCF). This aspect of soil behavior is described adequately, provided the unsaturated soil model represents the soil well.

3. *Change in the Soil Porosity*

Most solutions to the transient seepage equation allow the porosity (or void ratio) of the soil to change with time as a function of changes in effective stress. However, in order to make the solution only a function of the change in head with time, changes in total stress are often ignored or assumed to be zero. The change in effective stress and therefore the change porosity are then only a function of the change in pore pressure. In other words, the pore pressures are

"uncoupled" from changes in total stress. Without this assumption, the use of constitutive relations would be required.

The assumption of no change in total stress is reasonably accurate when the hydraulic boundary conditions are not associated with changes in the boundary loads, such as changes in the phreatic surface due to pumping of an unconfined aquifer. However, for cases with ponded water loads, the change in pore pressure must not be uncoupled from the change in total stress. Uncoupling results in pore pressures that do not respond immediately to changes in confining stress, as shown by Alonso and Pinyol (2011) and as illustrated later for Pilarcitos Dam. Uncoupled transient seepage analysis allows no means of considering pore pressure changes due to shear-induced volume change tendencies.

Impact of Soil Compressibility on Transient Seepage Analysis

Uncoupled transient seepage analyses often inappropriately ignore the compressibility of the soil structure. The relationship between effective stress and porosity is commonly represented in geotechnical engineering using the coefficient of volume compressibility, m_v (units of stress^{-1}), which is the slope of the one-dimensional strain vs. effective stress relationship and is inversely proportional to the stiffness of the soil. For small deformations, the change in porosity with time in Eq. (2-2) can be simplified to

$$\frac{Dn}{Dt} = \gamma_w m_v \frac{dh}{dt} \tag{2-3}$$

where:

γ_w = unit weight of water and

m_v = coefficient of volume compressibility.

Assuming that water is incompressible and that the system is homogeneous and ***k*** is aligned with the coordinate system (for illustration purposes only, not necessary for transient seepage analysis), Eq. (2-3) and (2-4) can be simplified to

$$k_h \frac{\partial^2 h}{\partial x^2} + k_v \frac{\partial^2 h}{\partial y^2} = n \frac{DS}{Dt} + S\gamma_w m_v \frac{dh}{dt} \tag{2-4}$$

where:

k_h = hydraulic conductivity in the horizontal (x) direction, and

k_v = hydraulic conductivity in the vertical (y) direction.

For saturated conditions, S is constant and equal to 1.0, which yields

$$\frac{k_h}{\gamma_w m_v} \frac{\partial^2 h}{\partial x^2} + \frac{k_v}{\gamma_w m_v} \frac{\partial^2 h}{\partial y^2} = \frac{dh}{dt} \tag{2-5}$$

or

$$c_h \frac{\partial^2 h}{\partial x^2} + c_v \frac{\partial^2 h}{\partial y^2} = \frac{dh}{dt} \tag{2-6}$$

where:

c_h = coefficient of consolidation in the horizontal (x) direction, and

c_v = coefficient of consolidation in the vertical (y) direction.

Equation (2-6) shows that the rate of change in head in the saturated zone is completely controlled by the coefficients of consolidation. The total heads (and pore pressures) determined by transient seepage analysis will be highly dependent on the values of k **and** m_v used in the analysis, since both of these parameters influence c_v and c_h. The SWCC, HCF, and initial moisture content and matric suction will also impact the results but only in the unsaturated zone. Accurate values of both k and m_v must be used or the analysis will not model the actual soil response.

The coefficient of volume compressibility is commonly considered in one of the following ways in uncoupled transient seepage analysis:

- Incompressible soil – makes transient seepage solely a function of the unsaturated soil properties.
- Calculated from the slope of the SWCC at zero pore pressure. In this case, m_v is "buried" in the program and the user is not encouraged to consider its impact on the results.
- Explicitly defined – This method is appropriate. If m_v is not known, values of c_v from the literature (e.g. Duncan et al. 1990) can be used along with k_s to calculate m_v.

Table 2-1 summarizes typical values of hydraulic conductivity and compressibility parameters for soil types common to embankment dams and levees. The values of k_s generally vary over two orders of magnitude. A wider range of values is listed for compacted clay, for which the hydraulic conductivity is strongly influenced by the degree of compaction and moisture content at compaction. The typical values of c_v are those recommended by Duncan et al. (1990) and have a similar range of two orders of magnitude. Values for the coefficient of volume compressibility were calculated from the typical values of k_s and a value of c_v in the middle of the provided range.

Table 2-1. Typical values of k_s (after USACE 1986 and Benson and Trast 1995), c_v (after Duncan et al. 1990), and m_v (calculated) for common embankment soil types.

	Soil Type	Coefficient of Hyd. Conductivity, k_s, (ft/day)	Coefficient of Consolidation, c_v, (ft^2/day)	Coefficient of Volume Compressibility, m_v, (1/psf)
English units	Coarse Sand	30 – 3000	10,000 – 100,000	5×10^{-6} – 5×10^{-4}
	Fine Sand	0.3 – 30	100 – 10,000	5×10^{-6} – 5×10^{-4}
	Silty Sand	0.03 – 3	10 – 1000	5×10^{-6} – 5×10^{-4}
	Silt	3×10^{-4} – 3×10^{-2}	0.5 – 100	5×10^{-7} –5×10^{-5}
	Soft Clay	3×10^{-6} – 3×10^{-4}	0.002 – 0.2	2×10^{-6} – 2×10^{-4}
	Compacted Clay	3×10^{-6} – 3×10^{-2}	0.05 – 5	9×10^{-8} – 9×10^{-4}
	Soil Type	Coefficient of Hyd. Conductivity, k_s, (cm/s)	Coefficient of Consolidation, c_v, (cm^2/s)	Coefficient of Volume Compressibility, m_v, (1/kPa)
Metric units	Coarse Sand	0.01 – 1	100 – 10,000	$9\text{x}10^{-7}$ – 9×10^{-5}
	Fine Sand	1×10^{-4} – 1×10^{-2}	1 – 100	9×10^{-7} – 9×10^{-5}
	Silty Sand	1×10^{-5} – 1×10^{-3})	0.1 – 10	9×10^{-7} – 9×10^{-5}
	Silt	1×10^{-7} – 1×10^{-5}	5×10^{-3} – 1	9×10^{-8} – 9×10^{-6}
	Soft Clay	1×10^{-9} – 1×10^{-7}	2×10^{-5} – 2×10^{-3}	5×10^{-7} – 5×10^{-5}
	Compacted Clay	1×10^{-9} – 1×10^{-5}	5×10^{-4} – 5×10^{-2}	2×10^{-8} – 2×10^{-4}

Coupled Transient Seepage Analyses

The importance of pore pressure coupling with total stress, especially for rapid drawdown, has been recognized by some researchers. They have used complex constitutive models have been used to couple changes in pore pressure to changes in total stress boundary conditions while at the same time solving the transient seepage equation.

Pariseau et al. (1997) performed fully coupled finite element analyses of pore pressures in excavated mine slopes, taking into account the changes in total stress as well as changes in the compressibility of water. In 2007, Berilgen employed a transient seepage analysis for RDD which was coupled with Biot consolidation theory and a non-linear soil hardening constitutive model. More recently, Pinyol et al. (2008) and Alonso and Pinyol (2011) have used fully coupled finite element analyses to analyze pore pressures following rapid drawdown. In their models, the soil was represented by the elastic-plastic Barcelona Basic Model. Thermal effects are also considered in some of these analyses. Alonso and Pinyol have focused mostly on case histories where pore pressures were measured following intentional drawdown and the dams did not fail, such as Glen Shira and Alcova Dams. These analyses show that coupling of pore pressures to changes in total stress and the compressibility of the soil both have dramatic effects on the calculated pore pressure response.

Requirements for Accurate Pore Pressure Predictions

Fully coupled transient seepage analysis could theoretically predict accurate pore pressures provided the constitutive model accounts for all aspects of the soil behavior in terms of its volume change tendencies or pore pressure response. The following discussion outlines the modeling requirements for accurate predictions of pore pressures for loading or unloading due to

water level changes. Rapid drawdown is shown to be a simpler case to analyze than flood loading.

To predict pore pressures caused by fluctuating water levels, a numerical model must accurately:

- Model the initial conditions in terms of both total and effective stress,
- Model saturated and unsaturated hydraulic conductivity, and
- Model soil response to changes in load and hydraulic boundary conditions.

"Initial" Conditions Before Water Level Change

Initial stresses must be accurately modeled because the final pore pressures will depend on these stresses. Accurate analysis of embankment stresses is not a trivial task because soil properties, such as elastic modulus, E, and Poisson's ratio, ν, are stress dependent and non-linear. Numerical analyses must be performed in stages using a non-linear model, if the magnitude and orientation of the stresses are to be determined correctly. Figure 2-2 shows an example of the stages in which an embankment might be numerically "built" and loaded in a finite element model.

Steady state conditions prior to the water level change must be determined. The distribution of suction or the degree of saturation must be defined throughout the unsaturated zone. For levee flood loading, the initial stress conditions as well as degree of saturation throughout the embankment must be determined. By definition, the upstream slope of a dam will be saturated at the start of a rapid drawdown.

The calculations to determine initial stresses should be partially or fully coupled with the pore pressures. In other words, equilibrium in the embankment should be solved in terms of

effective stress. Effective stress strength parameters and constitutive properties, should be used throughout.

The modeling requirements for initial conditions in a compacted embankment are summarized in Table 2-2 for the cases of flood loading and rapid drawdown.

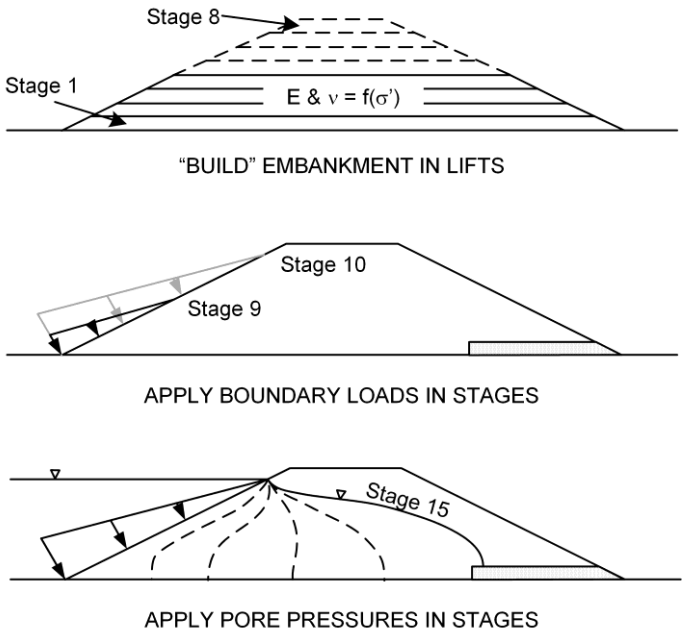

Figure 2-2. Modeling initial embankment stress conditions for rapid drawdown by staged analysis to accommodate soil non-linearity.

Table 2-2. Requirements for numerical modeling of pore pressure changes due to changing boundary conditions

	Modeling Requirement	Flood Loading	Rapid Drawdown
Initial Conditions	Nonlinear, stress dependent constitutive properties, from drained tests	Yes	Yes
	Build embankment, apply boundary loads, and apply long-term pore pressures in stages	Yes	Yes
	Initial distribution of S throughout the embankment	Yes	No[A]
	Pore pressures defined by steady state numerical seepage analysis	Yes	Yes
Steady Seepage	Representative k_s, dependent on net normal stress $(\sigma - u_a)$	Yes	Yes
	HCF – dependent on net normal stress	Yes	Yes[B]
	SWCC – dependent on net normal stress	Yes	No[A]
	m_v – dependent on net normal stress	Yes	Yes
Design Condition	Δu_B – change in pore pressure in response to change in normal stress	Yes f(S)	Yes B = 1.0
	Δu_A – change in pore pressure in response to change in shear stress, depends on σ', stress path, and stress orientation	Yes Also f(S)	Yes
	Δu_h – change in pore pressure in response to change in head	Yes	Yes
	Combine Δu_B, Δu_A, and Δu_h	Yes	Yes

[A] Saturation will be 100% in the zones applicable to rapid drawdown analysis
[B] HCF is required to determine steady state seepage in current FEA seepage analysis programs

Saturated and Unsaturated Seepage

The initial seepage conditions within the embankment will affect the development of pore pressures when the water level changes. Modeling groundwater flow requires accurate values of saturated hydraulic conductivity, k_s, for each soil type. For design or case studies, k_s will preferably come from high quality laboratory tests on samples representative of the field conditions and should be varied over the possible range to reflect uncertainty. In all cases, k_s must be representative of the type of soil being modeled.

Calculation of seepage through the unsaturated zone requires knowledge of the change in soil properties as saturation and matric suction changes. The SWCC and HCF can be measured in the laboratory or estimated based on soil properties. Sleep (2011) suggested that using one of the established methods of estimation is just as accurate as laboratory measurements due to the variability of unsaturated soil properties.

Most formulations of transient flow consider the SWCC, HCF, and m_v to be constant throughout a soil mass and are not dependent on the full stress state. The SWCC and HCF typically used in transient seepage analysis assume that the net normal stress, which is defined as the total normal stress minus pore air pressure $(\sigma - u_a)$, is equal to zero or very low. In reality these relationships and the soil compressibility will vary as the soil changes volume in response to changes in net normal stress. A realistic evaluation of transient flow would incorporate stress dependent expressions for the SWCC, HCF, and m_v. Very complex constitutive theories (e.g. Pham and Fredlund 2011) relating unsaturated behavior to both matric suction and net normal stress are starting to become available for simple stress paths. The modeling requirements for saturated and unsaturated flow are summarized in Table 2-2.

Response to Changing Boundary Conditions

Realistic finite element analysis of pore pressures must be coupled to include the effects of changed boundary loads. For rapid drawdown, the critical condition for stability occurs in the upstream slope where saturated conditions prevail. In terms of Skempton's parameters, pore pressures will decrease immediately an amount equal to the decrease in confining stress ($\Delta\sigma_3$) and will also increase or decrease in response to the change in shear stress ($\Delta\sigma_1 - \Delta\sigma_3$), depending on the magnitude of $\bar{A}$. While B can be set equal to 1.0 throughout the saturated zone,

the value of $\bar{A}$ will vary throughout the embankment and will be a function of the initial stresses, stress path, and principal stress rotation during drawdown.

The coupled pore pressure response is much more complicated when the embankment begins in a primarily unsaturated state, such as the flood loading case. B will be less than 1.0 due to the presence of a compressible air phase in the pore fluid. $\bar{A}$ will be a function of saturation as well as stress and stress state.

While pore pressures in the saturated zone change instantaneously due to boundary load changes, a time dependent response to the changing hydraulic boundary conditions will occur governed by Eq. (2-2). The numerical model must be able to combine the coupled pore pressures with the changes due purely to transient flow. These pore pressures must be allowed to increase or dissipate with time as steady state conditions are approached.

The modeling requirements to incorporate soil response to changing boundary conditions are summarized in Table 2-2. For both the initially saturated (rapid drawdown) and unsaturated (flood loading) cases, a realistic treatment of the coupled response would require a sophisticated constitutive model that is calibrated for a wide variety of stress paths and incorporates both saturated and unsaturated behavior.

The complexity of the soil behavior and the many relationships that must be modeled for fully-coupled analysis of transient pore pressures make the problems very difficult. The coupled analyses that have been performed (e.g. Alonso and Pinyol 2011) give valuable insight into phenomena such as rapid drawdown and the evolution of pore pressures during unloading. Practically speaking, the complexity of these models makes them unsuitable for routine evaluation of stability during rapid drawdown or flood loading.

Stability Analyses

If effective stress analysis is to be used for slope stability problems like rapid drawdown, the impact of all aspects of soil behavior on the pore pressures must be understood and modeled. The impacts of simplifying assumptions that ignore important aspects of soil behavior need to be evaluated. In order to be meaningful, transient seepage analyses must account for the importance of

- Coupled behavior. If this is ignored, the predicted pore pressures will not be meaningful. Changes in pore pressure due to changes in confining stress are not enough. The effects of changes in shear stress on pore pressures must also be modeled.
- Soil compressibility (via c_v or m_v). Both soil compressibility and hydraulic conductivity control the speed at which saturated soil can deform and respond to changes in pore pressure caused by changes in boundary conditions. Inaccurate modeling of compressibility will lead to the inaccurate variation of pore pressure with time, and inaccurate evaluations of stability.

Examples

Two examples are presented to illustrate some of the problems associated with uncoupled transient seepage analysis. These examples are not meant to advocate the use of such analyses or show how to perform the realistic coupled analyses detailed in Table 2-2. Rather, the impact of coupled behavior and soil compressibility are clearly shown through the application of uncoupled transient seepage analysis.

Example 2-1 – Pilarcitos Dam

Pilarcitos Dam is a 78 ft (23.8 m) high homogenous earth dam in the San Francisco, CA area. The dam was built from compacted sandy clay with a total unit weight of 135 pcf (21.2 kN/m^3). The lower 58 ft (17.7 m) of the upstream slope is inclined at 2.5H:1V, and the upper 20 ft (6.1 m) is inclined at 3H:1V.

A rapid drawdown slide occurred in Pilarcitos Dam in 1969 after the reservoir level was lowered 35 ft (10.7 m) over the course of 43 days. This case has been considered by a number of researchers, including Duncan et al. (1990) and Fredlund et al. (2011) as a means of validating both total and effective stress rapid drawdown analysis procedures. Laboratory strength tests were performed on samples from the embankment by Wahler and Associates (1970). The hydraulic conductivity of the clay was reported to be 1.3×10^{-9} ft/s (4×10^{-8} cm/s).

Transient seepage analyses were performed using Slide v.6.020 to illustrate the effects of k and m_v (or c_v) on the predicted pore pressures and the stability following drawdown. Three values of k_s were considered: the measured value 1.3×10^{-9} ft/s (4×10^{-8} cm/s) and two higher values, 1.3×10^{-7} and 1.3×10^{-5} ft/s (4×10^{-6} and 4×10^{-4} cm/s). The value of m_v was varied for each value of k_s such that the value of c_v ranged from a reasonable value of 1.8×10^{-1} ft^2/day (1.9×10^{-3} cm^2/s) to an excessively high value of 1.8×10^{4} ft^2/day (193 cm^2/s).

In the unsaturated zone, the compacted sandy clay at Pilarcitos Dam was represented by the SWCC and HCF shown in Figure 2-3 after van Genuchten (1980). Model parameters from a compacted clay with similar Atterberg limits selected from the literature (Tinjum et al. 1997). The HCF was shifted appropriately for the three values of k_s used.

After each transient seepage analysis was performed, the stability of the upstream slope of Pilarcitos Dam was assessed using Spencer's limit equilibrium method. While most of the

analyses ignored the effects of matric suction on shear strength, some analyses followed Fredlund et al. (1978) to account for increases in strength due to matric suction.

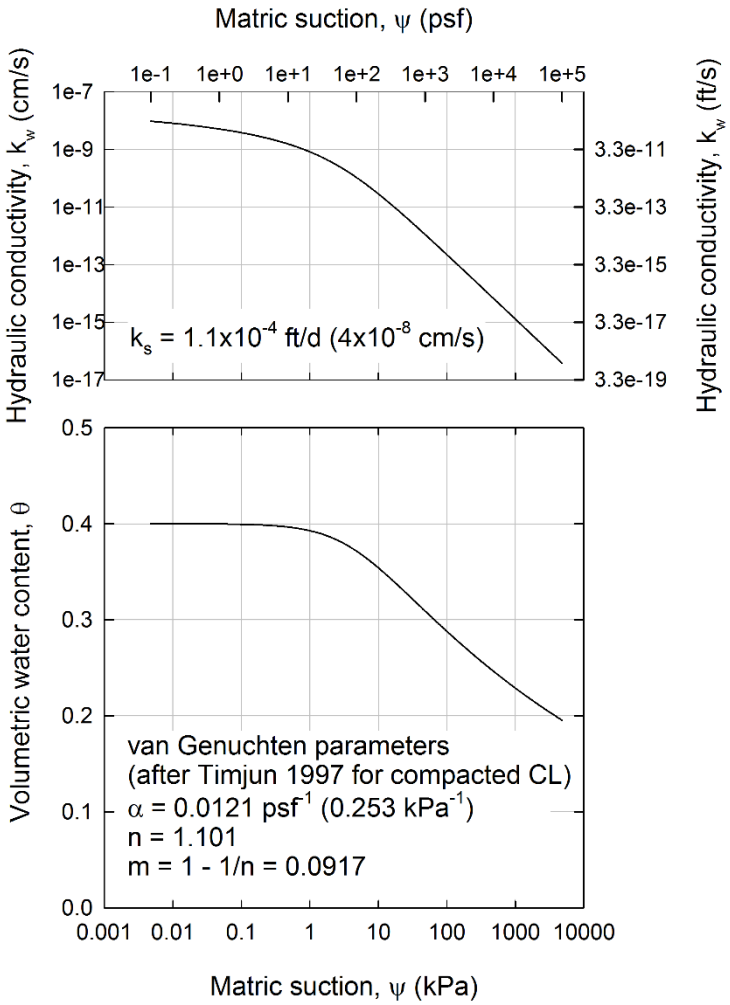

Figure 2-3. Hydraulic conductivity function and soil-water characteristic curve assumed for Example 2-1 analyses.

Pore Pressures at t = 43 days

After 43 days, the pore pressure was determined in each seepage analysis at Point A, which was located 40 ft (12.2 m) above the base and 145 ft (44.2 m) from the toe of the embankment. The steady state pore pressure at this point was 1935 psf (93 kPa). The depth of water above this point is 14 ft (4.3 m) so the decrease in total vertical stress after drawdown is (14)(62.4) = 874 psf (42 kPa). Using Bishop's method with $\overline{B}$ = 1, the pore pressure after drawdown would be

1935 – 874 = 1061 psf (51 kPa). Barrett and Moore's (1975) recommendation of $\overline{B}_h$ = 0.8 for a homogeneous dam yields a final pore pressure of 1236 psf (59 kPa). Based on these simple calculations, the pore pressure at Point A should be about 1250 psf or less after drawdown, a decrease about 685 psf due solely to the coupling of pore pressures to total stresses.

The pore pressures predicted at Point A by the uncoupled transient seepage analyses are shown in Figure 2-4(a), plotted against the coefficient of consolidation to combine the effects of k_s and m_v. The typical range of c_v for compacted clay is indicated. Analyses with the same c_v but different k_s yield the same pore pressure within this range because the saturated behavior is governed by Eq. (2-6), which depends on c_v. The pore pressures are close to zero for the highest k_s, and large c_v, because the soil has a relatively high unsaturated hydraulic conductivity and low compressibility in this case. This allows the transient seepage to proceed toward the steady state condition more rapidly.

Figure 2-4(a) shows that transient seepage analyses with realistic values of c_v result in pore pressures higher than the upper bound of 1250 psf predicted by the simple $\overline{B}$ methods. In order for the transient seepage analysis to calculate a value of pore pressure at Point A less than 1250 psf, c_v must be nearly one order of magnitude higher than the upper end of the typical range for compacted clay. Neither the $\overline{B}$ method nor uncoupled transient seepage can correctly model pore pressures induced by the changes in shear stress.

Soil mechanics requires that the pore pressures in a saturated embankment change in equal proportion to the decreased total confining stress, just as pore pressures in an undrained triaxial sample respond to changes in cell pressure. Because its formulation assumes no change in total stress, uncoupled transient seepage cannot be used to calculate correct values of pore pressure using a realistic value of c_v. Pore pressures in the expected range can only be obtained by

artificially increasing c_v (and the soil stiffness) to numerically allow the soil to drain more quickly.

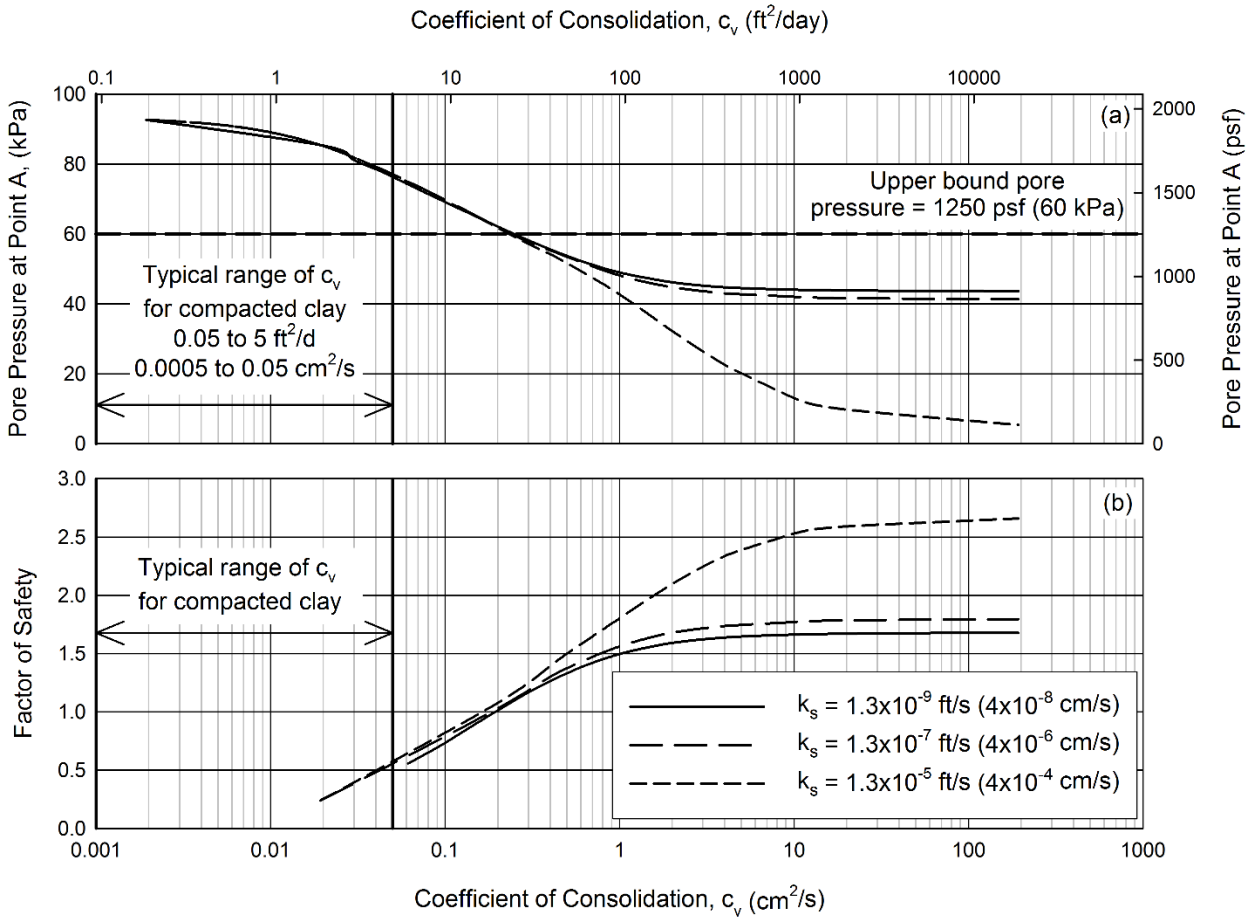

Figure 2-4. Effect of c_v on pore pressures and factor of safety based on transient seepage analysis, Pilarcitos Dam, t = 43 days. The measured k_s was 1.3×10^{-9} cm/s.

Factor of Safety at t = 43 days

The factor of safety for the circle shown in Figure 2-5 was evaluated using drained strength parameters and the pore pressures from each seepage analysis. This is the critical failure surface from the Duncan et al. (1990) rapid drawdown method, which has a total stress F = 1.04. Although this is not the critical circle for the effective stress analyses discussed here, comparing factors of safety for this slip surface provides a means of assessing the effects of pore pressures

on stability. As shown in Figure 2-5, a c_v of about 18 ft^2/day (0.19 cm^2/s) is required for F = 1, if the measured value of k_s is used.

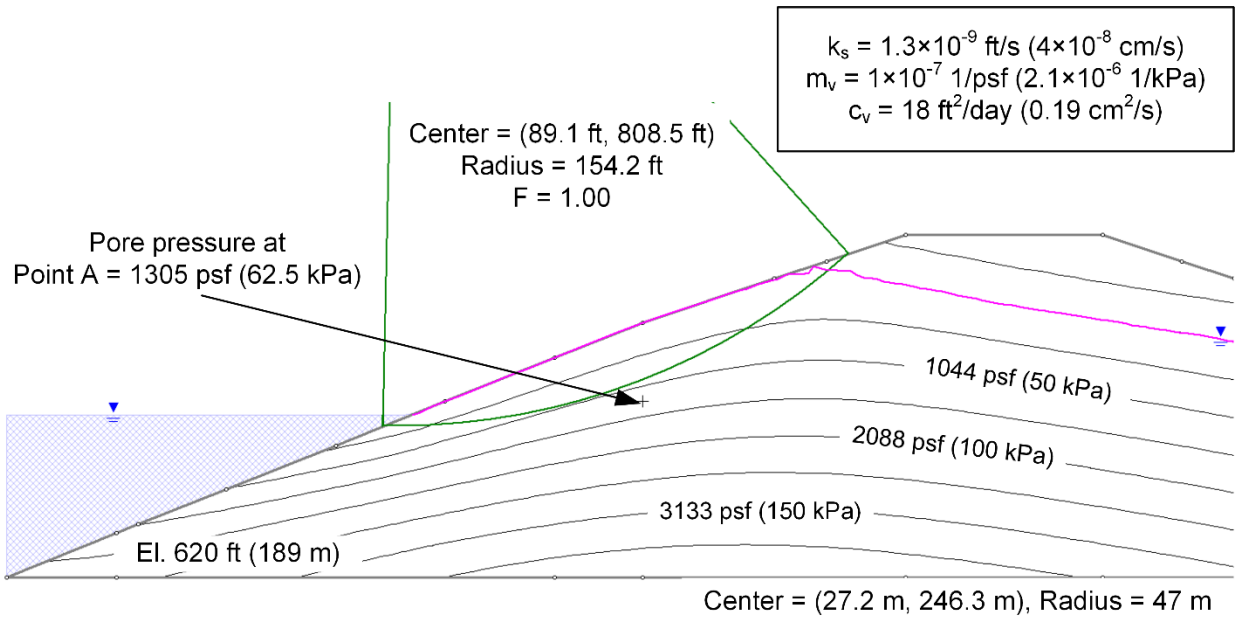

Figure 2-5. Pilarcitos Dam – critical circle from analysis by Duncan et al. (1990), and values of c_v, k_s and m_v that result in F = 1.0 in effective stress stability analyses.

The effective stress factors of safety after 43 days of drawdown are plotted against c_v in Figure 2-4(b) for each value of k_s. When c_v is too high (very stiff soil or high hydraulic conductivity), excess pore pressures dissipate quickly and the factor of safety is high. The factor of safety is less than 0.5 when c_v falls within the typical range for compacted clay. For c_v below 0.9 ft^2/day (0.01 cm^2/s), the factor of safety could not be calculated because the pore pressures calculated by the transient seepage analysis exceed the total overburden stress along part of the failure surface.

The expected factor of safety for Pilarcitos Dam is about 1.0. Figure 2-4(b) shows that effective stress rapid drawdown analysis using pore pressures from uncoupled transient seepage can predict F ranging from 0.1 to 1.7 for the correct value of k_s. This variation occurs simply by varying a single parameter that has been ignored by many researchers and undoubtedly many

practitioners. The reason for these changes in F can be clearly seen by comparing Figure 2-4(a) and (b). As c_v increases, the pore pressures decrease, the effective stresses increase, and the factor of safety also increases.

The effects of matric suction on strength and the factor of safety were considered for the cases using the measured k_s. The failure surface was almost entirely below the phreatic surface for these cases as shown in Figure 2-5, such that most of the pore pressures were positive. The factor of safety increased, on average, only about 0.005 due to the effects of suction, if the friction angle with respect to matric suction, ϕ^b (Fredlund et al. 1978), was assumed to be half of ϕ'.

Based on this examination of the rapid drawdown failure of Pilarcitos Dam, it is clear that uncoupled transient seepage analyses cannot accurately predict pore pressures following rapid drawdown. Effective stress rapid drawdown analyses which incorporate these pore pressures are equally inaccurate.

Example 2-2 – Landslide levee stability during flood loading

Landside stability analysis of levee slopes during flood loading is another condition to which transient seepage analyses have been applied. A hypothetical levee of silty sand built on a clay foundation is analyzed in this example. The initial soil conditions are given in Figure 2-6(a). The initial position of the phreatic surface is at the top of the clay foundation on both sides of the levee.

The levee was subjected to an 18 ft (5.5 m) water level rise in 2 days followed by sustained high water for 28 days as shown in Figure 2-6(b). Slide v. 6.022 was used to evaluate transient seepage and slope stability. The SWCC and HCF for both soils were represented by the curves

shown in Figure 2-7. The distribution of pore pressures after 30 days was calculated using c_v for the levee fill ranging from 2.8×10^{-4} to 2.8×10^{2} ft^2/day (1×10^{-7} to 0.1 cm^2/s).

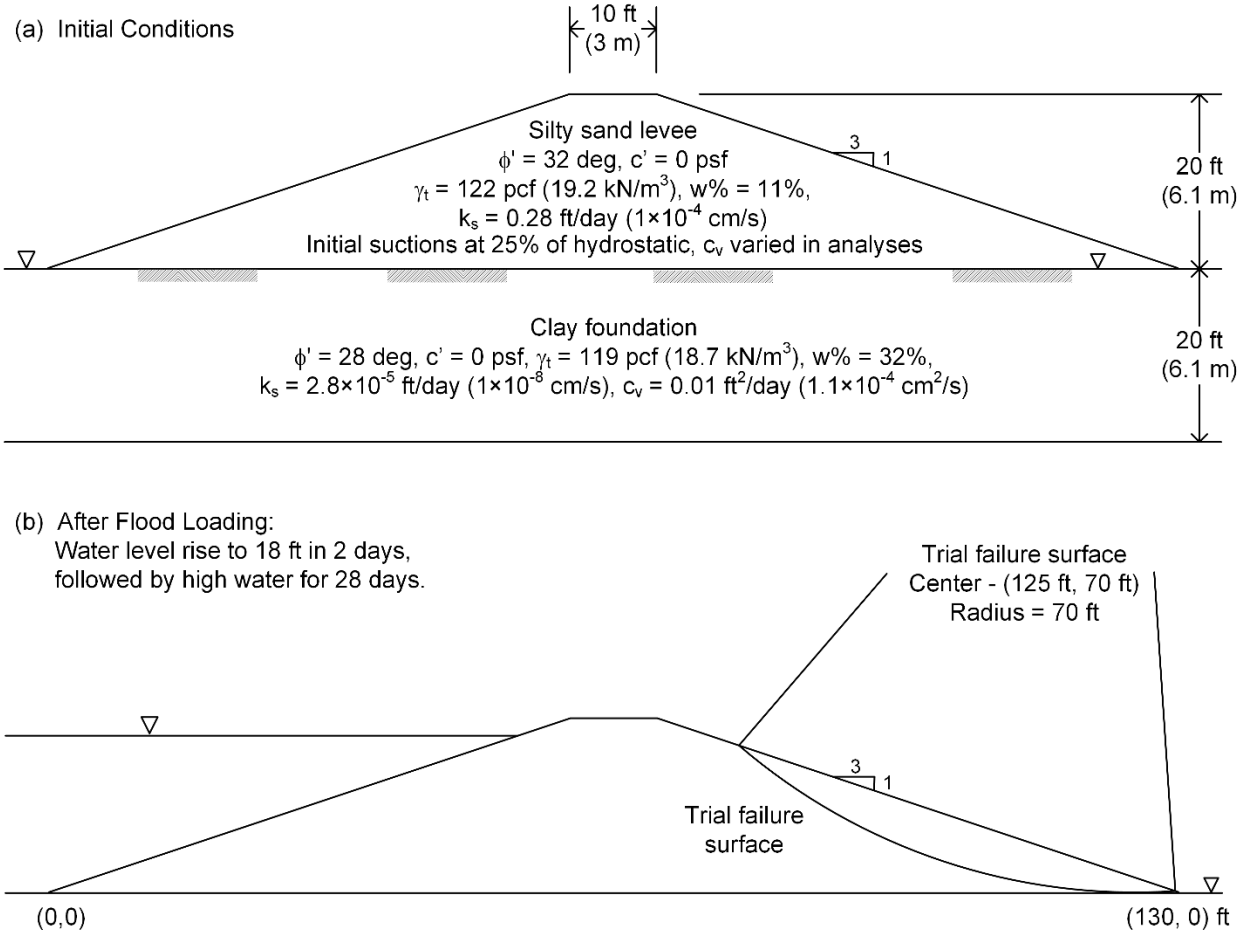

Figure 2-6. Initial conditions for levee in Example 2-2.

A non-critical trial failure surface was selected with its center 5 ft (1.5 m) left of the landside toe and 70 ft (21.3 m) above the base. The radius of the circle was 70 ft (21.3 m). The factor of safety was evaluated for this surface using the calculated pore pressures and drained strengths. Increases in strength due to matric suction were considered by some of the analyses, using ϕ^b equal to $\phi'/2$. The clay foundation was modeled with constant properties in both the seepage and stability analyses. The foundation had little influence on the transient seepage because of its low

hydraulic conductivity. The surface described above does not intersect the foundation; however the foundation strength may be important for the critical surface.

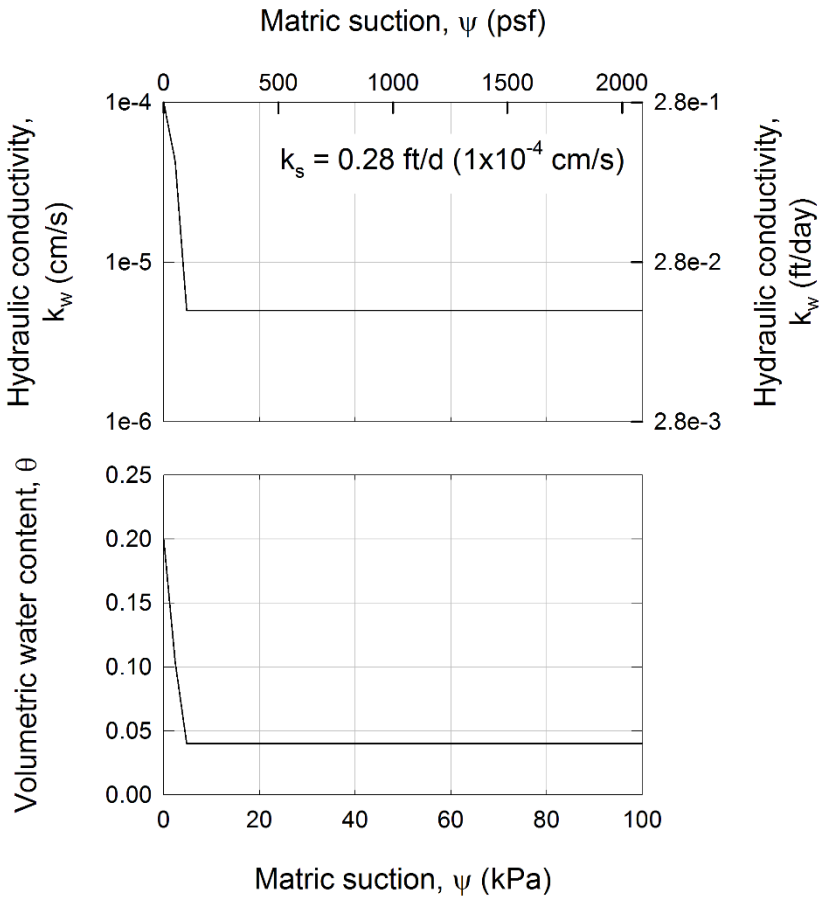

Figure 2-7. Hydraulic conductivity function and soil-water characteristic curve assumed for silty sand fill in Example 2-2

The factor of safety for the trial surface varied from greater than 1.9 at low c_v to about 1.05 for high c_v as shown in Figure 2-8. The typical range of c_v given by Duncan et al. (1990) for silty sand is shown shaded for comparison. For this geometry and trial surface, the most significant changes in factor of safety occur within the typical range of c_v. The compressibility assigned to the fill would clearly have a significant impact on conclusions regarding the stability of the landslide slope during a flood event, if transient seepage analysis were used to predict pore pressures for effective stress stability analysis.

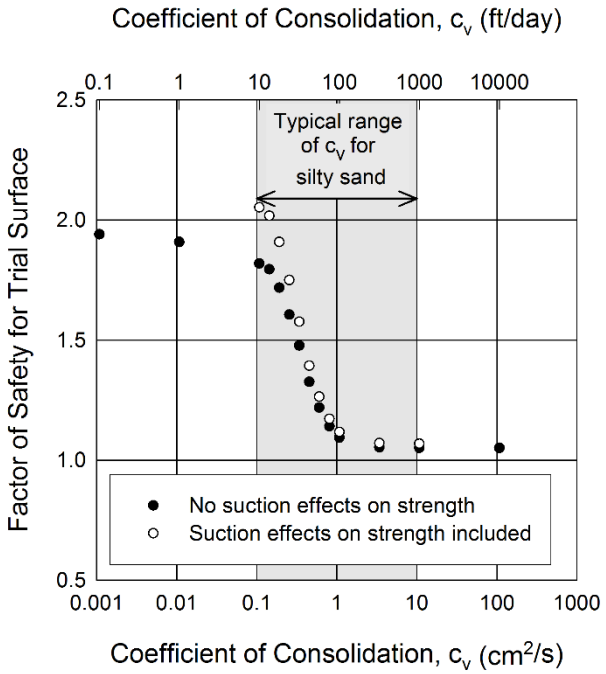

Figure 2-8. Factor of safety for the specified surface after one month of elevated water

The initial soil conditions, soil-water characteristic curve, and hydraulic conductivity function for the hypothetical levee in Example 2-2 are all simplified for illustration purposes. Coupling between boundary loads and pore pressures is also ignored. This example shows that the effect of soil compressibility represented by c_v cannot be ignored in transient seepage analyses even in cases where other simplifying assumptions may be justified. Stability analyses that employ transient seepage analysis to predict pore pressures must consider both compressibility and hydraulic conductivity in order to result in meaningful values of factor of safety.

Conclusions

Pore pressures predicted by Bishop's or Barrett and Moore's $\overline{B}$ methods can be used to establish an approximate upper bound for pore pressures after rapid drawdown which is useful to check the results of more complicated numerical analyses. These upper bound pore pressures are too high for well-compacted soil because the effects of shear dilatancy are ignored.

Uncoupled transient seepage analyses do not model the pore pressure response to either the change in confining or the change in shear stress. For this reason, the uncoupled method is inappropriate for predicting pore pressures when significant changes in boundary loading affect the region of concern. This is most significant for rapid drawdown because the boundary load changes on the same side of the embankment as the potential failure.

To achieve realistic results, coupled transient seepage analyses are required if effective stress stability analysis is used. These analyses must model soil behavior accurately, including saturated and unsaturated hydraulic conductivity, compressibility, and volume changes due to changes in shear stress (soil dilatancy). Such complex analyses are not feasible for most projects but are useful for enhancing our understanding of slope behavior during drawdown.

Soil compressibility cannot be ignored in transient seepage analysis. The rate of seepage development in the saturated zone, and the length of time required to reach steady state seepage is controlled completely by the coefficient of consolidation.

3. Stress System Effects on Undrained Strength

The appropriate undrained strength of compacted clay for rapid drawdown analysis may differ from that measured in the isotropically consolidated undrained (ICU) triaxial compression (TC) test because of the effects of anisotropy in the effective stress strength parameters and the influence of compaction prestress. Differences between the stress system imposed in the laboratory and that which prevails in the field also changes undrained strength. This latter group of stress system effects on undrained strength will be assessed in this chapter.

Inherent effective stress anisotropy can greatly affect the variation in shear strength with the direction of shearing. Soil may be weaker when sheared along certain planes or when stresses are applied in particular directions. This effect is highly dependent on the specific soil and is most often encountered in highly structured materials, such as varved clays. Inherent anisotropy is less likely to occur in compacted fills, at least at a scale measureable in the laboratory, and will not be considered by this analysis.

ICU triaxial compression tests are the most common type of laboratory test for obtaining consolidated undrained strengths, and are not likely to be replaced in practice by other more complicated tests. The purpose of this chapter is to compare the undrained strength measured in the ICU-TC test to the strength that is appropriate for the field stress system. These stress system effects have been divided into three groups:

- **Anisotropic consolidation** – The isotropic consolidation stresses in the ICU test differ from field conditions in which soil is typically consolidated under an anisotropic stress system.

- **Plane strain effects** – Unlike the field, failure does not occur in plane strain in the triaxial test because the intermediate principal stress must equal either the major or minor principal stress.
- **Principal stress rotation during shear** – Principal stress rotation from consolidation to failure has been shown to reduce undrained strength (e.g. Ladd et al. 1977). No stress rotation occurs during triaxial compression.

The undrained strength ratio (*USR*) will be used to compare these stress system effects. The *USR* can be defined as

$$USR = \frac{s_u}{\sigma'_{1c}} = \frac{\sigma_{df}}{2\sigma'_{1c}} \tag{3-1}$$

where:

s_u = undrained strength,

σ_{df} = deviator stress at failure, and

σ'_{1c} = major effective consolidation stress.

The use of *USR* allows s_u from different types of tests to be compared at different values of σ'_{1c}. The *USR* may not be constant over a large range of stress, so it is good practice to compare *USR* at similar values of σ'_{1c}, even for normally consolidated (NC) clays. Unless otherwise noted, failure has been defined as maximum principal stress difference.

The goal of this chapter is to develop a set of adjustment factors, denoted by an *R*, that will relate values of undrained strength measured with ICU triaxial tests to appropriate strengths for rapid drawdown analysis. The adjustment factors will be developed by examining the theoretical basis and experimental evidence available for each type of effect. The three factors will adjust for

Anisotropic consolidation: $R_K = USR_{ACU-TC} / USR_{ICU-TC}$ (3-2)

Plane strain: $R_{PS} = USR_{PSC} / USR_{ACU-TC}$ (3-3)

Stress rotation: $R_\rho = USR_\rho / USR_{PSC}$ (3-4)

where:

USR_{ACU-TC} = *USR* for anisotropically consolidated triaxial compression,

USR_{ICU-TC} = *USR* for isotropically consolidated triaxial compression,

USR_{PSC} = *USR* for plane strain compression, and

USR_ρ = plane strain *USR* for a principal stress rotation of ρ degrees.

Anisotropic Consolidation, R_K

The effects of the consolidation stress state on undrained strength have been considered by many researchers. Rutledge (1947) postulated that s_u is a function of solely σ'_{1c} for normally consolidated clay, which implies $R_K = 1$ or $USR_{ICU} = USR_{ACU}$. In Figure 3-1, Rutledge's hypothesis implies that all specimens consolidated on the dotted $\bar{A} = 1$ line will have the same undrained strength, where $\bar{A} = \Delta u / (\Delta\sigma_1 - \Delta\sigma_3)$. However, Henkel (1960) observed experimentally that higher σ'_{1c} was required to anisotropically consolidate a specimen to the same void ratio as an ICU specimen. Whitman et al. (1960) and Henkel and Sowa (1963) suggested that s_u was related directly to the mean effective consolidation stress, σ'_{mc}. If undrained strength depends only on σ'_{mc}, then all specimens consolidated along the dashed $\bar{A}$ = 1/3 line would have the same strength.

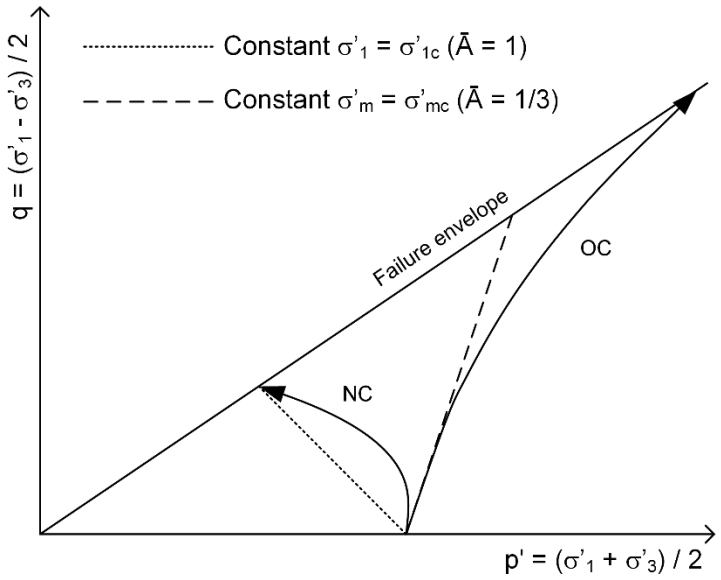

Figure 3-1. Typical undrained effective stress paths for normally consolidated and over-consolidated specimens compared with constant axial stress and constant mean stress paths

Figure 3-1 also shows the typical effective stress paths followed by normally consolidated (NC) and moderately to highly over-consolidated (OC) clays in undrained triaxial compression at constant water content. In general, effective stress paths for clays do not follow either the constant major effective stress or the constant mean effective stress lines. In both cases, the curvature of the effective stress paths means that $\bar{A}$ is not constant but varies as a function of strain and/or shear stress.

All of the stress states along the undrained (constant volume) stress paths in Figure 3-1 have the same water content or void ratio. Donaghe and Townsend (1978) observed that consolidated water contents for ACU tests were higher than those for ICU tests with the same σ'_{1c}. They related the volumetric strain during consolidation to both the effective octahedral normal and octahedral shear stress.

Attempts to Develop an Analytical Method for Calculating R_K

Taylor (1948) suggested that the undrained effective stress path after anisotropic consolidation will follow the same effective stress path for isotropic consolidation to the same water content. Taylor's assumption has been used to predict behavior following anisotropic consolidation from simpler ICU triaxial tests (e.g. Lowe and Karafiath 1960b). Henkel's 1960 data on remolded Weald clay appears to confirm Taylor's hypothesis. Others, such as Whitman et al. (1960) and Ladd (1965), have presented data in which the effective stress path for anisotropically consolidated specimens differed from those from isotropic consolidation to the same water content.

An analytical method has been developed to calculate R_K from the results of ICU triaxial compression tests, starting with Taylor's assumption that effective stress paths are unique for a particular consolidated water content. The method is derived in Appendix A. If the adjustment factor is desired for a particular principal consolidation stress ratio, PSR_c, the point at which this stress ratio is reached in an ICU test can be determined from the test data. The corresponding pore pressure parameter, $\bar{A}_c$, can also be determined from the data. It then follows from Taylor's assumption that the adjustment factor, R_K, can be calculated as

$$R_K = \frac{USR_{ACU-TC}}{USR_{ICU-TC}} = \frac{\bar{A}_c\left(PSR_c - 1\right) + 1}{PSR_c} \qquad (3\text{-}5).$$

where:

$USR_{ACU\text{-}TC}$ = *USR* for anisotropically consolidated triaxial compression,

$USR_{ICU\text{-}TC}$ = *USR* for isotropically consolidated triaxial compression,

$\bar{A}_c$ = pore pressure parameter in an ICU test at a given PSR_c, and

PSR_c = effective principal stress ratio at which R_K is desired.

As PSR_c and $\bar{A}_c$ vary during an ICU test, the value of R_K from Eqn. (3-5) will also vary.

The validity of this analytical method for obtaining R_K can be assessed by comparing values predicted with Eqn. (3-5) to those calculated directly from ICU and ACU test data. One such set of data is the triaxial compression tests performed by Donaghe and Townsend (1979) on East Atchafayala Basin Protection Levee (EABPL) clay and Vicksburg Buckshot clay (VBC).

Values $\bar{A}_c$ were determined at a range of PSR_c for four ICU tests from Donaghe and Townsend's data. Using Eqn. (3-5), the variation of R_K with PSR_c was calculated and is plotted in Figure 3-2. Specific values of R_K were calculated from the actual strengths measured in their triaxial tests. The relationship predicted by Eqn. (3-5) appears to provide a lower bound to the measured values. R_K is higher than the theoretical relationship because the ACU undrained strengths are slightly higher than would be predicted by Taylor's assumption.

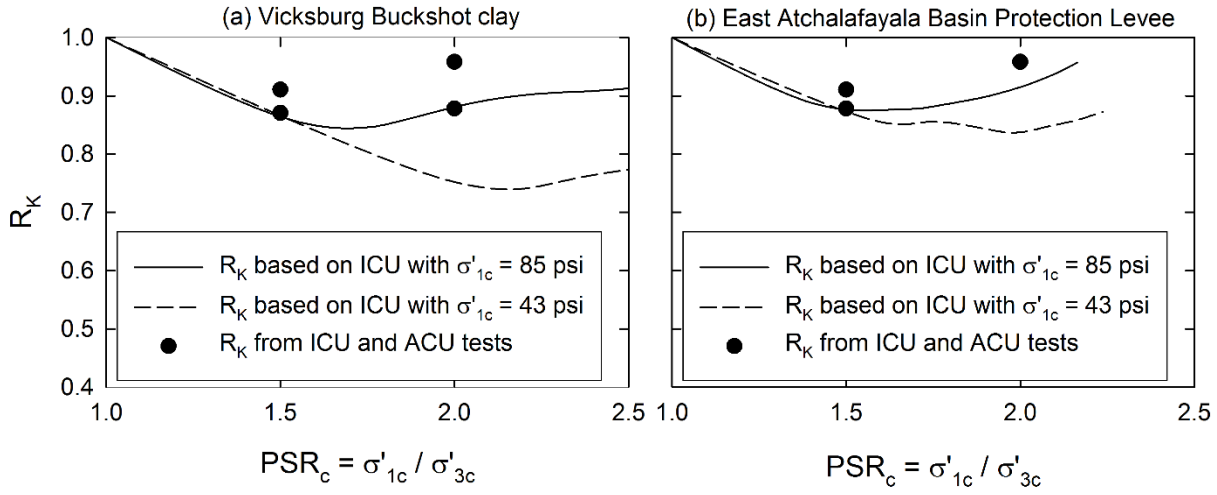

Figure 3-2. Calculated and measured values of R_K for normally consolidated VBC and EABPL (after Donaghe and Townsend 1979)

Donaghe and Townsend's ACU tests developed lower excess pore pressures at low strains compared to the ICU tests at similar stress ratios. The lower pore pressures led to higher undrained strengths than those expected for ICU tests consolidated to the same void ratio. Thus, contrary to Taylor's assumption, ICU and ACU specimens consolidated to the same water

content do not always follow the same effective stress path after consolidation, as reported by Whitman et al. (1960) and Ladd (1965).

ICU and ACU Data – Normally Consolidated Clays

Ladd (1965) and Mayne (1985a) both collected and compared ICU and ACU triaxial test data from the geotechnical literature. Ladd found that $USR_{ACU\text{-}TC}$ was less than $USR_{ICU\text{-}TC}$ for five out of six normally consolidated clays with R_K ranging from 0.82 to 1.1. Ladd concluded that the effective stress paths for triaxial compression tests are not unique, and that ICU tests cannot be used to predict ACU results. Surveying data from 42 NC clays, Mayne found that on average the value of R_K was 0.88 for triaxial compression in normally consolidated clay. From 14 over-consolidated clays, Mayne found that R_K ranges between 0.75 and 1 with an average value of 0.87. Mayne's analysis did not account for the effect of different consolidation stress ratios.

The test results from most of the references in Ladd (1965) and Mayne (1985a) were collected and reviewed. The value of R_K was determined as the ratio between the ACU and ICU undrained strength ratios. Where possible the undrained strength ratios were compared at similar values of σ'_{1c} to eliminate the influence of variation in *USR* with σ'_{1c}.

The collected data for 38 NC clays are presented in Figure 3-3. A detailed summary of the data is included in Appendix B. The values of R_K have been plotted against the degree of shear stress mobilization at consolidation to account for the fact that different soils have different principal stress ratios at failure. The degree of shear stress mobilization has been defined as the principal stress difference due to anisotropic consolidation divided by the principal stress difference at failure in an isotropically consolidated test.

Two clays have been isolated from the data set due to unusual behavior. The Santander clay (Sanchez et al. 1979) had unusually shaped stress paths, which were attributed by the authors to

the use of lubricated end platens. The data for this clay clearly represented different behavior from that seen in most TC tests. The Goose Lake clay specimens (Khera and Krizek 1967) were formed in a manner which oriented particles parallel to the specimen axis. This orientation was different than that encountered in most normally consolidated clays. Due to their deviation from typical behavior, these two clays have been disregarded in the analysis of the data. The 36 remaining clays have a median value of R_K of 0.9. If R_K is assumed to be constant with respect to mobilized shear stress at consolidation (or PSR_c), the standard deviation is about 0.1.

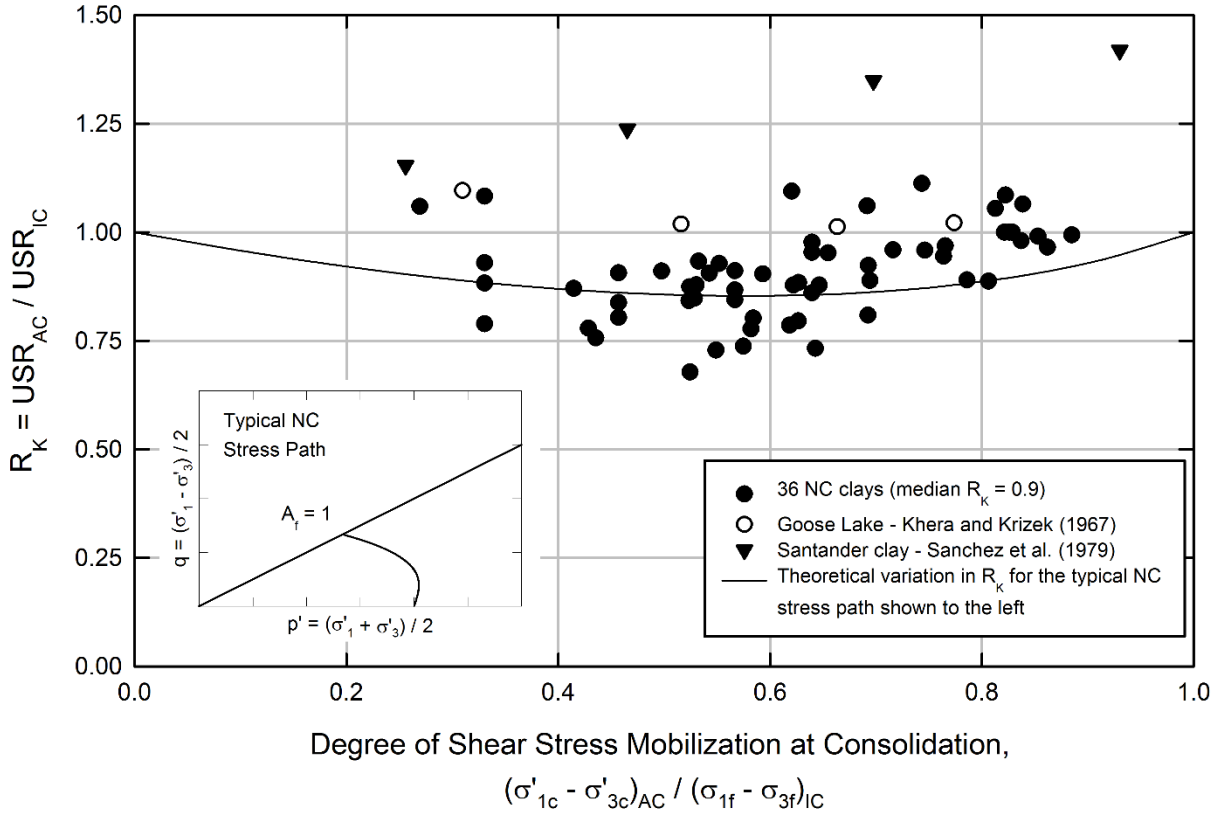

Figure 3-3. Variation in R_K with degree of shear stress mobilization based on published values (see Appendix B for data and references).

The theoretical relationship between R_K and degree of shear strength mobilization based on Eqn. (3-5) is shown by the solid line in Figure 3-3. This line corresponds to a typical NC stress

path with $\bar{A}_f = 1$ as shown in the lower left-hand corner of Figure 3-3. The data has a slightly concave upward trend, following the expected trend.

ICU and ACU Data – Overconsolidated Clays

The collected data for nine OC clays are presented in Figure 3-4 and summarized in Appendix B. The data have been separated into tests that were performed using K_0 consolidation and those in which the value of PSR_c was arbitrarily selected by the researchers. The overconsolidation ratio, *OCR*, is defined as the ratio of the maximum past major effective consolidation stress to the major effective consolidation stress prior to shear.

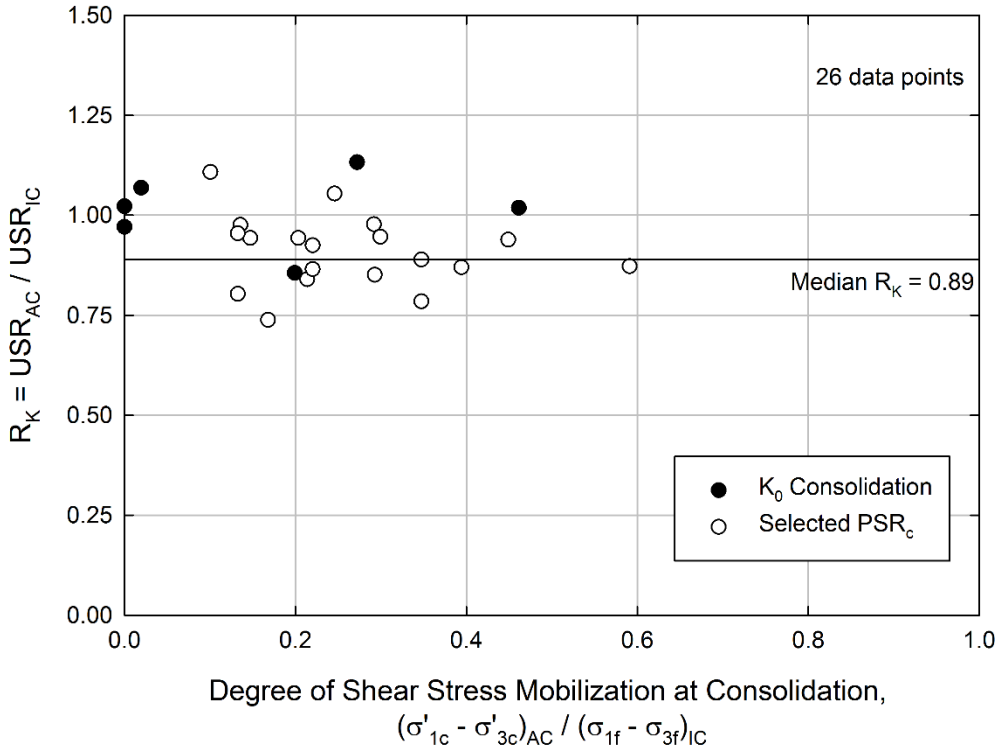

Figure 3-4. Variation of R_K for over-consolidated clay – different types of consolidation (see Appendix B for data and references)

In general, R_K decreases as the degree of shear stress mobilization increases and has a median value of 0.89 for overconsolidated conditions. If R_K is assumed to be constant, the standard deviation is about 0.1. Overconsolidated K_0 tests tend to have low mobilized shear stress as *OCR*

increases and K_0 approaches 1. The three tests with K_0 near 1 have R_K of about 1 as expected since the consolidation conditions were essentially isotropic.

The variation in R_K with *OCR* was also considered. No discernable trend in R_K was found in with respect to *OCR*.

ICU and ACU Data – Compacted Clays

Little data exists in the literature comparing the effects of isotropic and anisotropic consolidation on compacted clays. The effects of compactive prestress (similar to over-consolidation) on the *USR* make the behavior of compacted clays more difficult to assess. Data are presented in Figure 3-5 for four clays tested over a range of consolidation stress conditions. The Riverview clay was dilative and did not reach maximum deviator stress before the end of the tests, so 10% axial strain was chosen as a failure criterion. Detailed data and references are summarized in Appendix B.

The median value of R_K was 0.94 for these four compacted clays. If R_K is assumed to be constant, the standard deviation is about 0.12. A slight concave upward trend for compacted clays is observed in R_K with respect to the degree of shear stress mobilization during consolidation.

Since it is difficult to calculate an *OCR* for compacted clays, the effects of prestress are examined by plotting R_K against σ'_{1c} in Figure 3-6. The tests on Higgins clay and Monarch clay by Lee and Morrison (1970) were performed at very high consolidation stresses, mostly beyond the range of interest for rapid drawdown. The full range of consolidation stresses is shown in Figure 3-6(a). R_K tends to start below 1 and tends toward 1 at very high stresses. The tests in the lower stress range shown in Figure 3-6(b) indicate that R_K is consistently below 1 except at

stresses below about 50 psi (345 kPa). Below this stress, there is a considerable amount of scatter in the measured values of R_K.

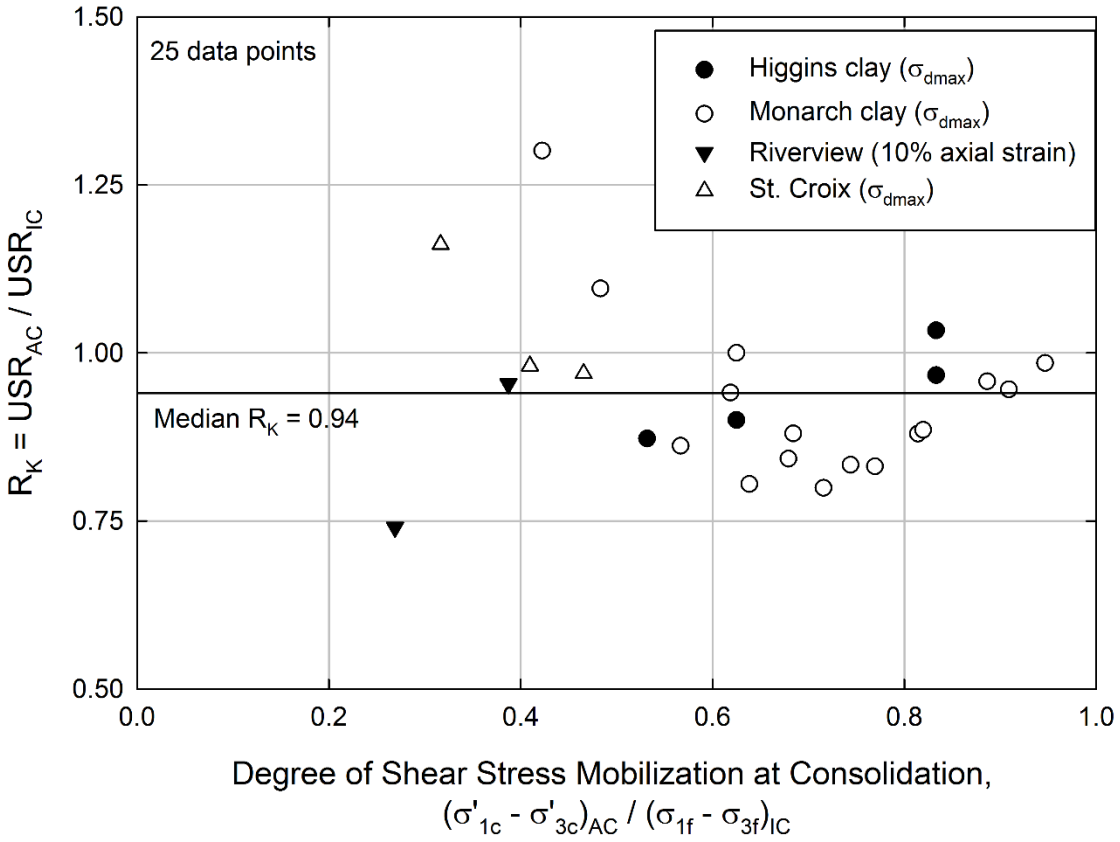

Figure 3-5. Variation of R_K with degree of shear stress mobilization for compacted clays (data from Lee and Morrison 1970, Castellanos 2011, Johnson and Lovell 1979)

Summary - R_K

The consolidated void ratio or water content of saturated clay is related to the major effective consolidation stress but is also influenced by the consolidation shear stress. For normally consolidated clays, this is especially true for consolidation stress ratios that mobilize shear stresses midway between isotropic and failure. This implies that s_u is not a function solely of σ'_{1c}.

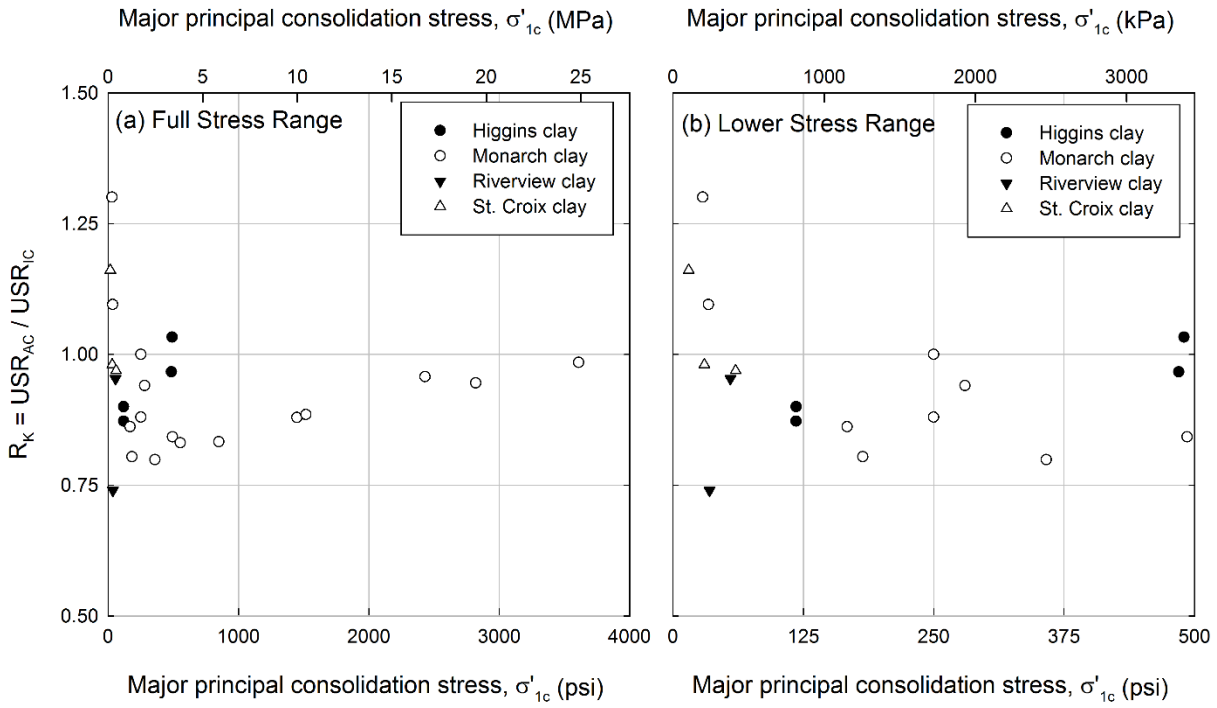

Figure 3-6. Variation in R_K with consolidation stress, σ'_{1c} – (a) full range and (b) lower stress range

Taylor's assumption of a unique relationship between effective stress path and void ratio has sometimes been used to calculate ACU strengths directly from ICU test data. ACU tests develop less excess pore pressure at low strains, which leads to higher undrained strengths than those implied by Taylor's assumption. For this reason, ACU strengths are more appropriately obtained from specific tests or from empirically based adjustment factors, like R_K. The following median values of R_K were found based on a review of the literature:

- NC clay: R_K = 0.9, standard deviation = 0.1
- OC clay: R_K = 0.89, standard deviation = 0.1
- Compacted clay: R_K = 0.94, standard deviation = 0.12

Plane Strain Effects, R_{PS}

Triaxial vs. Plane Strain Conditions

The triaxial test used in conventional geotechnical laboratory testing applies an axisymmetric stress system, such that the intermediate principal stress is always equal to either the major or the minor principal stress. In contrast, slope stability problems are most often evaluated in two-dimensions, assuming that plane strain conditions prevail and the intermediate principal stress is not equal to either the minor or major principal stress.

Henkel and Wade (1966) showed that σ'_2 is approximately equal to $K_0 \times \sigma'_1$ during undrained plane strain shear. Bishop (1966) suggested that the effects of the intermediate principal stress could be assessed using

$$b = \frac{\sigma_2 - \sigma_3}{\sigma_1 - \sigma_3} \tag{3-6}$$

where:

b = intermediate principal stress ratio between 0 and 1.

If K_0 is about 1-sin ϕ', the plane strain value of σ'_2 is equal to about $0.5(\sigma'_1 + \sigma'_3)\times\cos^2\phi'$ (Bishop 1966). Using the same assumptions, b can be approximated by $(1 - \sin \phi')/2$ for plane strain, resulting in values of b in the range of 0.2 (ϕ' = 37°) to 0.3 (ϕ' = 24°).

Ideally, the results of plane strain triaxial tests would be used for stability slope stability computations, but practically speaking, plane strain tests remain in the realm of research because of the specialized equipment and expertise required to perform these tests. Since plane strain tends to increase both drained and undrained strength, it is often considered conservative to ignore these effects as an additional safety factor when using strength parameters from triaxial

tests (Duncan and Wright 2005). Even so, it is appropriate to consider the adjustment factor, R_{PS}, when examining the factors that affect undrained strength for rapid drawdown.

Theoretical Basis for R_{PS}

Henkel and Wade (1966) and Vaid and Campanella (1974) found that the octahedral shear stress at failure was approximately equal for triaxial and plane strain tests. Based on this approximation, Ladanyi (1967) showed that the undrained strength in plane strain is expected to be about 15% higher than that measured in triaxial compression, assuming a Poisson's ratio, ν, of 0.5, i.e. R_{PS} = 1.15. For ν ranging between 0.4 and 0.5 and ϕ' between 25 and 35°, Ladanyi's equations can be used to show that R_{PS} theoretically varies between 1.1 and 1.15, if the octahedral shear stress is equal at failure for plane strain and triaxial conditions.

Experimental Data for R_{PS}

Undisturbed / Remolded Clay

The theoretical values of R_{PS} presented in the previous section can be validated by examining experimental data from the literature. Ladd and DeGroot (2003) report an R_{PS} value of 1.09 for compression based on anisotropically consolidated tests on six undisturbed and remolded clays. These data along with four additional sets of test results are presented in Table 3-1. The average value of R_{PS} from the ten clays in Table 3-1 is 1.12.

Results from isotropically consolidated triaxial compression and plane strain compression tests are given in Table 3-2. While these tests do not include the effects of anisotropic consolidation, the values of R_{PS} are similar to those found in Table 3-1.

Compacted Clay

Lee and Morrison (1970) presented the results of ICU and ACU triaxial compression tests on two compacted clays. Specimens of Monarch kaolinite (LL = 44, PI = 21) were compacted to

dry unit weights corresponding to between 95% and 99% of Standard Proctor maximum dry density at water contents between 3 and 5% wet of optimum. Specimens of Higgins clay (LL = 38, PI = 21) were compacted to dry unit weights corresponding to between 98% and 99% of Modified Proctor maximum dry density. The Higgins clay samples were compacted to two different water content ranges: 2-3% dry of optimum and about 6.5% wet of optimum. Lee and Shubeck (1971) performed plane strain compression tests on the same two clays. The plane strain test specimens were reportedly compacted in the same ranges as the triaxial test specimens; however, specific compaction conditions for each test were not reported.

Table 3-1. Comparison of undrained strength ratios in triaxial compression and plane strain compression for ten normally consolidated (K_0) clays

Soil	LL	PI	$USR_{ACU\text{-}TC}$	USR_{PSC}	R_{PS}	Source
San Francisco Bay Mud (undisturbed)	88	45	0.35	0.37	1.05	Duncan and Seed (1966)
Weald clay (remolded)	46	26	0.26	0.28	1.08	Henkel and Wade (1966)
Boston Blue clay (remolded)	41	21	0.33	0.34	1.03	Ladd et al. (1971)
Portsmouth sensitive clay (undisturbed)	35	15	0.27	0.35	1.29	Ladd and Edgers (1972)
Atchafalaya clay (undisturbed)	95	75	0.24	0.31	1.29	Ladd and Edgers (1972)
Spestone Kaolinite (remolded)	72	32	0.21	0.26	1.26	Parry and Nadarajah (1973) and Hambly (1972)
Haney clay (undisturbed)	44	18	0.27	0.30	1.11	Vaid and Campanella (1974)
Connecticut Valley varved clay (undisturbed)	65	39	0.25	0.28	1.12	Ladd et al. (1977)
AGS CH clay (undisturbed)	71	40	0.32	0.37	1.15	Ladd et al. (1977)
Hokkaido clay (remolded)	86	49	0.31	0.35	1.13	Mitachi and Kitago (1980)
				Average value:	1.12	

Table 3-2. Comparison of undrained strength ratios for three isotropically consolidated (NC) clays tested in true triaxial and hollow cylinder tests.

Soil	LL	PI	USR_{ICU-TC}	USR_{PSC}	R_{PS}	Source
Kaolinite[A] (remolded)	57	25	0.43	0.45	1.05	Broms and Casbarian (1965)
Kaolinite[B] (remolded)	57	25	0.43	0.44	1.03	Broms and Casbarian (1965)
Osaka clay, σ'_{1c} = 2 kg/cm^2 (remolded)[C]	69	49	0.40	0.42	1.07	Shibata and Karube (1965)
Osaka clay, σ'_{1c} = 1 kg/cm^2 (remolded)	64	37	0.47	0.61	1.29	Shibata and Karube (1967)
Osaka clay, σ'_{1c} = 2 kg/cm^2 (remolded)	64	37	0.41	0.49	1.19	Shibata and Karube (1967)

[A] Results from hollow cylinder tests with no stress rotation, $b = 0 \approx$ TC and $b = 0.25 \approx$ "plane strain"
[B] Results from hollow cylinder tests with no stress rotation, $b = 0 \approx$ TC and $b = 0.5 \approx$ "plane strain"
[C] Results from "true" triaxial compression tests, $b = 0 =$ TC and $b = 0.24 \approx$ "plane strain"

Figure 3-7 shows the undrained strengths of compacted Monarch kaolinite for triaxial tests with PSR_c of 2 and 2.25 and plane strain tests. This data suggests that the strengths are essentially the same and that $R_{PS} = 1$ for Monarch clay. For compacted Higgins clay, Figure 3-8 shows plane strain strengths that are slightly higher ($R_{PS} = 1.05$) than those from triaxial compression.

Lee and Morrison's tests suggest that an increase in strength due to plane strain may not be experienced by all compacted clays. It is difficult to assess whether this is the true behavior of the compacted clay or a side effect of other factors. One factor that may have affected these results is the initial compaction conditions of the clays. Recent triaxial testing on compacted Oak Harbor clay (Chapter 6) has shown that the undrained strengths in ICU and ACU tests vary considerably due to small changes in the relative compaction. The relative compaction of the Monarch clay specimens varied over 4%, which could have led to significant differences in strengths especially at low stresses. The compaction conditions for the plane strain tests were not given in detail, so it is not possible to assess whether this is the actual cause for deviation in

the trend. The Higgins clay triaxial specimens were compacted to a much tighter range of initial conditions, which presumably was also the case for to the plane strain specimens. This smaller range of initial dry unit weights allows the two types of test to be compared more accurately. The Higgins clay results show a slight increase in strength for plane strain.

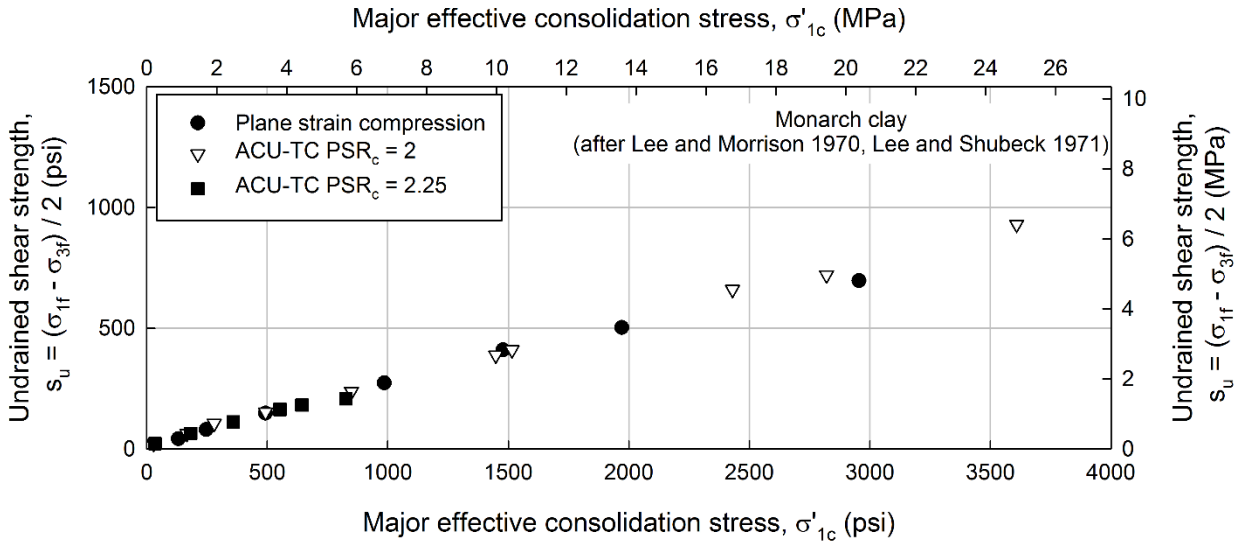

Figure 3-7. Variation in s_u with major effective consolidation stress for compacted Monarch kaolinite (after Lee and Morrison 1970 and Lee and Shubeck 1971)

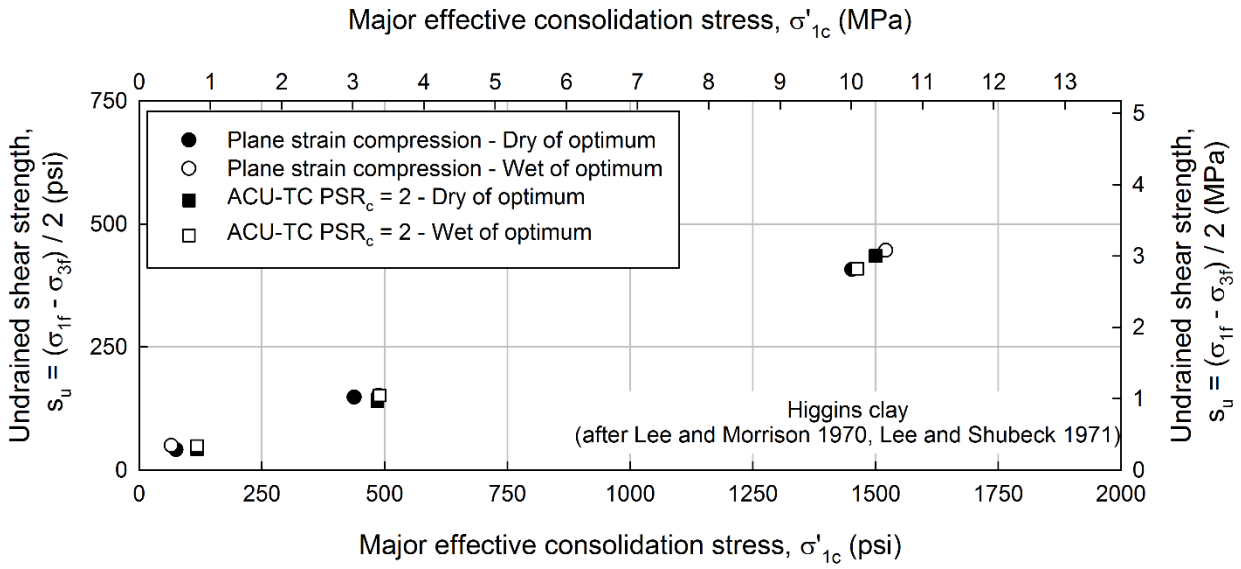

Figure 3-8. Variation in s_u with major effective consolidation stress for compacted Higgins clay (after Lee and Morrison 1970 and Lee and Shubeck 1971)

Summary - R_{PS}

Based on theoretical considerations and the available data, a working value of R_{PS} = 1.1 is recommended for relating undrained strengths in triaxial compression to plane strain.

Additional data on the behavior of compacted clays in plane strain are needed, especially for the relatively low stresses that are important for rapid drawdown analysis.

Principal Stress Rotation, R_ρ

The final stress system effect to be considered is principal stress rotation during loading from consolidation to failure. Under field and some laboratory conditions, the orientation of the stress system applied to a soil element is able to rotate in response to new loading conditions. One way to quantify this change is to measure the angle of rotation, ρ, of the major principal stress as illustrated in Figure 3-9.

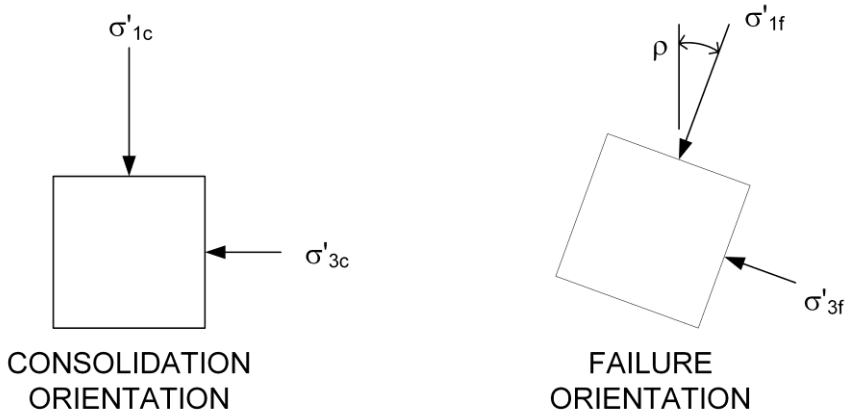

Figure 3-9. Rotation of principal stresses from consolidation to failure.

Hansen and Gibson (1949) explained the theoretical variation of *USR* due to stress system for a soil, assuming isotropy with respect to shear strength parameters and compressibility. The *USR* predicted in this manner was greatest for active conditions (compression) and least for passive conditions (extension).

Duncan and Seed (1966) observed that undrained strength anisotropy in clay can be divided into two components: 1) inherent anisotropy due to differences in effective stress strength parameters depending on the orientation of the failure plane and 2) differences in the pore pressure response during undrained loading caused by the orientation of the applied stress system, such as pictured in Figure 3-9. Based on the results of plane strain compression and extension tests, Duncan and Seed (1966) predicted that the plane strain *USR* for San Francisco Bay Mud should be highest for $\rho = 0°$ (compression), reach a minimum when ρ is approximately 45° (≈DSS) and then increase as ρ approaches 90° (extension). They confirmed this general trend using UU triaxial tests trimmed to different orientations. Duncan and Seed attributed most of the variation in undrained strength to an altered pore pressure response caused by principal stress rotation.

Ladd et al. (1977) and Ladd and DeGroot (2003) have compiled *USR* from triaxial compression (TC), direct simple shear (DSS), and triaxial extension (TE) tests as plotted in Figure 3-10. The failure mode and plasticity index to both affect the *USR*. However, Figure 3-10 is somewhat misleading because all three tests have different relative σ'_2 or different *b*. In order to accurately compare strengths, the results of compression, direct simple shear, and extension should be compared at a similar value of *b*, preferably corresponding to plane strain for slope stability. Problems also exist with the use of triaxial extension tests to measure strength, which will be discussed in the following section.

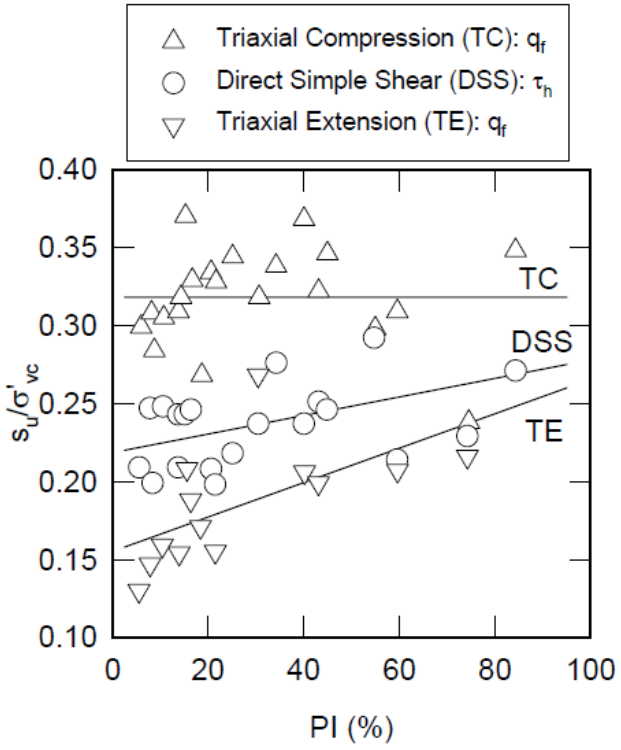

Figure 3-10. Undrained strength ratios from CK_0U tests on NC clays and silts (from Ladd and DeGroot 2003 – determined fair use)

Problems with Triaxial Extension Tests

Triaxial extension tests have often been assumed to provide adequate shear strength parameters for the $\rho = 90°$ condition. However, the triaxial extension test has several problems, which make it inappropriate for determining shear strength. The triaxial extension test:

- Imposes a stress system dissimilar to field conditions,
- Produces non-unique results for $\rho = 90°$,
- Has difficulties with test specimens and procedure, and
- Requires more advanced equipment and expertise to perform.

As a result of these problems, triaxial extension tests are not an appropriate means for assessing undrained strengths for slope stability evaluations.

Dissimilar Stress System

The foundation soils at the toe of an embankment or beyond the toe in a soft foundation are loaded in plane strain lateral compression, which is equivalent to plane strain extension. In this case, the major and minor principal stresses rotate 90° but the intermediate principal stress remains oriented parallel to the slope. Laboratory tests have shown that the parameter *b* is in the range of 0.2 to 0.3 at failure as shown in Figure 3-11(a).

The ACU triaxial extension test begins with the major consolidation stress applied vertically, and the minor and intermediate consolidation stresses equal to the triaxial cell pressure as shown in Figure 3-11(b). During undrained shear, the vertical stress is decreased and reaches the cell pressure at very low strains. As the vertical stress continues to decrease, the cell pressure becomes the major and intermediate stress, while the vertical stress becomes the minor principal stress. For most of the test, σ_1 and σ_2 are equal, resulting in *b* of 1. The only design condition where this occurs in geotechnical engineering is at the center of an excavation.

Broms and Casbarian (1965) showed that $\bar{A}_f$ and ϕ' both increase as the intermediate principal stress increases (*b* increases) based on the results of hollow cylinder tests with no stress rotation ($\rho = 0°$). The friction angle stopped increasing once *b* exceeded 0.4, resulting in the highest *USR* for tests with *b* of 0.3 to 0.4, which is approximately equal to plane strain. Shibata and Karube (1965) present similar results for true triaxial compression tests with different values of *b*. The undrained strength ratio increases slightly as *b* increases up to about 0.34 after which point the *USR* begins to decrease. Their results are also plotted in Figure 3-12.

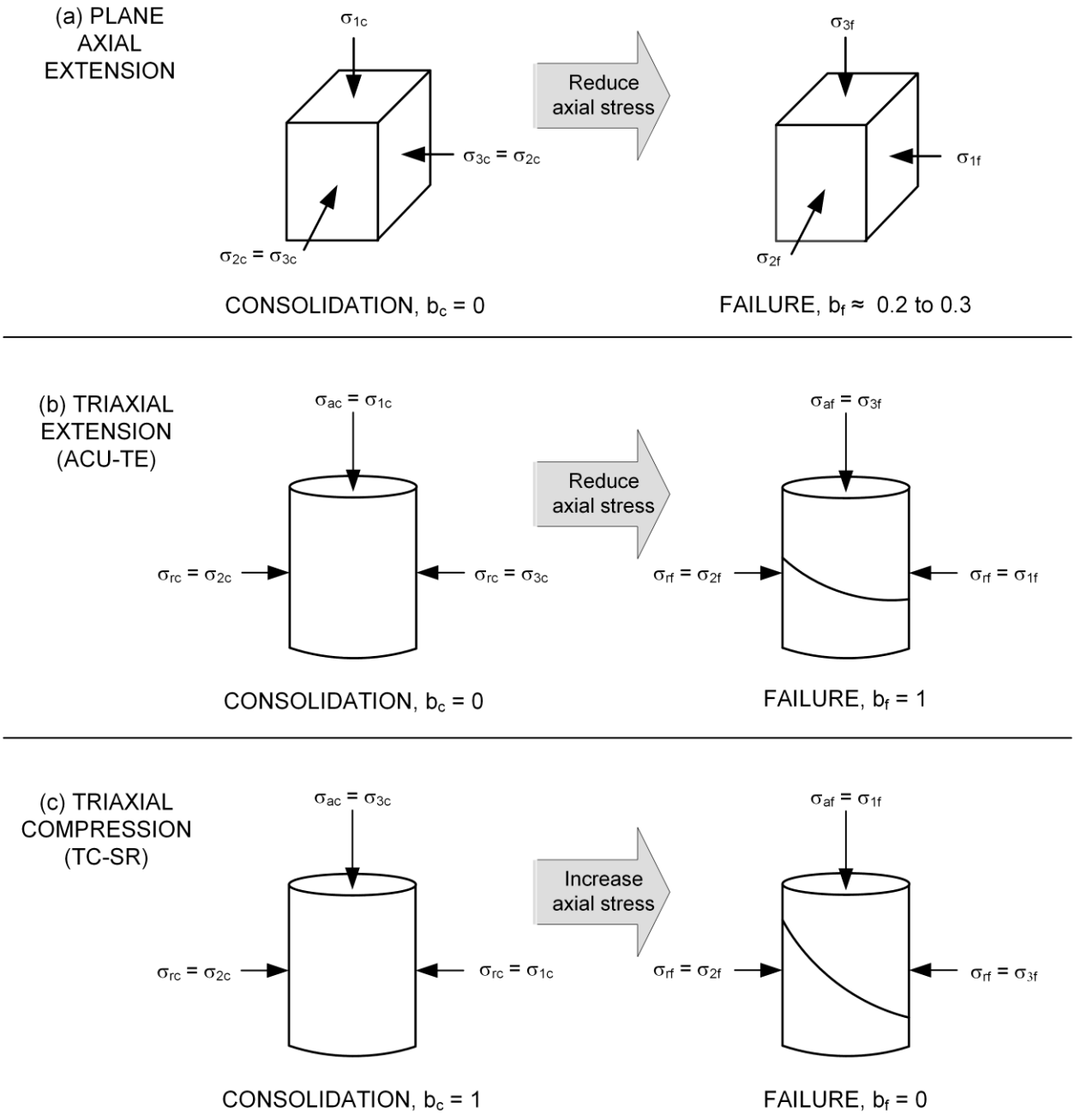

Figure 3-11. Comparison of stress states for (a) plane strain extension (PSE), (b) triaxial extension (TE), and (c) triaxial compression with stress rotation (TC-SR)

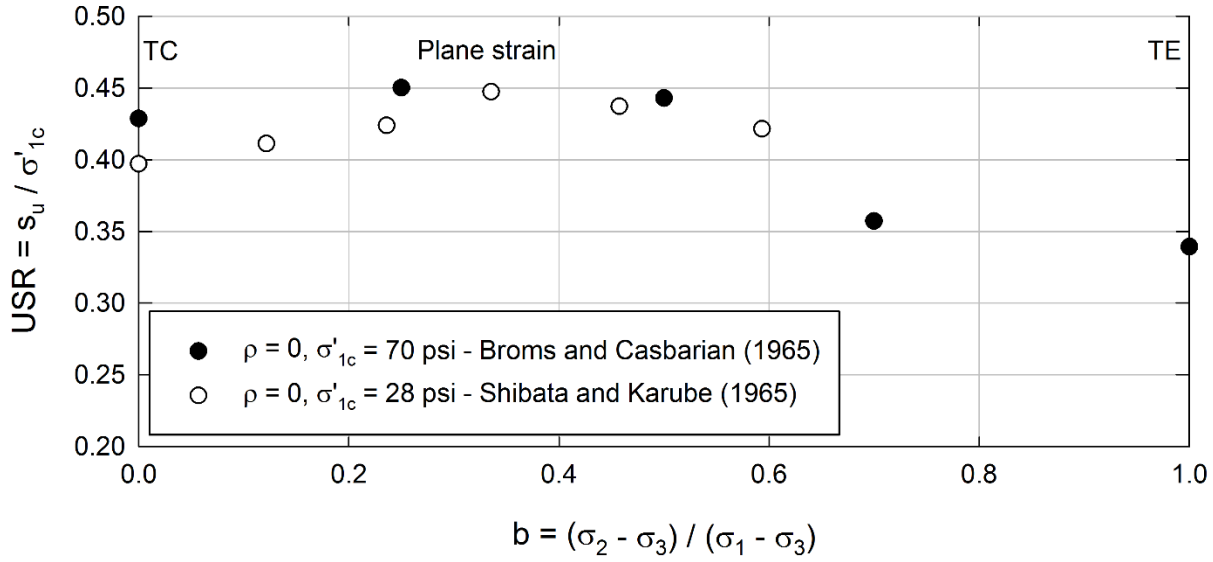

Figure 3-12. Effects of intermediate principal stress level, *b*, on *USR* (after Broms and Casbarian 1965, and Shibata and Karube 1965)

The variation in *USR* shown in Figure 3-12 is solely due to changing σ'_2 and is not due to stress rotation. Based on these results, the undrained strengths from TE tests ($b = 1$) would be expected to be 20% less than those from TC tests ($b = 0$), solely due to the effect of σ'_2.

Because of the effect of the intermediate principal stress, it is difficult to directly model field conditions in the laboratory. The effect of *b* must either be corrected prior to analysis or recognized as conservative and ignored, if appropriate. The effect of the intermediate principal stress does not vary along a failure surface and is inherently different from the effects of principal stress rotation. Figure 3-12 makes it clear that the $b = 0$ condition (TC) test yields much closer strength to the actual plane strain conditions than the $b = 1$ condition imposed by the triaxial extension test. The high intermediate principal stress is an irreconcilable flaw in the triaxial extension test.

Non-Unique Results for $\rho = 90°$

Principal stress rotation corresponding to $\rho = 90°$ can be also obtained in triaxial compression as shown in Figure 3-11(c). Triaxial compression tests with stress rotation (TC-SR) are performed as follows.

- Anisotropically consolidate the test specimen in a triaxial cell with the major and intermediate principal stress equal to the cell pressure and the minor principal stress equal to the axial stress. In this case, $b = 1$ at consolidation, which is less problematic for measurement of undrained strength than $b = 1$ during shear.
- Shear the test specimen in triaxial compression by increasing the axial stress. The principal stresses will rotate as the axial stress becomes greater than the cell pressure.

TC-SR tests were performed by Whitman et al. (1960) on a remolded specimen of Mississippi Backswamp clay and by Duncan and Seed (1965) on an undisturbed specimen of San Francisco Bay Mud. For these two clays, Table 3-3 shows that the TC-SR test mode caused some decrease in the *USR* compared to equivalent CK_0U TC tests. The reduction in undrained strength measured in the TC-SR tests is much less than that for triaxial extension tests.

Table 3-3. TC-SR tests compared to conventional TC tests

Soil	*USR*			TE / TC from Figure 3-10	Source
	TC-SR	Conventional CK_0U-TC	TC-SR / TC		
MS Backswamp clay (PI = 39)	0.24	0.26	91%	62%	Whitman et al. (1960)
San Francisco Bay Mud (PI=45)	0.29	0.35	83%	66%	Duncan and Seed (1965)

A principal stress rotation of 90° also occurs whenever specimens are allowed to swell under K_0 conditions to $K_0 > 1$ (*OCR* greater than about 4 to 6) and then sheared in triaxial compression. Henkel and Sowa (1963) report the TC strength for a Weald clay specimen with *OCR* = 8, in

which stress rotation occurred. The undrained strength from this specimen matched the trend from the other tests in which the principal stresses did not rotate during shear.

Difficulties with TE Specimens and Procedure

TE specimens tend to form "necks" as shown in Figure 3-13. A neck is a region of non-uniform strain that tends to precede the formation of shear bands (Lade et al 1996). As the cross-sectional area of the specimen decreases at a neck, the axial stress increases, which leads to more strain and an unstable condition. The cross-sectional area of the specimen at the neck cannot be readily determined making the axial stress unknown. Triaxial compression samples also change dimensions during undrained shear. However, instability does not develop in the same manner because the cross-sectional area is increasing.

Figure 3-13. Necking in two TE specimens of compacted Oak Harbor clay

The literature contains many examples of problems with necking from triaxial extension tests on both sand and clay (e.g. Rutledge 1947, Balasubramaniam and Waheed-Uddin 1977, Lade et al. 1996, Long and Menkiti 2007). Necking is often associated with undrained strengths that are

lower than expected. For example, Long and Menkiti report undrained strengths from TE tests on Dublin boulder clay were only 25% of those measured in TC.

Yamamuro and Liu (1995) ran TE tests on remolded clay and tried to suppress necking by using lubricated end platens and decreasing the height to diameter ratio. Shorter specimens were found to be less susceptible to necking. Lade et al. (1996) enforced more uniform strain conditions in TE tests on sand by using lubrictated end platens, short specimens, and harnesses to limit shear banding and necking. Significantly higher strengths were reported in TE tests where strains remained uniform.

Wu and Kolymbas (1991) found that factors such as axial force measurement, membrane correction, and the effects of gravity impact TE tests more significantly than TC tests. Wu and Kolymbas point out that slight specimen defects, such as a void, soft zone or inhomogeneity, can provide a starting point for necking. This is especially problematic for compacted test specimens because even carefully prepared specimens tend to have some void spaces on the sides. In the TE tests on Oak Harbor clay presented in Chapter 7, necks invariably occurred in zones where larger voids were present in the sides of the compacted specimens.

Reviewing the Cooperative Triaxial Shear Research Program, Rutledge (1947) concluded that TE tests on sand were unreliable for comparison with compression tests. Similarly, after considerable study and experimentation, Lade et al. (1996) concluded "the conventional triaxial extension test is *not suitable* for determination of stress-strain and strength behavior of soils because it will invariably produce incorrect results" (emphasis added).

Advanced Equipment and Expertise

A final disadvantage of TE tests is the requirement for more advanced testing equipment and expertise. At a minimum, extension tests require a loading piston that can be threaded into both

the load cell and the top specimen platen. The triaxial cell must also be secured during testing to prevent it from lifting off the load frame base. In order for stress rotation to occur in the tests, anisotropic consolidation must be used, which may add a level of difficultly to the test depending on the type of triaxial equipment available.

Addressing the problems highlighted by Lade et al. (1996) and Wu and Kolymbas (2007) would require more specialized testing procedures, such as lubricated end platens and side drainage, harnesses, unconventional specimen dimensions, load cells inside of the triaxial chamber, and special membrane correction factors. All of these add difficulty and potential for error to the tests.

Experimental Data for R_ρ

Table 3-4 summarizes the results for nine clays on which plane strain tests were performed with different amounts of principal stress rotation. Ladd et al. (1977) presented some of this data; however, it should be noted that they report values of shear stress on the failure plane, τ_{ff}, rather than s_u for the compression and extension tests.

Based on test results from 50 normally consolidated clays, Mayne (1985b) concluded that the *USR* from DSS was typically between 65 and 75% of the *USR* determined in ACU triaxial compression. The decrease in strength noted by Mayne matches well with the values of $R_{\rho = 45}$ in Table 3-4.

The variation in R_ρ with principal stress rotation is plotted in Figure 3-14 for six of the clays in Table 3-4. The value of R_ρ decreases from 1 to about 0.6 to 0.75 at $\rho = 45°$. R_ρ continues to decreases as the stress system rotates to $\rho = 90°$ for the low plasticity soils (A and B). The undrained strength ratio in plane strain extension is constant or increases as the stress system

rotates to $\rho = 90°$ for higher plasticity soils. The undrained strength in DSS is not always a good average between the three failure modes as is sometimes assumed (e.g. Ladd and DeGroot 2003).

Table 3-4. Effects of stress rotation on the USR of nine NC clays

Soil	USR_{PSC}	USR_{DSS}	$R_{\rho=45}$	USR_{PSE}	$R_{\rho=90}$	Source
Kaolinite[A] (remolded)	0.44	0.29	0.66	0.44	0.98	Broms and Casbarian (1965)
San Francisco Bay Mud (undisturbed)	0.37	0.25	0.68	0.27	0.73	Duncan and Seed (1966), Duncan and Dunlop (1969)
Boston Blue clay (remolded)	0.34	0.25	0.74	0.19	0.56	Ladd et al. (1971)
Portsmouth sensitive clay (undisturbed)	0.35	0.20	0.57	0.16	0.44	Ladd and Edgers (1972)
Spestone Kaolinite (remolded)	0.26	---	---	0.15	0.58	Parry and Nadarajah (1973), Hambly (1972)
Haney clay (undisturbed)	0.30	---	---	0.17	0.57	Vaid and Campanella (1974)
AGS CH clay (undisturbed)	0.37	0.25	0.68	0.24	0.64	Ladd et al. (1977)
Connecticut Valley varved clay (undisturbed)	0.28	0.17	0.59	0.25	0.90	Ladd et al. (1977)
Hokkaido clay (remolded)	0.35	---	---	0.26	0.74	Mitachi and Kitago (1980)

Notes: Refer to Table 3-1 or Table 3 for Atterberg Limits
$R_{\rho=45} = USR_{DSS} / USR_{PSC}$ and $R_{\rho=45} = USR_{PSE} / USR_{PSC}$
[A] Hollow cylinder tests with $b = 0.5 \approx$ "plane strain" and $\rho = 45° \approx$ DSS

The variation in undrained strength ratio with plasticity index under compression, direct simple shear, and extension will be considered in the following sections. The strengths will be considered for plane strain conditions with the goal of improving Figure 3-10.

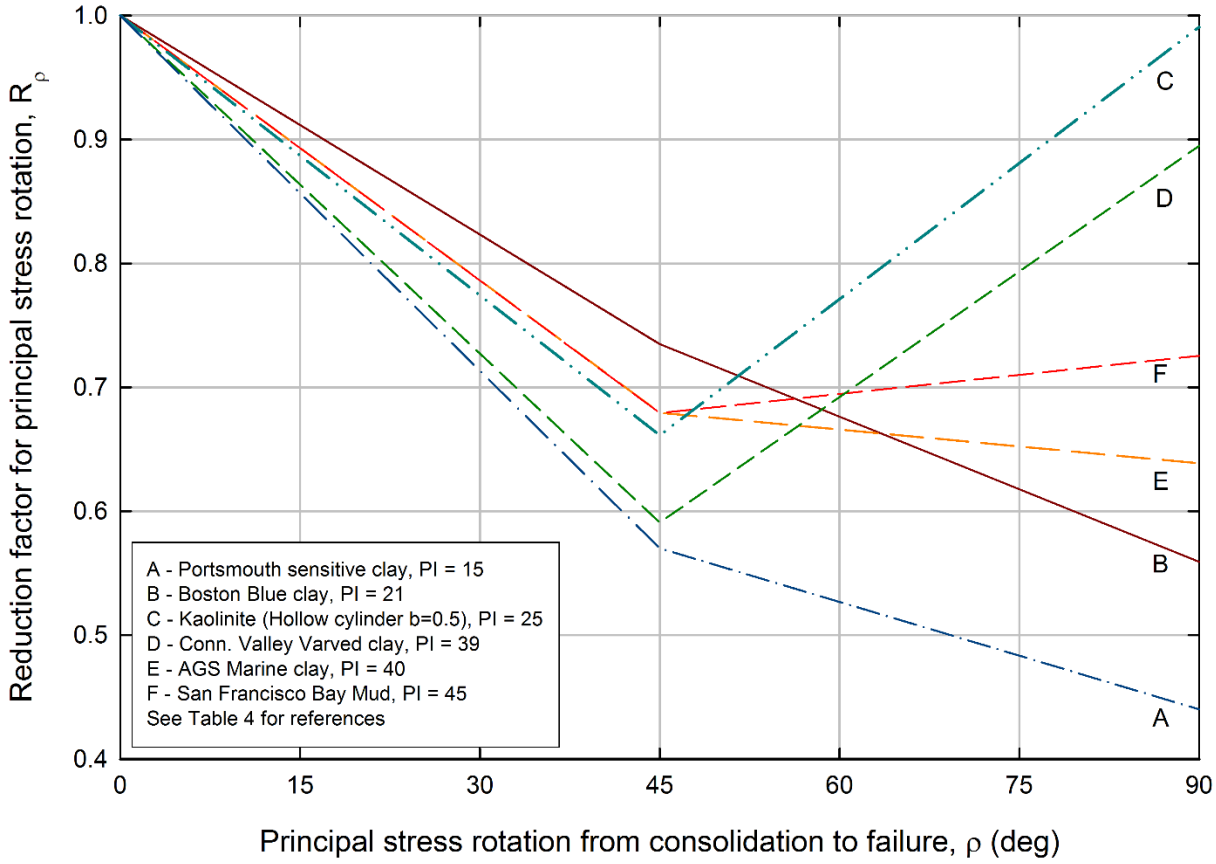

Figure 3-14. Reduction in factor for principal stress rotation measured for particular clays – all results are from plane strain tests

Plane Strain Compression ($\rho = 0^{\circ}$)

Figure 3-15 presents a compilation of test results from triaxial and plane strain tests on normally consolidated clays. The triaxial test strengths were adjusted to equivalent plane strain values by first applying the factors R_K = 0.9 and R_{PS} = 1.1, as appropriate. The results from actual plane strain tests agree well with the adjusted triaxial results. The plane strain compression *USR* decreases slightly with increasing PI. This trend corresponds to a decrease in the drained friction angle with increasing PI such as that presented in Holtz and Kovacs (1981) for normally consolidated clays tested in triaxial compression.

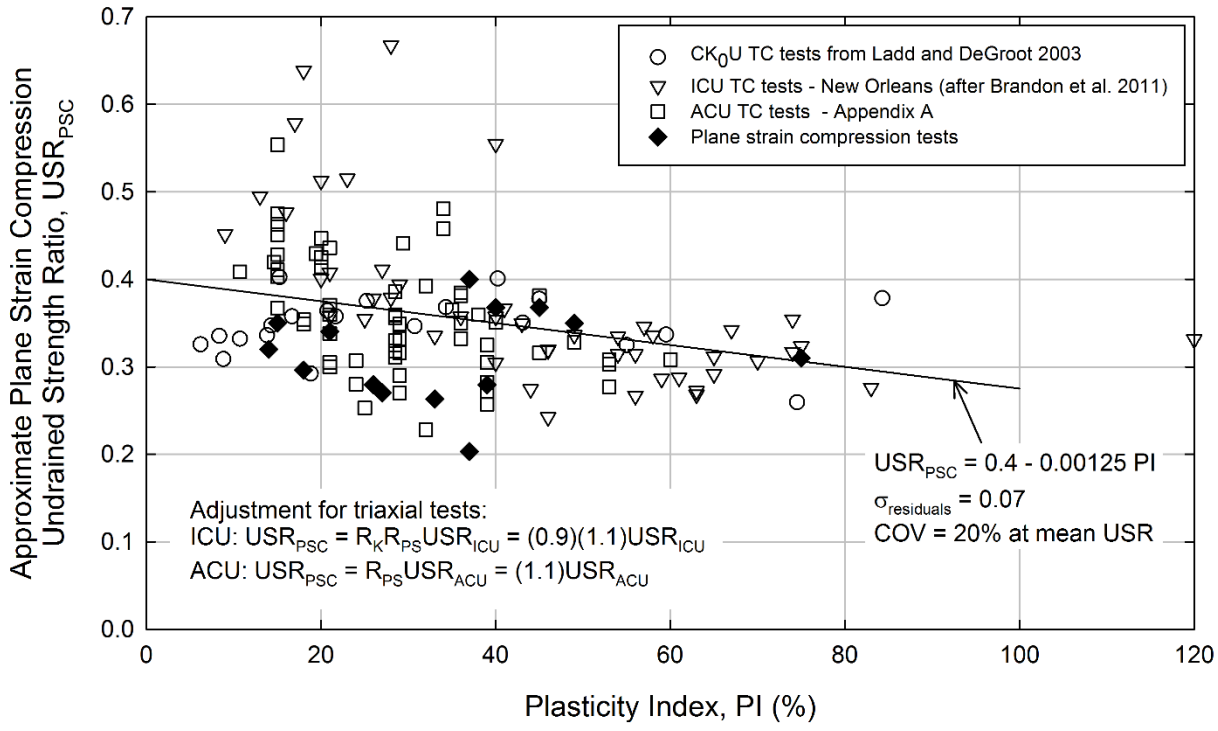

Figure 3-15. Undrained strength ratios for plane strain compression as a function of plasticity index for normally consolidated clays

Direct Simple Shear ($\rho \approx 45^{\circ}$)

Figure 3-16 presents the results of two sets of direct simple shear tests – the data from Ladd and DeGroot (2003) and data collected by Brandon et al. (2011) from New Orleans clays. The undrained strength ratio in DSS has a slight upward trend with increasing PI. The *USR* ranges from about 0.26 at PI = 0 to about 0.28 at PI = 100.

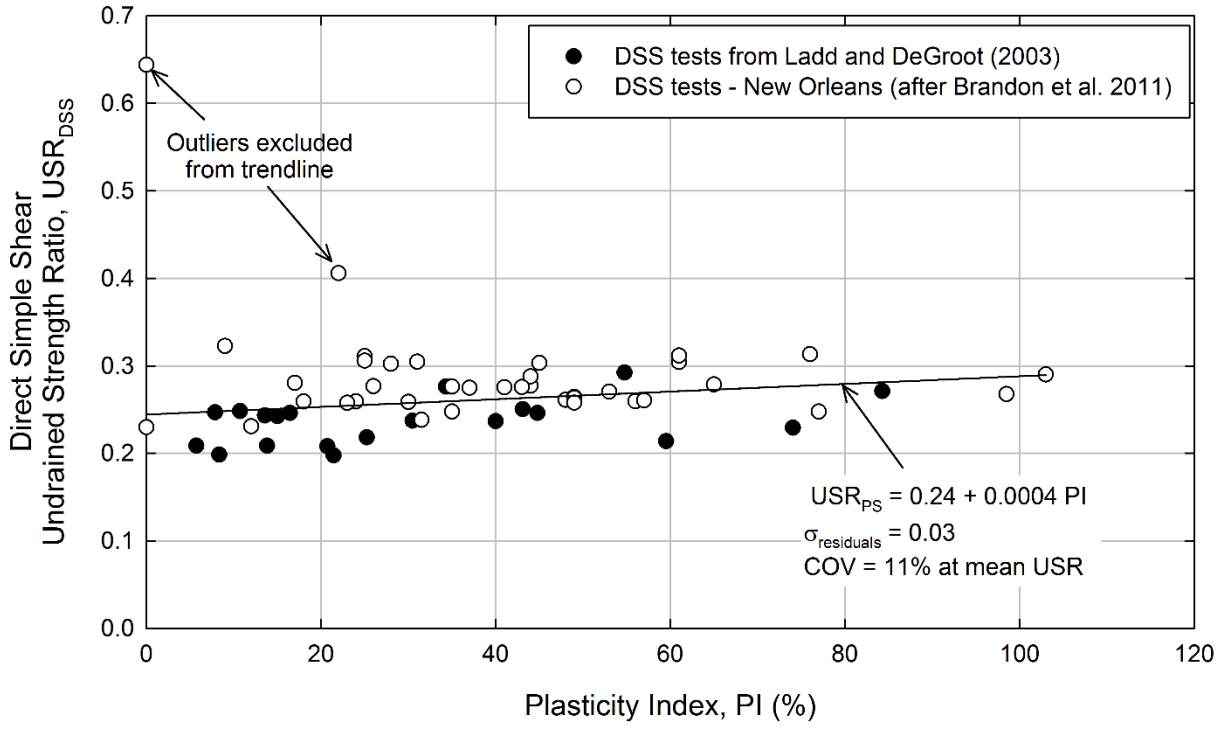

Figure 3-16. Variation of undrained strength ratio for direct simple shear with plasticity index for normally consolidated clays

Plane Strain Extension ($\beta = 90^{\circ}$)

Figure 3-17 presents the results of nine plane strain extension tests on normally consolidated clay from the literature. The *USR* for plane strain extension shows an upward trend with increasing PI, similar to that shown for triaxial extension in Figure 3-10. TE results were not included due to the problems discussed previously.

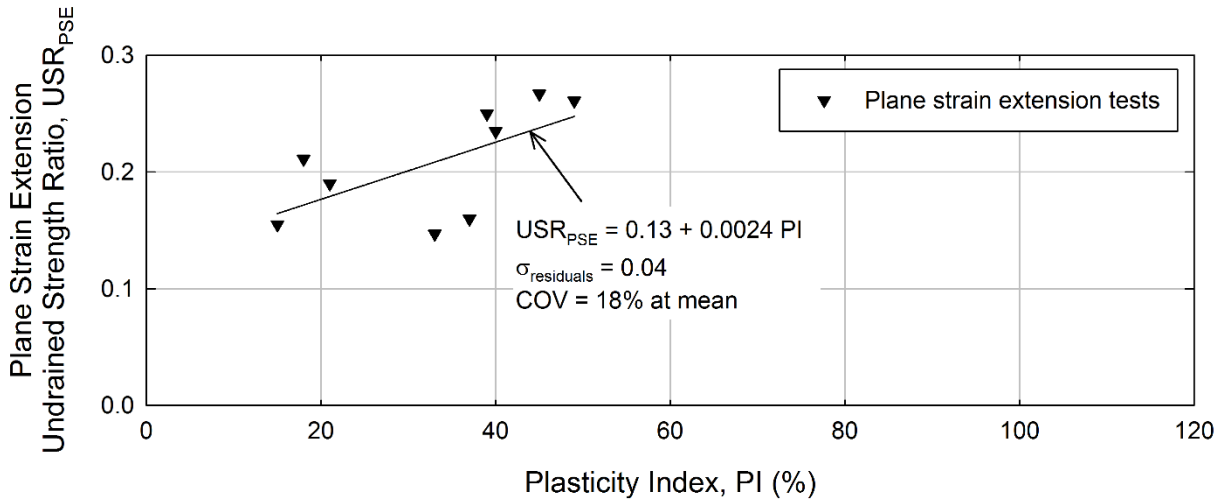

Figure 3-17. Variation of undrained strength ratio for plane strain extension with plasticity index for normally consolidated clays (see Table 3-4 for references)

Combined Graphs

Figure 3-18 summarizes plane strain test results on normally consolidated clays. This is a more consistent version of Figure 3-10 because the strengths all represent plane strain conditions.

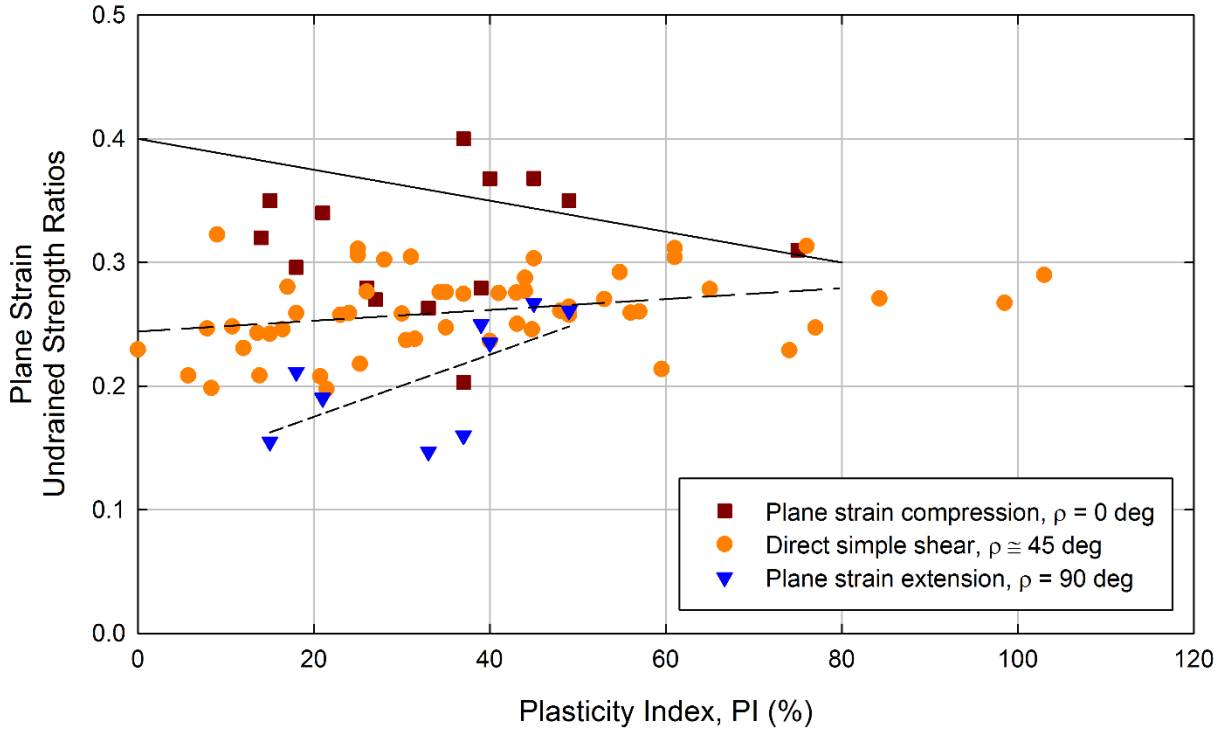

Figure 3-18. Undrained strength ratios from plane strain tests with three values of ρ. The trend for PSC is also based on adjusted TC data that has been left off the plot for clarity.

The trends in Figure 3-18 were used to calculate R_ρ at particular values of PI as shown in Figure 3-19. These idealized relationships can be compared to the measured variation for particular soils given in Figure 3-14. The trends are very similar especially for ρ=0 to 45˚, suggesting that Figure 3-19 is a good tool for predicting the approximate effect of principal stress rotation on undrained strength.

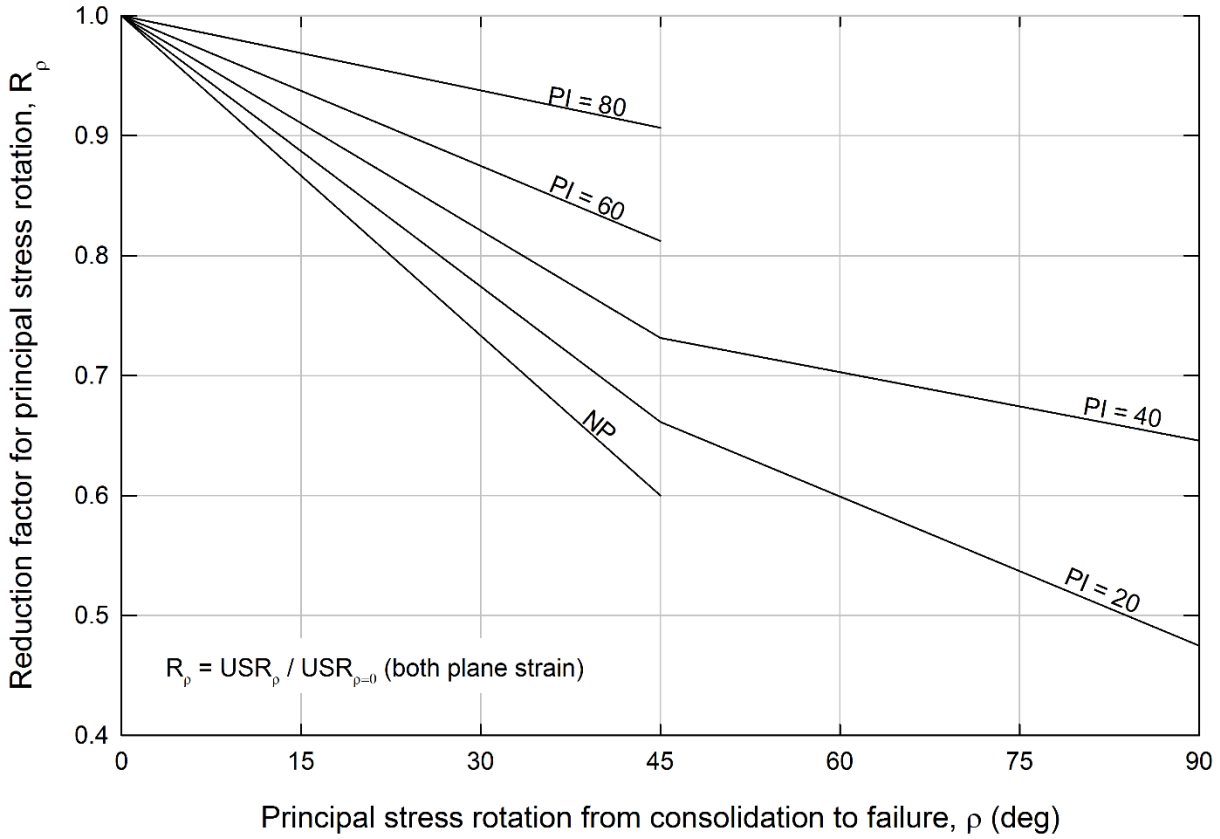

Figure 3-19. Relationship between R_ρ and ρ based on the typical variation in *USR* with PI at specific values of ρ. Plane strain extension results are only available for 15 < PI < 50.

Overconsolidated Clays

Very few plane strain compression or extension tests have been reported for overconsolidated samples. The data is too sparse to develop relationships similar to those for NC clays. Figure 3-20 from Ladd and DeGroot (2003) illustrates the variation in *USR* with *OCR* for the AGS marine clay. These results suggest that overconsolidation does not affect the relative proportion of the undrained strengths from the different failure modes. For example, undrained strength in compression is still greater than the strength in DSS at a given OCR. Figure 3-20 suggests that the values of R_ρ should be approximately constant regardless of OCR.

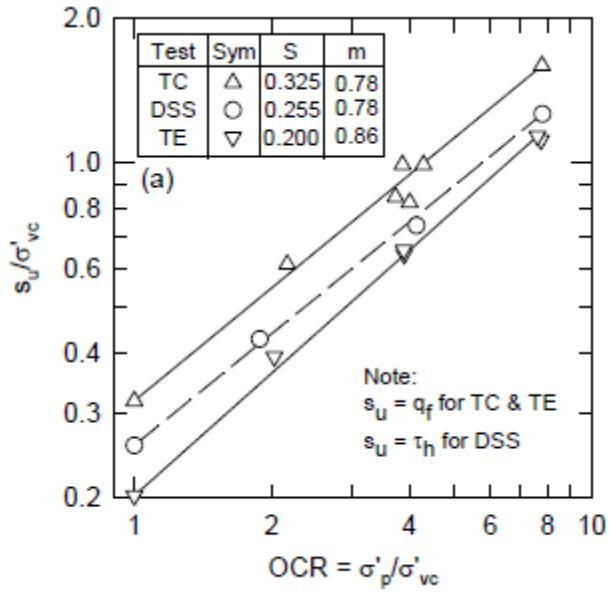

Figure 3-20. Variation in *USR* with *OCR* for AGS Plastic Marine Clay (from Ladd and DeGroot 2003 – determined fair use)

Summary – R_ρ

The available data on principal stress rotation show that undrained strength decreases as principal stresses rotate during undrained loading from consolidation to failure. Slope stability calculations should account for this decrease in undrained strength.

The triaxial extension test is an unreliable measure of undrained strength for $\rho = 90^\circ$ although it is commonly used for this purpose.

The adjustment for principal stress rotation, R_ρ, should be performed at a consistent value of intermediate principal stress ratio, *b*, preferably corresponding to plane strain. R_ρ can be approximated for a given PI and amount of stress rotation, ρ, using Figure 3-18 and Figure 3-19.

Undrained Strength for RDD

The appropriate undrained strength for rapid drawdown can be obtained for compacted clays from ICU triaxial compression tests using the adjustment factors presented in this chapter. The

laboratory test data on the stress system effects is sparse for compacted clays. The adjustment factors from undisturbed and remolded soils must be used until more specific values are measured.

The following procedure is suggested for obtaining undrained strengths for compacted clays for rapid drawdown analysis.

1. Determine undrained strengths from ICU triaxial compression tests over an appropriate range of σ'_{1c}, resulting in a relationship for $s_{u\text{-}ICU}$ as a function of σ'_{1c}. This relationship is often approximated well by a power curve.
2. Multiply the $s_{u\text{-}ICU}$ curve by R_K (median value = 0.9 to 0.94) to account for effects of anisotropic consolidation.
3. Multiply the result of Step 2 by R_{PS} (typical value = 1.1) to adjust to plane strain compression.
4. Pick an average or spatially varying value of stress rotation during shear, ρ. Use Figure 3-19 and the plasticity index to select R_ρ to account for the effects of stress rotation.
5. The shear strength adjustments can be combined and calculated as

$$s_{u-ADJ} = R_K R_{PS} R_\rho s_{u-ICU} \tag{3-7}$$

where:

$s_{u\text{-}ADJ}$ = plane strain anisotropically consolidated undrained strength, accounting for stress rotation.

Applying the typical values yields

$$s_{u-ADJ} = (0.9)(1.1) R_\rho s_{u-ICU} \approx R_\rho s_{u-ICU} \tag{3-8}$$

Compacted clay fill for dams and levees will often have PI in the range of 0 to 40. For an average stress rotation in the range of 30 to 45°, Figure 3-19 and Eqn. (3-8) indicate that the

average undrained strength appropriate for plane strain field conditions will be about 20 to 40% less than that measured in ICU triaxial compression tests.

Variability of Adjustment Factors

The adjustment factors, R_K, R_{PS}, and R_ρ, are all typical values based on compilations of laboratory test data. If these factors are not measured directly for a given soil, they represent random variables with an associated uncertainty. The typical or recommended adjustment factors are given along with the coefficients of variation and standard deviations in Table 3-5. The standard deviations for R_K and R_{PS} were estimated directly from the data for each case.

Table 3-5. Statistical parameters for the adjustment factors (PI in range of 20 to 40)

	R_K	R_{PS}	R_ρ	$R_T = R_K \times R_{PS} \times R_\rho$
Typical value	0.9	1.1	0.7	0.7
Standard deviation, σ	0.10	0.06	0.17	0.19
Coefficient of variation, *COV*	11%	5.5%	24%	27%

For R_ρ, the standard deviations were first calculated for each of the plane strain correlations in Figure 3-18. The values of R_{45} and R_{90} are the quotient of USR_{45} or USR_{90} to USR_{PSC}. The variance was estimated for these quotients using (Frishman 1971)

$$Var\left(R_\rho\right) = Var\left(\frac{Y}{X}\right) = Var\left(Y\right)Var\left(X\right) + Var\left(Y\right)\left(E\left(1/X\right)\right)^2 + Var\left(1/X\right)\left(E\left(Y\right)\right)^2 \qquad (3\text{-}9)$$

where:

Var(Y) = variance of USR_ρ,

Var(X) = variance of USR_{PSC},

E(1 / X) = expected value of 1 / USR_{PSC}, and

E(Y) = expected value of USR_ρ.

This calculation was performed for values of USR45, USR90, and USRPSC calculated at plasticity indices of 20 and 40. The coefficients of variation given in Figure 3-15 to Figure 3-17 were used to calculate the variances. The results of these calculations are summarized in Table 3-6.

Table 3-6. Statistical parameters for various values of ρ

Rotation, ρ (deg)	PI = 20		PI = 40	
	Mean R_ρ	*COV*	Mean R_ρ	*COV*
0	1.00	---	1.00	---
45	0.66	23%	0.73	22%
90	0.47	29%	0.65	25%
"Average" for RDD	0.7	26%	0.8	23%

In the last column of Table 3-5, the variance of the product of the three *R* factors was calculated assuming the adjustment factors are independent (e.g. Frishman 1971) using

$$\begin{aligned} Var\left(R_K R_{PS} R_\rho\right) = {} & Var\left(R_K\right)Var\left(R_{PS}\right)Var\left(R_\rho\right) + Var\left(R_K\right)Var\left(R_{PS}\right)\left[E\left(R_\rho\right)\right]^2 + \\ & Var\left(R_\rho\right)Var\left(R_{PS}\right)\left[E\left(R_K\right)\right]^2 + Var\left(R_K\right)Var\left(R_\rho\right)\left[E\left(R_{PS}\right)\right]^2 + \\ & Var\left(R_K\right)\left[E\left(R_{PS}\right)\right]^2\left[E\left(R_\rho\right)\right]^2 + Var\left(R_{PS}\right)\left[E\left(R_K\right)\right]^2\left[E\left(R_\rho\right)\right]^2 + \\ & Var\left(R_\rho\right)\left[E\left(R_{PS}\right)\right]^2\left[E\left(R_K\right)\right]^2 \end{aligned} \quad (3\text{-}10)$$

The standard deviation and coefficient of variation for R_T were then calculated from the variance and mean value of R_T. These are listed in the last column of Table 3-5.

4. Finite Element Stress Analysis of Embankments

The stress state within an embankment does not have a closed form analytical solution (Perloff et al. 1967). In 1967, Clough and Woodward made a major advance by calculating stresses within embankments using linear elastic finite element analysis (FEA). They accounted for soil nonlinearity using a stepwise linear procedure.

Duncan and Chang (1970) developed a hyperbolic elastic stress-strain model that calculated the tangent modulus as a function of the soil strength parameters, the confining stress, and model parameters that could be derived from standard laboratory tests. Kulhawy (1969) applied the Duncan-Chang model to the construction of embankments and added a stress-dependent formulation of Poisson's ratio.

The geotechnical literature provides little comprehensive guidance for performing stress analysis of embankments using modern, commercial finite element programs. Potts and Zydravkovic (2001) covered five embankment case studies, which focused mostly on predicting deformations and modeling stability. They also discussed methods for modeling embankment construction over soft ground, using techniques such as reinforcement and staged construction.

The purpose of this chapter is to provide straightforward guidance for the analysis of stresses within embankments, particularly water retaining structures such as dams and levees. This type of analysis is useful for calculating consolidation stresses for consolidated-undrained stability analyses like rapid drawdown.

It is difficult to assess whether or not the stresses calculated by finite element analyses are "correct." This chapter will focus on the steps required to obtain reliable and reasonable results from finite element stress analysis. This discussion on high-quality finite element stress analysis of embankments includes the following elements:

- Non-linear constitutive theory
- Embankment geometry and loading
- Staged construction
- Initial stress conditions
- Element type and finite element mesh
- Applied boundary conditions, such as distributed loads and pore pressures

Constitutive Theory

Finite element analyses relate changes in stress to changes in strain in each element through the use of constitutive theory, such as discussed by Potts and Zydravkovic (1999)

$$\{\Delta\sigma\} = [D]\{\Delta\varepsilon\} \tag{4-1}$$

where

$\{\Delta\sigma\}$ = vector of changes in stress (total or effective) in the element,

$[D]$ = matrix of constitutive relations, and

$\{\Delta\varepsilon\}$ = vector of change in strain in the element.

Either drained (effective stress) or undrained finite element analyses can be performed. For drained analyses, specified pore pressures are subtracted from the total stress vector. In this case, the *[D]* matrix must contain constitutive properties corresponding to effective stresses, which are obtained from drained tests, such as consolidated drained (CD) triaxial or one-dimensional consolidation tests. Effective stress shear strength parameters are also used. For analysis of undrained conditions, constitutive parameters obtained from undrained tests are used.

Some FE programs, such as Phase^2 (Rocscience), allow pore pressures to be considered directly in the solution of effective stress problems but do not calculate changes in pore pressure caused by changes in loading or deformation. Phase^2 refers to this type of effective stress

analysis as *partially coupled* (Rocscience 2014). In other words, a change in pore pressure causes a change in effective stress, which in turn causes deformation of the model. However, changes in loading are not directly coupled to changes in pore pressure.

Many different constitutive models are available. This chapter focuses on the Duncan-Chang hyperbolic model with stress-dependent bulk modulus. The hyperbolic model can be used for both effective stress and undrained problems, provided the constitutive and strength parameters are determined in a manner consistent with the formulation.

The parameters required for the hyperbolic elastic model may vary depending on the particular FE program. This model and the methods for obtaining the parameters are explained more fully in Duncan et al. (1980). In Phase^2, the following parameters are required for effective stress analyses:

- Modulus number, K – used to calculate the elastic modulus at zero deviator stress
- Modulus exponent, n – used to define the change in E_i with change in σ'_3
- Unloading modulus number, K_{ur} – used to calculate the modulus for unloading and reloading, which is assumed to be independent of deviator stress
- Failure ratio, R_f – used to relate the ultimate deviator stress corresponding to the hyperbolic curve fit to the peak value observed in the laboratory tests.
- Strength parameters, ϕ' and c'

As shown in Figure 4-1, the initial modulus, E_i, at a given σ'_3 is calculated by

$$E_i = Kp_a\left(\frac{\sigma'_3}{p_a}\right)^n \tag{4-2}$$

where:

p_a = atmospheric pressure in same units as stress.

As strain occurs and a deviator stress ($\sigma_1 - \sigma_3$) develops, the tangent modulus, E_t, becomes

$$E_t = E_i \left[1 - \frac{R_f \left(1 - \sin\phi'\right)\left(\sigma_1 - \sigma_3\right)}{2c'\cos\phi' + 2\sigma'_3 \sin\phi'} \right]^2 \quad (4\text{-}3).$$

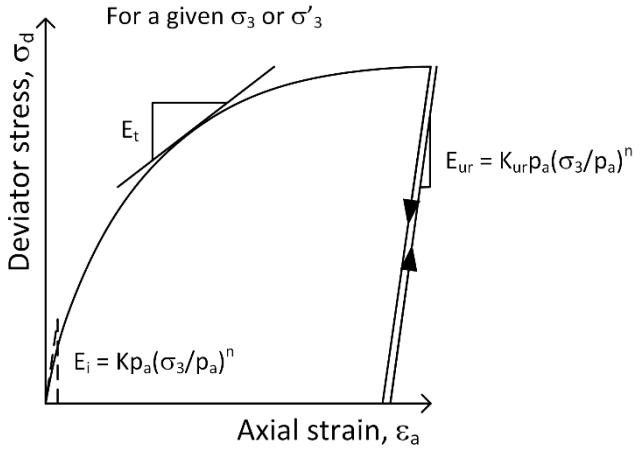

Figure 4-1. Depiction of the elastic moduli used in the Duncan-Chang hyperbolic constitutive model

The modulus during unloading and reloading, E_{ur}, is defined by Eqn. (4-2) with K replaced by K_{ur}, and is not affected by the shear stress or strength parameters. The value of K_{ur} is often assumed to be in the range of 1.2 to 3 times larger than K (Duncan et al. 1980).

Figure 4-2 illustrates the failure ratio, R_f. The hyperbola fit to the initial portion of the test data approaches an ultimate deviator stress, $(\sigma_1 - \sigma_3)_{ult}$, that exceeds the maximum principal stress difference, $(\sigma_1 - \sigma_3)_{max}$, measured in the test. R_f accounts for this difference and allows the constitutive behavior to be expressed in terms of the measured $(\sigma_1 - \sigma_3)_{max}$, or the Mohr-Coulomb strength parameters as in Eqn. (4-3). The calculated stress-strain curve will follow the hyperbola fit to the test data until the deviator stress reaches $(\sigma_1 - \sigma_3)_{max}$, from which point a very small positive value of E_t is used (Duncan and Chang 1970).

The original version of the Duncan-Chang model behaves elastically during unloading and allows the stress state to exceed the failure envelope. A check can be added to the Duncan-

Chang model that allows elements to become plastic if the stresses reach the yield surface. In Phase^2, the *Plastic* option can be selected separately for each Duncan-Chang material. This type of plastic check is appropriate for any condition.

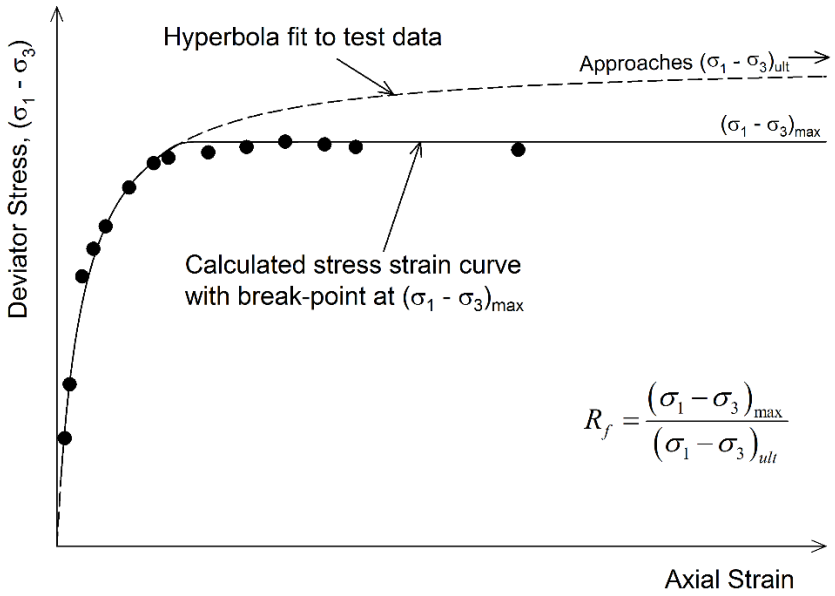

Figure 4-2. Hyperbolic Duncan-Chang stress-strain curve

The volume change properties of soil are also non-linear and can be expressed in a stress-dependent fashion. In Phase^2, the following parameters are required:

- Bulk modulus number, K_b – used to calculate the stress-dependent bulk modulus
- Bulk modulus exponent, m – used to define the change in bulk modulus with confining stress

The bulk modulus, B_t, is calculated for a given σ'_3 by

$$B_t = K_b p_a \left(\frac{\sigma'_3}{p_a} \right)^m \qquad (4\text{-}4).$$

In Phase^2 the tangent Poisson's ratio, ν_t, is calculated and used:

$$\nu_t = 0.5\left(1 - \frac{B_t}{3E_t}\right) \qquad (4\text{-}5).$$

Embankment Geometry and Loading

The cross-sectional geometry of the embankment should be modeled accurately based on the available information about the planned or existing conditions. Modern FE programs allow many different soil zones and complex geometries to be analyzed.

Element boundary conditions must be assigned to all the nodes along the edges of the FE model. These boundary conditions will either allow the nodes to be unrestrained, or provide restraint in one or more directions as appropriate to represent the conditions at each edge. An analyst should understand the different types of boundary conditions, such as free, fixed, or roller (displacement allowed in only one direction). For embankment problems where the foundation is not modeled, the nodes along the bottom of the embankment will generally be fixed.

Limit equilibrium analyses of slope stability often only consider one half of the embankment, such as the upstream slope for rapid drawdown. A single-slope embankment FE model would have a vertical boundary (likely near the centerline), which would be assigned a vertical roller boundary condition, allowing no lateral strain. However, the water retained by earth dams and levees imposes an asymmetric load. Unless the embankment crest is very wide, reservoir loading will cause lateral displacement along any vertical section through the embankment. Modeling only the upstream half of a water retaining structure will not allow stresses to develop in a realistic manner. This approximation will affect the embankment stresses that are calculated when asymmetric loading is present.

Element Type and Mesh

Accuracy in finite element embankment stress analyses is improved by the use of smaller elements or a more refined mesh, which is particularly important in regions of the model where stresses are changing quickly. Element shape can also influence the results. According to Potts

and Zydravkovic (1999) meshes of regular elements produce better results compared to irregular shapes or elements with large aspect ratios.

The effect of element shape and size is illustrated below in Figure 4-3. The two parts of this figure show the same region from two non-linear finite element models of the same embankment. The only difference between the two models was the type of elements and the mesh. Figure 4-3(a) shows that an irregular mesh of triangles, such as many programs automatically generate, results in irregular contours of σ'_3. The pattern in the stress contours clearly follows the element shape in some regions. The smaller and uniformly shaped elements in Figure 4-3(b) result in much smoother contours of σ'_3.

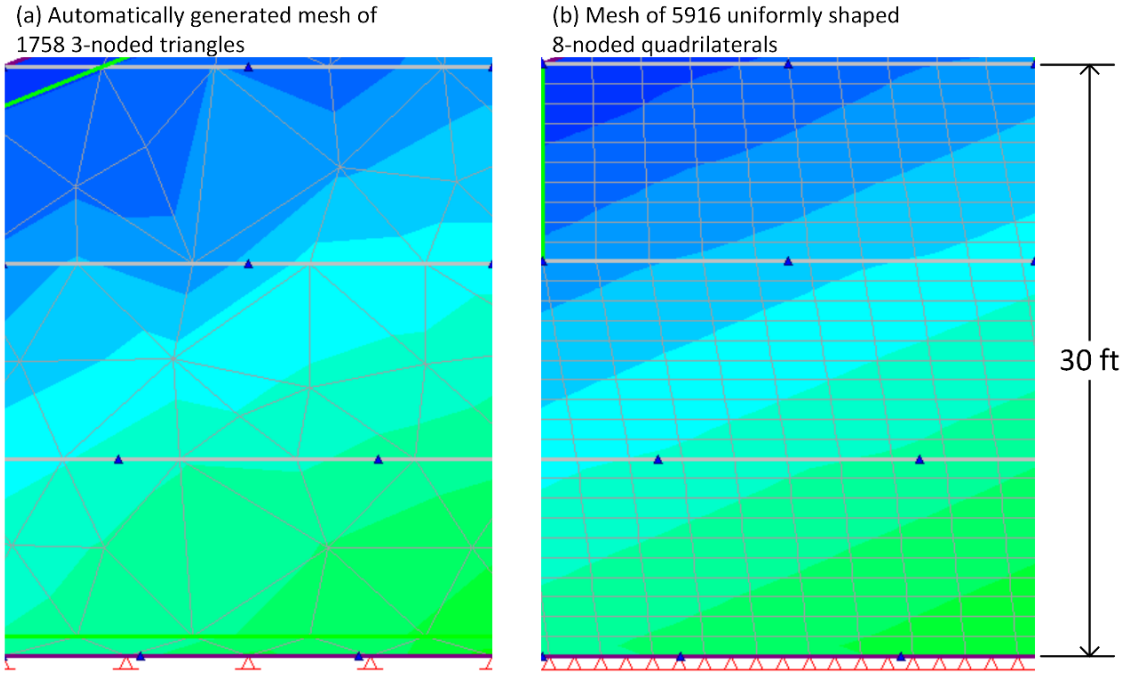

Figure 4-3. Contours of σ'_3 for two different types of finite element mesh. Thin gray lines are the element boundaries.

For embankment stress analyses using non-linear constitutive theory, the following guidelines have been found to give smooth, reasonable results.

- Use 8-node quadrilateral elements with approximately the same shape throughout the embankment. The element aspect ratio should be approximately equal to the embankment slope.
- Use an element height of 1 ft or 1% of the embankment height for embankments over 100 ft high. This approximates the actual lift thickness in the field.

Staged "Construction"

FE embankment models should be "built" in the analysis in a manner that mimics the actual construction process. In this process, layers of elements are added to the model in increments or stages, and equilibrium is recalculated for every stage. Stress dependent constitutive properties are thus allowed to change in each stage as the stresses change in the numerical model. The effects of non-linearity are allowed to develop by this process.

Staged construction is required to predict embankment displacements correctly even if linear elastic properties are used (Kulhawy 1969). Kulhawy found that eight to ten stages were sufficient to predict displacements accurately. If the embankment construction sequence is known, good modeling practice would be to use that sequence. Otherwise the elements may be added in horizontal layers of approximately equal thickness, as convenient to the geometry of the problem. Kulhawy's recommendations were limited by the available computational resources to a relatively small number of elements and stages. With modern computers, the use of thousands of elements and many stages is not prohibitive.

Irregularities in the orientation of the stress system were found to occur when elements were added to models in stages more than one element thick. Contours of the angle, θ, between σ'_1

and vertical are shown in Figure 4-4 for two non-linear FE analyses, which differed only in the thickness of the stages in which the elements were added. Both analyses used 1 ft (.3 m) high uniformly shaped elements. The general trend in the distribution of θ is the same for both analyses. However, in Figure 4-4(a), discontinuities in θ occur at each stage boundary, which in turn caused the stresses contours to be irregular. The smoothest stress contours were obtained in this research when elements were added in stages one element thick.

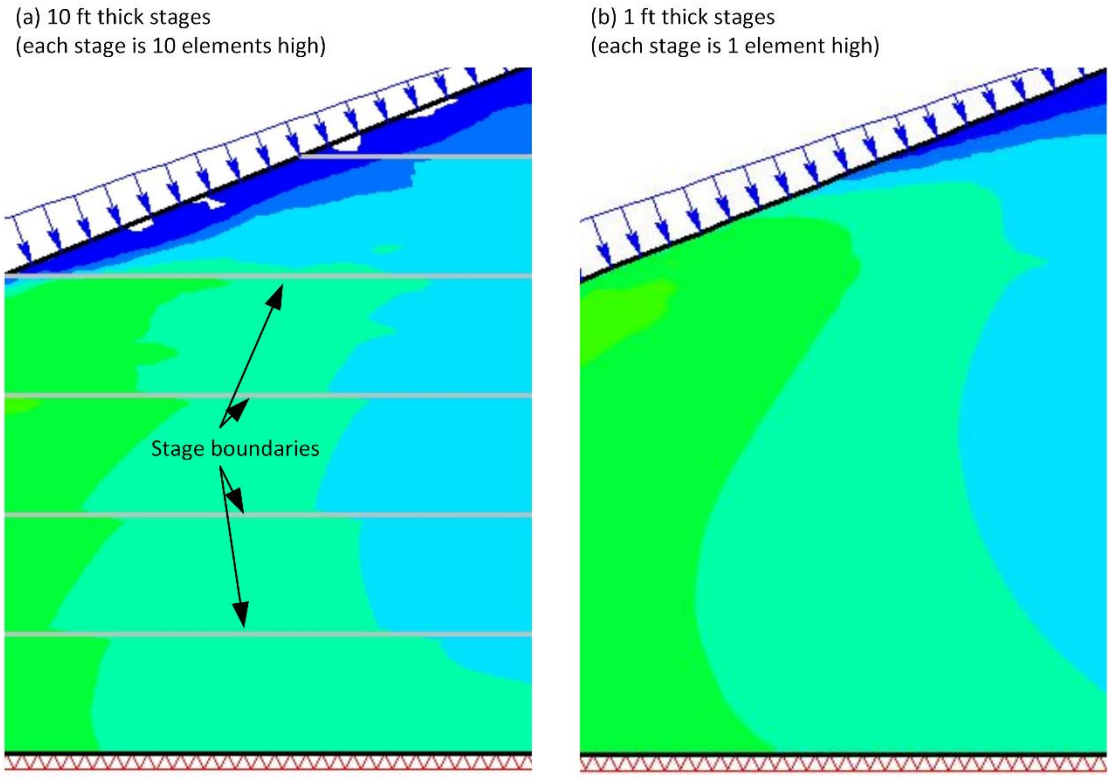

Figure 4-4. Contours of stress inclination angle, θ, for two models with different stage thickness. For clarity, stage boundaries are not shown in (b).

For example, a 75 ft (23 m) high embankment should be modeled using elements that are 1 ft (0.3 m) high, which is close to the thickness of a lift of fill in the field. The elements should be added to the model in layers 1 ft (0.3 m) thick, resulting in 75 stages to build the embankment. An example of the method used to create a staged embankment model in Phase^2 is included in Appendix C.

Initial stress conditions

Gravity loading (or body forces) associated with the weight of the elements is the primary loading for an embankment. Gravity loads are calculated based on the unit weight of the fill and volume of the element and are assigned when the elements are first "turned on" in the analysis. As these gravity loads are assigned to the elements, the mesh will deform in response, resulting in an initial deformed state. Horizontal stresses will develop that are directly related to the constitutive properties of the elements and the lateral constraints applied by the boundary conditions. For laterally constrained elements with constant ν, the ratio of minor to major effective stress, K_0, will be equal to $\nu / (1-\nu)$. Calculation of initial horizontal stresses in this manner will yield correct results, and K_0 will be less than 1.0, which is always the case for primary loading. Conditions with K_0 greater than 1.0 can be modelled by loading and then unloading the model, following the process by which $K_0 > 1.0$ conditions occur in nature.

Many finite element programs, including Phase^2, allow an initial stress system (called *Field Stress* in Phase^2) to be applied to the elements when they are first added to the model. Initial vertical stresses are calculated and assigned based on the weight of the element and any overlying elements. The vertical stresses counteract the gravity loads such that no deformation occurs in the element during the stage in which it is added. Horizontal stresses are calculated based on a user-specified ratio of horizontal to vertical effective stress. The benefit of this type of model is that the elements do not deform solely due to their own weight. In a staged model, elements from the previous stages are no longer controlled by the initial stress system and will deform according to the constitutive properties.

For problems starting with level ground, the initial stress state can be calculated in a straightforward manner. Vertical stress is controlled by the requirements of vertical equilibrium

while horizontal stress will be defined by K_0. For this reason, stresses in level ground can be initialized by applying gravity loads in a single stage, sometime referred to as the "gravity turn-on" method. If K_0 is known, it can be specified, and elements can be initialized with no deformation. Alternatively, horizontal stresses can be allowed to develop from the gravity loads, and displacements can be set to zero following the initial stage. These two methods should give the same horizontal stresses provided that the value of K_0 corresponds to the value of ν. The level ground problem is valuable for understanding the uses and limitations of different initial condition options available in a FE program. This example has been worked out using different initial conditions options in Appendix C.

Initial stresses in slopes are more complicated because the soil is not restrained laterally and horizontal stresses may vary from K_0 conditions. Kulhawy (1969) found that the initial conditions in slopes are best approximated using staged analyses that mimic the process by which the slope was formed. For example, initial stresses in a natural slope may be calculated starting with level ground and progressively removing (excavating) elements to form the slope. Multiple stages of analysis may be required to establish the initial conditions. Likewise, an embankment can be modeled by adding layers of elements in stages.

Table 4-1 illustrates the effects of construction stages on the end of construction stresses and displacements calculated with FEA for a simple 25 ft (7.6 m) high embankment with 3H:1V slopes. A reservoir boundary load and pore pressures corresponding to a simple phreatic surface were applied to the model in stages after the last layer of elements was added.

Table 4-1 shows that a model with at least 8 stages and a user-specified initial value of K_0 will result in a good estimate of horizontal stresses and the correct trends in displacement. With each subsequent stage of the model, elements from previous stages will adjust to the stresses

from new elements or loads according to their constitutive properties. In this way, the effect of the assumed K_0 is diminished and the correct trend in the end of construction displacement is maintained. For compacted soils, it is reasonable to assume that K_0 is initially greater than or equal to 1 due to "locked-in" stresses from compaction (Duncan et al. 1991).

Table 4-1. Effect of staging on initial stresses and displacements in embankments

Initial stress method	σ'_h	End of construction displacements	Relative displacement for stages following construction
Body forces only (single stage)	Based on material properties, esp. ν	Incorrect	Correct trend
Specify K_0 (single stage)	Depend on user-specified K_0	Incorrect	Correct trend
Specify K_0 (>8 stages)	Based mostly on material properties, esp. ν	Correct trend	Correct trend

Applied Boundary Conditions

Boundary conditions applied to the nodes along the edges of a finite element model are discussed in detail in most references on the use of the finite element method (e.g. Potts and Zydravkovic 1999). For FE models of water retaining embankments, boundary water pressures and internal pore pressures bear further discussion.

Boundary Water Pressures

The water retained by an embankment will impose a boundary pressure normal to the surface of the embankment. If stresses are desired within an embankment that retains water, these pressures must be included in the analysis. In the non-linear analyses performed in this study, boundary water pressures were applied in at least eight stages, which resulted in reasonable

stress distributions. Staging the boundary water pressure allows the element properties to adjust to the changes in confining stress. This requires that additional stages be added to the model after all the layers of soil elements have been added.

Changes in total stress during rapid drawdown may also be calculated by finite element analysis. The boundary water pressure during drawdown should also be changed in stages if non-linear soil properties are being considered.

Internal Pore Pressures

The initial pore pressures before rapid drawdown are usually assumed to correspond to a steady state condition. The steady state condition will develop some time after the reservoir has been filled, if the hydraulic conductivity of the fill is relatively low. Steady state pore pressures can be determined from separate FE seepage analyses or an assumed phreatic surface. These steady state pore pressures should be applied to the embankment in additional stages in order for nonlinearity to be considered.

Transient seepage analysis was considered as a means of mimicking the progression of seepage and the development of pore pressures within the embankment following reservoir filling. However, the results of transient seepage analyses depend heavily on the initial pore pressures (Sleep and Duncan 2013), which in this case would be the pore pressures present following embankment construction and reservoir filling. Pore pressures following compaction will depend on the relative compaction and compaction water content (Sherman and Clough 1968, Rao et al. 1977) as well as the construction schedule and the weather during fill placement (Terzaghi and Peck 1967). Because the post-construction pore pressures will be complex and must be assumed in most cases, transient seepage analyses were judged to be no more accurate than the use of a simpler method to estimate initial pore pressures.

The following method for applying internal pore pressures to a finite element model of a water retaining embankment was developed:

- Start with pore pressures equal to zero throughout the embankment as the elements are initially "constructed" using total unit weight for the fill.
- Calculate the steady state pore pressures throughout the embankment using a separate FE seepage analysis.
- Determine the number of stages, *N*, in which the pore pressures will be applied.
- Increase the pore pressure by the appropriate percentage in each stage to divide the application of the pore pressures to the model into *N* stages (e.g. increase the pore pressures by 25% in each stage if four pore pressure stages are used).

Guidelines for High-Quality Embankment Stress Analyses

- Use non-linear constitutive theory, such as Duncan-Chang hyperbolic, with strength and constitutive parameters determined from drained tests for effective stress analysis and undrained tests for total stress analysis.
- Use eight-node quadrilateral elements that are 1 ft thick or no more than 1% of the embankment height.
- Build the embankment in stages one element thick.
- Assign horizontal stresses equal to the vertical stress when the elements are added.
- Apply boundary water pressures to dam and levee models in multiple stages, likely following the addition of all the layers of elements. If reservoir filling is likely to occur during construction, the boundary water pressures could be applied simultaneously with the addition of elements to the model.

- Calculate pore pressures corresponding to steady state seepage or other applicable state. Apply these pore pressures in stages to the embankment.

Two examples of finite element stress analysis for embankments are included in the following sections. Two additional examples are provided in Appendix C, which illustrate details regarding initial conditions and staged construction specifically within the context of Phase[2].

Example 4-1: Pilarcitos Dam

Geometry and Material Properties

Pilarcitos Dam is a 78 ft (23.6 m) high homogenous earth dam built from compacted sandy clay with a total unit weight of 135 pcf (21.2 kN/m^3). The lower 58 ft (17.6 m) of the upstream slope is inclined at 2.5H:1V, and the upper 20 ft (6.1 m) is inclined at 3H:1V. The long-term water level was 6 ft (1.8 m) below the crest. The embankment geometry is shown in Figure 4-5.

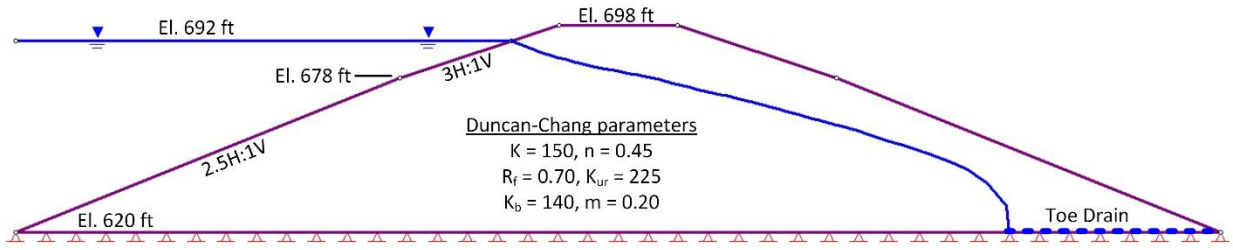

Figure 4-5. Pilarcitos Dam geometry (the geometry of the downstream slope and the presence and location of the toe drain were assumed)

A rapid drawdown slide occurred in 1969 after the reservoir level was lowered 35 ft (10.6 m) over the course of 43 days. This case has been examined by a number of researchers, including Wahler and Associates (1970) and Duncan et al. (1990). Isotropically consolidated undrained triaxial compression tests with pore pressure measurements performed by Wahler and Associates (1970) resulted in effective stress strength parameters of c' = 0 psf and ϕ' = 45°. Since drained

test results were not available, the hyperbolic parameters shown in Figure 4-5 were assumed following recommendations for compacted clay in Duncan et al. (1980).

Mesh, Staging, and Boundary Conditions

The embankment was modeled using 7332 eight-noded quadrilateral elements, each 1 ft (0.3 m) high. A fixed boundary condition was specified at the bottom of the embankment. The elements were added to the model in 78 stages with K_0 specified as 1.0 during the stage the elements were added to the mesh. The boundary water pressure corresponding to the full reservoir depth of 72 ft (21.8 m) was added in eight equal stages. The plastic option was used for the Duncan-Chang model.

Steady state pore pressures were calculated using FE seepage analysis performed in Slide v.6.0. An 80 ft (24.2 m) long horizontal toe drain was assumed to be present starting at the downstream toe. The drain prevented the phreatic surface from reaching the downstream face but had little effect on the pore pressures in the upstream part of the dam. This was considered acceptable because stresses were desired only for the upstream slope for rapid drawdown analysis. The pore pressures were applied in five stages using the simple method described earlier. Phase[2] allows the pore pressures to be assigned at (x,y) points in the model, from which the pore pressures for each element are determined by interpolation.

Results

The effective consolidation stresses and stress system orientation are summarized in Figure 4-6. Proceeding from the crest to the toe, the stress system rotates such that σ'_1 was inclined nearly parallel to the slope. This rotation transferred stress from higher in the slope to the toe elements, causing the contours of σ'_1 to be narrower near the toe. This means that σ'_1 was significantly higher than the vertical effective stress near the toe. The regions of green and

orange in Figure 4-6(c) are regions of high shear stress approaching the failure envelope. Some of the elements in these regions have yielded during the unloading caused by the decrease in effective stress as the pore pressures were increased to the steady state values.

The Pilarcitos Dam stress analysis was performed using Phase2 v. 8.018 64 bit on a laptop computer with a 2.70 GHz Intel® Core™ i5-3340M processor and 7.89 GB of usable memory. The run time was 18.6 minutes.

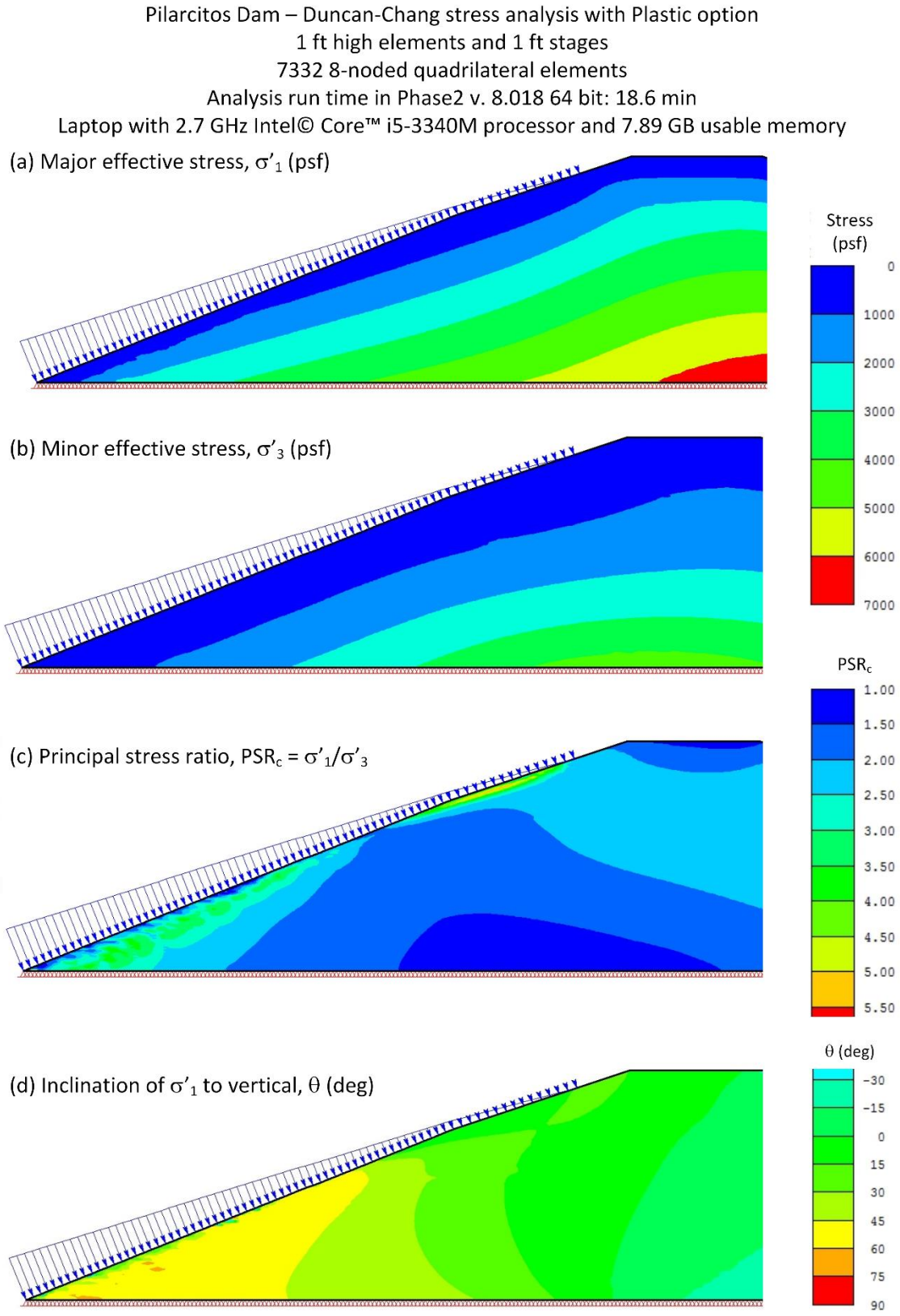

Figure 4-6. Non-linear FE consolidation stress analysis of Pilarcitos Dam

Example 4-2: Walter Bouldin Dam

Walter Bouldin Dam was built by the Alabama Power Company in 1967. The only means of seepage control was a horizontal drain below the downstream slope of the dam. In 1975, a rapid drawdown failure occurred when the water level in the reservoir dropped 32 ft (9.7 m) over the course of 5-1/2 hours. This catastrophic drawdown rate was caused by the failure and breach of a different section of the dam. The dam cross-section was obtained from Whiteside (1976) and is shown in Figure 4-7. The soils were poorly compacted, which contributed to both the main dam breach and the RDD failure.

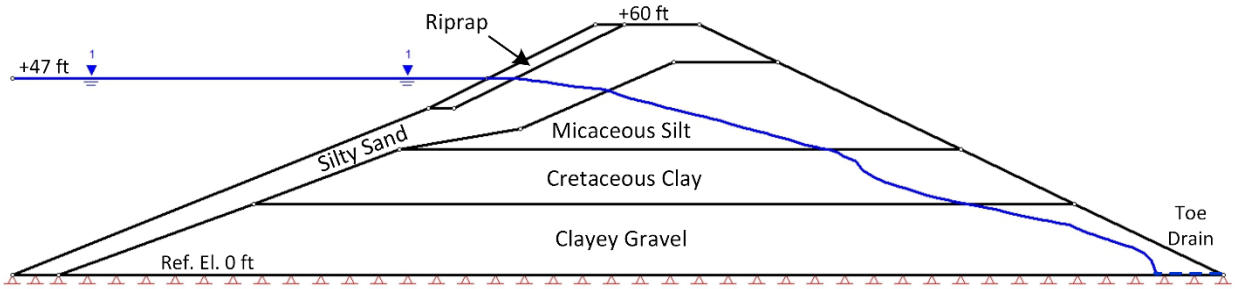

Figure 4-7. Cross-section of Walter Bouldin Dam (after Whiteside 1976). Note – length of the toe drain was assumed.

Material Properties

Whiteside (1976) performed ICU triaxial compression tests and one-dimensional consolidation tests on the samples from the failed portion of Walter Bouldin Dam. The drained strength parameters reported by Whiteside were used in the analysis and are summarized in Table 4-2.

Hyperbolic parameters for the finite element analysis were determined from the consolidation tests following the method described by Clough and Duncan (1969). The minor effective stresses during the test were estimated by assuming values of K_0 = 1-sin ϕ'

corresponding to friction angles from the ICU tests. The initial elastic modulus for each consolidation increment were calculated after Clough and Duncan (1969) as

$$E_i = \frac{1+e_0}{a_v}\left[1-\frac{2K_0^2}{1+K_0}\right]\Bigg/\left[1-\frac{R_f(\sigma_1-\sigma_3)}{(\sigma_1-\sigma_3)_f}\right]^2 \qquad (4\text{-}6)$$

where:

e_0 = the initial void ratio in the consolidation test,

a_v = coefficient of compressibility, and

K_0 = ratio of horizontal to vertical effective stress.

Average values of a_v were calculated at each consolidation stress from the previous and following consolidation increments. Values of E_i were normalized by atmospheric pressure, p_a, and plotted against the normalized consolidation stress in Figure 4-8(a).

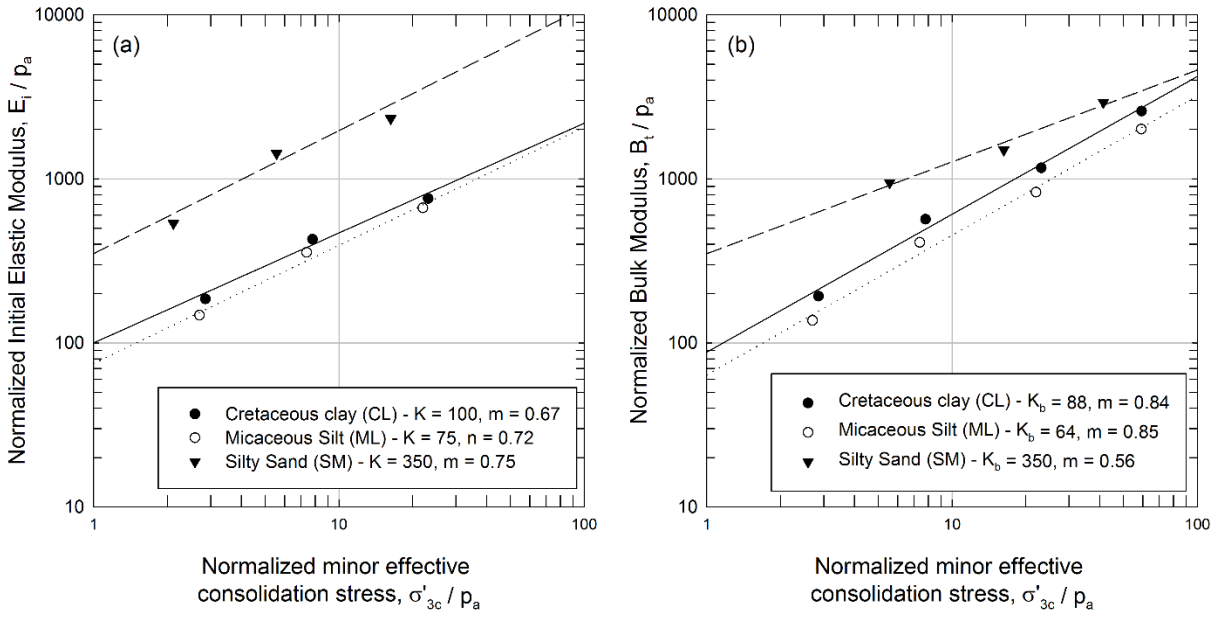

Figure 4-8. Use of consolidation test data to determining the Duncan-Chang parameters for a) elastic modulus and b) bulk modulus – Walter Bouldin Dam

The bulk modulus parameters were determined from the consolidation tests in a similar manner. The bulk moduli were calculated from each consolidation increment as

$$B_t = \frac{\Delta V/V}{\Delta \sigma'_{mean}} \tag{4-7}$$

where:

$\Delta V/V$ = volumetric strain for each consolidation increment and

$\Delta \sigma'_{mean}$ = change in mean effective stress.

The normalized bulk moduli are plotted in Figure 4-8(b) along with the curve fit determined for each soil type. The strength and hyperbolic parameters used for Walter Bouldin Dam are listed in Table 4-2. The riprap was modeled as linear elastic with ϕ' = 40°, E = 1,000 ksf and ν = 0.3.

Table 4-2. Hyperbolic parameters for Walter Bouldin Dam

Soil	Strength		Hyperbolic Elastic Parameters				Bulk Modulus	
	ϕ'	c' (psf)	K	n	R_f[A]	K_{ur}[B]	K_b	m_b
Silty Sand	32.7°	240	350	0.75	0.9	525	350	0.56
Silt	22.5°	220	75	0.72	0.85	112	64	0.85
Cret. Clay	22.7°	110	100	0.67	0.85	248	88	0.84
Gravel[C]	26°	1300	600	0.50	0.90	900	500	0.50

A R_f values assumed from CU test results
B The unloading modulus was assumed to be 1.5 times greater than K (Duncan et al. 1980)
C No tests were performed on the gravel layers, values were assumed

Mesh, Staging, and Boundary Conditions

The dam was modeled with a mesh of 4290 eight-node quadrilaterals. The base of the embankment was assumed to be fixed because details regarding the dam foundation were not available. The 1 ft (0.3 m) high elements were of relatively uniform size and shape within each

zone and generally had an aspect ratio of three or less. The elements were added to the model in 1 ft (0.3 m) stages with equal initial horizontal and vertical stresses ($K_0 = 1$). The boundary water pressure was applied to the upstream face in ten stages after building the embankment in 60 lifts.

Steady state pore pressures were calculated using a separate finite element seepage analysis performed using Slide v.6.0. The seepage analysis assumed a 16 ft (4.8 m) long, zero pressure toe drain along the downstream base to keep a seepage face from developing at the downstream slope. The analyses used hydraulic conductivities based on Whiteside's (1976) consolidation test results as given in Table 4-3. The horizontal hydraulic conductivities were assumed to be twice the values measured in the consolidation tests. The internal pore pressures were stepped up to the steady state values in four stages.

Table 4-3. Hydraulic conductivity of fill materials for Walter Bouldin Dam (based on consolidation test results from Whiteside 1976)

Soil	Measured Vertical Hydraulic Conductivity, k_v ft/s (cm/s)	Assumed Horizontal Hydraulic Conductivity, k_h[A] ft/s (cm/s)
Silty Sand	1.8×10^{-7} (5.4×10^{-6})	3.5×10^{-7} (1.1×10^{-5})
Silt	5.9×10^{-8} (1.8×10^{-6})	1.2×10^{-7} (3.6×10^{-6})
Cretaceous Clay	1.2×10^{-8} (3.6×10^{-7})	2.4×10^{-8} (7.2×10^{-7})
Gravel[B]	5.0×10^{-7} (1.5×10^{-5})	1.0×10^{-6} (3.0×10^{-5})

[A] k_h assumed to be twice the measured value of k_v

[B] No tests were performed on the gravel layers, values were assumed

Results

The results of the Walter Bouldin Dam construction stress analysis are presented in Figure 4-9. The entire dam was modeled but only the upstream slope is shown here. As shown in Figure 4-9(a), a region of lower σ'_{1c} is present near the middle of the upstream slope. This

occurs as stresses arch over the softer silt and clay layers. Embankment zones with significantly different stiffness will exhibit this type of behavior. It is important to model accurately significant differences in stiffness between embankment zones to achieve accurate stress calculations.

Figure 4-9(b) shows the minor effective consolidation stresses. The effect of different stiffness and bulk modulus is very evident in this plot. The clay layer is softer and develops much higher σ'_3 than the underlying gravel. Differences in stiffness and bulk modulus will affect the consolidation shear stress and stress ratio calculated by finite element analysis.

The orientation of the consolidation stress system is illustrated in Figure 4-9(c). Discontinuities in the inclination angle between σ'_1 and vertical exist at the material boundaries. This fluctuation in inclination angle was caused by the differences in σ'_{1c} and σ'_{3c} across material boundaries. As stresses arch through the stiffer silty sand, the major effective stress aligns almost parallel to the slope over the softer clay layer.

Walter Bouldin Dam – Duncan-Chang stress analysis with Plastic option
1 ft high elements and 1 ft stages
4290 8-noded quadrilateral elements
Analysis run time in Phase2 v. 8.018 64 bit: 6.9 min
Laptop with 2.7 GHz Intel© Core™ i5-3340M processor and 7.89 GB usable memory

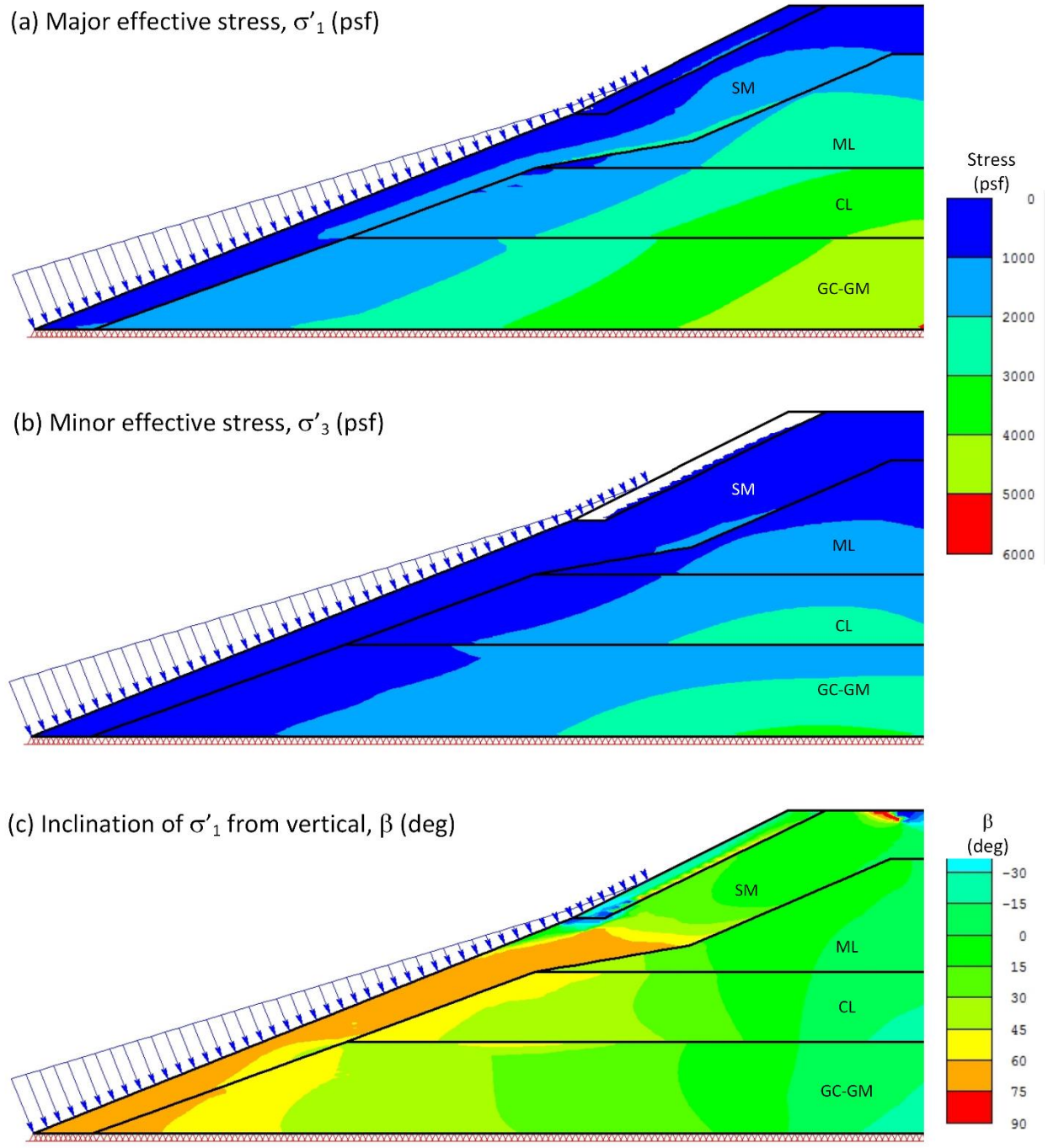

Figure 4-9. Walter Bouldin Dam consolidation non-linear stress analysis

5. Evaluation of Limit Equilibrium RDD Procedures

Undrained strength (total stress) analyses are the conventional way to address short-term loading conditions in geotechnical engineering, including rapid drawdown. Undrained strengths are determined as a function of the effective consolidation stresses that existed prior to the change in load. Rapid drawdown methods that use undrained strengths rely on a staged procedure. The consolidation stresses are calculated in the first stage using drained strength parameters, full reservoir, and steady state seepage. The corresponding undrained strengths are then estimated and used in a second stage to evaluate embankment stability with the reservoir level lowered.

Basis of Limit Equilibrium RDD Procedures – Lowe and Karafiath (1960a, b)

Lowe and Karafiath (1960a, 1960b) proposed a method for determining effective consolidation stresses and the resulting undrained strengths from limit equilibrium analysis. Their method and subsequent multi-stage undrained strength methods rest on three primary assumptions:

1. Limit equilibrium analysis of an embankment under the steady state seepage condition can be used to determine the effective normal and shear consolidation stresses acting on discrete parts of a trial failure surface.
2. Principal stresses do not rotate from consolidation to failure.
3. Undrained strength following anisotropic consolidation can be approximated from ICU triaxial compression tests.

Assumption 1 provided a relatively simple means of estimating the stresses on a trial failure surface in a slope. The accuracy of the undrained strengths for RDD will depend directly on the accuracy of this assumption. At any given point within an embankment, the stress state assumed

by Lowe and Karafiath's assumptions varies for every trial failure surface drawn through that point.

Assumption 2 implies that the orientation of the principal stresses is known as shown in Figure 5-1. The shear and normal stress calculated by limit equilibrium can then be located on a Mohr circle, and the corresponding principal stresses can be calculated. The effective consolidation stress ratio, K_c, can be calculated for each slice along a trial failure surface using (USACE 2003)

$$K_c = \frac{\sigma'_{1c}}{\sigma'_{3c}} = \frac{\sigma'_{fc} + \tau_{fc}\dfrac{\sin\phi' + 1}{\cos\phi'}}{\sigma'_{fc} + \tau_{fc}\dfrac{\sin\phi' - 1}{\cos\phi'}} \tag{5-1}$$

where:

σ'_{fc} = effective normal stress on the slice base at consolidation,

τ_{fc} = shear stress on the slice base at consolidation, and

ϕ' = effective stress friction angle.

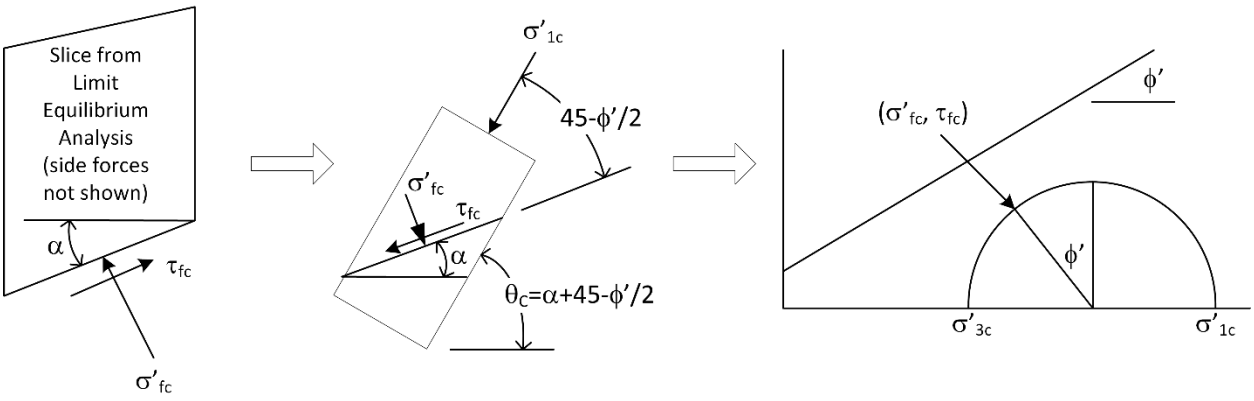

Figure 5-1. Logic used to obtain principal stresses from limit equilibrium, using Lowe and Karafiath's assumptions 1 and 2

K_c will be constant if *c'* is equal to zero, as the normal and shear stresses will be in equal proportion for every slice on the failure surface because the factor of safety is the same for every slice in limit equilibrium analysis.

Assumption 3 interprets the undrained (R) and the drained (S) envelopes from ICU triaxial compression tests as the two bounding extremes of consolidation, $K_c = 1$ and $K_c = K_f$. The $K_c = 1$ and $K_c = K_f$ envelopes are defined as illustrated by Figure 5-2. For each ICU triaxial test, the effective stresses on the failure plane at failure, σ'_{ff} and τ_{ff}, are determined from the effective stress Mohr circle. For the $K_c = 1$ envelope, τ_{ff} is plotted against the isotropic consolidation stresses, recognizing that the consolidation stresses are the same on every plane and therefore are equal to σ'_{fc}. For the $K_c = K_f$ envelope, τ_{ff} is plotted against the effective stress on the failure plane at failure, σ'_{ff}, which is equated with σ'_{fc}. The $K_c = K_f$ envelope is identical to the drained strength envelope. These envelopes are typically represented as straight lines but curved envelopes can be used in some software (Slide v6.0, UTEXAS). For simplicity, this chapter will only consider linear envelopes.

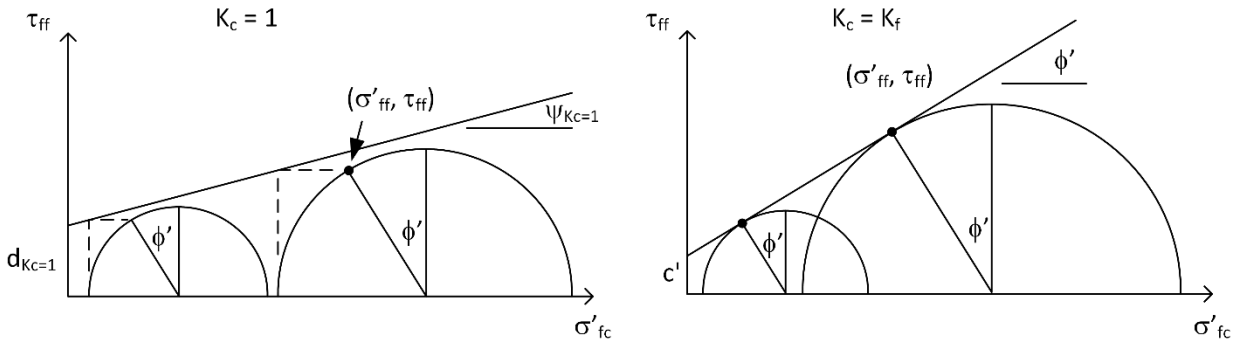

Figure 5-2. Method for plotting the $K_c = 1$ (left) and $K_c = K_f$ (right) envelopes

The $K_c = 1$ and $K_c = K_f$ envelopes for a poorly compacted clay from the Walter Bouldin Dam case study (Whiteside 1976) and a hypothetical well compacted silty clay (Duncan et al. 1990) are plotted in Figure 5-3. The normal stress intersection point of the envelopes, $\sigma'_{fc\text{-}A}$, can be

used as a measure of the level of compaction for the soil. Well-compacted soils tend to dilate at consolidation stresses leading to negative pore pressures and higher values of $d_{Kc=1}$ compared to poorly compacted soils. As $d_{Kc=1}$ increases, $\sigma'_{fc\text{-}A}$ also increases.

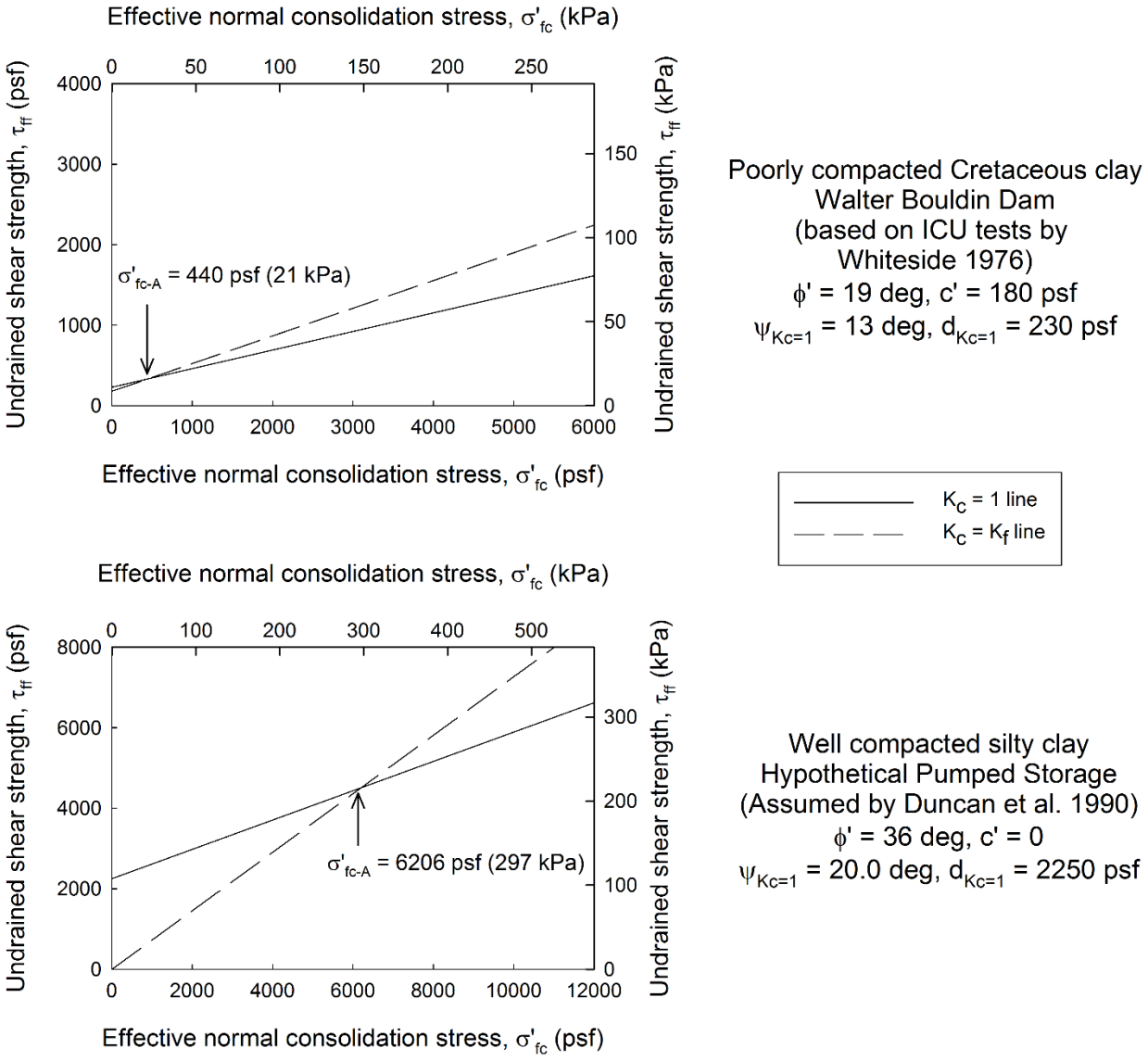

Figure 5-3. Examples of $K_c = 1$ and $K_c = K_f$ envelopes for two soils –poorly compacted clay (data from Whiteside 1976) and well compacted silty clay (hypothetical example from Duncan et al. 1990)

Lowe and Karafiath (1960b) presented two methods for determining strength from ICU triaxial tests and particular values of σ'_{fc} and K_c. The first method was based on a concept

advocated by Taylor (1948), who interpreted the effective stress vector curve for the failure plane in an ICU test as successive anisotropic consolidation states. The second method, attributed to Karafiath, assumed that the pore pressure coefficient, $\bar{A}_f$, is the same for isotropic and anisotropic consolidation. After Lowe and Karafiath, subsequent work on multi-stage RDD methods focused mostly on different methods of estimating undrained strength from the drained and undrained ICU envelopes. The current state of practice uses linear interpolation between the two envelopes along with a third stage to account for partial drainage as proposed by Duncan et al. (1990) and included in USACE (2003).

The accuracy of Lowe and Karafiath's three assumptions will be assessed in the following sections. This evaluation aims to better understand the effects of each assumption on undrained strength and any limitations or shortcomings that result. Rapid drawdown methods, such as Duncan et al. (1990), based on these assumptions use values of undrained strength that are lower than the strengths measured directly by ICU triaxial compression tests. The source and amount of this strength reduction will be explored in this chapter.

Method for Evaluating Lowe and Karafiath's Assumptions

Lowe and Karafiath's first two assumptions provide a means for obtaining the consolidation stress state in terms of two variables, σ'_{fc} and K_c. The undrained strength used for the drawdown stage depends on these two variables.

Finite element analysis provides a tool for calculating the stress state in an embankment, which Lowe and Karafiath did not have available to them. In this chapter, the stress state calculated from limit equilibrium (LE) and Lowe and Karafiath's assumptions will be compared to stresses predicted by non-linear, finite element stress analyses (FEA) of the same problems.

Although it is an approximation itself, the FEA stress state is more accurate than that predicted by limit equilibrium. Two examples will be used:

- Pilarcitos Dam – In this case, the dam geometry is known (Figure 5-4) and the ICU-TC strength of the dam soil is well-defined. Lowe and Karafiath's assumptions as implemented by the Duncan et al. (1990) (DWW) method gave a factor of safety close to 1 for this failure, meaning that the DWW undrained strengths are on average correct. A non-linear FEA was performed for Pilarcitos Dam in Chapter 4. The FEA and LE stresses will be compared along the DWW critical failure surface.

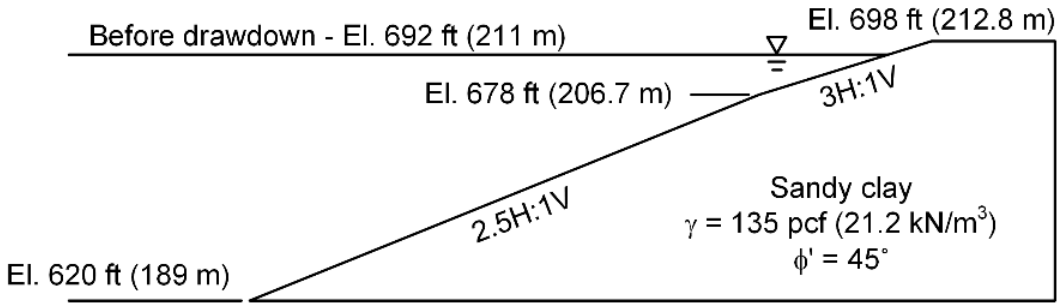

Figure 5-4. Upstream slope geometry of Pilarcitos Dam

- Hypothetical example – The upstream half of a 100 ft (30.5 m) high embankment with a 100 ft (30.5 m) wide crest and a 3H:1V slope will be also considered as shown in Figure 5-5. The soil was modeled as homogeneous with strength parameters ϕ'=30° and c'=0 psf, and a total unit weight of 130 pcf (20.4 kN/m^3). Stresses along four trial failure surfaces were determined using limit equilibrium (Spencer) and finite element analysis. The finite element model of the slope used non-linear elastic Duncan-Chang soil parameters typical of compacted clay (K = 150, n = 0.45, R_f = 0.7, K_{ur} = 225, K_b = 140, m = 0.2). The FE model was built in stages, and the reservoir load was added in

increments. The steady state pore pressures corresponded to a horizontal phreatic surface 10 ft (3 m) below the crest.

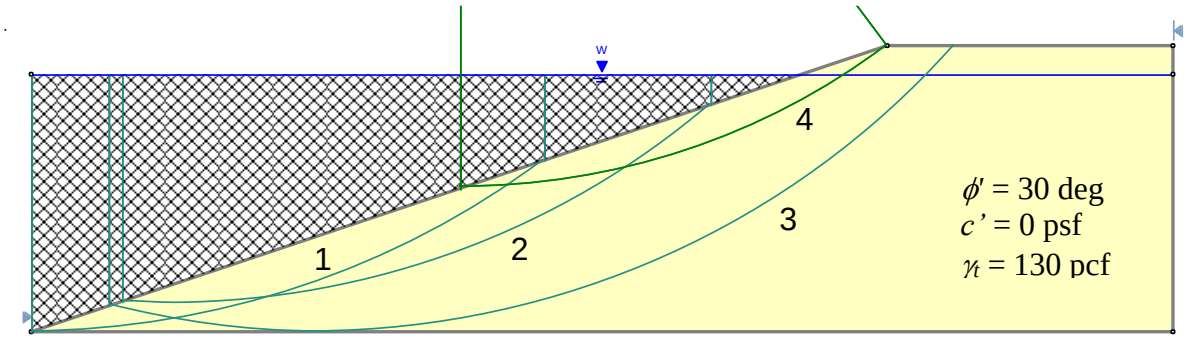

Figure 5-5. Hypothetical slope geometry and failure surfaces analyzed

Assumption #1 – Obtaining Stresses from Limit Equilibrium

Pilarcitos Dam

Figure 5-6 compares the effective normal and shear consolidation stresses on the critical failure surface for Pilarcitos Dam. The effective normal stresses from LE and FEA agree relatively well. The FEA values of σ'_{fc} are on average 12% lower than those from the FEA. The normal stress on the slice base is influenced mostly by vertical equilibrium so the values should be in close agreement. The shear stress from FEA is greater near the toe and the crest of the failure surface. The FEA shear stress ranged from 50% higher to 15% lower than that calculated by LE.

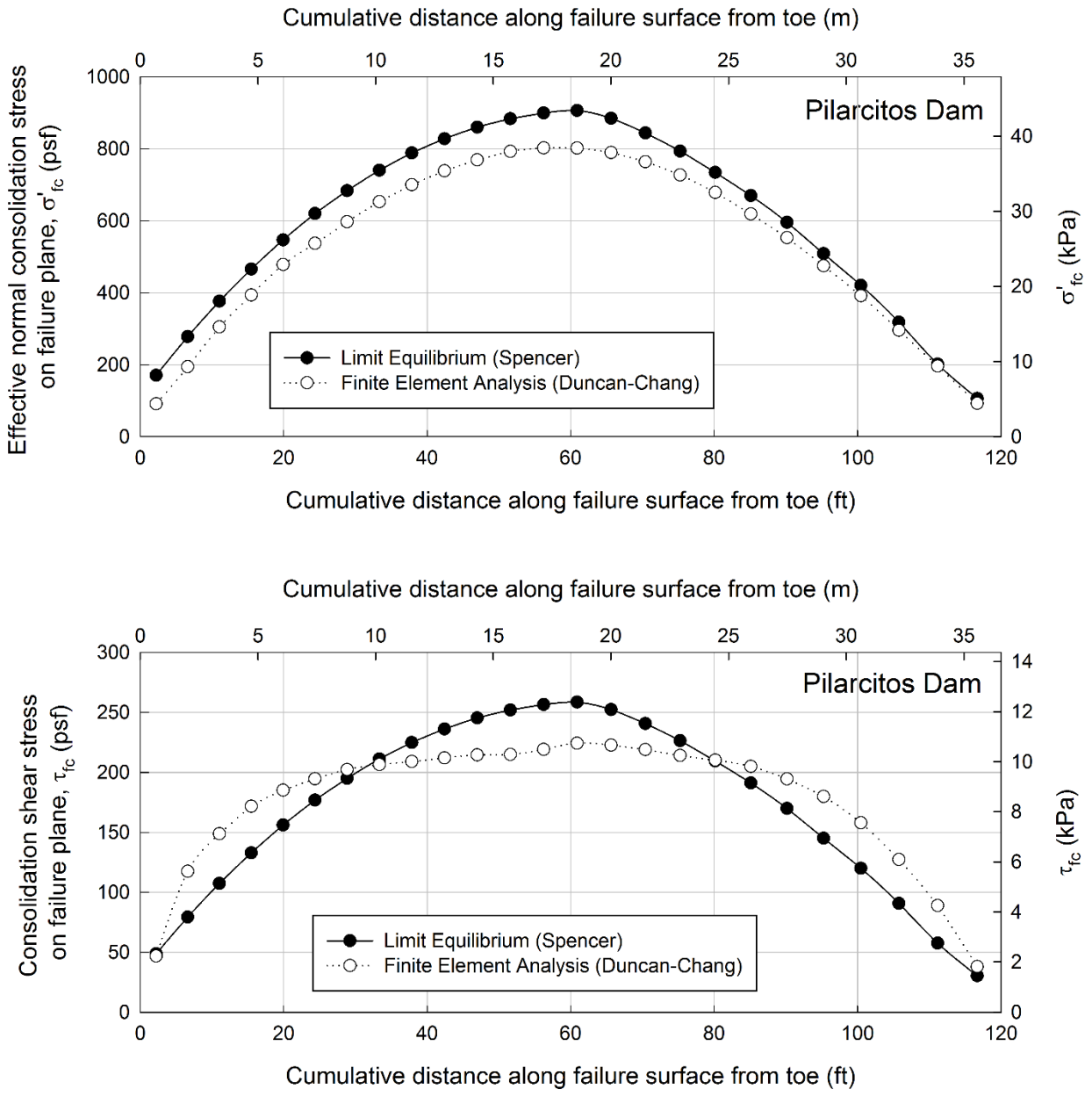

Figure 5-6. Comparison of σ'_{fc} and τ_{fc} along the DWW critical circle for Pilarcitos Dam

Hypothetical Slope

The factors of safety and DWW consolidation stress ratios for the four slip surfaces in the hypothetical slope are listed in Table 5-1. The FEA factors of safety for these particular surfaces have been calculated based on strength as suggested by Kulhawy (1969)

$$F = \frac{\sum \left(c' + \sigma'_{fc} \tan\phi'\right)\Delta L}{\sum \tau_{fc} \Delta L} \tag{5-2}$$

where:

F = factor of safety (either average for all slices or local for one slice) and

ΔL = length of slice base.

Table 5-1. Details for hypothetical slope trial surfaces

Surface	Center (ft)	Radius (ft)	Stage 1 –Factor of Safety (All Slices)		K_c
			Limit Equilibrium	Finite Element (Eqn. 2)	
1	(0, 300)	300	1.82	1.86	1.90
2	(50, 300)	290	1.85	1.89	1.88
3	(100, 300)	300	1.96	1.98	1.82
4	(150, 300)	250	1.75	1.74	1.94

The effective normal consolidation stresses are compared in Figure 5-7 for the four trial failure surfaces. The agreement between LE and FEA is seen again to be quite close. On average, the effective normal stresses from FEA are within 2% of the LE values.

As seen in Figure 5-8, the distribution of shear stresses along each surface differs significantly between the two methods. Limit equilibrium tends to predict lower τ_{fc} over the downslope part of the surface and higher shear stress on the upslope side. The LE shear stresses for Surfaces 3 and 4 drop back below the FEA values near the crest of the slope.

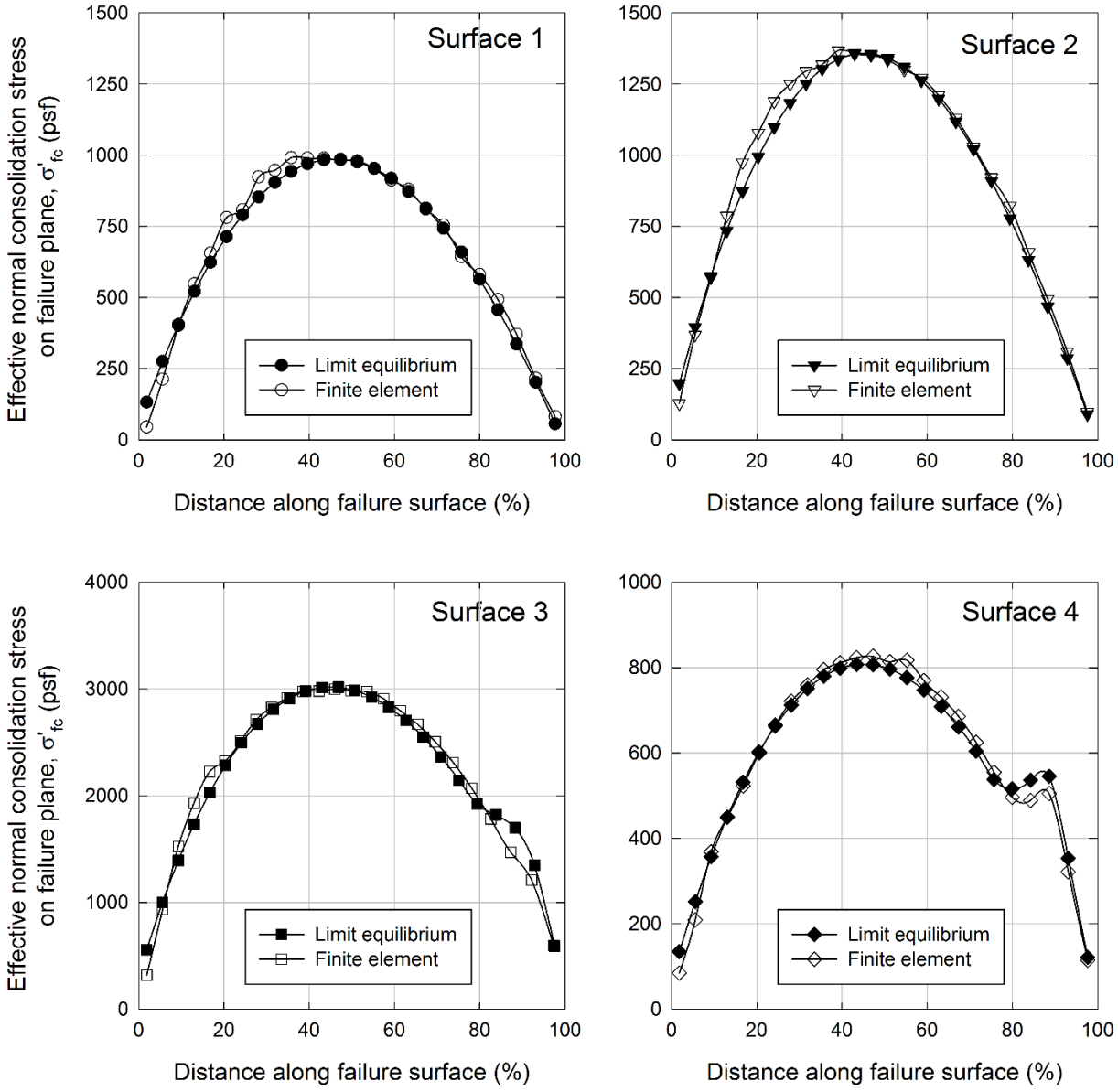

Figure 5-7. Effective normal consolidation stress along four trial surfaces for the Hypothetical Slope

Limit equilibrium analysis results in a different distribution of shear stress because it assumes a constant factor of safety along the failure surface. Figure 5-9 shows the average factor of safety determined using Eqn. (5-2) as well as the local F along the failure surfaces. The local F is calculated by Eqn. (5-2) using the stresses from a single slice base. Comparison of Figure 5-8 and Figure 5-9 shows that limit equilibrium predicts the same shear stress whenever the local F

from FEA matches the average *F* from FEA. If the local *F* is lower than average, limit equilibrium will calculate a lower shear stress and vice versa.

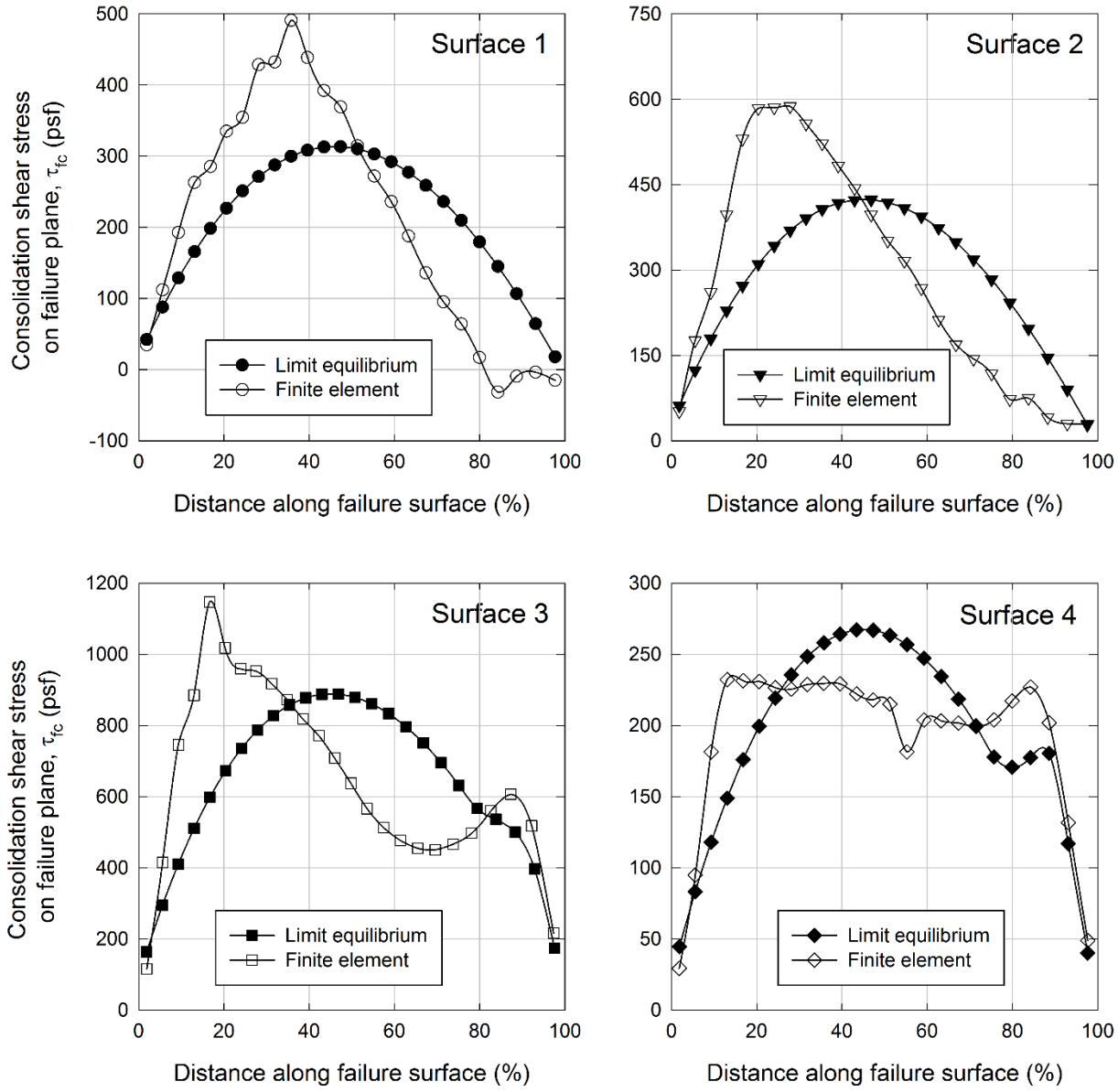

Figure 5-8. Consolidation shear stress along four trial surfaces for the Hypothetical Slope (distances are measured from toe of the failure surface). Note: Divide by 20.88 to obtain τ_{fc} in kPa

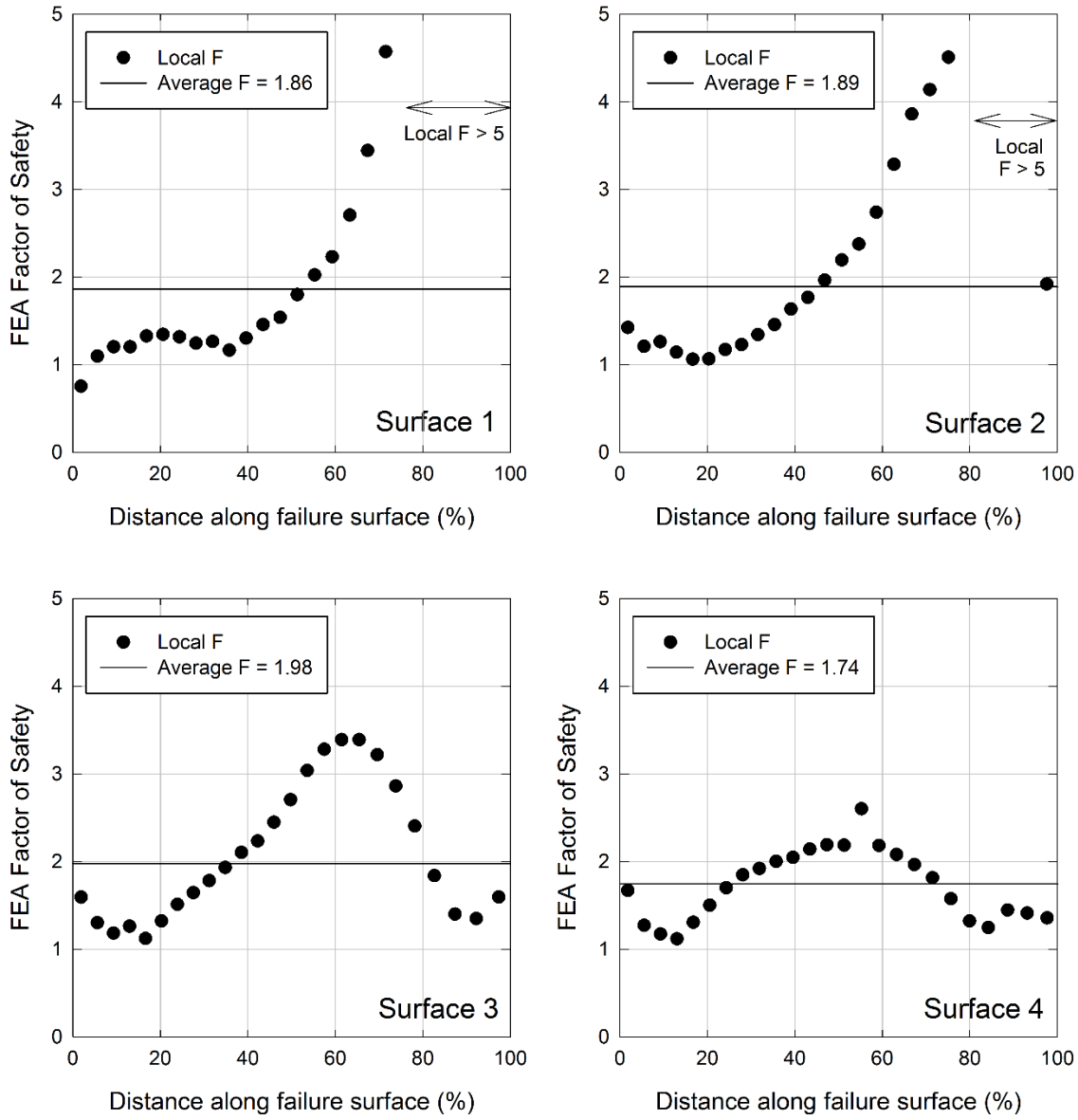

Figure 5-9. Local and average factor of safety along the four failure surfaces based on FEA stresses

A few simple checks were made on equilibrium for the FE analyses. The effective weight of soil above each failure surface was determined from the effective normal and shear stresses. This was compared with the weight of the soil and water determined from the slice geometry and soil unit weight minus the buoyant force at the bottom of each slice. The FE stresses yielded effective weights within 0.5% of those based on geometry.

The total shear force can be found by numerically integrating the shear stress along a given failure surface. The values from the LE and FE methods were found to be within 1% of each other. As required by statics, limit equilibrium calculates the same average shear stress as FEA for a particular trial surface even though it does not calculate the same distribution of shear stress.

Implications of Assumption #1 for Rapid Drawdown Analysis

These two examples suggest that limit equilibrium and finite element analysis predict similar distributions of effective normal stress along a trial failure surface. The average difference in σ'_{fc} was about 12% or less for these examples. This is encouraging for limit equilibrium based RDD analysis because the undrained strengths are directly related to the effective normal consolidation stress, making σ'_{fc} the most influential factor on the calculation of strength. The use of effective normal stresses from limit equilibrium appears to be justified from comparison of the LE and FE results. Exceptions to this generalization may occur where the slope geometry is more complex or layered soils of different stiffness are present. In the latter case, significant differences might be expected if arching occurs through stiffer soil layers. Further investigation into these effects is warranted.

Lowe and Karafiath's Assumption #1 is less accurate with regard to τ_{fc} as a direct result of the constant factor of safety for every slice inherent to the limit equilibrium procedure. For the hypothetical slope surfaces, the FEA value of τ_{fc} ranged from nearly 100% above to more than 100% below the LE value.

The shear stresses will affect the undrained strength for rapid drawdown because they are used to calculate K_c with Eqn. (5-1). Where τ_{fc} is too low, K_c will tend to be too low and vice versa. Changing K_c has a different effect on the undrained strength predicted by the DWW

method depending on the location of σ'_{fc} with respect to the envelope intersection point (see Figure 5-3). At higher stresses than $\sigma'_{fc\text{-}A}$, the LE method will predict lower strength than FEA when the limit equilibrium values of τ_{fc} and K_c are lower than the values calculated by FEA. Table 5-2 summarizes the other possible effects of differences in τ_{fc} on undrained strength for RDD. If undrained strength based on FEA analysis is assumed to be more accurate, the limit equilibrium method will tend to be unconservative wherever it is less than the FEA strength.

Table 5-2. Effect of differences in consolidation shear stress on undrained strength for RDD

For slices with:	LE τ_{fc} > FEA τ_{fc}	LE τ_{fc} < FEA τ_{fc}
$\sigma'_{fc} > \sigma'_{fc\text{-}A}$	LE strength < FEA strength	LE strength > FEA strength
$\sigma'_{fc} < \sigma'_{fc\text{-}A}$	LE strength > FEA strength	LE strength < FEA strength

Assumption #2 – No Principal Stress Rotation

Lowe and Karafiath's second assumption was that no principal stress rotation occurs between consolidation and failure. This allows the consolidation stresses to be located on a Mohr circle and K_c to be calculated. This section will examine the mathematical relationship between K_c and the stress orientation assumption, followed by results from the two example slopes.

Equations for K_c based on F and ϕ'

A LE trial failure surface has a constant factor of safety, F. Assuming that $c' = 0$, the shear strength mobilized at each slice can be represented by the mobilized friction angle, ϕ'_{mob}, defined as

$$\tan\phi'_{mob} = \frac{\tan\phi'}{F} \tag{5-3}$$

which is also equal to

$$\tan\phi'_{mob} = \frac{\sigma'_{fc}}{\tau_{fc}} \tag{5-4}$$

Equations (5-3) and (5-4) can be combined, yielding

$$\frac{\sigma'_{fc}}{\tau_{fc}} = \frac{\tan\phi'}{F} \tag{5-5}.$$

Three options will be considered for determining K_c as illustrated in Figure 5-10.

Option 1: Lowe and Karafiath's Assumption

Option 1 follows Lowe and Karafiath, assuming no rotation of principal stresses. Dividing the top and bottom of Eqn. (5-1) by σ'_{fc} gives

$$K_c = \frac{1 + \frac{\tau_{fc}}{\sigma'_{fc}} \frac{\sin\phi'+1}{\cos\phi'}}{1 + \frac{\tau_{fc}}{\sigma'_{fc}} \frac{\sin\phi'-1}{\cos\phi'}} \tag{5-6}.$$

For cases with $c' = 0$, Eqn. (5-5) can be inserted into Eqn. (5-6), removing σ'_{fc} and τ_{fc} from the expression,

$$K_c = \frac{1 + \frac{\tan\phi'}{F} \frac{\sin\phi'+1}{\cos\phi'}}{1 + \frac{\tan\phi'}{F} \frac{\sin\phi'-1}{\cos\phi'}} \tag{5-7}.$$

Finally, Eqn. (5-7) can be simplified to

$$K_c = \frac{F\cos\phi' + \tan\phi'(\sin\phi'+1)}{F\cos\phi' + \tan\phi'(\sin\phi'-1)} \tag{5-8}.$$

Using Eqn. (5-8), the variation of K_c with F can be calculated for various values of ϕ'. Figure 5-11 shows that most of the change in K_c occurs as the factor of safety drops below 2.

Option 1: Lowe and Karafiath's Assumption

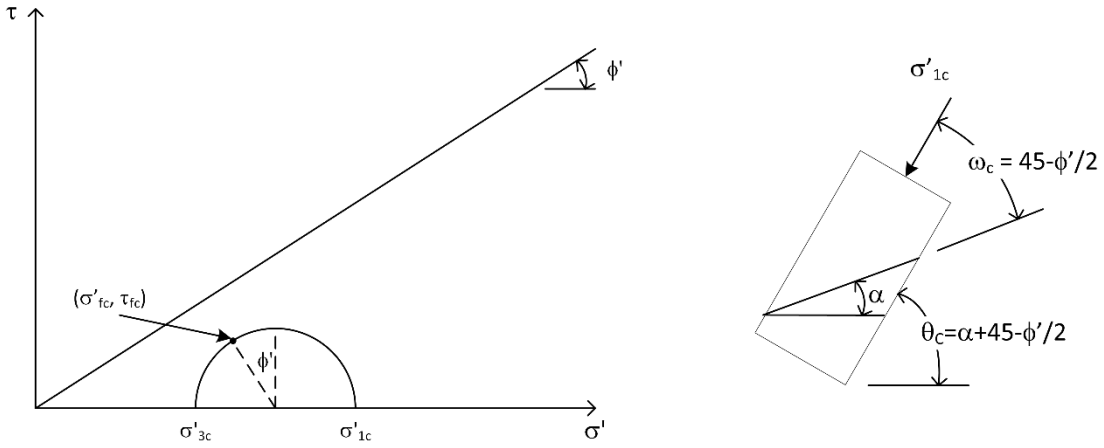

Option 2: Maximum obliquity assumption

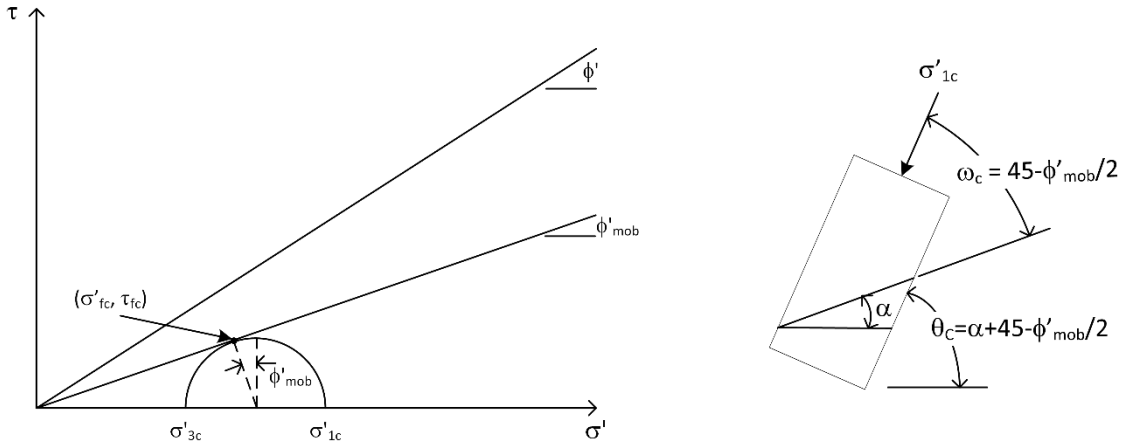

Option 3: Arbitrary Orientation

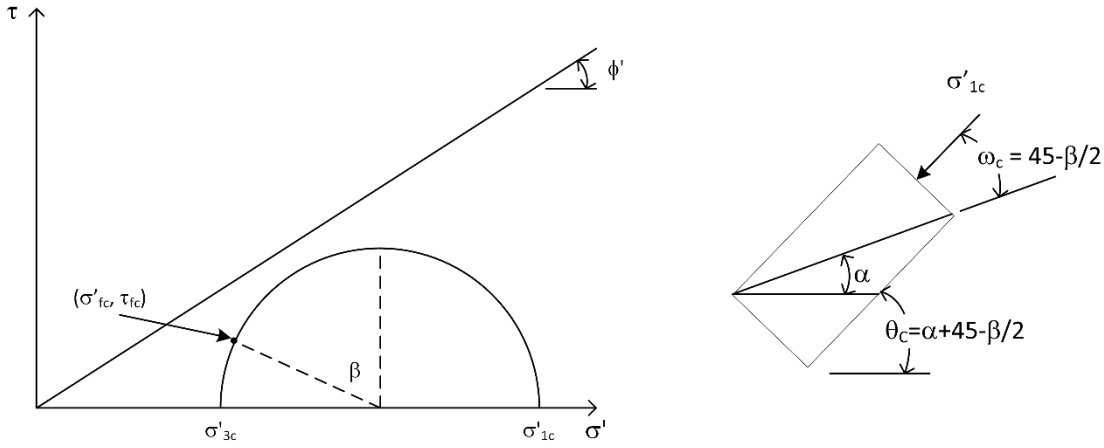

Figure 5-10. Three options for determining K_c from stresses on a plane, σ'_{fc} and τ_{fc}

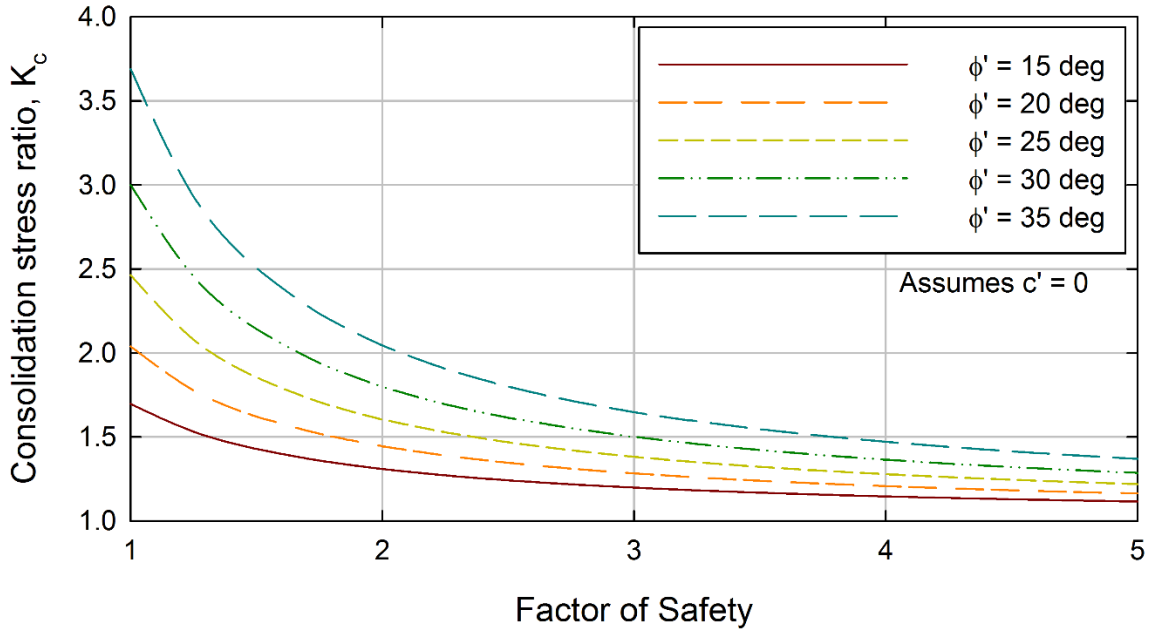

Figure 5-11. Relationship between K_c and F assuming no principal stress rotation from consolidation to failure ($c' = 0$)

Option 2: Maximum obliquity assumption

Instead of assuming no stress rotation, suppose that the consolidation stresses, σ'_{fc} and τ_{fc}, are at the point of maximum obliquity for ϕ'_{mob} on a Mohr circle. The stress ratio at consolidation, K_c, is simply the familiar obliquity relation

$$K_c = \frac{\sigma'_{1c}}{\sigma'_{3c}} = \frac{1+\sin\phi'_{mob}}{1-\sin\phi'_{mob}} \tag{5-9}$$

This is the minimum value of K_c for a given factor of safety because it is the Mohr circle with the least obliquity that can be drawn through the stresses, σ'_{fc} and τ_{fc}.

Option 3: Arbitrary orientation

Following the principles of Option 1, an arbitrary angle, β, can also be selected to orient the consolidation stresses on the Mohr circle, as shown in Figure 5-10. The consolidation stress

ratio in this case can be calculated by replacing ϕ' with β for the orientation terms of Eqn. (5-6 to (5-8), resulting in

$$K_c = \frac{\sigma'_{fc} + \tau_{fc}\dfrac{\sin\beta + 1}{\cos\beta}}{\sigma'_{fc} + \tau_{fc}\dfrac{\sin\beta - 1}{\cos\beta}} = \frac{F\cos\beta + \tan\phi'(\sin\beta + 1)}{F\cos\beta + \tan\phi'(\sin\beta - 1)} \tag{5-10}$$

As β increases, the major effective consolidation stress approaches an orientation parallel to the failure plane, and σ'_{fc} approaches the minor principal stress. For typical values of ϕ', the magnitude of principal stress rotation from consolidation to failure ranges from 0° for $\beta = \phi'$ to about 30° (away from the failure plane) if $\beta = 90°$. This amount of stress rotation falls between that induced by the compression and direct simple shear failure modes.

Implications of Consolidation Stress Orientation

The calculated value of K_c is influenced by the assumption made regarding the stress orientation. Figure 5-12(a) shows that Options 1 (no stress rotation) and 2 (maximum obliquity) result in almost the same relationship between F and K_c. Figure 5-12(b) plots the variation of K_c with F for various values of β (Option 3). As β increases above ϕ', σ'_{1c} becomes closer to parallel with the failure plane and K_c increases significantly for a given factor of safety.

Figure 5-12 can be rearranged to examine the variation of K_c at particular values of F, as shown in Figure 5-13. The lines in Figure 5-13 have been truncated at $\beta = \phi'_{mob}$, which is the lower bound of K_c for a given F. The upper bound is K_f where the K_c is constrained by the drained shear strength of the soil. As β increases, the value of K_c will increase if F is held constant. The lines intersect the K_f boundary at progressively lower values of β as F approaches 1.0.

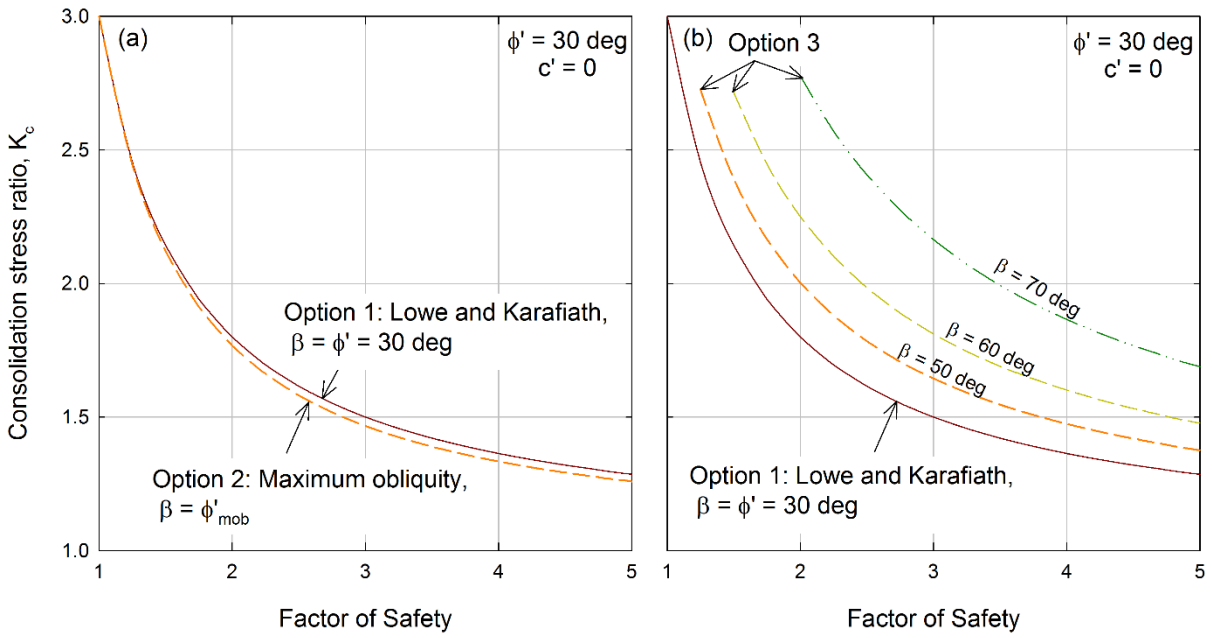

Figure 5-12. Comparison of the relationship between K_c and F for: (a) No principal stress rotation (Option 1) and maximum obliquity assumption (Option 2), (b) Option 1 and arbitrary orientation (Option 3).

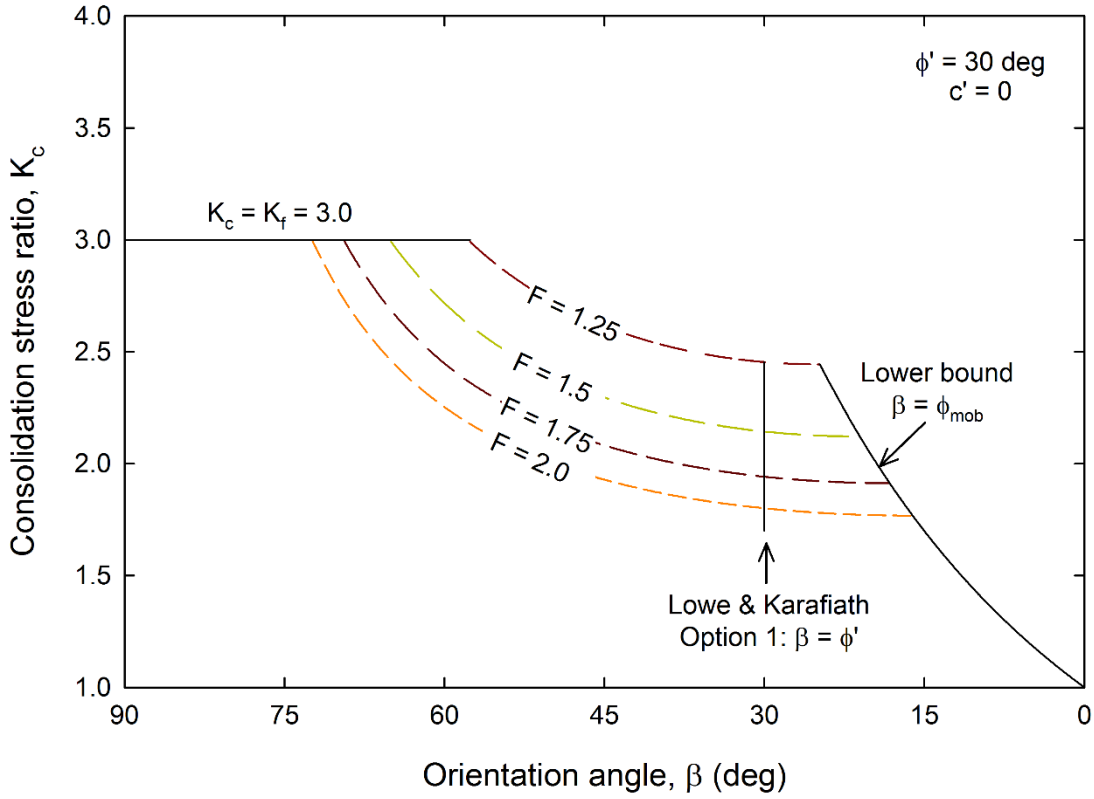

Figure 5-13. Relationship between K_c and the assumed consolidation stress orientation, β

Figure 5-13 indicates that Lowe and Karafiath's assumption results in a value of K_c that is close to the minimum for a given factor of safety. Thus, K_c from limit equilibrium will usually be equal to or less than the true value, assuming the consolidation stresses are correct. The implications of this conclusion on undrained strength are illustrated in Figure 5-14. Two general possibilities are evident:

1. $\sigma'_{fc} < \sigma'_{fc\text{-}A}$ – the undrained strength, τ_{ff}, obtained by assuming no stress rotation will be equal to or greater than the strength corresponding to the true K_c. The assumption that $\beta = \phi'$ is *unconservative* in this region.
2. $\sigma'_{fc} > \sigma'_{fc\text{-}A}$ – the undrained strength, τ_{ff}, obtained by assuming no stress rotation will be equal to or less than the strength corresponding to the true K_c. The assumption that $\beta = \phi'$ is *conservative* in this region.

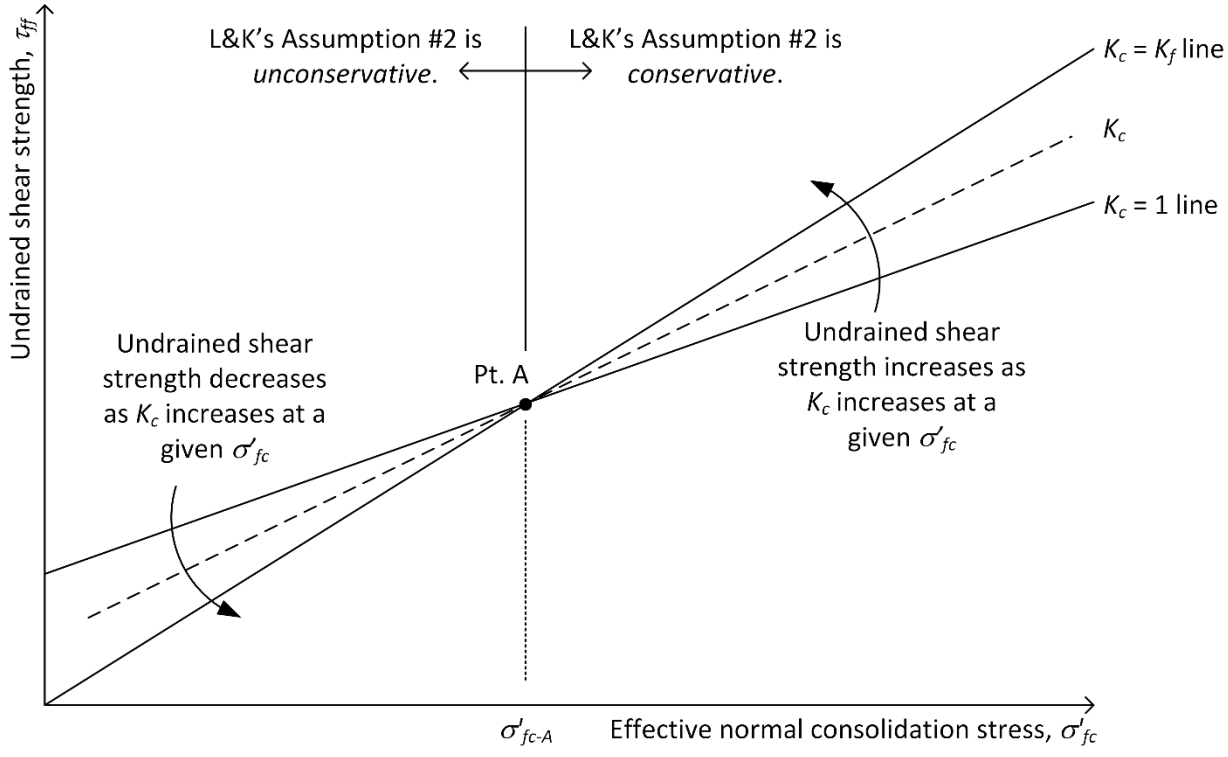

Figure 5-14. Effect of increasing K_c on undrained strength from linear interpolation method

If $\sigma'_{fc\text{-}A}$ lies in the middle of the range of stresses present in an embankment, undrained strengths based on Lowe and Karafiath's assumption will tend to be too high at shallow depths and too low deeper within the embankment. Stresses on relatively horizontal planes tend to have higher normal stress than planes which are closer to vertical. Thus the undrained strength calculated for steep planes will tend to be too high while the strength for flat planes will tend to be too low. These trends will tend to bias the predicted failure surfaces toward deep, basal failures. This may be part of the reason why the Walter Bouldin Dam failure mechanism predicted by the DWW method is deeper than the observed failure.

For a poorly compacted clay, such as Pilarcitos Dam, almost all of the embankment will be at a stress state higher than $\sigma'_{fc\text{-}A}$ (Figure 5-3). Lowe and Karafiath's assumption about stress orientation appears to be conservative in this case. On the other hand, a well-compacted clay will have a high value of $\sigma'_{fc\text{-}A}$, as illustrated by the silty clay properties in Figure 5-3. Duncan et al. (1990) state that $\sigma'_{fc\text{-}A}$ for this clay corresponds to a submerged depth of about 80 ft (24 m). At depths shallower than 80 ft (24 m), the assumption of no stress rotation from consolidation to failure may lead to an unconservative estimate of undrained strength for well-compacted soil.

Example: Pilarcitos Dam

The major effective consolidation stresses from LE and FEA are compared for Pilarcitos Dam in Figure 5-15(a). The FE values of σ'_{1c} are lower than the LE values by as much 33%, even though the normal and shear stresses from LE and FEA were quite close for Pilarcitos Dam. This difference in σ'_{1c} is the result of assuming no stress rotation from consolidation to failure.

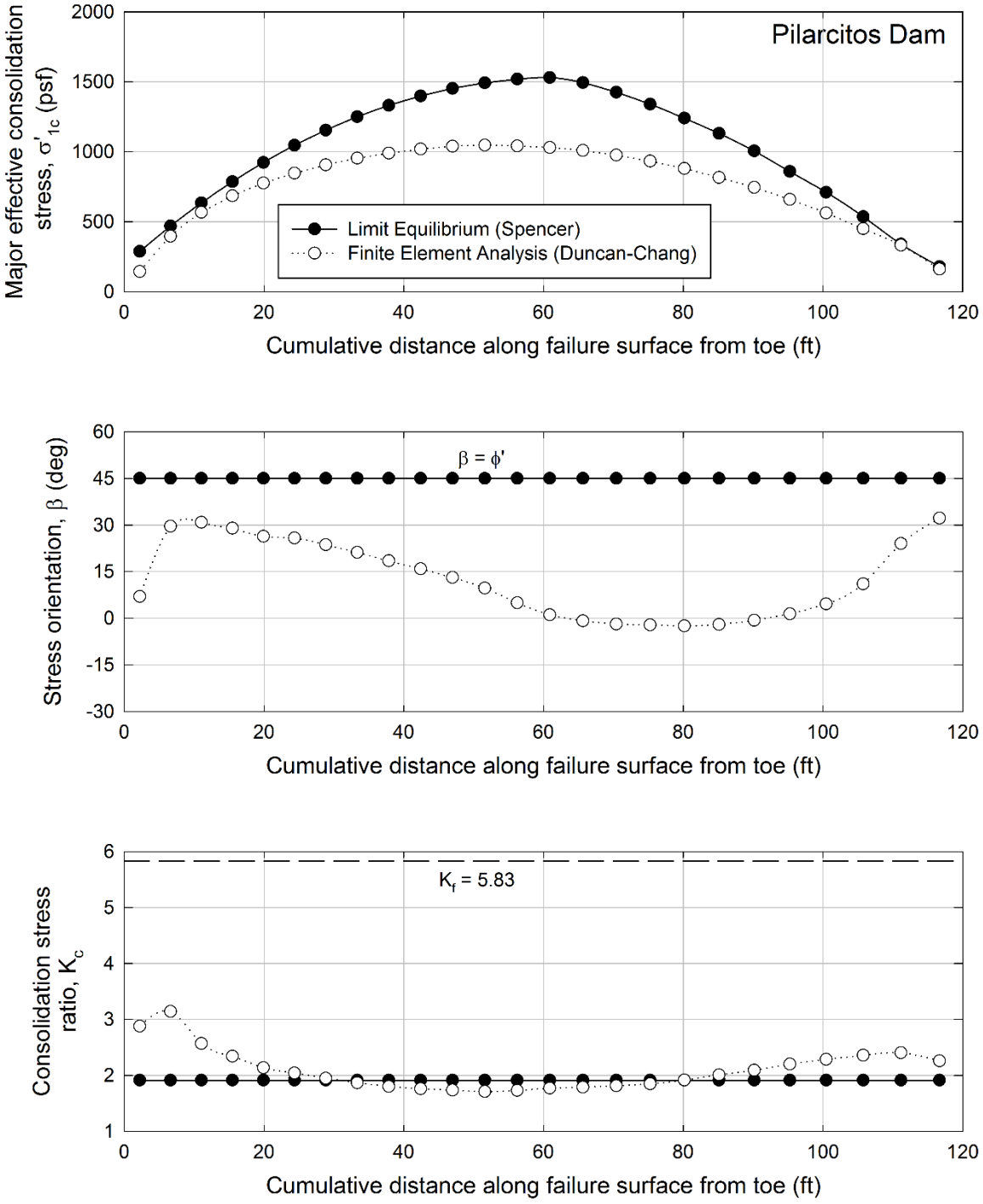

Figure 5-15. Comparison of σ'_{1c}, β, and K_c along the DWW critical circle for Pilarcitos Dam. Note: 1 kPa = 20.89 psf and 1 m = 3.28 ft.

The orientation of the consolidation stress system along the critical failure surface is plotted in Figure 5-15(b). The FE values of β are less than those implied by Lowe and Karafiath's

assumption of no stress rotation. The FEA consolidation stresses were oriented closer to the maximum obliquity condition, which leads to almost the same K_c as assuming no principal stress rotation. This explains why the two methods yield very similar values of K_c as indicated in Figure 5-15(c). The FEA K_c values are on average 10% higher than those from limit equilibrium.

The Pilarcitos Dam analyses illustrate two things about the orientation assumption:

- Values of σ'_{1c} obtained from limit equilibrium by Lowe and Karafiath's assumptions will not be consistently the same as the FEA, even if σ'_{fc} and τ_{fc} are similar to the FEA values.
- Lowe and Karafiath's assumptions can predict similar values of K_c to finite element analysis even if σ'_{1c} is quite different from FEA.

Example: Hypothetical Slope

Values of σ'_{1c}, β, and K_c from LE and FEA are shown for Surfaces 1 and 3 in Figure 5-16. For Surface 1, the FEA values of σ'_{1c} are up to 62% higher than those from LE. The consolidation value of β is greater than 30° (ϕ') over most of the surface 1. The differences in β and τ_{fc} (see Figure 5-8) result in FEA values of K_c about 50% higher than those from Lowe and Karafiath's assumptions. On the other hand, the FEA and LE values of σ'_{1c} for Surface 3 match quite well and β is at most 15° higher than ϕ'. With β values in this range, the differences in K_c are mostly due to τ_{fc}. Referring to Figure 5-8, the FEA K_c is higher than the LE value wherever the FEA τ_{fc} is higher than that from LE.

Examining all four surfaces from the hypothetical slope finite element analysis, K_c ranged from 60% above to 25% below the LE values. This range is the result of the combined effects of differences in σ'_{fc}, τ_{fc}, and stress system orientation. Because the assumption of no stress

rotation is close to the minimum value of K_c, the limit equilibrium K_c will more often be lower than the finite element analysis value.

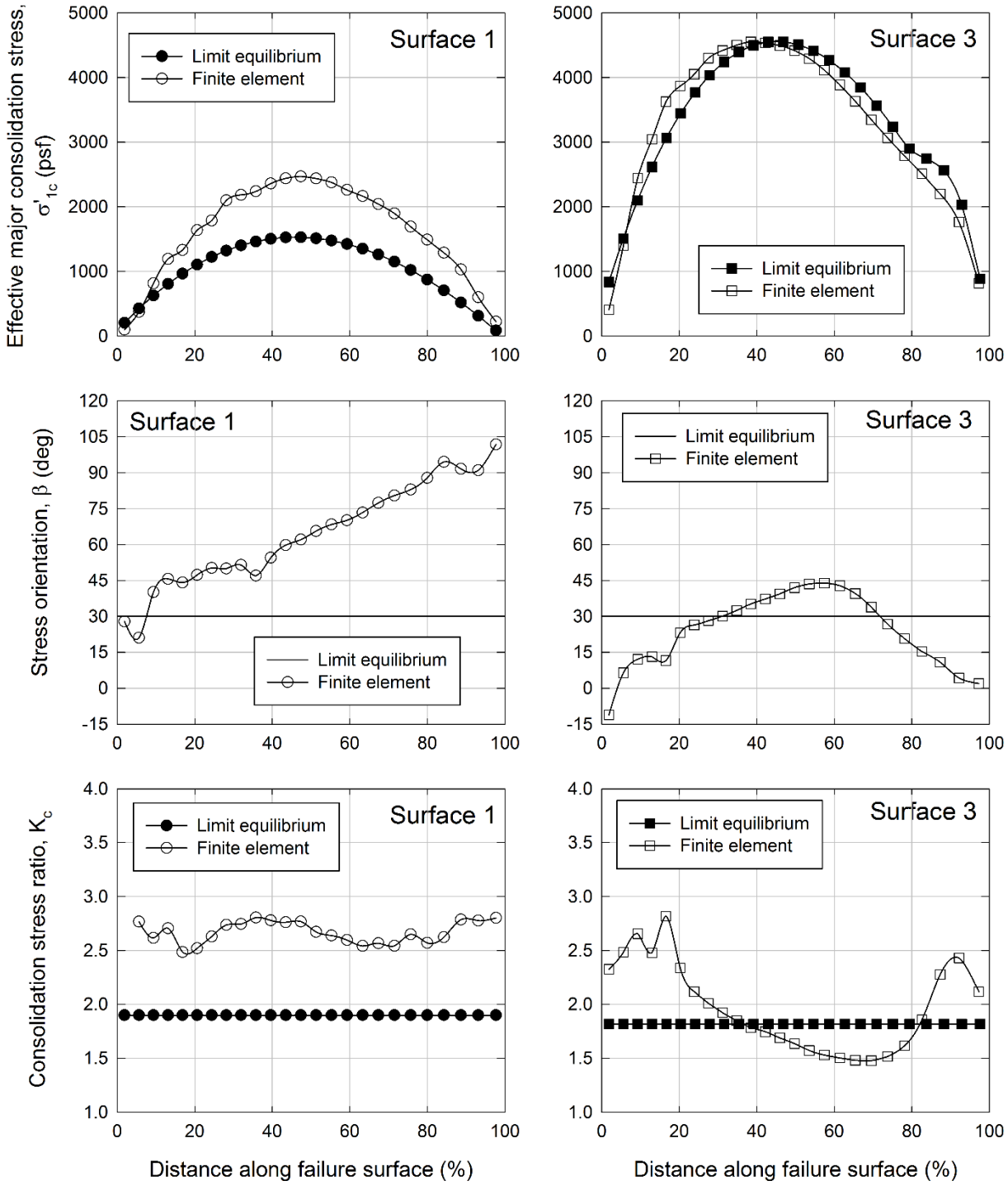

Figure 5-16. Comparison of σ'_{1c} and K_c for surfaces 1 and 3 of the Hypothetical Slope

Conclusions Regarding the Stress Orientation Assumption

Based on this review of Lowe and Karafiath's assumption of no principal stress rotation, the following conclusions have been made:

- Explicit formulas for K_c have be developed in terms of ϕ' and factor of safety when $c' = 0$. These formulas allow the effects of Lowe and Karafiath's $\beta = \phi'$ assumption on K_c to be directly assessed.
- The assumption of no stress rotation leads to a value of K_c that is very close to the minimum possible value for a set of consolidation stresses and factor of safety. Other assumptions regarding the stress orientation can lead to significantly higher stress ratios. The resulting strengths tend to be unconservative at low σ'_{fc} and conservative at high σ'_{fc}.
- The hypothetical slope FEA results suggest that σ'_{1c} tends to be oriented more parallel to likely failure surfaces than implicitly assumed by Lowe and Karafiath, i.e. β tends to be greater than ϕ'.
- The difference between K_c from limit equilibrium and K_c from FEA is affected by the differences in both the shear stress and the stress orientation. Taking both of these into account, Lowe and Karafiath's method tends to underestimate K_c.

Assumption #3 – Predicting ACU strengths with ICU tests

The third assumption made by Lowe and Karafiath was that ACU strengths can be estimated from ICU-TC tests.

ACU Strengths vs. Strength from Linear Interpolation

The original procedures for predicting ACU strength proposed by Lowe and Karafiath were validated using the results of a few ICU and ACU tests on poorly saturated specimens. In this section, the results of ICU and ACU triaxial compression tests on five compacted clays are used

to assess how well the linear interpolation procedure or DWW method (Duncan et al. 1990) predicts ACU strengths. The following steps have been followed for the five available sets of data:

1. Determine the $K_c = 1$ and $K_c = K_f$ envelopes from the ICU-TC data, obtaining the parameters ϕ' and c' for the $K_c = K_f$ line and $\psi_{Kc=1}$ and $d_{Kc=1}$ for the $K_c = 1$ line. The strength parameters for these five clays are summarized in Table 5-3.
2. Each ACU test was consolidated to a particular K_c and has a value of σ'_{fc} based on the consolidation stresses and ϕ'. The linear interpolation procedure is used to calculate the *predicted* undrained strength by linear interpolation, $\tau_{ff\text{-}DWW}$, for each ACU-TC test.
3. Calculate the corresponding ICU-TC undrained strength, $s_{u\text{-}ICU}$, that corresponds to the value of σ'_{1c} from each ACU-TC test. The $K_c = 1$ line can conveniently be used to determine $\tau_{ff\text{-}Kc=1}$, which can be converted to $s_{u\text{-}ICU}$ by dividing by cos ϕ'.

The undrained strengths, $\tau_{ff\text{-}DWW}$, obtained by the DWW method should be correct on average because the method yields a reasonable factor of safety for the Pilarcitos and Walter Bouldin case studies. Differences between $\tau_{ff\text{-}DWW}$ and either $s_{u\text{-}ACU}$ or $s_{u\text{-}ICU}$ must be due to differences between the triaxial tests and conditions in the field.

Table 5-3. Strength parameters for five compacted clays

Soil	$K_c = K_f$ line		$K_c = 1$ line	
	ϕ' (deg)	c' (psf)	$\psi_{Kc=1}$ (deg)	$d_{Kc=1}$ (psf)
Riverview	31.8	369	20.1	1372
St. Croix	19.6	248	15.0	476
Oak Harbor	25.8	144	27.5	317
Monarch	24.1	1260	14.5	4066
Higgins	24.1	985	19.7	2843

Ref: Riverview - Castellanos (2011); St. Croix – Johnson and Lovell (1979); Monarch and Higgins – Lee and Morrison (1970).

The undrained strengths from ACU tests are compared with the corresponding $\tau_{ff\text{-}DWW}$ values from linear interpolation in Figure 5-17 for strengths below 100 psi, which is a practical range of stress for RDD. The undrained strengths predicted by linear interpolation are significantly lower than those measured for anisotropically consolidated compacted clays. At very high consolidation stresses above 100 psi (not shown in Figure 5-17), the predicted and measured values match quite closely for Monarch kaolinite and Higgins clay. However, at these stresses, the interpolated and ACU undrained strengths both approach the ICU-TC strength and a match would be expected.

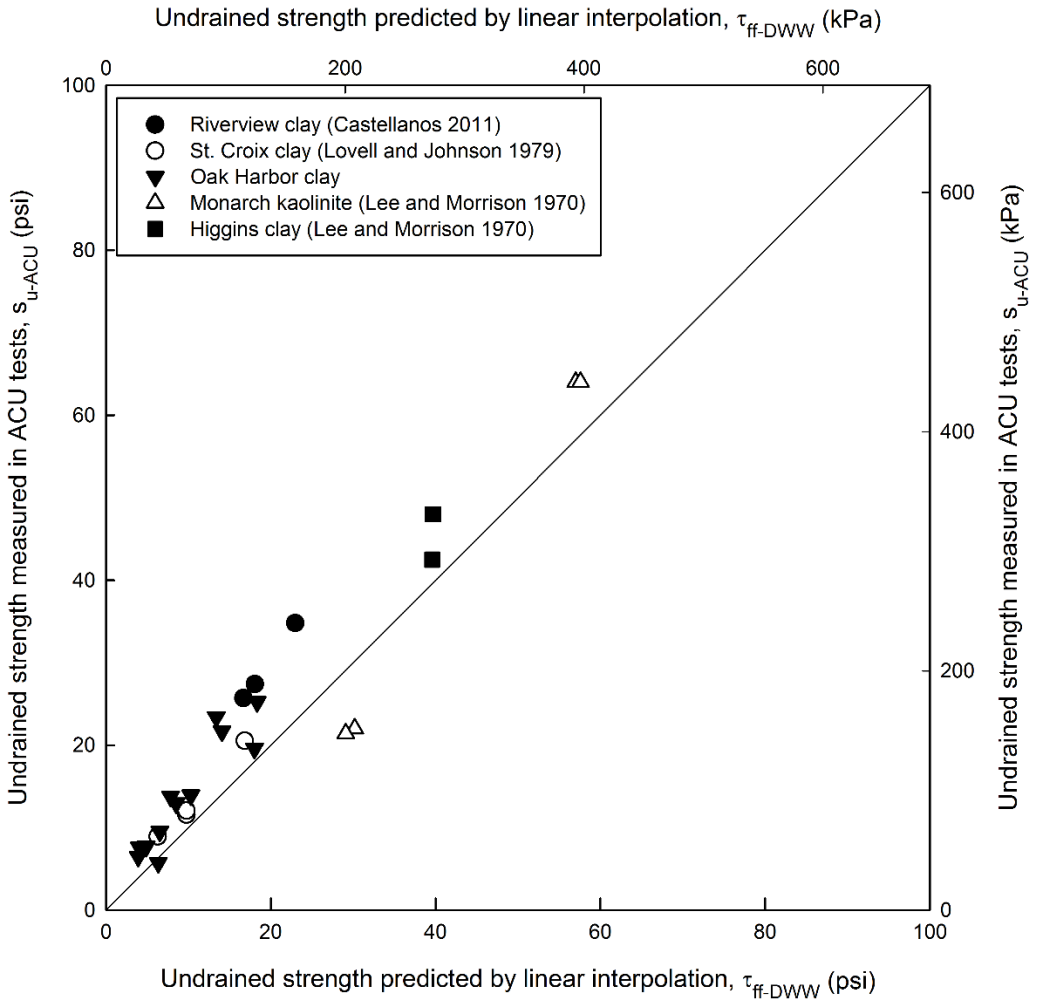

Figure 5-17. Comparison of undrained strengths obtained by ACU tests with those predicted by linear interpolation for five compacted clays.

The triaxial tests on compacted Oak Harbor clay (discussed in more detail in Chapters 6 and 7) can be examined to further understand the differences in methods of obtaining strength. Using the value of σ'_{fc} from each of the twelve Oak Harbor ACU-TC tests, $s_{u\text{-}ICU}$ was calculated from the $K_{c=1}$ envelope and ϕ', and $\tau_{ff\text{-}DWW}$ was determined by linear interpolation. These two calculated strengths along with the measured ACU strengths are plotted for Oak Harbor clay in Figure 5-18. All three strengths are plotted against the actual major effective consolidation stress from the ACU tests. Again, it is clear that linear interpolation predicts lower strengths than those that result from actual ACU tests.

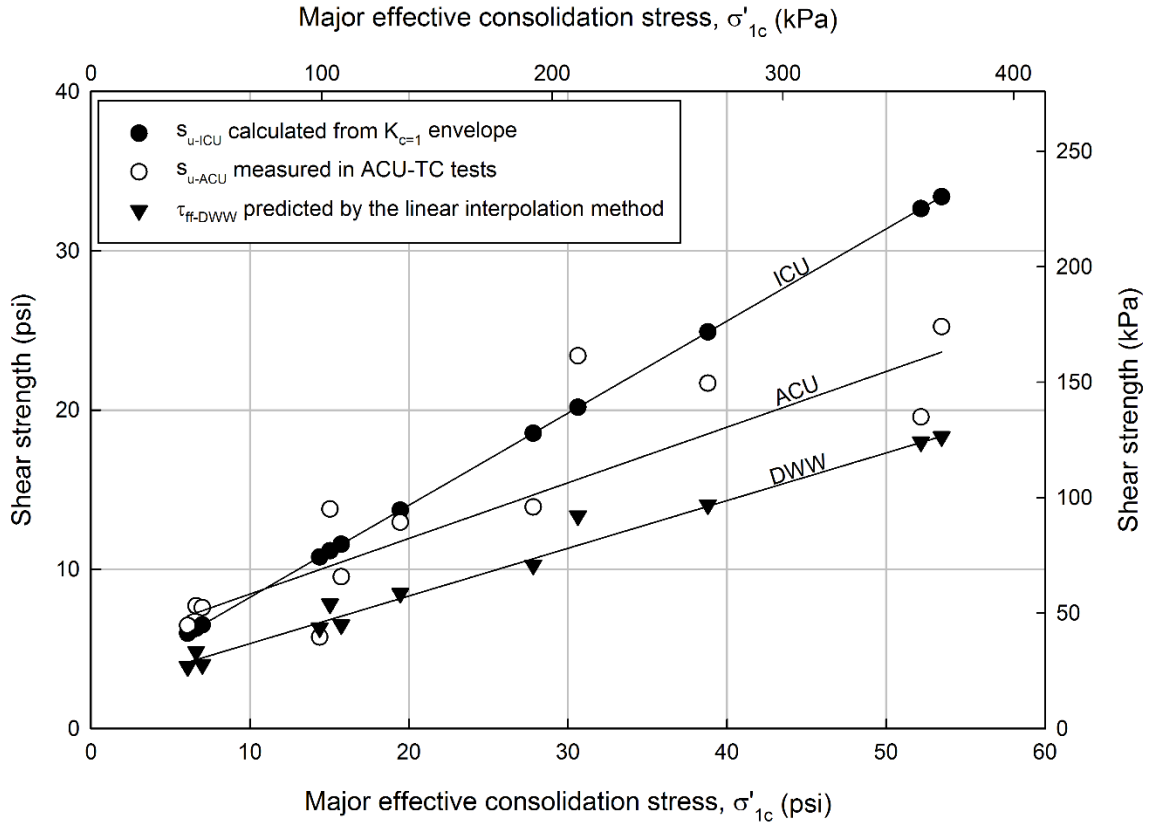

Figure 5-18. Comparison of undrained strengths from ACU tests with predicted ICU and τ_{ff} strengths, Oak Harbor clay

Based on the test data in Figure 5-18, the idealized relationship shown in Figure 5-19 has been developed for undrained strength for rapid drawdown. Linear interpolation produces an

undrained strength relationship that is significantly lower than that from ACU tests but that appears to be correct on average, since it results in the correct factor of safety for the Pilarcitos and Walter Bouldin dams. Thus, the combined effects of Lowe and Karafiath's assumptions must adjust the ICU strengths for other factors in addition to anisotropic consolidation, including stress system effects like principal stress rotation and plane strain.

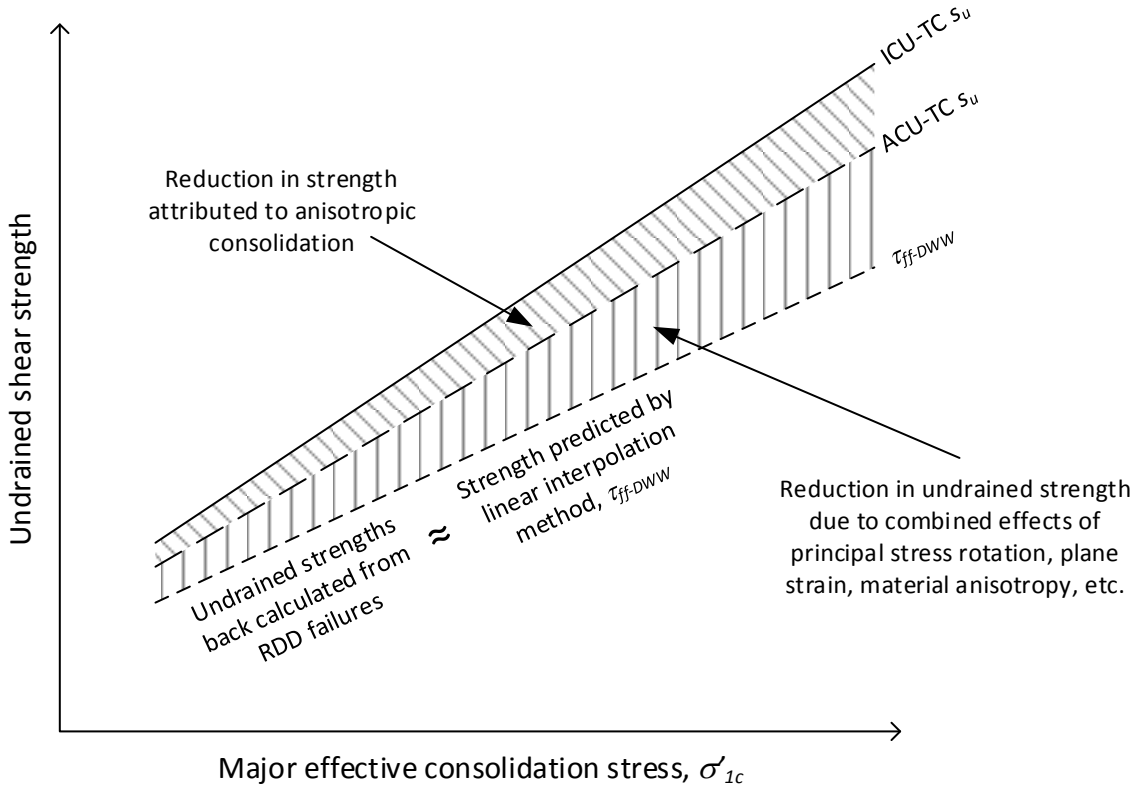

Figure 5-19. Idealized relationship between undrained strength and consolidation stress for RDD

Adjustment to Undrained Strength Caused by Linear Interpolation

Lowe and Karafiath's $K_c = 1$ and $K_c = K_f$ envelopes can be transformed into a relationship between undrained strength and major effective consolidation stress, similar to Figure 5-19. The ICU-TC and ACU-TC strengths are easily expressed in these terms directly from the test results. A derivation of $\tau_{ff\text{-}DWW}$ in terms of σ'_{1c} with interpolation in terms of σ'_{fc} can be found in

Appendix D. With both strengths expressed as functions of σ'_{1c}, the ratio of undrained strength from linear interpolation can be compared to that from the ICU-TC tests as

$$R_{DWW} = \frac{\tau_{ff-DWW}}{s_{u-ICU}} \quad (5\text{-}11).$$

R_{DWW} will vary with K_c and somewhat with σ'_{1c}. The average value of R_{DWW} from 100 to 2000 psf (4.8 to 98 kPa) has been calculated for the five compacted clays in Table 5-3 as well as the soils from Pilarcitos and Walter Bouldin dams. The values are summarized in Table 5-4. The values of R_{DWW} for K_c = 2, which is common for many trial failure surfaces, ranged between 0.52 and 0.83. At K_c = 2, the linear interpolation procedure reduces the ICU-TC undrained strengths by a factor of about 20% to 50% for rapid drawdown analysis, provided σ'_{1c} is predicted accurately. The same calculations were performed for K_c of 1.5 and 3.0, which are 25% below and 50% above K_c = 2. Comparisons between limit equilibrium and FEA earlier in this chapter found that the FEA value K_c was in this range compared to the limit equilibrium values. The differences in K_c were the result of the approximations made by Lowe and Karafiath's first two assumptions.

The reduction factors in Table 5-4 are those due solely to the linear interpolation procedure. They assume that σ'_{1c} and K_c are accurately calculated by LE. As seen in Figure 5-15 and Figure 5-16, it is likely that both of these values can differ significantly from the FEA results. The undrained strengths that result from Lowe and Karafiath's assumptions and the linear interpolation procedure combine the effects of interpolation with differences in σ'_{1c} and K_c. For this reason, the $\tau_{ff\text{-}DWW}$ line in Figure 5-19 is only positioned correctly with respect to $s_{u\text{-}ICU}$ if plotted against the correct values of σ'_{1c}.

Table 5-4. Average R_{DWW} for σ'_{1c} between 100 and 2000 psf for nine compacted soils

Soil	Average value of $R_{DWW} = \tau_{ff\text{-}DWW} / s_{u\text{-}ICU}$ for:		
	$K_c = 1.5$	$K_c = 2$	$K_c = 3.0$
Higgins	0.85	0.81	0.77
Monarch	0.86	0.83	0.80
Oak Harbor	0.73	0.64	0.52
Pilarcitos	0.58	0.52	0.45
Riverview	0.76	0.71	0.64
St. Croix	0.86	0.81	0.76
Walter Bouldin CL	0.83	0.76	0.68
Walter Bouldin ML	0.83	0.77	0.69
Walter Bouldin SM	0.77	0.71	0.64

Note: For soils with $c' > 0$, interpolation was performed using the method in appendix D.

Example: Pilarcitos Dam

Undrained shear strengths were calculated using linear interpolation along the DWW critical circle for Pilarcitos Dam. Likewise, σ'_{1c} values from the finite element analysis were used along with a power curve relationship developed from the Pilarcitos data (discussed in Chapter 8) to calculate undrained strengths corresponding to ICU-TC.

The strengths calculated by each method are compared in Figure 5-20. The ratio between the average strength based on Lowe and Karafiath's assumptions and the average ICU-TC strength based on the FE stresses is 0.62. This reduction is higher than that predicted in Table 5-4 for Pilarcitos Dam. The difference is caused by the limit equilibrium σ'_{1c} values that are on average 28% higher than those from FEA as seen in Figure 5-15, which increases the average DWW strength.

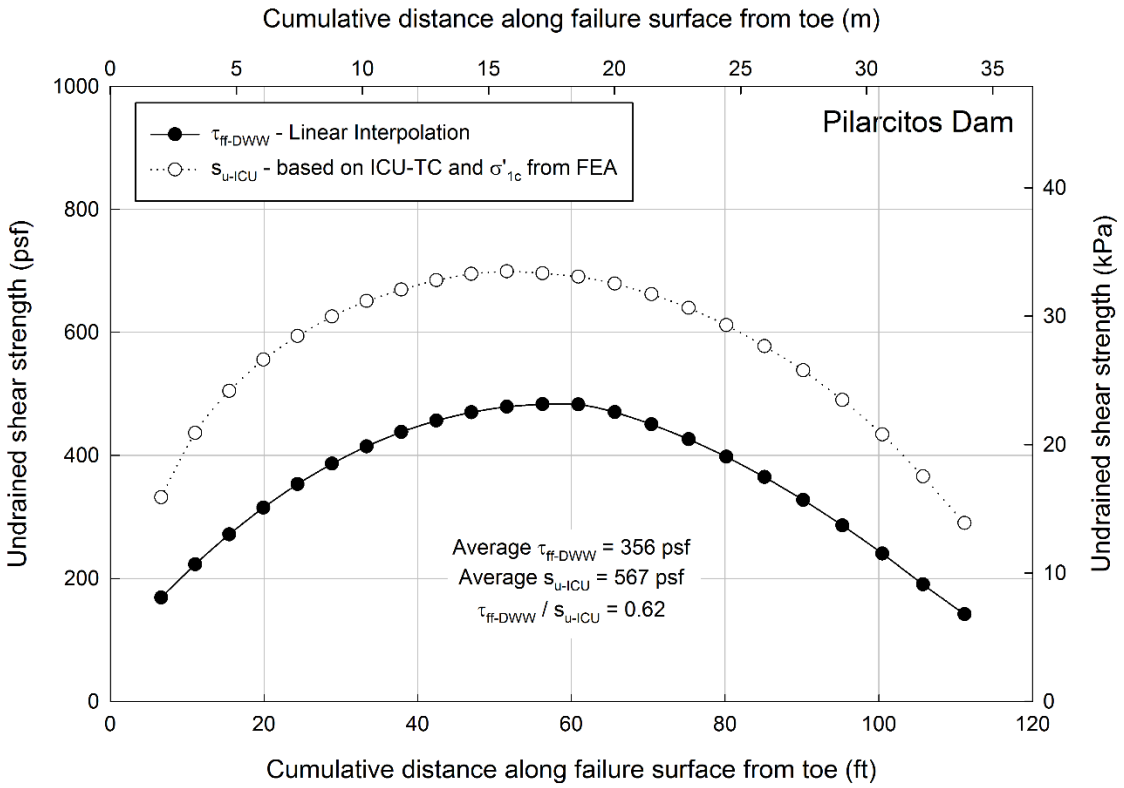

Figure 5-20. Comparison of undrained shear strength along the DWW critical circle for Pilarcitos Dam

Summary

The linear interpolation method of determining undrained strengths for rapid drawdown analysis has been examined using laboratory data, analytical, and numerical methods. The following conclusions can be made:

- Linear interpolation causes a reduction in undrained strength that is greater than the reduction caused by anisotropic consolidation.
- The additional reduction in strength can be thought of as accounting for the combined effects of factors such as plane strain, principal stress rotation, compaction prestress, and anisotropic strength parameters.
- The linear interpolation method causes a reduction in strength that is generally in the range of 20 to 40% for nine soils.

Conclusions

The effects of Lowe and Karafiath's assumptions on undrained strength for rapid drawdown are summarized in Table 5-5.

Table 5-5. Conclusions regarding the practical implications of Lowe and Karafiath's assumptions for RDD analysis

Assumption	Conclusions	Practical Implications
#1: Stresses on slice bases from limit equilibrium can be used to estimate the consolidation stress state.	• Limit equilibrium predicts σ'_{fc} within about 12% of FEA. • The average LE shear stress matches FEA but the shear stress distribution may be very different.	• σ'_{fc} is a good stress on which to "anchor" the strength prediction for LE analysis of rapid drawdown. • Differences in τ_{fc} lead to differences in K_c, which can decrease or increase undrained strength.
#2: No principal stress rotation occurs from consolidation to failure. This allows the LE stresses to be located on a Mohr circle and K_c to be calculated.	• The actual K_c is likely equal to or greater than the L&K value. • FEA values of K_c for four example surfaces ranged from 60% higher to 25% lower than the LE values.	• Low K_c will tend to over-estimate strength for low consolidation stresses or well-compacted soils. • Low K_c will tend to under-estimate strength for high consolidation stresses or poorly-compacted soils.
#3: The K_c=1 and K_c=K_f envelopes from ICU-TC tests can be used to approximate the effects of anisotropic consolidation. The DWW linear interpolation method is the state of practice.	• Linear interpolation causes more reduction than that due to anisotropic consolidation. • Differences in the predicted stress state effect the magnitude of the reduction.	• Linear interpolation accounts for strength reduction due to multiple stress system factors. • Linear interpolation results in undrained strengths that are about 60 to 80% of the ICU-TC strength.

6. Triaxial Tests on Compacted Clays for Consolidated-Undrained Conditions

Introduction

Effective procedures have been developed for consolidated-undrained triaxial tests on saturated clays, but tests on compacted clays involve additional factors for which procedures are not so well established. Because compacted samples are not saturated at the beginning of a test, consideration must be given to the procedures used for applying the confining pressure and back pressure so that the tests best represent the behavior of the clay in an embankment in the field. The test results discussed in this chapter show the behavior of a compacted clay during back pressure saturation and consolidation, and provide a basis for recommendations for performing consolidated-undrained tests on compacted clays.

Compacted clay is used widely for the construction of embankments for earth dams, levees, and roadways. Some design conditions, such as rapid drawdown, require undrained strengths for compacted clay after it has been consolidated under the weight of the overlying embankment and saturated due to seepage. In this case, the undrained strength of the clay must be measured using consolidated-undrained (CU) laboratory tests.

The volume change and shearing behavior of compacted clay is influenced greatly by the initial clay structure, which is related to the compaction method; compaction water content, w; and compacted unit weight, $\gamma_{d\text{-}comp}$ (e.g. Seed et al. 1960, Johnson and Lovell 1979). Compacted clays will tend to swell at some combinations of w, $\gamma_{d\text{-}comp}$, and consolidation stress, and will tend to compress at higher pressures. The initial conditions and dry unit weight after consolidation affect the undrained strength by changing the pore pressure response during undrained loading.

The undrained strength of soil, including compacted clay, will also be affected by factors such as overconsolidation, consolidation stress state, and principal stress rotation during loading. Literature regarding the effect of these factors on the undrained strength of compacted clays is sparse.

This study chapter considers the effects of anisotropic consolidation on the undrained strength of a compacted lean clay. The influence of the initial compacted conditions observed in the tests, and the challenges involved in testing compacted soils are discussed, and guidelines for addressing these challenges are outlined.

Literature Review

Volume Change during Saturation

Seed et al. (1960) found that the unit weight and *w* after saturation depend on both the initial compaction conditions and the effective stress during saturation, σ'_s, which is equal to the cell pressure minus back pressure (*CP-BP*) in the triaxial test. Seed et al. compacted specimens at a range of dry unit weights and water contents, and allowed the specimens to saturate at either 6.9 kPa or 241 kPa. Once the specimens were saturated, the drainage valves were closed, the cell pressure was changed to 98 kPa, and the specimens were sheared undrained. It was observed that specimens compacted dry of optimum swell more than those compacted wet of optimum to the same initial dry unit weight and saturated at the same σ'_s. The increase in swell leads to lower unit weights after consolidation and lower undrained strengths for the specimens compacted dry of optimum. This effect of compaction water content on strength is more pronounced for specimens saturated at low effective stress.

Johnson and Lovell (1979) performed CU triaxial compression tests on compacted clay specimens that were saturated at stresses between 3 and 10 psi (21 and 69 kPa) and then

isotropically consolidated to stresses ranging from 10 to 40 psi (69 to 276 kPa). Johnson and Lovell found that the tendency to swell (from compaction to end of consolidation) decreased with increased initial saturation and increased consolidation stress, σ'_c. Specimens with higher compacted unit weight were more likely to swell.

Both Seed et al. and Johnson and Lovell found that the unit weight after consolidation, $\gamma_{d\text{-}cons}$, for compacted clays depends on the combined effects of the compaction water content, relative compaction, σ'_s, and σ'_c. For example, the behavior of two specimens, A and B, compacted to the same $\gamma_{d\text{-}comp}$ at different w is shown in Figure 6-1. If the same σ'_s, and σ'_c are used, the unit weight after consolidation for specimen B will be greater than that for specimen A.

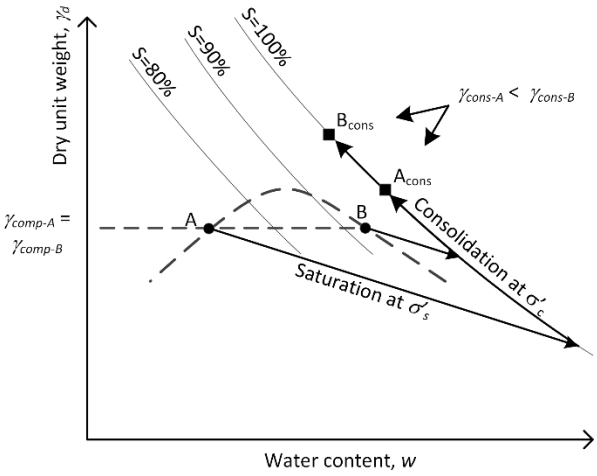

Figure 6-1. Effect of compaction water content on volume change during saturation at σ'_s and consolidation at σ'_c (after Seed et al. 1960, Johnson and Lovell 1979)

One-dimensional consolidation of compacted clay has been studied by Barden (e.g. 1965, 1971, 1974) and DiBernardo and Lovell (1979). Barden found that the consolidation behavior was affected by the degree of saturation and the continuity of the air phase. Dry of optimum, the air phase tends to be continuous, and air can flow easily. As saturation increases, the air phase becomes discontinuous near the optimum water content, and the air permeability drops

drastically. This change influences the shape of the compaction curve and the compressibility of the compacted clay. DiBernardo and Lovell (1979) performed consolidation tests on clay specimens compacted at a range of water contents. The compacted specimens exhibited a change in compressibility similar to that due to overconsolidation. They labeled the stress at which the compressibility changed abruptly the "apparent prestress," which is analogous to preconsolidation stress in natural soils. Wet of optimum specimens had a lower apparent prestress compared to specimens prepared dry of optimum to the same compacted unit weight. Many of DiBernardo and Lovell's tests were performed without saturating the specimens. However, some of the tests were back pressure saturated at a particular vertical effective stress, rebounded and then reloaded. When this procedure was used, the apparent prestress was reduced to the vertical effective stress that was applied during saturation. The reduction in prestress occurred particularly for specimens compacted dry of optimum. The tests show that saturation at effective stresses below the apparent prestress can remove some of the prestressing effects caused by compaction.

More recent research into the behavior of compacted clays has focused on unsaturated conditions, such as that performed by Vanapalli et al. (1999) and Sivakumar and Doran (2000). Particular emphasis has been placed on the development of constitutive models for unsaturated soil, including compacted clays (e.g. Alonso et al. 1990, Alonso et al. 2013).

Sivakumar and Wheeler (2000) examined the predicted constitutive behavior as suction approaches zero and provided insight into the volume changes that occur during saturation. They observed that suction following compaction is mostly affected by the compaction water content. The decrease in suction caused by saturation produces a decrease in effective stress and an associated increase in volume. Their tests showed that a lower water compaction water

content leads to higher initial suction and a greater potential for swelling due to saturation. Sivakumar and Wheeler also found that soils compacted at different water contents behave differently in isotropic consolidation and may need to be treated as different soils from a constitutive perspective.

Shear Strength in Undrained Tests

Seed et al. (1960) and Johnson and Lovell (1979) found that the compaction water content had only a minor effect on the magnitude of drained strength parameters. Rather, differences in the compacted unit weight and compaction water content caused different pore pressure response during shear. Johnson and Lovell (1979) observed that the pore pressure parameter, $\bar{A}_f$, increased as compacted unit weight and initial saturation decreased, and as consolidation stress increased.

Seed et al. (1960) presented results from two specimens compacted to different initial dry unit weights and water contents. The unit weights and water contents were selected so that, when the specimens were saturated and consolidated at the same effective stress, they reached the same final dry unit weight and water content. A trial and error approach was required to arrive at the same final state ($\gamma_{d\text{-}cons}$, w, and σ'_{3c}). The stress-strain response of the two specimens is illustrated in Figure 6-2, which clearly shows the effect of compaction w. The specimen compacted dry of optimum had greater initial stiffness and gained little strength with continued strain. The clay compacted wet of optimum was less stiff and continued to gain strength with axial strain. At large strain, the strengths were similar regardless of compaction conditions.

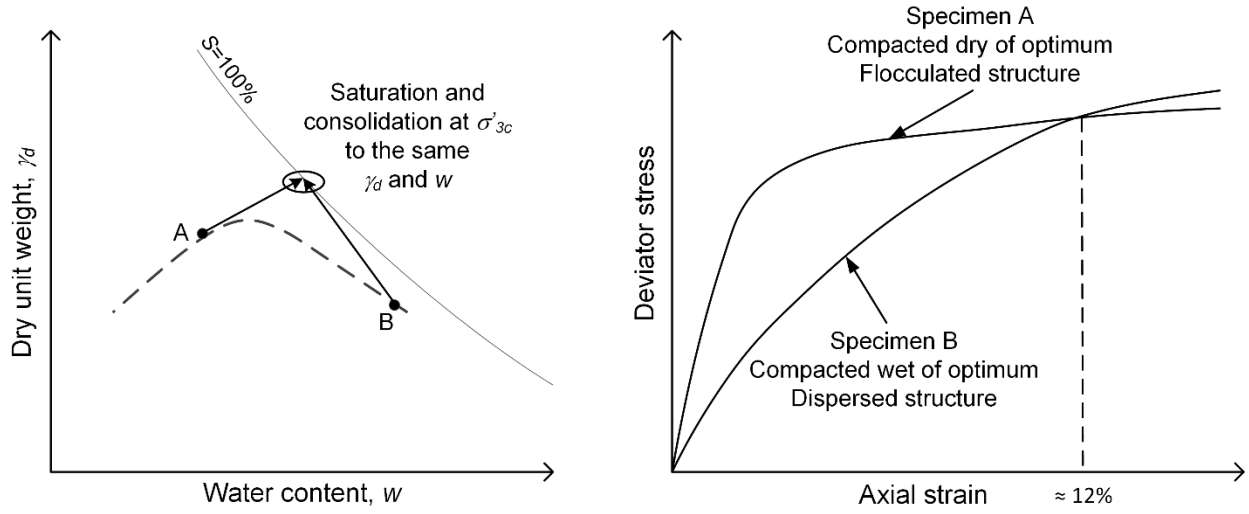

Figure 6-2. Undrained behavior of compacted clay specimens with the same final conditions and different molding unit weight and *w* relative to optimum (after Seed et al.1960)

Lee and Haley (1968), Lee and Morrison (1970), and Lee and Shubeck (1971) tested specimens of compacted clay consolidated at very high stresses (σ'_{vc} up to 3,600 psi or 24 MPa) applicable to deeper zones within large embankment dams. Strengths from anisotropically consolidated (ACU) triaxial compression tests were found to be lower than strengths from ICU tests with the same σ'_{vc}. Plane strain ACU compression tests presented by Lee and Shubeck (1971) resulted in similar strengths to those measured by ACU triaxial compression tests.

Failure Criterion

Clays compacted wet of optimum typically have stress paths that are strain-hardening up to high strains (e.g. Seed et al. 1960, Johnson and Lovell 1979), especially for tests run near or below the apparent prestress. Lee and Morrison (1970) showed that a well-defined maximum deviator stress will occur for compacted clays, similar to normally consolidated soils, at very high consolidation stresses.

Seed et al. (1960) showed that selection of a failure criterion for strain-hardening soils can be problematic, especially for undrained strengths. They suggested that the maximum effective

principal stress ratio is possibly the most appropriate failure criterion, but noted that it can only be determined if pore pressures are measured. Various limiting axial strain criterion have been used ranging from 5% (Wang et al., 1982) to 15% (Fleming and Duncan, 1990) to 25% (Seed et al. 1960). When failure is defined by a particular axial strain for strain-hardening soil, it is important to consider whether negative pore pressures have developed and if cavitation is likely to have occurred.

Properties of Oak Harbor Clay and Specimen Preparation

A large bulk sample of brown lean clay was obtained from a stockpile at an active construction site in Oak Harbor, Ohio in May 2012. The clay had been recently excavated from an over-consolidated glacio-lacustrine deposit. The sample was transported to the Virginia Tech laboratory in sealed plastic buckets. The entire sample was pressed through a No. 4 (4.75 mm) sieve using a small metal trowel to remove gravel-sized particles. The amount of gravel removed was estimated to be less than 1%. The sieved soil was thoroughly mixed to obtain a uniform sample and was returned to sealed buckets to keep the clay in a moist condition at water content of about 26%. The index properties of Oak Harbor clay are summarized in Table 6-1.

Table 6-1. Properties of Oak Harbor clay

Property	ASTM No.	Value
Liquid Limit	D4318	47
Plastic Limit	D4318	22
% Silt (2-75 μm)	D422	53%
% Clay (<2 μm)	D422	44%
Specific gravity of solids, G_s	D874	2.822
Standard Proctor γ_{dmax}	D698	108 pcf (17.0 kN/m^3)
Standard Proctor w_{opt}	D698	18.0%
Modified Proctor γ_{dmax}	D1557	120 pcf (18.9 kN/m^3)
Modified Proctor w_{opt}	D1557	13.6%

For each group of strength or compressibility tests that was performed, a portion of the Oak Harbor clay sample was air-dried to the desired water content. If an increase in water content was required, distilled water was added to the clay using a spray bottle. Once the desired water content was reached, the clay was stored in a sealed plastic container until specimens were to be compacted. The target compaction condition was a dry density of 108 pcf (17.0 kN/m^3) at a water content of 20%, which corresponds to a water content 2% above optimum and 100% of standard Proctor maximum dry unit weight, $\gamma_{d\text{-}max}$. Relative compaction, *R.C.*, is used in this study and is defined as

$$R.C. = \frac{\gamma_{d-comp}}{\gamma_{d-\max}} \times 100\% \qquad \text{(6-1).}$$

The strength and compressibility of the compacted clay was determined using consolidation and triaxial tests. Consolidation specimens were compacted directly in the consolidation ring in five lifts using a Harvard miniature compactor set to a tamper force of 20 lbf (89 N). The compacted surface of each lift was scarified with a knife prior to placement of the next lift. Triaxial specimens were compacted in ten lifts of approximately equal moist mass with 22 tamps per lift. The compacted surface of each lift was scarified with a knife prior to placement of the next lift. The triaxial specimens were formed inside of a mold with a diameter of 1.31 inches (3.34 cm) and a height of 2.81 inches (7.14 cm). Following compaction, the specimens were extruded, trimmed to remove rough edges, and measured. The triaxial compression test specimens were mounted in the triaxial cell soon after compaction, and the saturation process was started.

One-Dimensional Consolidation Tests

Two one-dimensional consolidation tests (ASTM D2435-11) were performed using automated load actuators mounted in bench-top load frames. The purpose of these tests was to determine the apparent prestress caused by compaction. The triaxial tests can be better interpreted when the consolidation state with respect to the apparent prestress is known. The consolidation curves are shown in Figure 6-3, and the relevant test results are summarized in Table 6-2. The specimen for CON-1 was allowed to swell for about 2 days at a vertical stress of 1.7 psi (12 kPa) after inundation and prior to further loading. In test CON-2, swelling was prevented at the start of the test, and the one-dimensional swell pressure of the compacted clay was found to be 5.2 psi (36 kPa).

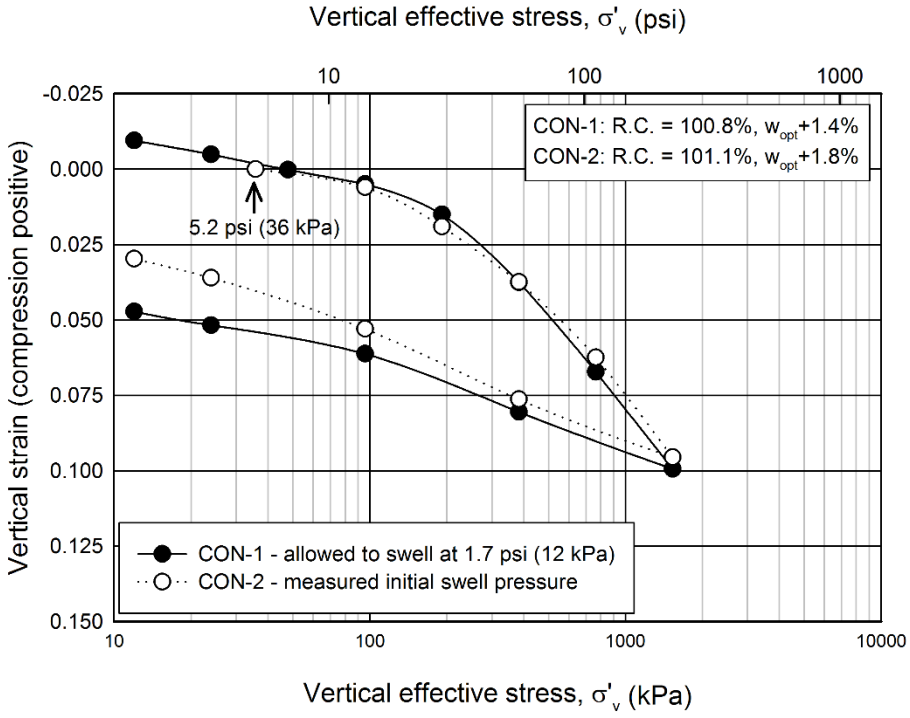

Figure 6-3. One-dimensional consolidation curves for compacted Oak Harbor clay

Despite differences in the initial technique used, the two specimens exhibited very similar one-dimensional consolidation behavior. This is likely because the specimens were compacted

wet of optimum and were less susceptible to structural changes caused by swelling. The apparent prestress was determined using Casagrande's procedure and was found to be about 40 psi (276 kPa) for the two specimens, which had an *R.C.* of 101%. The coefficient of consolidation determined using the Casagrande method ranged between 0.1 and 0.3 ft^2/day (4 and 12 cm^2/hr) for vertical effective stresses above 29 psi (200 kPa), which falls within the range reported by Duncan and Wright (2005) for compacted clay.

Table 6-2. Consolidation test results for compacted Oak Harbor clay

Test	Relative comp., *R.C.*	Compacted *w*	Modified compr. index, $C_{c\varepsilon}$	Modified recompr. index, $C_{r\varepsilon}$	Apparent prestress, σ'_p	Coeff. of consol., c_v above σ'_p
CON-1	100.8%	19.4 (w_{opt}+1.4%)	0.11	0.03	42 psi (290 kPa)	0.1 – 0.2 ft^2/d (4 – 8 cm^2/hr)
CON-2	101.1%	19.8 (w_{opt}+1.8%)	0.11	0.035	38 psi (262 kPa)	0.2 – 0.3 ft^2/d (8 – 12 cm^2/hr)

Consolidated-Undrained Testing of Compacted Clays

Thirty-six triaxial compression tests were performed, 24 with isotropic consolidation and twelve with anisotropic consolidation. The range in compaction conditions for each type of test is summarized in Table 6-3. The range of compaction expected in the field on most projects will likely be at least as large as that represented by these tests. Depending on locale, climate, and the condition of the borrow area, different ranges of water content might be expected in the field. Details for the ICU and ACU triaxial compression tests are summarized in Table 6-4 and Table 6-5, respectively. The test specimens were mounted in triaxial cells with 1.42 inch (3.6 cm) diameter porous stones at each end. The triaxial cells provided top and bottom drainage and had two ports at each end to allow drain lines to be easily deaired. Filter paper was not used at the

ends or along the sides of the specimens. The specimens were encased in two, 0.002 inch (0.05 mm) thick latex membranes. Rubber O-rings were used to seal the membranes to the end platens. The tests were performed using automated load actuators mounted in bench-top load frames. Cell pressure and back pressures (pore pressure) were applied and measured using either automated flow pumps or a manual pressure panel.

Table 6-3. Range of compaction conditions for ICU and ACU triaxial compression tests

Test type	Initial Compaction Conditions (relative to ASTM D698-2012)			
	Mean *R.C.*	Range of *R.C.*	Mean *w*	Range from w_{opt}
ICU	99.0%	97.9 – 101.0%	19.4	+0.2 – +2.4
ACU	100.1%	96.9 – 102.9%	19.1	-1.7 – +1.9

Saturation

The triaxial compression specimens had initial saturations ranging from 74 to 92% with an average degree of saturation of 85%. Back pressure was used to saturate the specimens. The back pressure was increased until Skempton's B-parameter was found to be greater than or equal to 0.95, indicating saturation greater than 99%. For tests with higher consolidation stresses, the back pressure was limited by the safe cell pressure range, and additional time was required to achieve saturation.

Table 6-4. Isotropically consolidated undrained triaxial compression (ICU-TC) tests on Oak Harbor clay

Test	Compaction conditions			Confining stress during saturation (psi)	Consolidation		Failure (10% axial strain)			
	Compacted $\gamma_{d\text{-}comp}$ (pcf)	Relative Compaction, *R.C.*	Water content, *w*		Vertical stress (psi)	Horiz. stress (psi)	Water content, w_f	σ'_{1f} (psi)	s_u (psi)	$\bar{A}_f$
B-1	107.8	100%	20.0%	3.0	10	7	Swelled into piston during saturation			
B-2	108.5	101%	20.1%	7.2	15.2	14.1	Swelled into piston during saturation			
B-3	109.0	101%	20.1%	9.0	32.9	31.9	22.1%	54.6	24.7	0.04
B-4	108.9	101%	20.2%	16.6	55	55.6	21.5%	80.3	33.9	0.22
B-5	106.9	99%	20.4%	0.8	4.1	3.8	25.5%	8.5	5.1	0.04
B-6	107.7	100%	20.3%	0.7	5.0	4.6	26.1%	11.6	5.9	-0.11
D-1	106.2	98%	18.5%	2.4	6.9	6.9	26.9%	11.8	6.0	0.10
D-2	105.8	98%	18.2%	1.9	5.8	5.8	26.5%	8.3	3.8	0.17
D-3	106.1	98%	18.6%	2.0	6.6	6.6	26.4%	10.4	5.5	0.15
D-4	105.7	98%	18.8%	1.5	13.7	13.7	25.6%	18.5	9.5	0.24
D-5	105.8	98%	18.3%	2.3	13.6	13.6	25.6%	18.0	8.7	0.25
D-6	106.5	99%	19.4%	2.0	13.3	13.3	25.9%	18.6	8.8	0.19
D-7	106.4	99%	19.0%	2.4	21.1	21.1	24.4%	29.9	14	0.18
D-8	106.5	99%	19.0%	2.8	23.0	23.0	24.0%	31.6	14.9	0.21
D-9	106.2	98%	18.9%	2.7	21.1	21.1	24.0%	28.7	13.4	0.23
D-10	106.8	99%	19.3%	2.5	27.9	27.9	23.7%	37.0	17.1	0.23
D-11	106.5	99%	19.4%	1.7	49.7	49.7	22.1%	61.5	27.5	0.29
D-12	106.7	99%	19.4%	2.7	28.0	28.0	23.4%	39.5	18.1	0.18
D-13	106.9	99%	19.5%	2.3	34.7	34.7	22.8%	53.6	24.2	0.11
D-14	107.3	99%	19.4%	2.1	35.0	35.0	23.2%	48.6	21.9	0.19
D-15	107.7	100%	19.6%	2.8	34.8	34.8	23.0%	48.4	21.8	0.18
D-16	107.0	99%	19.8%	2.7	49.4	49.4	21.9%	80.5	36.3	0.07
D-17	106.7	99%	19.4%	2.9	25.3	25.3	23.4%	41.3	19.1	0.08
D-18	106.6	99%	19.7%	3.6	51.8	51.8	22.3%	64.8	28.6	0.27

Note: Divide unit weight in pcf by 6.366 to obtain kN/m^3, and multiply stress in psi by 6.895 to obtain kPa.

Table 6-5. Anisotropically consolidated undrained triaxial compression (ACU-TC) tests on Oak Harbor clay

Test	Compaction conditions			Confining stress during saturation (psi)	Consolidation		Failure (10% axial strain)			
	Compacted $\gamma_{d\text{-}comp}$ (pcf)	Relative Compaction, *R.C.*	Water content, *w*		Vertical stress (psi)	Horiz. stress (psi)	Water content, w_f	σ'_{1f} (psi)	s_u (psi)	$\bar{A}_f$
C-1	109.0	101%	19.5%	3.3	6.6	4.9	24.5%	15.0	7.7	-0.18
C-2	104.6	97%	18.0%	3.0	14.4	7.2	26.8%	11.7	5.7	0.28
C-3	107.4	100%	19.9%	1.9	27.8	13.5	23.6%	30.1	13.9	-0.19
C-4	111.1	103%	16.3%	2.2	53.5	26.1	21.1%	56.4	25.2	0.02
E-1	108.7	101%	19.6%	2.4	6.1	3.1	25.3%	11.8	6.5	-0.29
E-2	108.6	101%	19.9%	1.7	7.0	3.4	24.8%	14.2	7.6	-0.31
E-3	107.2	99%	19.5%	3.1	15.7	7.5	25.3%	19.9	9.5	-0.38
E-4	108.0	100%	19.8%	3.2	19.4	11.0	23.9%	28.1	13.0	-0.26
E-5	109.3	101%	19.7%	2.5	30.6	19.5	20.7%	48.5	23.41	-0.16
E-6	105.9	98%	19.1%	3.2	52.2	25.7	23.3%	46.8	19.6	-0.12
E-7	109.3	101%	19.0%	1.6	38.8	19.6	21.3%	44.6	21.7	-0.15
E-8	109.7	102%	19.5%	2.7	15.0	10.1	22.5%	29.0	13.8	-0.10

Note: Divide unit weight in pcf by 6.366 to obtain kN/m^3, and multiply stress in psi by 6.895 to obtain kPa.

[A] Consolidated with no lateral strain - $K_0 = 0.64$

Unsaturated specimens may have a tendency to swell if a low σ'_s is applied during back pressure saturation. The test procedure must address the tendency to swell in a consistent manner for all test specimens. Three options for saturation were considered:

1. Use constant volume saturation, which can be achieved by progressively increasing the effective stress to limit specimen volume change during saturation. This method is labor-intensive and difficult to perform precisely. It also precludes the use of consolidation stresses that are lower than the effective stress required to prevent swelling.
2. Saturate all of the specimens at approximately the same effective stress, which should be lower than the lowest desired consolidation stress. Depending on σ'_s, swelling may occur during saturation. This swelling may remove some of the prestress effects of compaction on the specimens, resulting in lower undrained strengths.
3. Saturate each test specimen at the final effective consolidation stress for that specimen. This method would not include a separate consolidation phase, and the coefficient of consolidation would have to be determined from a consolidation test or from an additional triaxial test which included a consolidation phase.

For this study, the desired range of σ'_{vc} was 4 to 55 psi (28 to 379 kPa), and the specimens were saturated following Option 2 above. In order to prevent over-consolidation of the specimens during saturation, the effective stress (*CP*-*BP*) during saturation ranged from 2 to 3 psi (14 to 21 kPa). The specimens swelled during the saturation procedure with volumetric strains ranging from 6 to 10%. The volume of water imbibed by the specimen during saturation was recorded using the flow pumps or pressure panel burettes. The saturation procedure often lasted several days.

Appropriately managing volume change during saturation was an important and difficult part of the testing procedure. Two lessons were learned about saturating compacted clays at effective stresses below the swell pressure.

1. Specimens should be allowed to reach a relatively constant volume prior to initiation of final consolidation, realizing that the swelling and saturation process can last multiple days. The first set of ICU test specimens (labeled with a B) were allowed to saturate for only one day prior to final consolidation. Specimens B-5 and B-6 first consolidated and then resumed swelling because a constant volume had not been reached in the one-day saturation phase. This resulted in consolidation curves that were difficult to interpret. Subsequent sets of tests were allowed to back pressure saturate (and swell) for two to three days to reach equilibrium prior to initiating final consolidation.
2. Specimens must be prevented from swelling into the loading piston during saturation. If swell is not prevented during saturation, the triaxial specimens will tend to swell both laterally and axially. If the piston is restrained and left in contact with the top platen during saturation, an axial load will be applied to the specimen, causing anisotropic consolidation or possibly failure. This occurred to the six B specimens, such that two of the specimens, B-1 and B-2, were judged to be no longer representative of isotropic consolidation and were not used. In subsequent tests, the loading piston was retracted to prevent contact with the specimen during the swelling that occurred during back pressure saturation.

Consolidation

Isotropic consolidation was performed by applying the consolidation stress in a single increment. For anisotropically consolidated specimens, the axial load and cell pressure were increased gradually by the software used to run the tests, maintaining the desired consolidation

principal stress ratio, $PSR_c = \sigma'_{1c} / \sigma'_{3c}$. PSR_c is equivalent to the stress ratio K_c used for rapid drawdown analysis, which is a common application of CU triaxial tests.

The target value of PSR_c in the ACU tests was 2.0. Based on the author's experience with limit equilibrium and finite element analyses of saturated embankments, PSR_c is often calculated to be about 2.0 throughout much of an embankment after consolidation and saturation under steady seepage. K_0 was measured for one compacted specimen and found to range from 0.67 to 0.64 at vertical (major) effective consolidation stresses, σ'_{vc}, of 8 to 31 psi (55 to 214 kPa), respectively. This corresponds to PSR_c of 1.5 to 1.6.

The specimen volume after consolidation was determined using Method B (ASTM D4767-2011). The saturation at the end of the test with $B \geq 0.95$ was assumed to be 100%, allowing the final specimen volume to be calculated. Specimen volume following saturation was calculated from the final volume and the measured volume change during consolidation. As a check, the saturated specimen volume was also determined from the initial specimen dimensions and the amount of water that flowed into the sample during saturation corrected for the initial volume of air. The two methods of calculating the saturated specimen volume were usually within 0.06 to 0.12 in^3 (1-2 mL), which was considered within the range of compliance for the system.

The volume changes measured in the triaxial tests are shown in Figure 6-4. Most of the specimens experienced positive volumetric strain (swell) from compaction to consolidation. The variation in volumetric strain at a given σ'_{vc} represents the combined effects of the initial *R.C.*, initial *w*, and experimental scatter. Since the initial conditions were all relatively similar, the effects of *R.C.* and *w* on volume change cannot be separated. Interestingly, the ICU tests reach a point of zero volumetric strain at a consolidation stress approximately equal to the apparent prestress from the consolidation tests. The ACU test specimens compress less, especially at high

σ'_{vc}, due to the lower mean effective stress applied during consolidation. Shear stress is also applied to the ACU specimens, which results in shear dilation or compression, and affects the magnitude of volume change during consolidation. Compared to the other ACU specimens, the K_0 specimen swelled less during saturation and consolidated more due to the higher lateral stress (K_0 = 0.64 rather than K = 0.5).

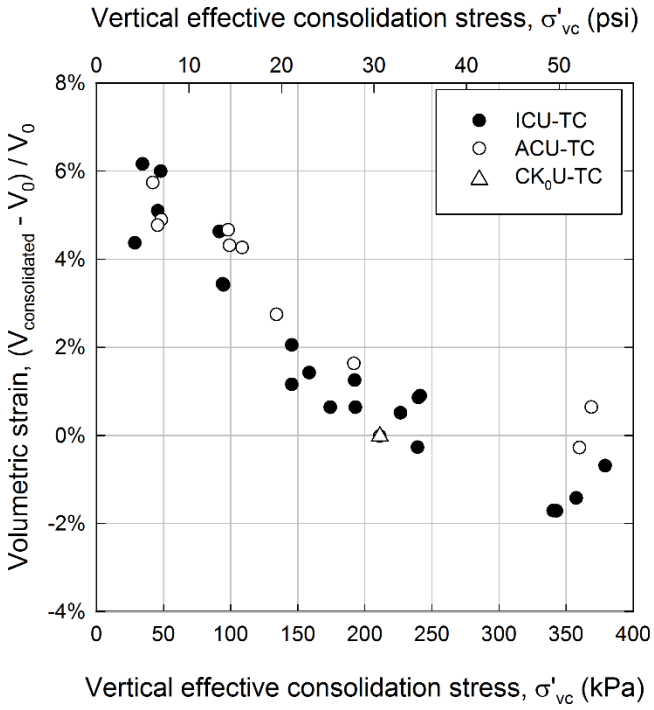

Figure 6-4. Volumetric strain measured in ICU and ACU tests on Oak Harbor clay

Figure 6-5 traces the paths followed by specimens B-6 and D-3 in γ_d-w space. The specimens were allowed to saturate at σ'_s of 0.7 and 2 psi (4.8 and 14 kPa), respectively. B-6 started at a higher relative compaction and higher initial saturation (*R.C.* = 99.7%, *S* = 90%) than D-3 (*R.C.* = 98.2%, *S* = 80%). Because of these differences in initial conditions, B-6 has a higher dry unit weight after consolidation, even though D-3 was subjected to a higher consolidation stress. As shown in Figure 6-5, B-6 also had a slightly higher undrained strength.

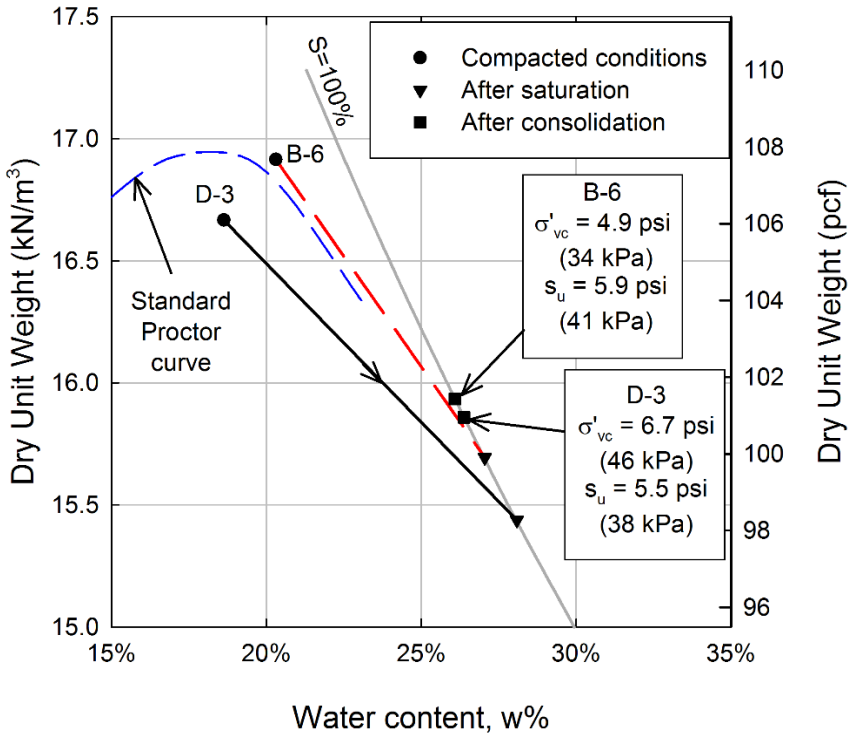

Figure 6-5. Changes in dry unit weight and moisture content from compaction to consolidation for two specimens of compacted Oak Harbor clay.

The dry unit weights of the specimens after consolidation are plotted against σ'_{vc} in Figure 6-6. The data have been separated by the values of relative compaction. The initial differences in compaction carry through to the consolidated state, even though most of the specimens were not prevented from swelling during the saturation phase. Specimens with higher initial values of *R.C.* have a higher dry unit weight after consolidation at a given σ'_{vc}.

At σ'_{vc} values greater than or equal to the apparent prestress of 40 psi (276 kPa) determined from the one-dimensional consolidation tests, the effects of initial compaction become less important, and the dry unit weights after consolidation begin to converge for the ICU tests. Because the initial conditions affect the dry unit weight after consolidation, an associated effect on the undrained shear strength should be expected.

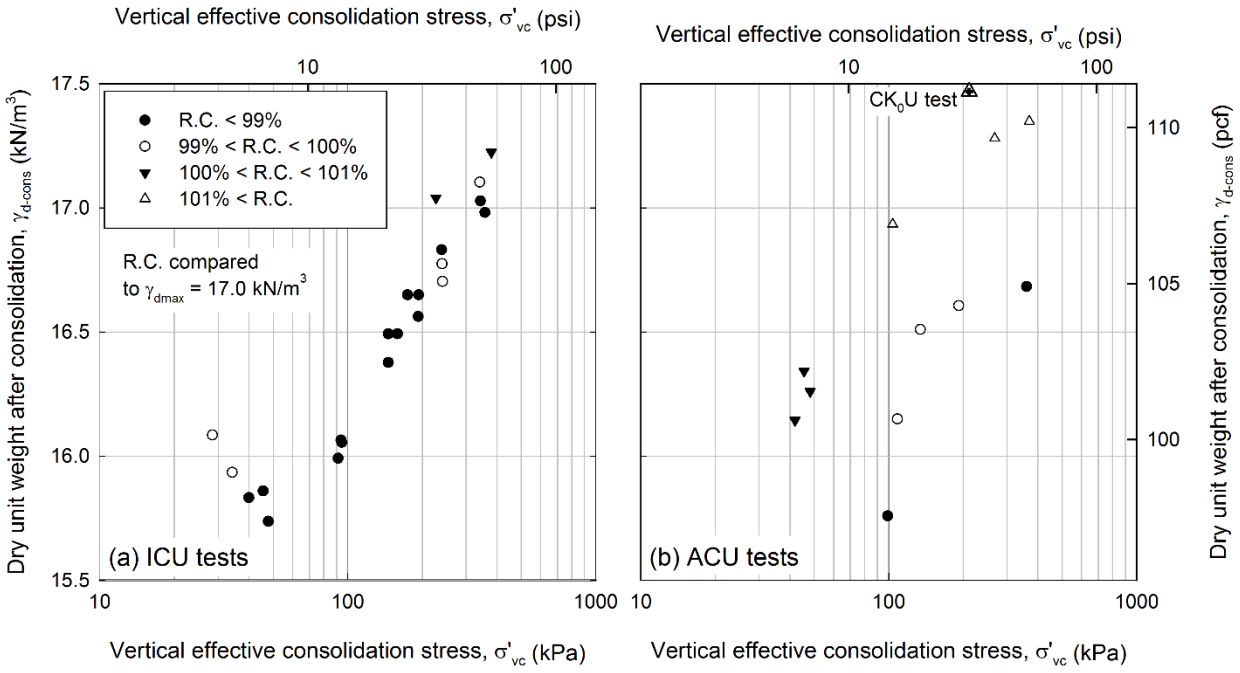

Figure 6-6. Effect of relative compaction on dry unit weight after consolidation (a) isotropic consolidation, (b) anisotropic consolidation

Recommendations for CU Testing of Compacted Clays

Based on the experience gained testing Oak Harbor clay, the following procedures are recommended for testing compacted clays under consolidated-undrained conditions.

The variation in specimen dry unit weight and compaction water content should be reduced as much as possible unless the effect of varying these parameters is being considered explicitly. Neither the *R.C.* nor *w* should range by more than 0.5% above or below the target value. If compaction within this tight of a constraint is not possible, the test results should be examined to determine if the compaction conditions influenced the dry unit weights after consolidation and undrained strengths.

Compacted specimens will be initially unsaturated and may have a tendency to swell if a low σ'_s is applied during back pressure saturation. The test procedure must address this tendency to swell in a consistent manner for all test specimens. Saturation of each test specimen at the final

effective consolidation stress for that specimen is the preferred method (Option 3). This method likely follows the field stress path most closely. A companion consolidation test would be required to provide coefficients of consolidation for determining appropriate strain rates.

The process of saturating compacted clay specimens does not occur quickly and requires relatively high back pressures, even for specimens compacted on the wet side of optimum. For example, specimens of the lean Oak Harbor clay took two to three days to finish swelling. Plastic clays with lower coefficients of consolidation and higher swell potential should be expected to take even longer to swell. If swelling is prevented by Option 1 or 3 above, specimens may still take a few days to reach an equilibrium volume.

Compacted specimens should be prevented from swelling into a locked loading piston during saturation. If the piston is locked and the specimen swells against it, axial loading will occur during saturation, changing the principal stress ratio, and potentially causing failure of the specimen.

Consolidated-Undrained Strength of Compacted Clays

The strain rate for the tests was determined in general accordance with ASTM D4767-2011, using the time to 50% consolidation measured in the ICU tests and assuming the effective strength envelope will be reached at about 4% axial strain. Most of the triaxial tests were sheared at an axial strain rate of 0.25%/hr. The fastest strain rate used was 0.5%/hr. Typical effective stress paths are presented for the ICU tests in Figure 6-7 and for the ACU tests in Figure 6-8.

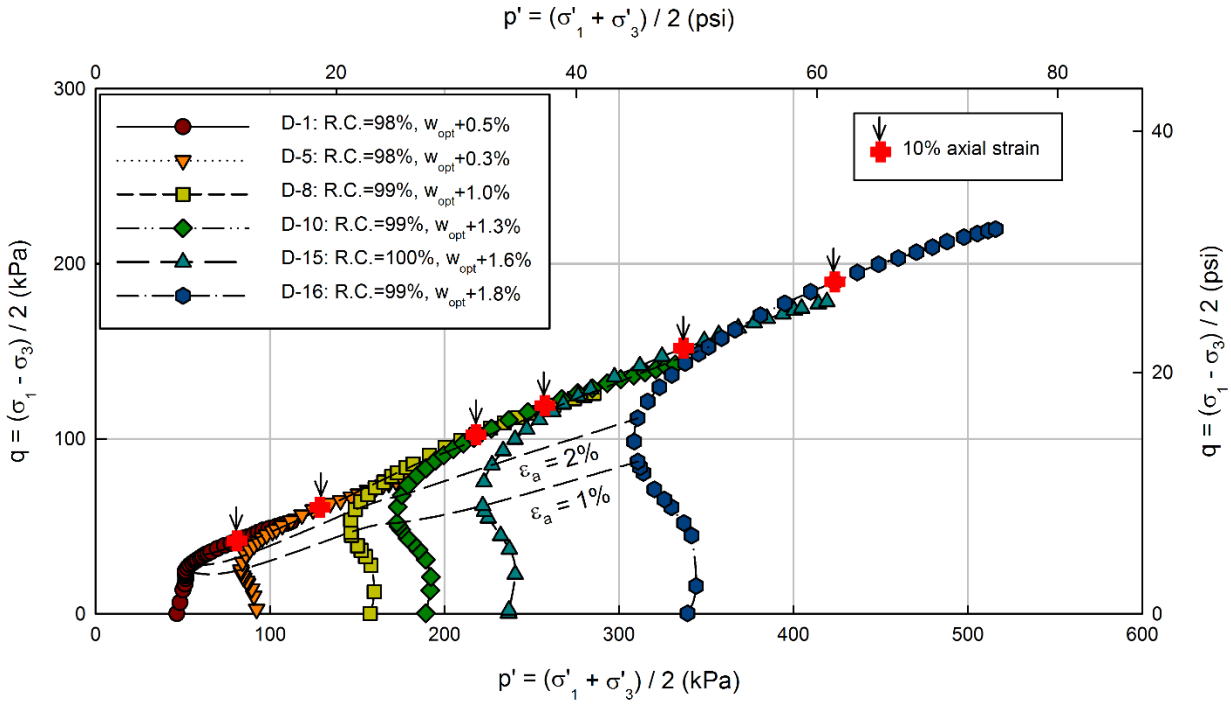

Figure 6-7. Typical effective stress paths for ICU triaxial compression tests on Oak Harbor clay

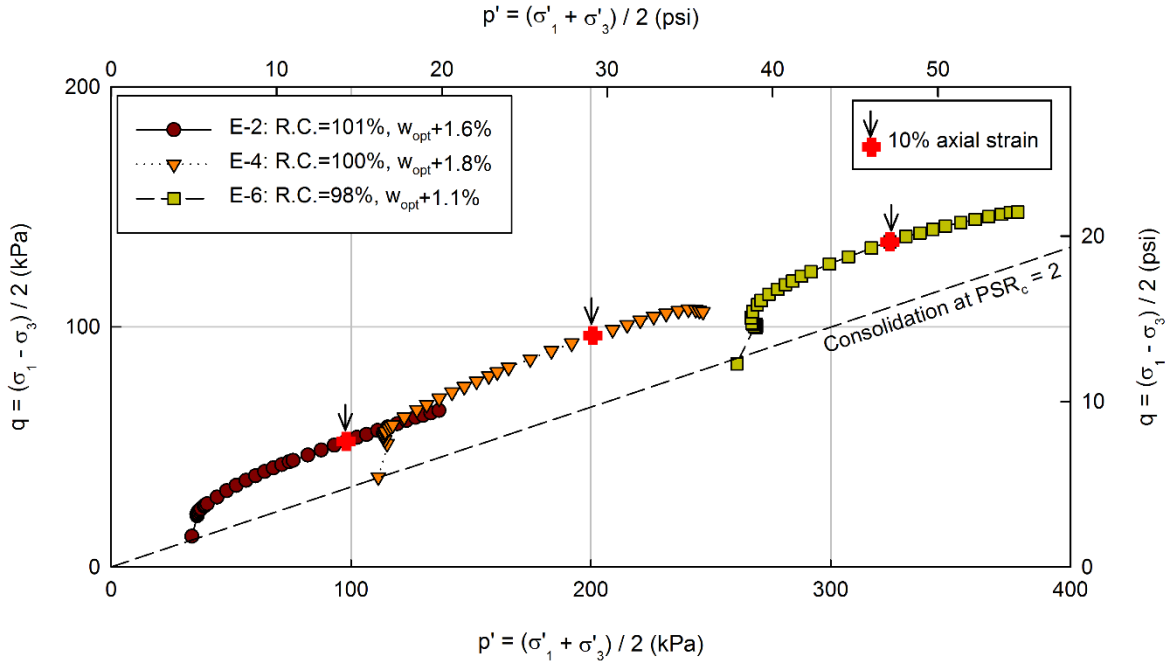

Figure 6-8. Typical effective stress paths for ACU triaxial compression tests on Oak Harbor clay

As noted by Seed et al. (1960), failure is difficult to define for strain-hardening specimens because the deviator stress continues to increase up to very large strains. The maximum principal stress difference depends mostly on the time when the test was terminated and therefore cannot be used as a failure criterion. Strengths are defined herein using the stresses at 10% axial strain. For the ICU tests, 10% axial strain occurred near or slightly above the point of the maximum effective principal stress ratio. At 10% axial strain, negative changes in pore pressure developed for one of the ICU tests and most of the ACU tests (see $\bar{A}_f$ values in Table 6-4 and Table 6-5). These negative changes in pore pressures were considered acceptable because cavitation does not occur in clays. An appropriate failure criterion must be selected with careful consideration of the pore pressures developed at failure and the soil type as well as the intended use of the shear strengths.

Effective Stress Strength Envelope

The effective stresses at 10% axial strain from both the ICU and ACU tests are plotted on the modified Mohr-Coulomb envelope in Figure 6-9. The type of consolidation did not affect the effective stress strength envelope of the compacted clay. Similarly, no discernable effect of the compaction conditions was found in the effective stress strength envelopes. The Oak Harbor data support the conclusion reached by Seed et al. (1960) and Johnson and Lovell (1979) that the initial compaction conditions affect the pore pressures that develop during shear and the undrained strengths, but not the effective stress shear strength envelopes.

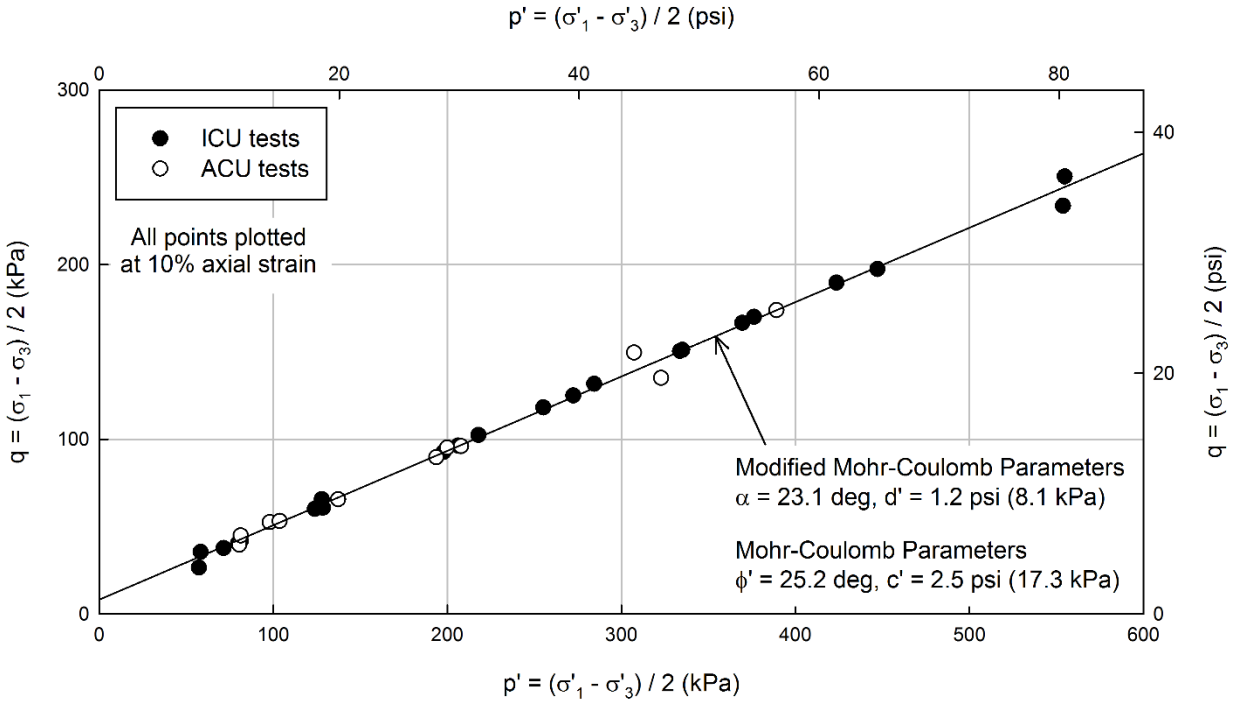

Figure 6-9. Modified effective stress strength envelope for triaxial compression tests on Oak Harbor clay

Undrained Shear Strength

Undrained strengths from the ICU triaxial compression tests are presented in Figure 6-10. The ACU strengths are given in Figure 6-11. For each type of test, the results have been separated into groups based on relative compaction. The undrained strengths from the tests are clearly influenced by relative compaction.

Power curves were fit to the strengths for each group of tests, individually, as shown in Figure 6-10 and to the ICU data as a whole (not shown). Similar curve fits were performed for the ACU test results.

The power curves have the form

$$s_u = a \times p_a \left(\frac{\sigma'_{vc}}{p_a} \right)^b \tag{6-2}$$

where:

a = empirical parameter controlling the overall slope of the fit,

b = empirical parameter controlling the curvature of the fit, and

p_a = atmospheric pressure in the same units as stress and strength.

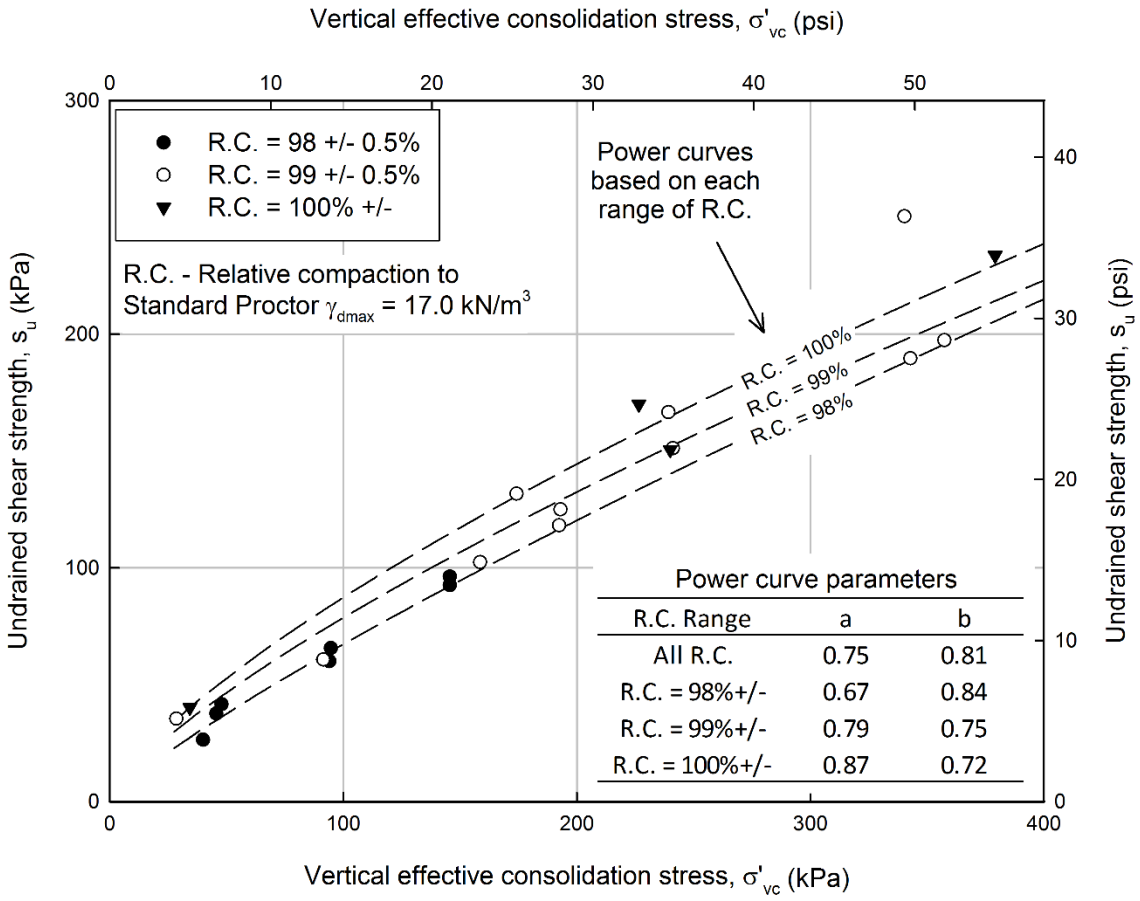

Figure 6-10. Undrained strength relationship for ICU tests on Oak Harbor clay

The power curves help to quantify the effects of relative compaction on strength. For both the ICU and ACU tests, the *a* parameters increase and the *b* parameters decrease as *R.C.*

increases. Based on these trends, the strength from an ICU test with σ'_{vc} of 3.6 psi (25 kPa) and an initial *R.C.* of 100% tends to be 50% higher than that with an *R.C.* of 98%. As the consolidation stress increases, the effects of compaction become relatively smaller as the consolidation stress approaches the apparent prestress.

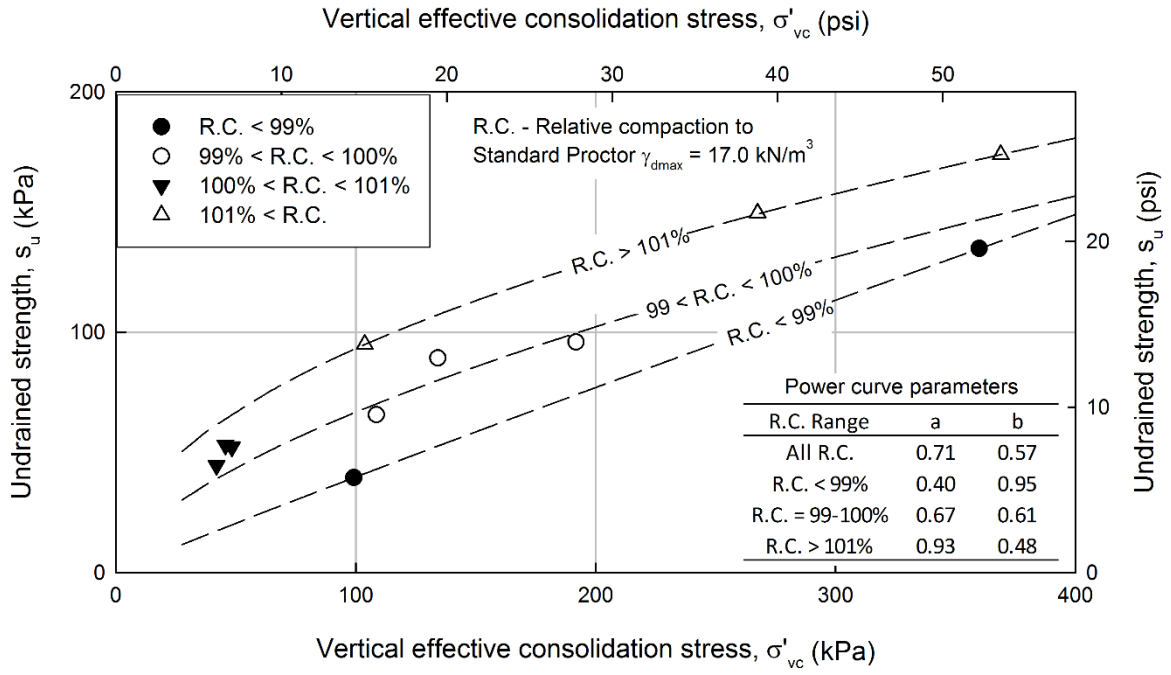

Figure 6-11. Undrained strength relationship for ACU ($PSR_c \approx 2$) tests on Oak Harbor clay

The influence of relative compaction on compacted clay is generalized in Figure 6-12 based on the Oak Harbor tests. As the consolidation stress approaches the apparent prestress, the consolidation lines tend to converge, meaning that the compaction conditions tend to have a greater influence on undrained strength at low consolidation stresses compared to high stresses.

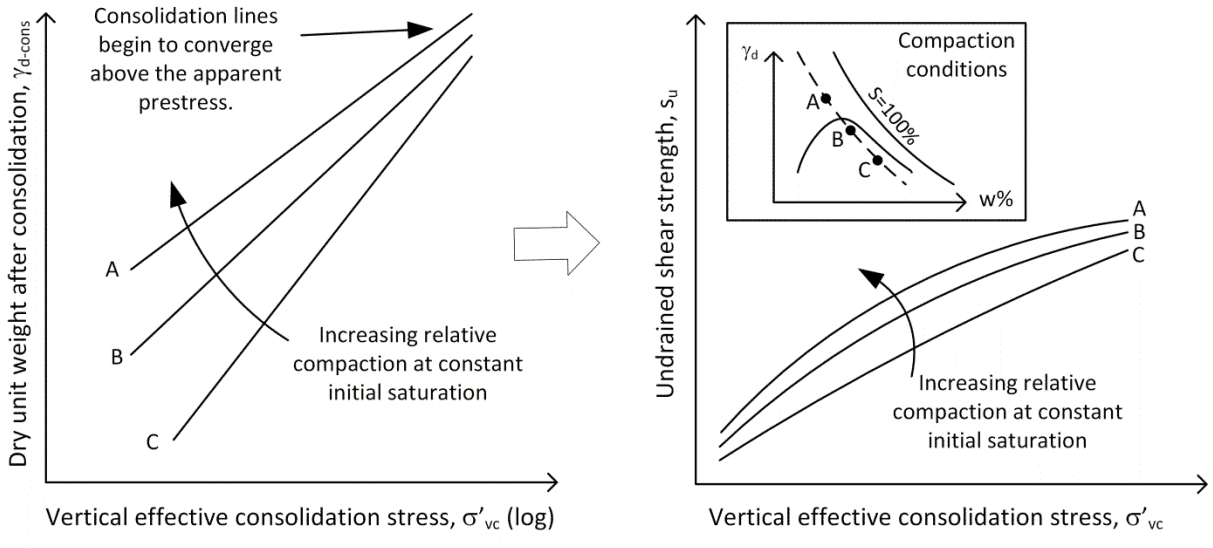

Figure 6-12. Influence of *R.C.* on dry unit weight after consolidation and undrained strength

Quantification of Variability in Undrained Strength

The power curve trend lines that were calculated for the whole range of *R.C.* might be used to predict field strengths for either the ICU or the ACU tests. These trends have an associated uncertainty caused by material variation, scatter in the laboratory test results, and variations in the initial conditions. The uncertainty in these strength trends can be assessed by examining residuals (difference between the measured and predicted strengths). The standard deviations, σ, of the residuals for the curve fits over the full range of *R.C.* were 2.2 psi (15 kPa) for the ICU tests and 2.5 psi (17 kPa) for ACU tests. Compared to the mean undrained strength for these tests, the coefficients of variation were 13% and 20% for the ICU and ACU tests, respectively.

Effect of Anisotropic Consolidation on Undrained Strength

The undrained strength trends corresponding to 100% *R.C.* for both ICU and ACU conditions are plotted in Figure 6-13(a). Dashed lines are plotted one standard deviation above and below the trend lines to illustrate the uncertainty in the relationships. Anisotropic consolidation results in lower strength for σ'_{vc} greater than 5.8 psi (40 kPa). At very low stresses, the initial

compacted condition dominates the undrained strength rather than consolidation stress state. The ratio of the ACU to the ICU strength is plotted in Figure 6-13(b). At a vertical effective consolidation stress of 44 psi (300 kPa), anisotropic consolidation with a PSR_c of 2 results in undrained strength that is 30% lower than the ICU strength.

Undrained strengths are often predicted based on the major effective consolidation stress, σ'_{1c}, which is equivalent to σ'_{vc} in the triaxial test. The Oak Harbor results show that undrained strengths based on σ'_{1c} and ICU tests will tend to be too high to represent anisotropic field conditions.

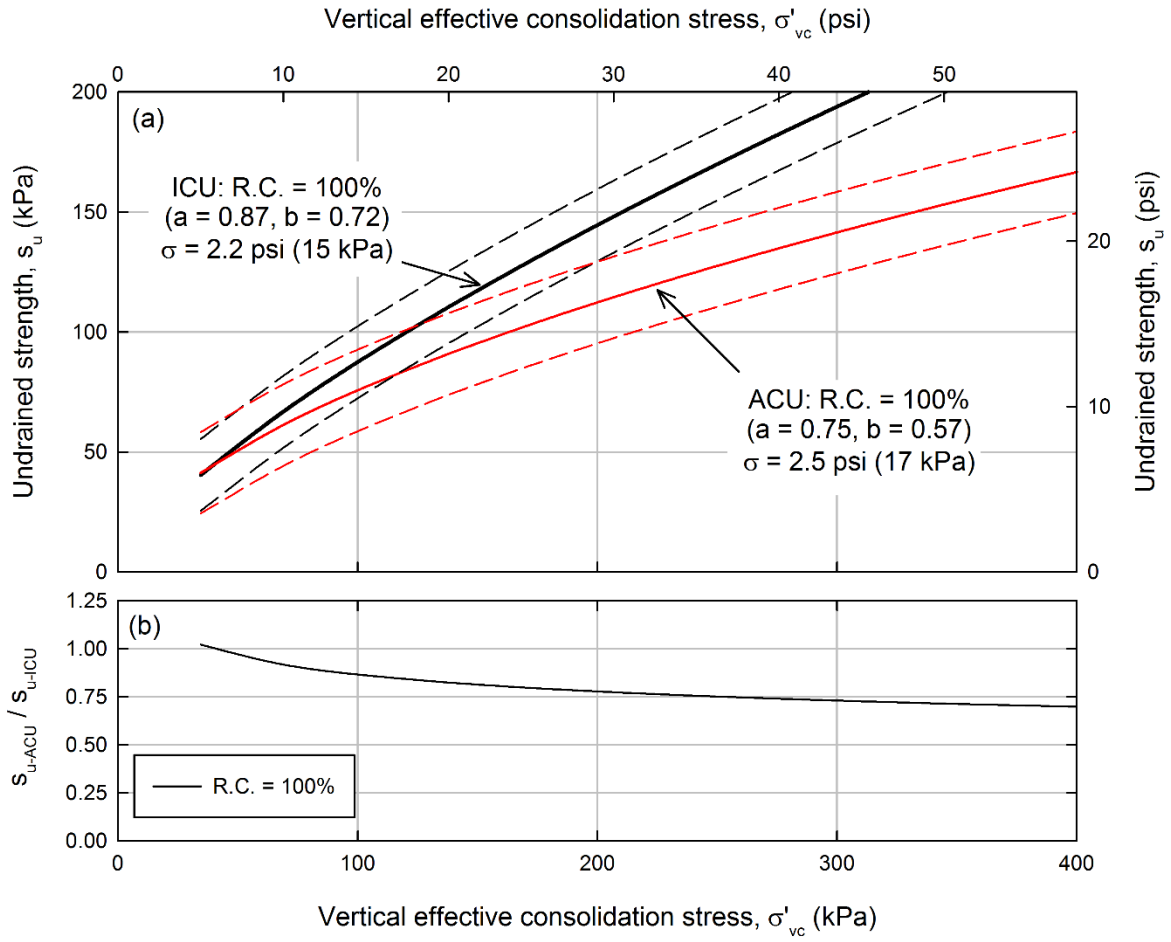

Figure 6-13. Comparison of ICU and ACU undrained strengths Oak Harbor clay (a) trends for *R.C.* = 100%, (b) ratio of ACU to ICU strengths

Summary and Conclusions

Consolidation and strength tests were performed on compacted specimens of a lean clay from Oak Harbor, Ohio. The importance of the initial compaction conditions on undrained strength were highlighted in these tests. The effects of anisotropic consolidation on the strength of compacted clay were investigated.

Initial compaction conditions have a significant impact on the volume change behavior and the undrained strength measured in CU tests. Test specimens should be prepared within 0.5% of the target dry unit weight and water content to achieve a consistent trend in undrained strength. Compacted clay specimens will be initially unsaturated and may tend to swell during the saturation. The effective stress (*CP-BP*) during saturation must be selected to prevent swelling or to allow consistent swelling during saturation. Further research is warranted into the effects of various saturation procedures on undrained strength. Test specimens must be prevented from swelling against the loading piston during saturation.

Oak Harbor clay exhibited strain-hardening behavior similar to many clays compacted wet of optimum. For this reason, maximum deviator stress cannot be used as a failure criterion. The stress at 10% axial strain was selected as the undrained strength for this study. The failure criterion must be selected carefully for strain-hardening soils, especially when the purpose is to evaluate undrained strengths. Undrained strengths can change significantly, depending on the failure criterion that is selected. The effective stress strength envelope is much less sensitive to the failure criterion for such materials.

The effective stress strength envelope of compacted Oak Harbor clay was not affected by the type of compaction or the initial compaction conditions, within the range of compaction tested. The undrained strength measured by ICU tests was greater than or equal to the strength

following anisotropic consolidation measured by ACU tests at the same vertical effective consolidation stress. Anisotropic consolidation results in a lower dry unit weight after consolidation at a given σ'_{vc}, which results in lower undrained shear strength. The reduction in strength due to anisotropic consolidation (PSR_c = 2) ranged from zero at low effective stress to about 30% at 44 psi (300 kPa).

7. Principal Stress Rotation and Undrained Strength of Compacted Clay

Introduction

Embankment slope stability is usually evaluated using undrained strengths whenever it is difficult to accurately predict field pore pressures following changes in the applied loads. Undrained strengths for some design conditions, such rapid drawdown or levee flood loading, must be determined for the soil after it has consolidated under the long term or steady state field effective stresses and pore pressures. Consolidated-undrained triaxial tests are required to provide strengths for these conditions.

One of the factors that influences undrained strength is rotation of the principal stress system during loading from consolidation to failure. Duncan and Seed (1966) considered the effects of principal stress rotation based on the reorientation of the stress system along a failure surface as shown in Figure 7-1. While the undrained condition is usually not critical for an excavated slope, it is useful for illustration. The different failure modes along such a surface are often approximated in the laboratory (e.g. Ladd et al. 1977) by

- Anisotropically consolidated undrained triaxial compression (ACU-TC) tests near the crest – Pt. A,
- K_0 consolidated direct simple shear (DSS) tests in the central region near Pt. B, and
- Anisotropically consolidated undrained triaxial extension (ACU-TE) tests near the toe – Pt. C.

Compacted clay is used widely for the construction of embankments for earth dams, levees, and roadways; however, the effect of principal stress rotation during loading on the undrained strength of compacted clays has not been well researched. A search of the geotechnical literature revealed no studies that considered the behavior of compacted clays under conditions that induce

principal stress rotation. This chapter presents the results of triaxial tests with stress rotation and direct simple shear tests on a compacted lean clay to help address this lack of data.

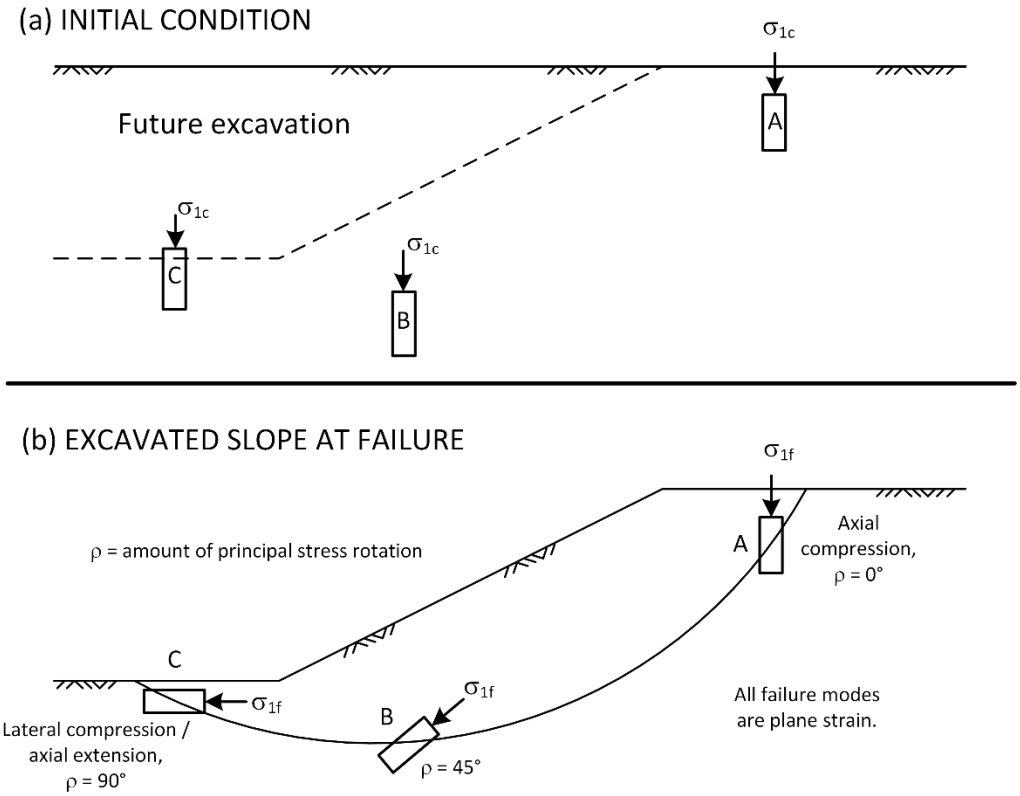

Figure 7-1. Reorientation of principal stress system along a failure surface. Failure modes assume σ_{1c} was vertical prior to failure (modified after Duncan and Seed 1966)

Literature Review

The undrained behavior of compacted clays has been described most comprehensively by Seed et al. (1960). They studied effects of many factors, such as compaction conditions, compaction type, strain rate, and thixotropy, on the as-compacted and saturated undrained strength of clays. For compacted clays saturated after compaction, they found that the undrained strength depended on the initial compacted unit weight, the compaction water content, and the effective stresses at which the clay was allowed to saturate and consolidate. These factors are important to consider when interpreting undrained strengths of compacted clays from laboratory test results, including tests that induce stress rotation. Seed et al. (1960) performed only

unconsolidated undrained (UU) and isotropically consolidated undrained triaxial compression (ICU-TC) tests so principal stress rotation was not addressed.

Duncan and Seed (1966) studied principal stress rotation in undisturbed San Francisco Bay Mud, using plane strain and triaxial tests. They predicted that the undrained strength ratio, *USR* = s_u / σ'_{1c}, would be highest for plane strain compression. The USR would reach a minimum when the stress system had rotated approximately 45° (≈DSS), and would increase again as the stress rotation approaches 90° in plane strain extension. This behavior was confirmed using unconsolidated-undrained triaxial tests on specimens trimmed at different angles from undisturbed samples of the Bay Mud.

Although plane strain compression and extension appropriately mimic the conditions in an embankment, tests with these failure modes require specialized apparatuses that are not available in most geotechnical laboratories. Anisotropically consolidated triaxial tests are often used instead when the effects of principal stress rotation are being considered. An empirical adjustment factor of 1.1 to 1.3 has been suggested by Ladd and DeGroot (2003) to account for the difference between triaxial conditions and plane strain. Chapter 3 showed that a value of 1.1 is most appropriate for this factor. The ability of triaxial extension tests to suitably replace plane strain extension will be explored in this chapter.

As also noted in Chapter 3, the difference between the stress systems imposed by different laboratory tests can be quantified in terms of the parameter, *b*, defined by Bishop (1966) as

$$b = \frac{\sigma'_2 - \sigma'_3}{\sigma'_1 - \sigma'_3} \tag{7-1}$$

where:

σ'_1 = major effective stress,

σ'_2 = intermediate effective stress, and

σ'_3 = minor effective stress.

Bishop (1966) showed that b is approximately equal to $0.5(\sigma'_1 + \sigma'_3)\times\cos^2\phi'$ for plane strain conditions. This means that the plane strain value of b is typically in the range of 0.2 (ϕ' = 37°) to 0.3 (ϕ' = 24°).

Principal Stress Rotation in Common Laboratory Equipment

Methods for inducing principal stress rotation in common undrained geotechnical testing equipment are discussed in this section. A 90° rotation of the principal stress system from consolidation to failure can be induced in the standard triaxial cell in two ways. A stress rotation between 45-ϕ'/2 to 45+ϕ'/2° likely occurs in the direct simple shear test; however the orientation of the stresses during shear cannot be definitively known.

Triaxial Extension Test

The anisotropically consolidated triaxial extension test is the most common means of inducing 90° stress rotation. In this test, the specimen is consolidated anisotropically with the vertical stress greater than the horizontal stress. The major effective stress is aligned with the specimen's vertical axis during consolidation, which corresponds to a soil element below level ground provided K_0 is less than 1.0. During an ACU-TE test, the vertical stress is reduced until the specimen fails as shown in Figure 3-11(b). The triaxial extension test has several problems that make it unsuitable for slope stability, which were discussed in detail in Chapter 3.

Triaxial Compression with Stress Rotation

The other alternative for inducing principal stress rotation in the triaxial test is to anisotropically consolidate the specimen with the horizontal stress greater than the vertical stress – Figure 3-11(c). The test specimen can then be loaded in triaxial compression while still inducing principal stress rotation. This method has been labeled TC-SR herein with the "SR"

standing for "stress rotation". The TC-SR test has $b = 0$ at failure, making the stress state at failure closer to the plane strain condition ($b \approx 0.2$ to 0.3) than the ACU-TE test. The stress conditions at consolidation and failure in both types of test are compared to plane strain in Figure 3-11.

TC-SR tests have been performed by Whitman et al. (1960) on remolded Mississippi Backswamp clay, and Duncan and Seed (1965) on undisturbed San Francisco Bay Mud. Whitman et al. (1960) measured an undrained strength ratio of 0.24 in their TC-SR test, which was only slightly lower than the *USR* of 0.26 obtained for an ACU-TC test. Duncan and Seed (1965) measured undrained strength ratios of 0.37 for plane strain vertical compression (Pt. A in Figure 7-1) and 0.27 for plane strain lateral compression (Pt. C in Figure 7-1). Duncan and Seed's TC-SR test resulted in a *USR* of 0.29, which is very similar to that measured for lateral compression, suggesting the TC-SR may be a close approximation to this failure mode for San Francisco Bay Mud.

The TC-SR system of consolidation stresses also varies from most field conditions since σ'_{2c} is not usually equal to σ'_{1c} in the field. During consolidation, the mean effective stress in the TC-SR test will be higher relative to σ'_{1c} than the mean effective stress during anisotropic consolidation with σ'_{1c} vertical. For very structured soils, the TC-SR test would not be appropriate because the directions of consolidation and loading will not be aligned correctly with respect to the soil structure.

Direct Simple Shear Tests

The effects of principal stress rotation on undrained strength are also commonly assessed using DSS tests. The DSS failure mode is often presented as a good "average" between extension and compression (Ladd and DeGroot 2003). These tests are commonly performed on

soft clay soils that will become the foundation for earth embankments. No strengths from DSS tests on compacted clay could be found in the geotechnical literature. Nevertheless, zones approaching a DSS failure mechanism may be present in compacted clay embankments for rapid drawdown, and strengths from the test may be applicable to compacted clays.

The DSS test has the advantage of incorporating both anisotropic consolidation (K_0) and plane strain shear conditions as shown in Figure 7-2. However, the stress state in the DSS test is not well defined because stresses are only measured on the top horizontal surface of the specimen and not on the sides. For this reason, assumptions must be made about the stress state at failure. The measured horizontal shear stress at failure, $\tau_{hf\text{-}DSS}$, is often assumed to be equivalent to the undrained strength. Ladd and Edgers (1971) found that the magnitude of $\tau_{hf\text{-}DSS}$ is usually between the maximum shear stress, $\tau_{max} = (\sigma_{1f} - \sigma_{3f})/2$, and the shear stress on the failure plane at failure, τ_{ff}. Thus, equating s_u with the measured horizontal shear stress is a conservative assumption with an error less than or equal to $\tau_{max} \times (1\text{-}\cos \phi')$.

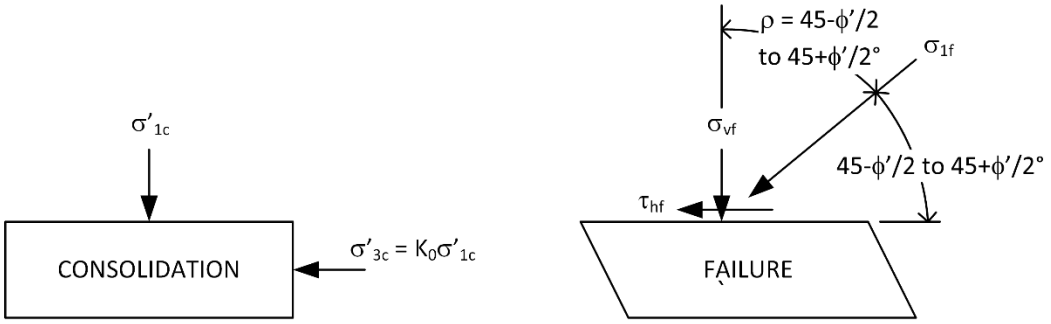

Figure 7-2. Rotation of stresses from consolidation to failure in the direct simple shear test. The orientation of σ_{1f} at failure is based on Ladd and Edgers (1971).

Many direct simple shear devices do not have a confining chamber for the test specimen and actually perform a drained test. In order to measure undrained strength in the DSS test, Bjerrum and Landva (1966) suggested that the total vertical stress on the specimen should be adjusted during shear to maintain a constant specimen volume. This causes the void ratio to remain

constant during shearing similar to truly undrained tests. The change in vertical stress during shear is assumed to be equal to the change in pore pressure that would be experienced in an equivalent undrained test (Bjerrum and Landva 1966, Dyvik et al. 1987). Theoretically, no pore pressure changes occur during the test, and the applied vertical stress is equal to the effective vertical stress.

Unlike the undisturbed soils commonly tested in the DSS device, compacted clay specimens will be initially unsaturated and will have a significant associated suction. When a vertical consolidation stress is applied in the DSS apparatus, the effective stress is not known if the specimen stays unsaturated and the suction remains. The consolidated void ratio of the unsaturated specimen will likely be different than that of a saturated specimen under the same applied vertical stress because suction will lead to a different effective stress. During shear the suction continues to affect the stress state and therefore influences the shear stress at failure. This means that the applied vertical stress is not equal to the effective vertical stress for the unsaturated specimen.

In order for the constant volume DSS to adequately mimic undrained shear, compacted clay test specimens should be saturated before shearing. This is very difficult since back pressure saturation of test specimens is not possible in many DSS devices. The compacted specimens will also have a tendency to change volume when inundated, which will depend on the compacted unit weight and water content. This swelling behavior must be dealt with in a consistent manner so that test specimens have similar structure at the beginning of consolidation.

Soil Properties and Specimen Preparation

Six triaxial and four direct simple shear tests were performed to quantify the effect of principal stress rotation on the undrained strength of a compacted clay. A glacio-lacustrine

brown lean clay from Oak Harbor, Ohio was used for the tests. The properties of clay were summarized in Table 6-1.

Test specimens were prepared by kneading compaction with a Harvard miniature compactor. The target compaction condition was a dry unit weight of 108 pcf (17.0 kN/m^3) and a water content of 20%. These conditions are 2% wet of optimum and have a relative compaction, *R.C.*, of 100% defined as

$$R.C. = \frac{\gamma_{d-comp.}}{\gamma_{d-\max}} \times 100\% \qquad (7\text{-}2)$$

where:

$\gamma_{d\text{-}comp.}$ = compacted dry unit weight, and

$\gamma_{d\text{-}max}$ = Standard Proctor maximum dry unit weight.

Triaxial specimens were compacted in a mold with a diameter 1.31 inches (3.34 cm) and a height of 2.8 inches (7.1 cm). The direct simple shear specimens were compacted in a trimming ring with a diameter of 2.6 inches (6.6 cm) and a height of 0.7 inches (1.8 cm). Both types of test specimen were extruded after compaction and mounted directly in the testing equipment. More details on the processing of the clay and specimen preparation can be found in Chapter 6.

Triaxial Tests

The results of the six triaxial tests are summarized in Table 7-1. The specimens were allowed to saturate and swell at effective stresses between 1.8 and 3.2 psi (12 and 22 kPa). During the saturation phase, a small vertical stress (less than 1.5 psi or 10 kPa) was applied in excess of the cell pressure to keep the top platen in contact with the top of the specimen.

Table 7-1. ACU triaxial tests– extension (TE) and compression with stress rotation (TC-SR)

Test # and Type	Compaction conditions			Confining stress during saturation (psi)	Consolidation		Failure (10% axial strain)			
	Unit weight, $\gamma_{d\text{-}comp}$ (pcf)	Relative Comp.[A], *R.C.* (%)	Water content, *w* (%)		Vertical stress (psi)	Horiz. stress (psi)	Water content, w_f (%)	σ'_{1f} (psi)	s_u (psi)	$\bar{A}_f$
G-1 - TE	108.7	100.6	18.4	3.2	14.1	7.4	24.0	11.8	7.3	0.47
G-2 – TE[B]	108.0	101.3	20.2	3.2	7.7	4.0	22.8	7.7	5.9	0.40
G-3 – TE	108.5	100.5	20.7	2.5	27.8	14.5	22.8	16.6	11	0.63
G-4 – TC-SR	107.2	99.2	20.0	3.1	14.4	28.1	22.9	36.2	17	0.19
G-5 – TC-SR	108.5	100.5	20.1	1.8	3.7	7.2	24.6	14.8	7.6	0.00
G-6 – TC-SR	109.1	101.0	19.6	2.8	7.2	14.2	23.0	28.4	14	-0.01

Note: 1 psi = 6.895 kPa, 6.37 pcf = 1 kN/m^3

[A] R.C. referenced to Standard Proctor (ASTM D698)

[B] Failure was defined as 3.6% axial strain because necking became evident at 4% axial strain.

After the specimens were saturated and reached equilibrium, they were anisotropically consolidated to a principal stress ratio, $\sigma'_{1c} / \sigma'_{3c}$, of about 2.0. Based on the author's experience with numerical analyses of embankment stresses, the average principal consolidation stress ratio is commonly about 2.0. K_0 was found in the triaxial cell to range from 0.67 to 0.64 for vertical (major) effective consolidation stresses between 8 and 31 psi (55 to 214 kPa), respectively. This corresponds to a principal stress ratio of 1.5 to 1.6.

The stress paths from the six triaxial tests are plotted in Figure 7-3. The axial stress in the extension tests dropped quickly during shear, and rotation of the stress system occurred at an absolute axial strain of less than 0.2%. The deviator stress for the TE tests reached a maximum just before the specimens began to neck.

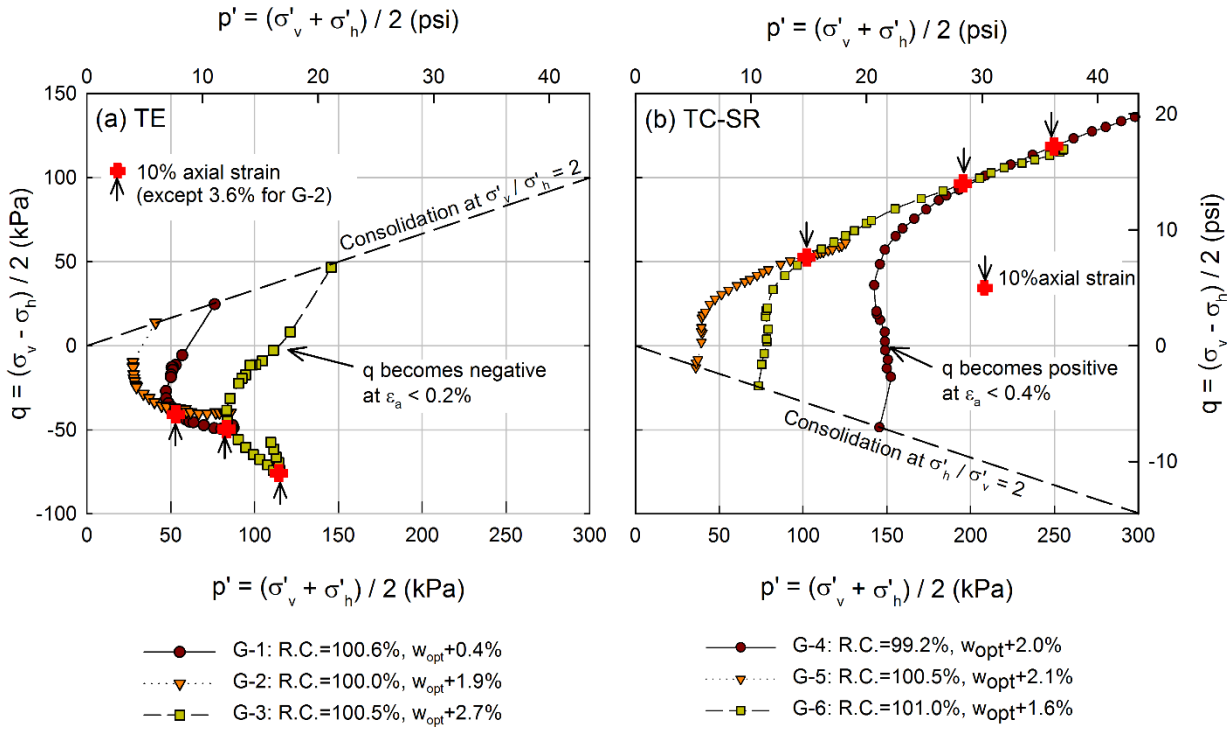

Figure 7-3. Stress paths for (a) TE and (b) TC-SR triaxial tests on Oak Harbor clay

Rotation of the stress system also occurred early in the TC-SR tests as shown in Figure 7-3(b) at axial strains less than 0.4%. The specimens developed positive pore pressures during

the early stages of shear and then began to dilate. The deviator stress increased throughout the duration of the tests. This type of strain hardening behavior is typical of clay compacted wet of optimum (Seed et al. 1960).

Undrained failure is difficult to define for straining hardening soils as noted by Seed et al. (1960). The maximum principal stress difference is often used to define failure for undrained triaxial tests. However, the principal stress difference continues to increase up to high strains for strain hardening soils so its maximum value depends mostly on the length of the test. The undrained strength in this study was defined as the maximum shear stress at 10% absolute axial strain for all the triaxial tests except G-2. Specimen G-2 reached a maximum principal stress difference at a strain of 3.6% just prior to the formation of a neck, which became evident when the specimen reached 4% axial strain. In undrained triaxial conditions, 10% axial strain is equivalent to 15% shear strain, which will be required for comparison with the direct simple shear test.

Figure 7-4 plots the undrained strengths from the TE and TC-SR tests against major effective consolidation stress. The trends in undrained strength for ICU and ACU triaxial compression tests on compacted Oak Harbor clay are also shown for *R.C.* = 100%. The TE undrained strengths are 25 to 55% lower than the ICU-TC strength trend and 20 to 30% lower than the ACU-TC trend. This fits well with the triaxial extension behavior usually observed for natural clays. For example, Ladd et al. (1977) found that undrained strength in TE tends to be 50 to 80% of that measured in ACU-TC tests.

Undrained strengths from the TC-SR tests are also plotted in Figure 7-4. In this case, the strengths match well with the average trend in the ICU triaxial compression once the effects of relative compaction and anisotropic consolidation are taken into account. The TC-SR specimens

have a mean consolidation stress about 17% lower than ICU specimens consolidated to the same σ'_{1c}. The relative compaction of specimens G-5 and G-6 was greater than 100% and the strengths match or lie above the ICU-TC trend for *R.C.* = 100%. Specimen G-4 had a *R.C.* of 99%, and a corresponding strength below the ICU trend.

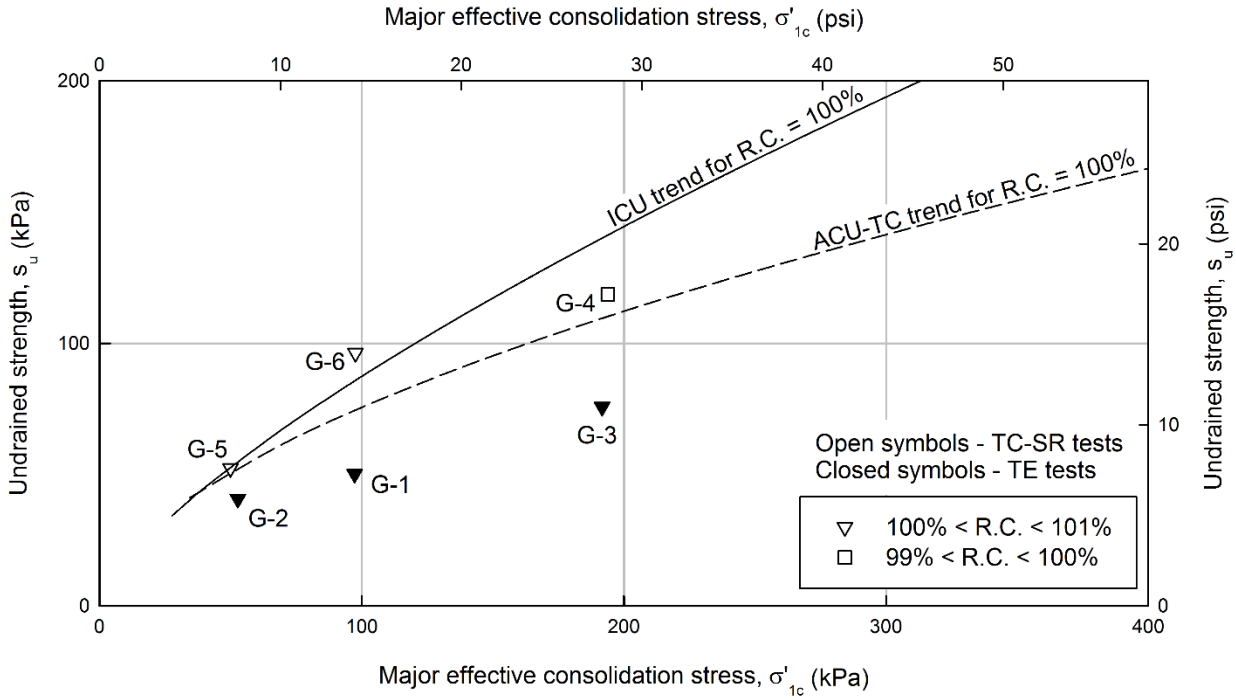

Figure 7-4. Undrained strengths from TE and TC-SR tests compared to trends from ICU and ACU TC tests on compacted Oak Harbor clay

Discussion

Figure 7-4 shows that triaxial extension and triaxial compression tests with stress rotation do not yield the same undrained strength, despite the fact that both types of test follow stress paths that cause a 90° principal stress rotation. The TC-SR tests resulted in nearly the same strength as the ICU triaxial compression tests, indicating that the 90° principal stress rotation alone did not decrease the strength of compacted Oak Harbor clay. The TE and TC-SR tests show that unique

undrained strengths for a 90° rotation of the stress system cannot be obtained from the triaxial test.

The triaxial extension test results confirm that these tests are not an appropriate means for determining undrained strengths for a principal stress rotation of 90° in slope stability evaluations. The TE test has a much higher intermediate principal stress at failure than that present in plane strain. The low strengths observed in the TE tests are primarily the result of this unrealistic stress system.

Based on the Oak Harbor clay results, the generalized relationships shown in Figure 7-5 are proposed to describe the relative behavior of compacted clay in various types of triaxial tests. A stress rotation of 90° appears to influence the undrained strength of the compacted clay little, if at all. The reduction in undrained strength from the ICU-TC to the anisotropically consolidated TC-SR tests can be attributed mostly to the slightly lower mean consolidation stress present in the TC-SR test. Table 7-2 summarizes the stress system for each test, the amount of stress rotation, and the approximate ratio between the undrained strength in a particular triaxial test to that in ICU-TC.

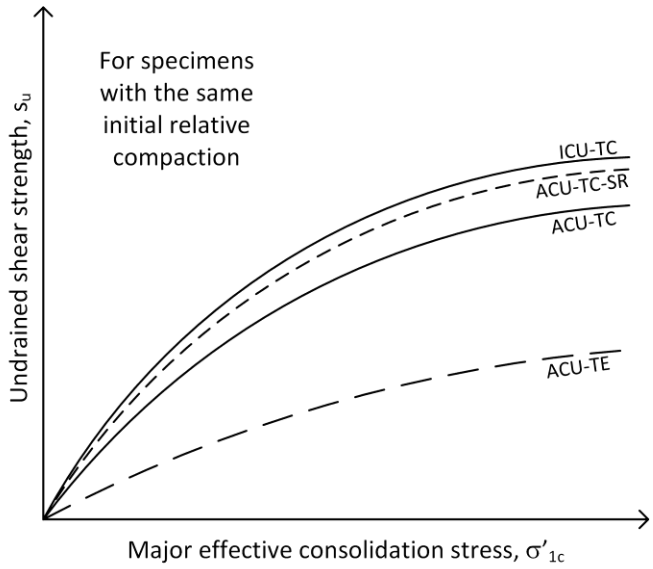

Figure 7-5. Relative position of strength relationships for various types of triaxial tests.

Table 7-2. Failure conditions, stress rotation, and relative strengths in triaxial tests on compacted clay.

Test	Intermediate principal stress ratio at failure, b_f	Rotation of stress system during shear (deg)	$s_{u\text{-}test} / s_{u\text{-}ICU}$
ICU-TC	0	0	---
ACU-TC-SR	0	90	0.90 – 1.00
ACU-TC	0	0	0.75 – 0.85
ACU-TE	1	90	≈ 0.50

Direct Simple Shear Tests

Four specimens of compacted Oak Harbor clay were tested in direct simple shear (DSS) as summarized in Table 7-3. The specimens were compacted to dry unit weights corresponding to relative compactions between 99 and 102% (D698) at water contents ranging from 18.4 to 19.8% (0.4 to 1.8% above optimum).

Table 7-3. Direct simple shear tests on compacted Oak Harbor clay

Test	Compaction conditions			Vertical stress during saturation (psi)	Vertical consolid. stress, σ'_{vc} (psi)	At Failure (Max τ_h)		
	Comp. γ_d (pcf)	Rel. Comp., *R.C.*[A]	Water content, w			Water content, w_f	$\tau_{hf} \approx s_u$ (psi)	Decrease in σ_v (psi)
F-1	106.7[B]	98.7%	18.4%	7	7	22.1%	1.9[C]	0.6
F-2	107.9	99.9%	19.7%	7.3	56	20.0%	17	17.7
F-3	107.3	99.4%	19.8%	7.1	28	21.4%	7	13.8
F-4	110.1	101.9%	19.5%	7.1	14	21.0%	3.4[C]	4.2

Note: 1 psi = 6.895 kPa, 6.37 pcf = 1 kN/m^3

[A] R.C. referenced to Standard Proctor (ASTM D698)

[B] Initial sample mass was not obtained. Compacted unit weight was based on final sample measurements.

[C] Possible slippage between platen and specimen. Shear stress may not be representative.

The initial saturation of the DSS specimens ranged between 80 and 92%. As discussed previously, DSS specimens should be saturated to accurately determine undrained strength for saturated conditions. Since back pressure was not possible with the equipment used for these tests, a head differential was applied immediately after the specimens were mounted in the test frame, allowing water to flow through the specimens. The saturation phase was performed at a vertical effective stress of about 7 psi (49 kPa), which was required to prevent significant vertical swell. The saturation phase lasted between 21 and 24 days. An average of 0.73 in^3 (12 mL) of water was forced through the specimens in this length of time, which corresponded to about one half the initial specimen void volume. Full saturation of the specimens could not be verified before testing but calculations based on final measurements suggested the saturation was close to 100%.

The horizontal shear and vertical normal stresses measured in the DSS tests are plotted in Figure 7-6. Failure was defined as the point of maximum horizontal shear stress, τ_{hf}. The undrained strength, s_u, was assumed to be equal to τ_{hf}. The decrease in vertical stress, σ_v, reported in the last column of Table 7-3 is the change in vertical stress required to maintain

constant volume during shear. The vertical normal stresses decreased monotonically for all four tests, indicating contractive behavior. The tests at low consolidation stresses exhibited signs of slippage between the top platen and the compacted specimen, and the strengths may not be representative of the entire specimen.

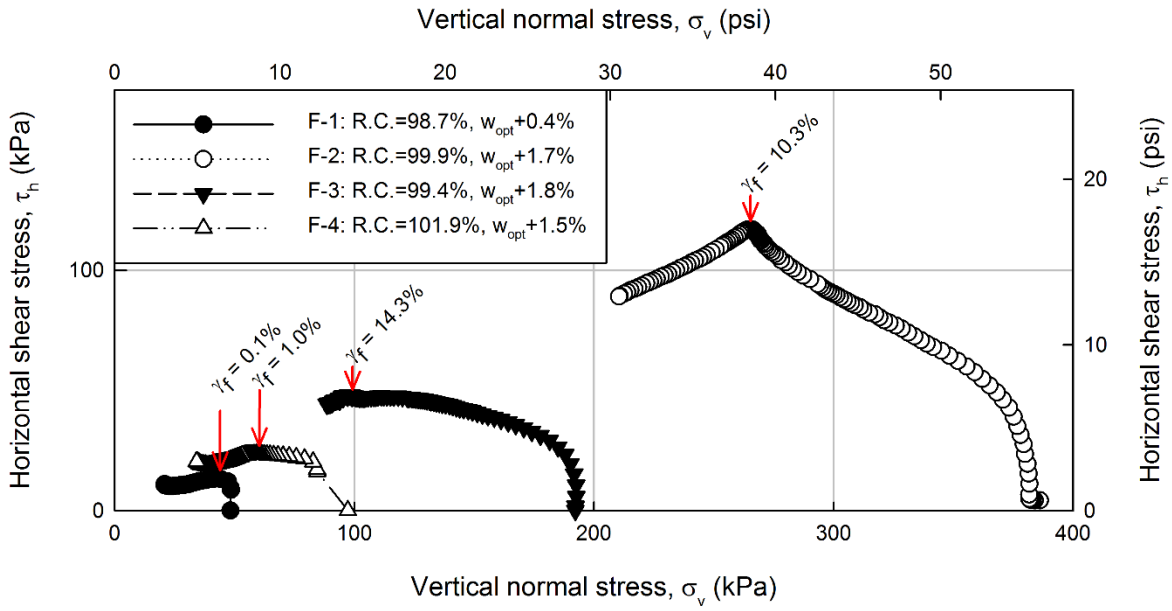

Figure 7-6. Horizontal and vertical stresses measured during shear in DSS tests on specimens of compacted Oak Harbor clay

Undrained strengths from the four DSS tests are plotted in Figure 7-7 along with strengths from the triaxial tests. The DSS strengths are significantly lower than all of the triaxial tests, even those in triaxial extension. As shown in Figure 7-7, the average undrained strength ratio was 0.27 for the DSS tests, which is closer to that expected for a normally consolidated clay rather than a compacted material. Castellanos (2014) performed ICU-TC tests on normally consolidated, remolded specimens of Oak Harbor clay and found an average USR of 0.33 for ICU-TC. On average, the DSS strengths were about 80% of those measured for normally consolidated specimens in triaxial compression.

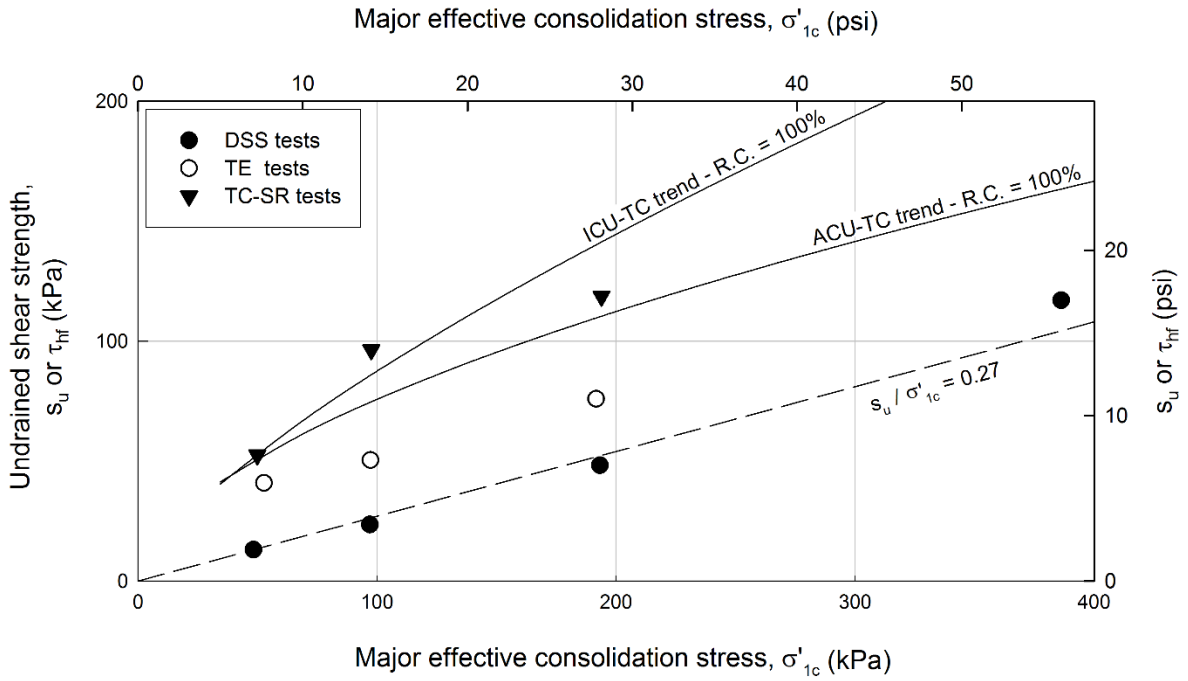

Figure 7-7. Undrained strengths from DSS compared to those from different types of triaxial tests for compacted Oak Harbor clay

Discussion

Application of the DSS to compacted clay must be further developed before conclusive arguments can be made regarding its usefulness and applicability for compacted clay. A few observations can be made based on the four DSS tests presented herein.

Stiff soils such as compacted clays are difficult to test in DSS at low normal stresses. The end platens tend to slip on the upper horizontal specimen surface. Platens with teeth or pins have been found to perform better for tests on stiff soils at low consolidation stresses (ASTM D6528).

Most compacted clays will be initially unsaturated and will have relatively low permeability. These two properties make saturation difficult in a conventional DSS device that does not allow back pressure. DSS tests on compacted clay should be performed in equipment that allows back pressure saturation.

The DSS tests performed for this study yielded strengths closer to those expected for a normally consolidated rather than a compacted soil. This may be due to the long saturation period at low effective stress. DiBernardo and Lovell (1979) found that the apparent prestress (similar to preconsolidation stress) measured in one-dimensional consolidation tests dropped to the vertical effective stress at inundation when specimens of compacted clay were saturated. A similar effect may have occurred in the DSS specimens in this study.

Regardless of the factors that complicate interpretation of the test results, principal stress rotation during loading in the DSS test appears to cause some reduction in strength in compacted clay.

Conclusions

Triaxial extension tests and triaxial compression tests with stress rotation do not yield the same undrained strength. Low strengths observed in triaxial extension tests are the result of the unrealistic stress system applied by the test as well as the influence of necking. The TC-SR tests had nearly the same strength as the ICU triaxial compression tests, indicating that a 90° principal stress rotation alone does not have a significant impact on the strength of compacted clay.

Direct simple shear tests are difficult to perform on compacted clays due to the stiffness of the material and the initial unsaturated condition of the specimens. Advances in direct simple shear testing techniques are required to successfully test compacted clays in this manner. Further development of this test method for compacted clays would be valuable to the profession.

8. Finite Element Methods for Evaluating Rapid Drawdown

The previous chapters have highlighted the problems with effective stress methods for rapid drawdown as well as the shortcomings of the multi-stage undrained strength methods based on limit equilibrium. The undrained behavior of soils, particularly compacted clays, has also been explored. This chapter introduces two methods for analyzing rapid drawdown using total stresses based on FEA. The first is based on linear elastic FEA and a simple adjustment to undrained strength to account for stress system effects. The appropriate adjustment factor, R_T, was based on back analysis of case studies and compared to the Duncan et al. or DWW (1990) limit equilibrium method. The second method is more rigorous in that it uses non-linear FEA to obtain consolidation stresses and attempts to account for the spatial variation in stress system effects throughout the embankment.

A practical RDD method based on FEA must use consolidated undrained strengths from a common laboratory test, preferably the ICU triaxial compression test. The method must account for the differences between the stress system imposed by the laboratory test and that present in the field conditions. In order to be useful in engineering practice, the method must be easily understood and implemented by geotechnical practitioners. For this reason, undrained strength should be represented in a straightforward manner that is consistent with common practice in geotechnical engineering.

Rational FEA Method

This section presents a practical rapid drawdown procedure that utilizes finite element analysis to determine the consolidation stresses and to evaluate embankment stability. The method consists of three steps: 1) consolidation stress analysis, 2) undrained strength evaluation, and 3) RDD stability analysis. This method could easily be "pre-packaged" as a module or

analysis option by a commercial FE software package. At present, it can be implemented in manual "stages."

Step 1: Consolidation Stress Analysis

The consolidated undrained strength of the embankment soil will be controlled by the effective consolidation stress state as well as the stress path from consolidation to failure. The major effective consolidation stress, σ'_{1c}, has been selected as the single parameter that will be used to calculate s_u for rapid drawdown analysis.

A detailed discussion of stress analysis for embankments is provided in Chapter 4. While non-linear stress analyses will provide a more accurate and realistic distribution of stresses, they also require significantly more experience with the finite element method and additional constitutive parameters. If these parameters cannot or are not determined accurately, the non-linear stress analysis will be no more accurate than a well-designed linear-elastic analysis. For the Rational FEA Method, linear elastic constitutive theory was adopted to determine the effective consolidation stresses.

The consolidation stress analyses for the Rational FEA Method should also use the following:

- Effective stress finite element analysis formulated such that stress analysis is partially coupled with pore pressures,
- Boundary loads imposed on the embankment, including water loads due to the full reservoir (dams) or high water level (levees),
- Steady state pore pressures applied throughout the embankment (for levees this assumes seepage develops quickly during flooding), and

- Three stages (gravity turn-on of embankment, application of boundary loads, and application of pore pressures) of loading to reduce the effects of initial stress assumptions.

After the stress analysis is complete, the values of σ'_{1c} are exported from the FE software at a large number of points spread throughout the model. The FE nodes may be a convenient set of points, if the number of nodes is not so large that the process becomes unwieldy. Alternatively, a grid of query points can be specified throughout the embankment. Specific methods for exporting stress values will depend on the computer program being used. At a minimum, the (*x, y*) coordinates of the points, and the values of σ'_{1c} must be obtained. These values can be pasted in a spreadsheet or input into an external computer program for use in Step 2.

Step 2: Undrained Strength Evaluation

Determination of the appropriate undrained shear strength for RDD is the most important step in the analysis. The Rational Method is based on undrained strength from ICU triaxial compression tests expressed as a function of σ'_{1c}, as shown in Figure 8-1. These tests are relatively easy to perform and have been the conventional test for obtaining rapid drawdown strength parameters. Because ICU tests are used by Duncan et al. (1990), both methods can be performed side by side using the same laboratory test data.

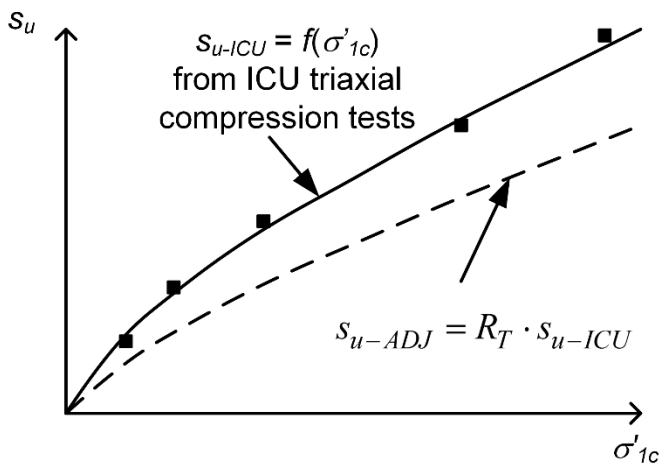

Figure 8-1. Typical relationship between undrained strength and consolidation stress.

The relationship between undrained strength and effective consolidation stress can be defined in any way that appropriately fits the data. If a mathematical relationship is used, it will preferably be simple and easy to use and should result in a strength relationship that passes through the origin. A two-parameter power curve (Eqn. 6-2) meets these criteria, representing ICU undrained strength, $s_{u\text{-}ICU}$, as a function of σ'_{1c} and curve fit parameters, *a* and *b*. The power curve parameters expressed in this form are dimensionless and are not dependent on the unit system. Guidance on determining *a* and *b* from test data can be found in Appendix E.

The ICU tests should bracket the expected consolidation stresses to represent the undrained strength well. Due to the non-linearity of the shear strength relationship at low consolidation stresses, tests at low consolidation stresses are especially important for soils that extend to the surface of the embankment.

As discussed in more depth in Chapter 3, ICU triaxial compression tests do not match the field consolidation or loading stress path. Stress system effects such as anisotropic consolidation, plane strain, and principal stress rotation will cause the field s_u to vary from that

measured in the ICU test. Other factors, such as anisotropic strength and deformation characteristics may also lead to differences in undrained strength.

The Rational Method accounts for these factors using an empirical adjustment factor, R_T. The factor is constant for all consolidation stresses and is applied equally at all points within the embankment. The adjusted undrained strength, $s_{u\text{-}ADJ}$, for use in RDD analysis becomes

$$s_{u-ADJ} = R_T \cdot s_{u-ICU} = R_T \cdot a \cdot p_a \left(\frac{\sigma'_{1c}}{p_a} \right)^b \quad (8\text{-}1)$$

where:

$s_{u\text{-}ICU}$ = undrained strength from ICU triaxial compression tests.

The adjusted undrained strength concept is shown in Figure 8-1. For each zone of the embankment, $s_{u\text{-}ADJ}$ can be determined using Eqn. (8-2) for each value of σ'_{1c} exported from the consolidation stress analysis. This will generate an array of strengths for each zone that must be imported back into the finite element software. Built-in tools in the FE software can be used to interpolate the adjusted undrained strength for each node.

The appropriate value of R_T will be determined later in this chapter by back calculation from case histories where failure occurred or by comparison to the Duncan et al. (1990) method. The results presented in Chapters 3 and 5 suggest that the appropriate value of R_T lies between 0.6 and 0.8 for rapid drawdown.

Step 3: RDD Stability Analysis

Embankment stability during rapid drawdown was evaluated in the third step. The undrained strengths determined in Step 2 may be used in conjunction with either limit equilibrium or finite element analysis. For continuity with the previous steps, finite element strength reduction

analysis was used. In general, the recommendations of Griffiths and Lane (1999) for strength reduction analysis were followed.

Strength reduction analysis is an iterative finite element method that systematically reduces/increases the shear strength of all the elements by a strength reduction factor, *SRF*. After each *SRF* is applied, equilibrium conditions are recalculated with overstressed elements yielding and distributing stress to other parts of the embankment. Many different definitions of failure have been suggested for strength reduction analysis as summarized by Griffiths and Lane (1999). The simplest and most common method defines failure as the point of non-convergence in the finite element solution. This definition of failure is illustrated conceptually in Figure 8-2.

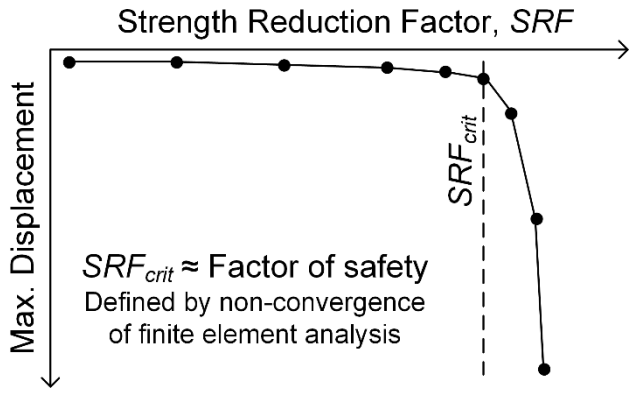

Figure 8-2. Non-convergence failure criterion for strength reduction analysis

The same finite element model from Step 1 can be reused in Step 3. A few modifications to the model are required. The Step 1 consolidation stress model should be saved to use for other iterations of the consolidation stress analysis that may be desired.

- Apply the calculated undrained strengths to each undrained zone. Free-draining zones that will remain drained during drawdown should be assigned the appropriate effective stress strengths.
- Change the constitutive properties for all zones to linear elastic-plastic. This allows the elements to yield when the strength reduction analysis is performed.

- Set the dilation angle, ψ, for all soils to zero (Griffiths and Lane 1999).
- Change to total stress finite element analysis.
- Delete one of the stages from the consolidation stress model, leaving two stages in the model. In the first stage, the elements should be initialized and a boundary load corresponding to the full water level should be applied. In the second stage, the boundary water load should be lowered to the drawdown water level.

The dissipation of excess pore pressures in soil zones close to drainage boundaries can be considered (similar to Stage 3 in DWW) by designating drained zones near the slope surface. However, these zones have been found to have little effect on the results if the undrained strength relationships pass through the origin as shown in Figure 8-1.

The undrained strength for each element was determined using the TIN interpolation scheme built into Phase^2 with the imported array of undrained strengths. The TIN interpolation option built into the software (SLIDE and Phase^2) was used for all of the cases studied in this research. The Rational FEA Method is summarized in Figure 8-3.

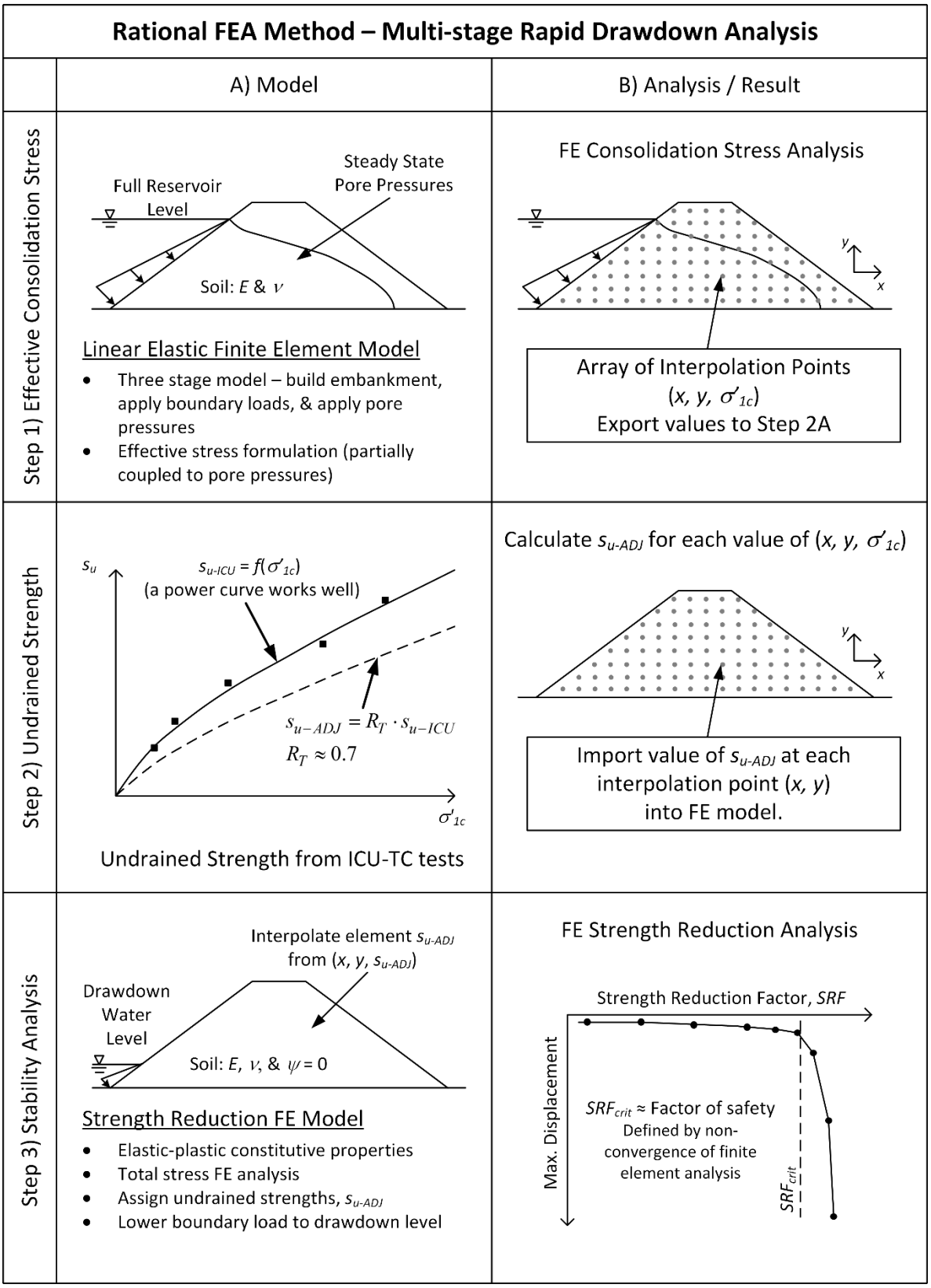

Figure 8-3. Summary of the Rational FEA Method for undrained rapid drawdown analysis

Examples of the Rational FEA Method

Pilarcitos Dam

The geometry of Pilarcitos Dam and details about the 1969 RDD failure were provided in Chapter 4. Wong et al. (1983) reported the total and effective stress Mohr circles from ten ICU triaxial compression tests. The undrained strength and major effective consolidation stress were determined for each of these tests. A power curve was fit to the data as shown in Figure 8-4. Although not explicitly stated in Wong et al. (1983), the undrained strengths are assumed to correspond to a maximum principal stress difference failure criterion. The stress-strain curves were not provided, and the original report could not be obtained to verify this assumption.

The Pilarcitos Dam finite element model was created using the software Phase^2 v.8.011. A rigid foundation was assumed, and the nodes along the base of the embankment were fixed. The consolidation stress analysis assumed linear elastic stress strain behavior with E = 225 ksf (10.8 MPa) for both the consolidation stress and drawdown analyses. Poisson's ratio, ν, was assumed to be 0.42 for the drained conditions, and 0.49 for undrained conditions. The drained zones in the drawdown analysis used an effective stress friction angle of 45° based on the Wahler and Associates (1970) tests at low confining stresses.

Strength reduction analysis using the ICU strengths resulted in a critical *SRF* of 1.39. An adjustment factor, R_T = 1 / 1.39 = 0.72 is required to obtain a factor of safety of unity. The predicted failure zone is illustrated by the contours of maximum shear strain plotted in Figure 8-5. The observed failure surface and critical failure surface predicted by the Duncan et al. (1990) method are also shown for comparison. The Rational FEA method predicts a very similar failure surface to the accepted limit equilibrium method. Neither predicts the actual failure mechanism although the failure depth is similar.

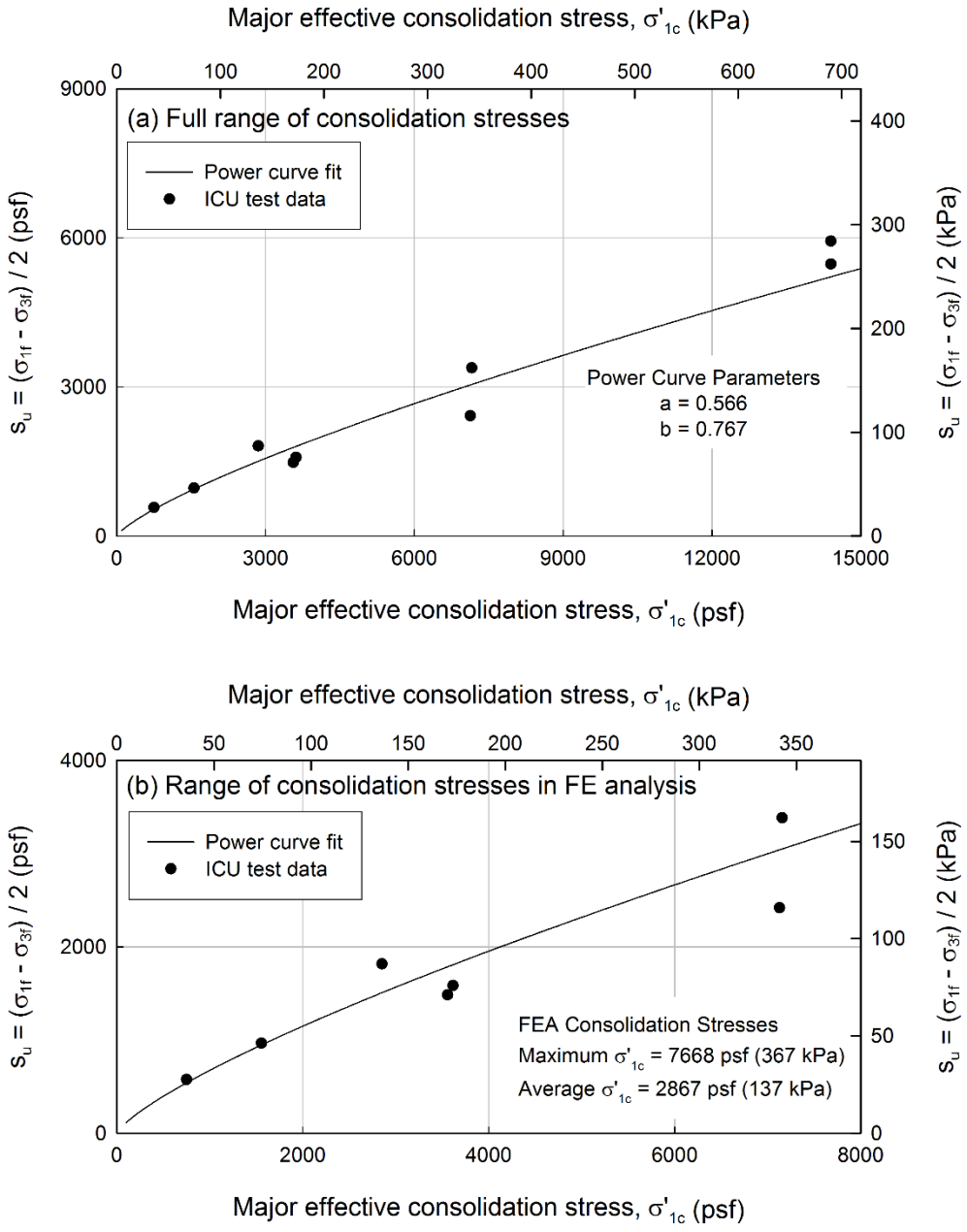

Figure 8-4. Undrained strength envelope for sandy lean clay at Pilarcitos Dam using a power curve fit – a) full range of test stresses, b) range of σ'_{1c} predicted by FE model.

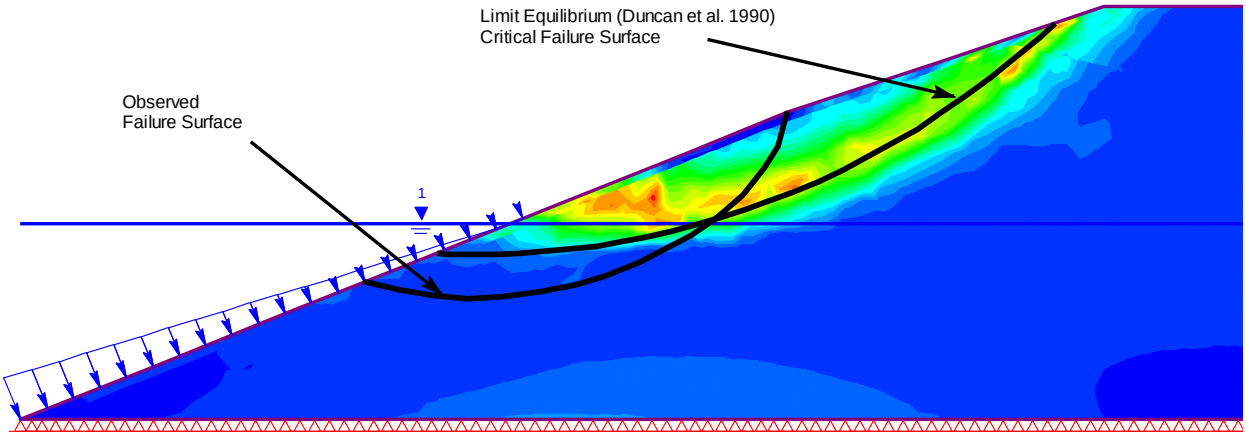

Figure 8-5. Maximum shear strain contours for Pilarcitos Dam illustrate failure mechanism. Note: Contours shown are for *SRF* = 1.43 to clarify the failure zone.

Walter Bouldin Dam

The geometry and the effective stress strength parameters for Walter Bouldin Dam were presented in Chapter 4 based on Whiteside's (1976) thorough investigation of the failure. ICU triaxial compression tests were performed by Whiteside on recompacted samples of the SC-SM, ML, and CL soils from the dam. The stress-strain curves for the CL soil are shown in Figure 8-6 as an example.

Two different definitions of strength were explored for Walter Bouldin Dam. First, maximum principal stress difference, σ_{dmax}, was used, following Whiteside and other researchers who used his strength parameters. As shown in Figure 8-6, the compacted soils were strain-hardening, and σ_{dmax} occurred at the end of each test at axial strains between 15 and 20%. The maximum principal stress difference does not produce a consistent interpretation of undrained strength. For this reason, the stress at 10% axial strain was selected as a second interpretation of undrained strength for Walter Bouldin Dam. The power curves for both definitions of strength are given in Figure 8-7. The power curve parameters are summarized in Table 8-1.

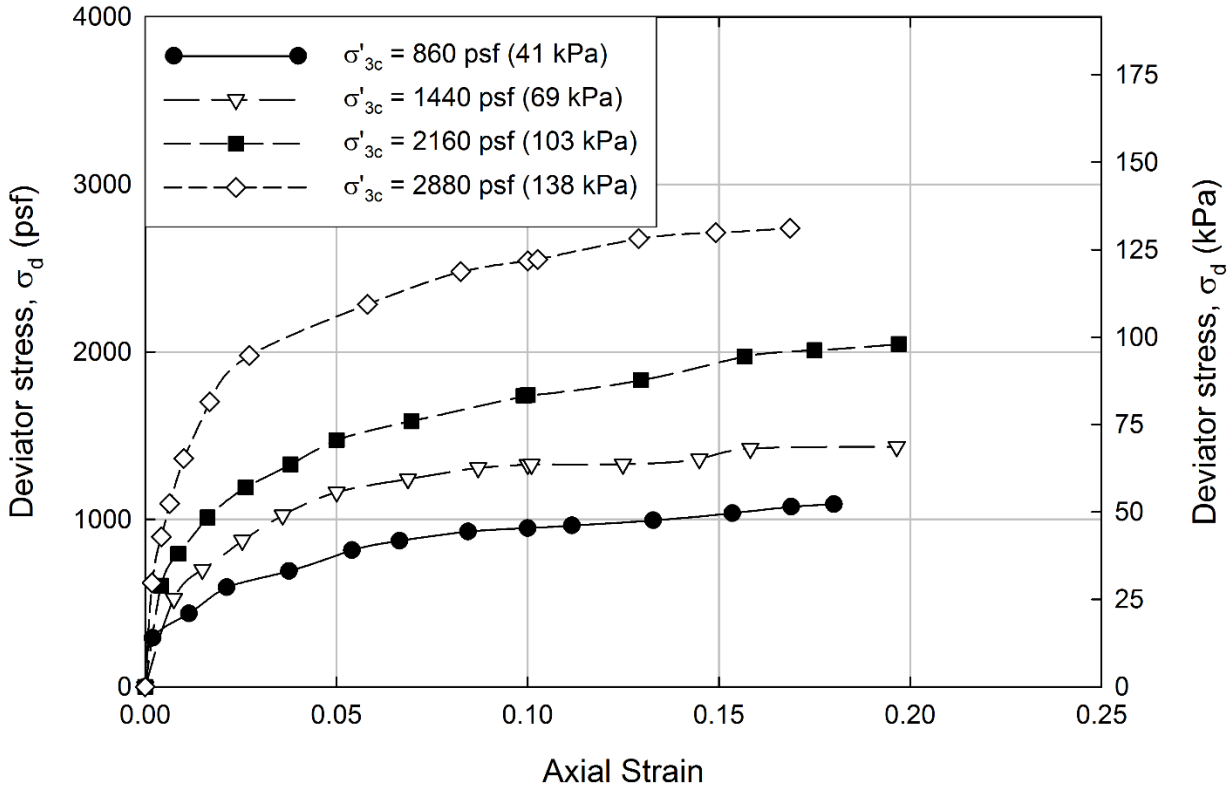

Figure 8-6. Deviator stress curves for Cretaceous clay (CL) layer (after Whiteside 1976)

For the finite element consolidation stress analysis, the elastic modulus for all soils was assumed to be 1,000 ksf (48 MPa). The riprap and base layer of clayey sandy gravel were assigned $\nu = 0.3$, while $\nu = 0.35$ was assumed for the other three soils. Pore pressures corresponding to the full reservoir height of 47 feet (14.3 m) above the base of the embankment were assigned throughout the cross-section, assuming a horizontal piezometric surface. The nodes along the base of the embankment were fixed while the downstream boundary was restrained in the horizontal direction.

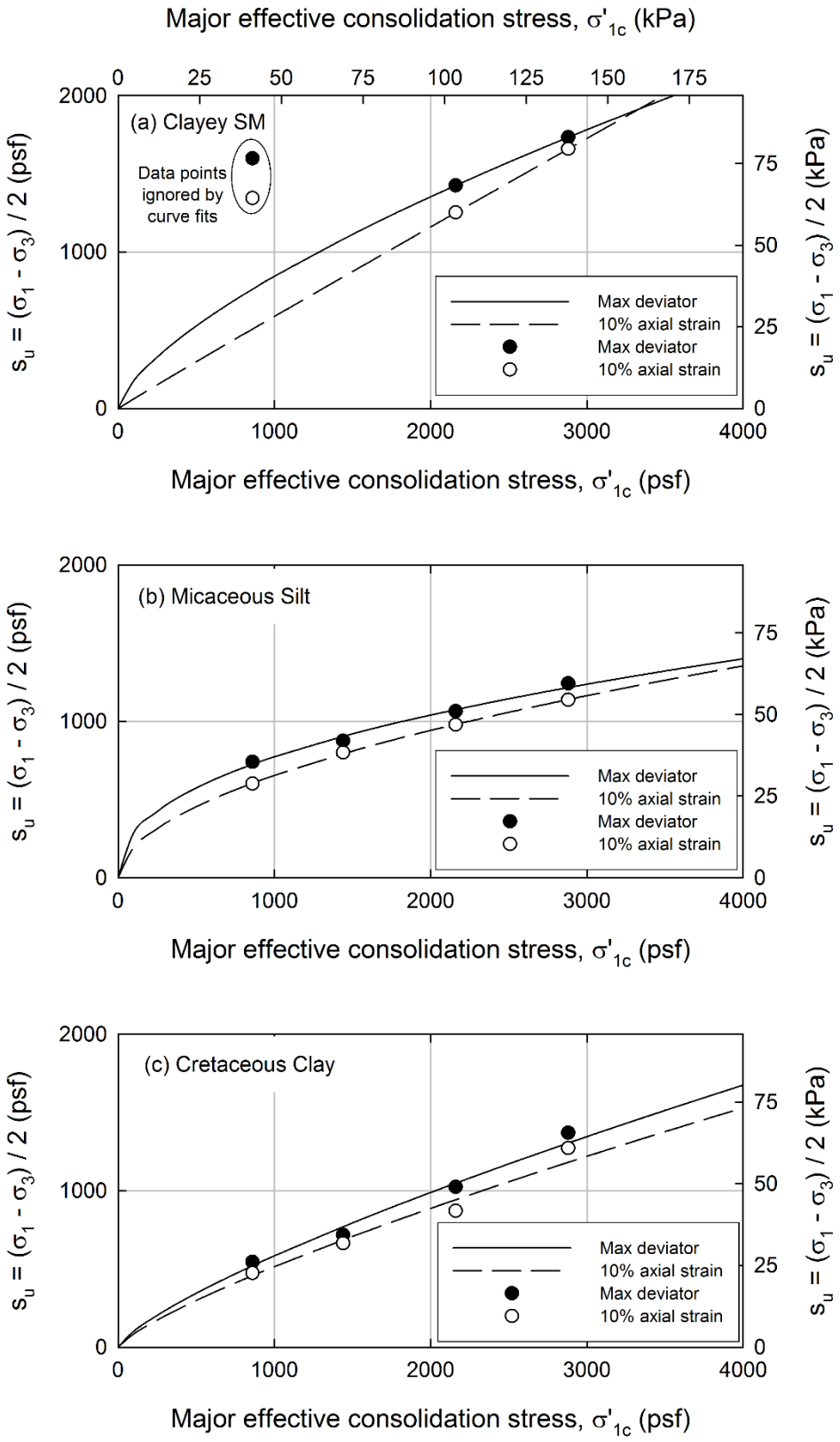

Figure 8-7. Power curve fits for three undrained soils in Walter Bouldin Dam analyses

Table 8-1. Power curve parameters for Walter Bouldin Dam soils – two definitions of strength

Soil	Maximum principal stress difference		10% axial strain	
	a	*b*	*a*	*b*
Clayey silty sand	0.665	0.679	0.581	0.978
Micaceous silt	0.504	0.429	0.459	0.526
Cretaceous clay	0.488	0.761	0.438	0.787

Maximum Deviator Stress

The ICU maximum deviator strengths resulted in SRF_{crit} of 1.56 and a corresponding value of R_T = 1 / 1.56 = 0.64. This is slightly misleading because the strength reduction method also factors the strength of the base clayey gravel layer. The predicted failure surface extends into the clayey gravel if the full ICU strengths are used for the undrained soils. With reduced strengths and R_T = 0.63, the shear strain contours shown in Figure 8-8 were obtained at the critical *SRF* of 1.0.

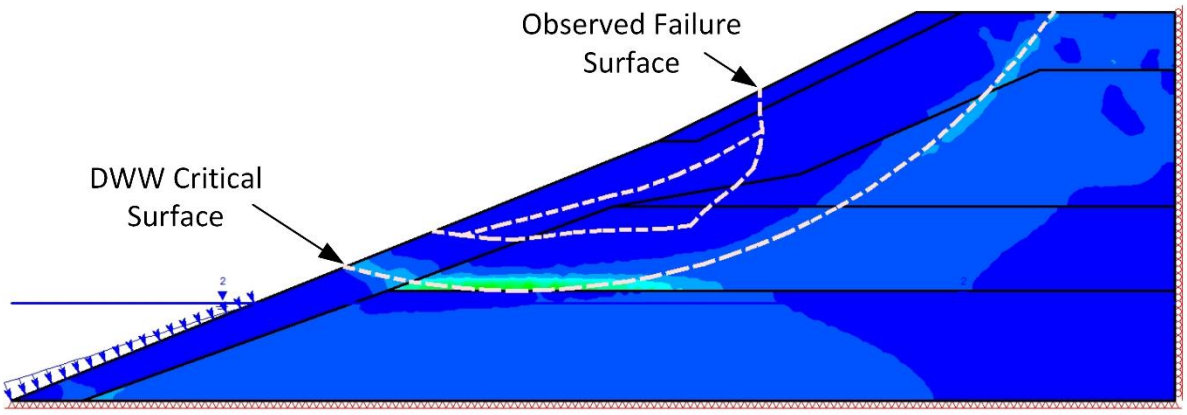

Figure 8-8. Shear strain contours for Walter Bouldin Dam – maximum deviator stress: R_T = 0.63 and SRF_{crit} = 1.0

10% Axial Strain

The RDD analyses were repeated with the 10% axial strain strengths given in Figure 8-7. A minimum ICU strength of 500 psf (24 kPa) was assigned to the SM layer to prevent a shallow failure from occurring just below the riprap zone. The increased strength was justified because the 10% axial strain power curve is very conservative at low normal stresses. This SM minimum strength assumption only affected about 5% of the critical failure zone.

The critical *SRF* was 1.4 (R_T = 1/1.4 = 0.71) when strength was defined as the shear stress at 10% axial strain. Using R_T of 0.71 yields a critical *SRF* of 1.0 for Walter Bouldin Dam with strengths corresponding to 10% axial strain. Shear strain contours are shown in Figure 8-9.

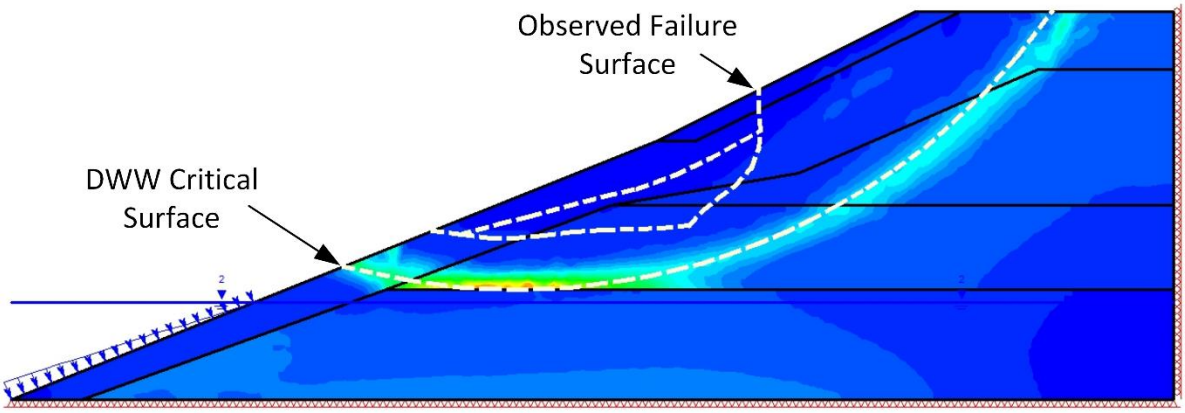

Figure 8-9. Shear strain contours for Walter Bouldin Dam – 10% axial strain: R_T = 0.71 and SRF_{crit} = 1.0

Marchand Levee Failure

A levee failure occurred along the Mississippi River near Marchand, LA in 1983, which was attributed, at least partially, to rapid drawdown (USACE 1984). The river stage began rising in February 1983 and peaked at El. 33 to 34 ft (10 to 10.4 m) on May 31. The river stage fell to elevation 4.6 ft (1.4 m) by August 23, which according to the USACE (1984) report on the

failure was the fastest drawdown on record after a flood of this magnitude. The failure is shown in an aerial photo in Figure 8-10.

Figure 8-10. Aerial view of Marchand levee failure, looking downstream (from USACE 1984)

A cross-section of the riverbank was obtained 11 days before the failure as part of regular maintenance procedures. A sounding of the riverbed was performed after the failure so that the post-failure geometry is approximately known. The slope geometry and soil profile are provided in Figure 8-11.

The levee fill consisted of silt for which no shear strength data was available. The USACE analyses assumed an undrained cohesion of 200 psf (9.6 kPa) and a friction angle of 20°. The total unit weight of this soil layer was 117 pcf (18.4 kN/m^3). In this study, undrained strengths equivalent to ICU triaxial compression were assumed to follow a power curve with parameters, *a*

= 0.75 and b = 0.6, relating s_u to σ'_{1c}. Since the levee fill is shallow and relatively thin, its strength has little impact on the failure.

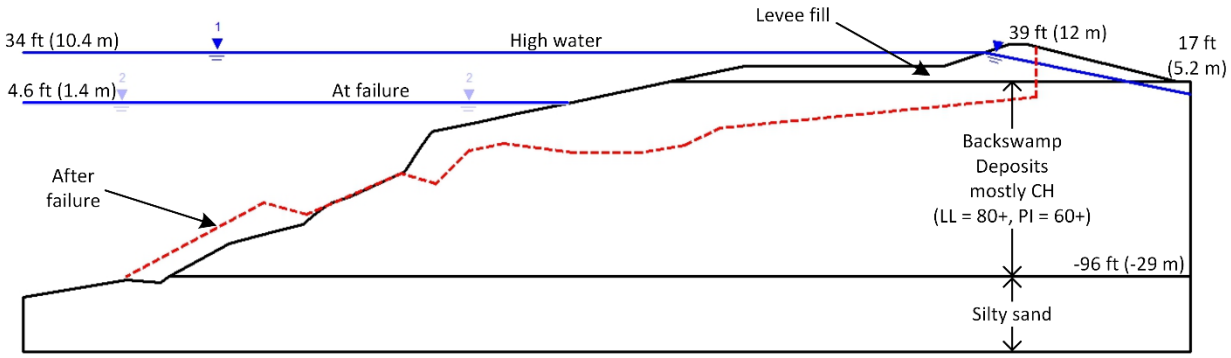

Figure 8-11. Marchand levee failure – cross sections before and after failure (after USACE 1984)

Undrained shear strengths were determined for the backswamp deposits from two undisturbed borings, one from 1969 and another performed soon after the failure. Twenty-one sets of three UU triaxial compression tests were performed. ICU tests (without pore pressure measurements) were completed on samples from elevations 4, -57, and -63 feet (1.2, -17.4, and -19.2 m). The average strengths from the sets of UU tests are plotted in Figure 8-12. The interpretation used in the USACE analyses of the failure is also shown. The USACE trend was appropriately conservative for the design of a new setback levee and was also based on strengths from tests (possibly unconfined compression tests) on split-barrel samples. The backswamp deposits had total unit weights ranging from 96 to 117 pcf (15.1 to 18.4 kN/m^3).

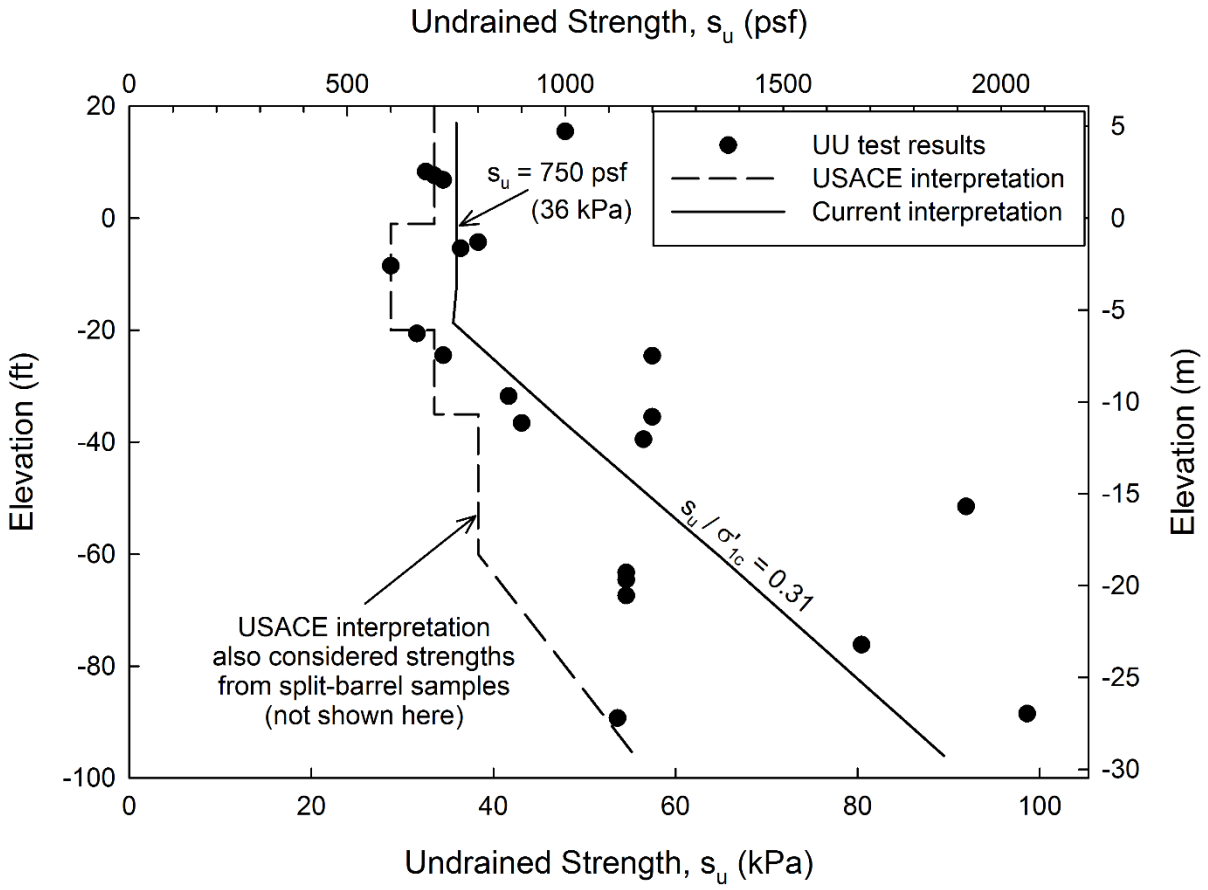

Figure 8-12. Undrained strength of backswamp deposits at Marchand levee failure (data from USACE 1984)

The undrained strength interpretation used in this analysis is shown in Figure 8-12 and represents the mean strength from the UU and ICU tests. Above El. -18 ft (-5.4 m), the average undrained strength of 750 psf (35.9 kPa) was selected, representing an over-consolidated crust. Below this crust, strengths were calculated based on an undrained strength ratio of 0.31, which was chosen using the strength vs. consolidation stress plot, Figure 8-13. The UU tests and ICU test with a high LL form a consistent trend. The other ICU test was from a thin silty layer with lower LL and was not considered in the trend.

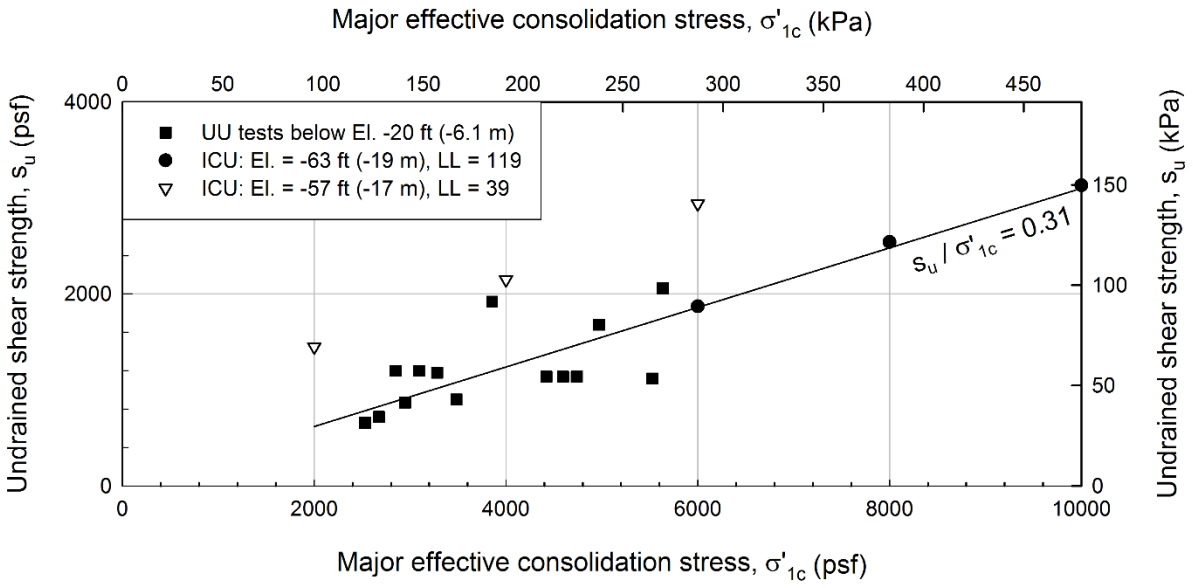

Figure 8-13. Undrained strength relationship for triaxial compression tests below El. -18 ft (-5.4 m) based on data from USACE (1984)

The silty sand layer below the backswamp deposits was modeled using ϕ' = 30° and c' = 0, based on the USACE analysis. This layer was assumed to remain drained during drawdown. A total unit weight of 122 pcf (19.2 kN/m^3) was used.

The effective consolidation stresses for the high water condition were determined using a linear elastic finite element model. Twelve soil layers were used following the USACE analysis, one for the levee fill, ten for the backswamp deposits, and one for the base of silty sand. The layers were assigned elastic moduli ranging from 100 to 500 ksf (4.8 to 24 MPa) and Poisson's ratios between 0.3 and 0.4, based on unit weight. The elements were initialized using the *Field Stress and Body Force* option in Phase with an effective horizontal to vertical stress ratio of 1.0. Pore pressures corresponding to the high water level shown in Figure 8-11 were added in a second stage. The major effective stresses, σ'_{1c}, were exported from the FE model results at each node and were used to calculate undrained strengths for the levee fill and the backswamp deposits deeper than El. -18 ft (-5.4 m).

Initially the σ'_{1c} from the FEA were used in conjunction with the trends in Figure 8-12 and Figure 8-13 to predict undrained strength. The resulting strengths were too low, and the submerged bank was unstable regardless of the water level.

The backswamp deposits near the river channel will be overconsolidated due to the erosion of overburden. The backswamp deposits were assumed to be previously consolidated to effective consolidation stresses, σ'_p, equivalent to level ground at El. 17 ft (5.2 m), which was the bottom of the levee. Based on this assumption, the amount of overconsolidation caused by the erosion of the river channel could be calculated as $OCR = \sigma'_p / \sigma'_{1c\ (FEA)}$. The over-consolidated strengths were then approximated by $s_{u\text{-}OC} = s_{u\text{-}NC} \times OCR^{0.8}$. These strengths are based on the results of triaxial compression tests and have not been adjusted for stress system effects.

The strengths calculated based on FEA and adjusted for over-consolidation were imported into the Marchand FE model, and strength reduction analysis was performed with the water level lowered. With these unadjusted shear strengths, the SRF_{crit} was greater than 1.0. The reduction factor, R_T, required to produce a critical *SRF* of 1.0 was determined to be 0.65. R_T was applied to all the soil layers except the lower silty sand. The distribution of $s_{u\text{-}ADJ}$ in the slope is shown in Figure 8-14.

The failure surface is indicated by the contours of maximum shear strain in Figure 8-15. The analysis matches the observed failure well. The predicted failure zone intersects the levee on the landside as shown by the landslide scarp in Figure 8-10. The surface of the riverbed after the failure corresponds well to the predicted failure surface. Comparing the initial and final ground surfaces, it is evident that a significant amount of the landslide must have been eroded by the

river during the flood. Erosion at the toe of the submerged riverbank may also have played a role in triggering the landslide.

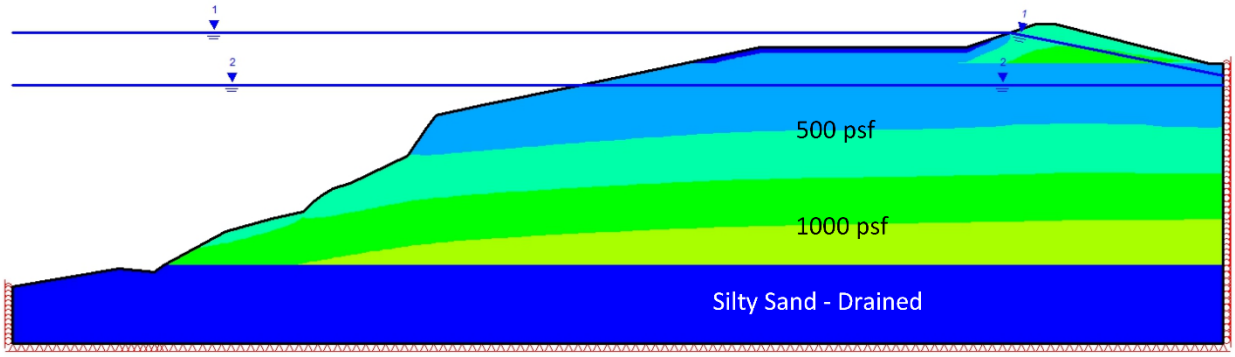

Figure 8-14. Contours of $s_{u\text{-}ADJ}$ (R_T = 0.65) considering overconsolidation due to erosion of river channel– Marchand levee

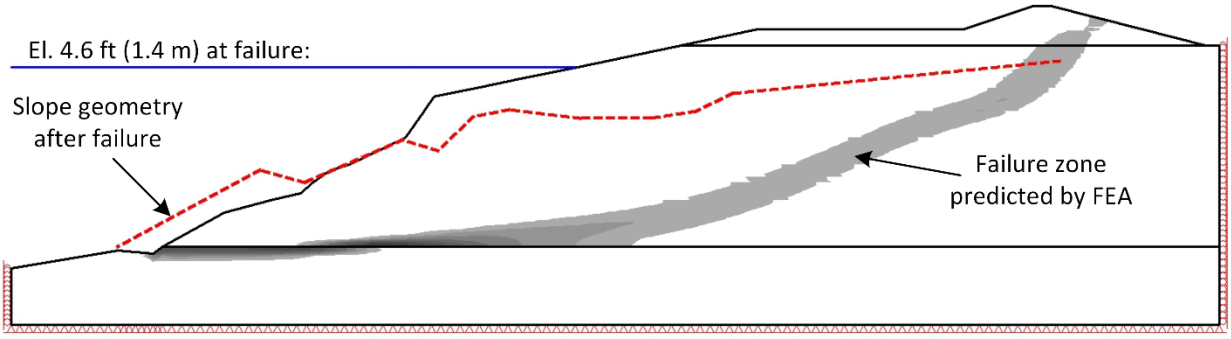

Figure 8-15. Zone of maximum shear strain at Marchand levee from strength reduction analysis – SRF_{crit} = 1.0, R_T = 0.65 (Note: Shear strains for SRF = 1.06 are plotted to clarify the predicted failure zone)

Cobbs Creek Dam (data used with permission)

The final example examines calculations for the Cobbs Creek Dam, which was in the design phase in 2013. The author was involved in a review of rapid drawdown analyses for this structure. Following that review, revisions were made to the design. The analysis presented herein is not representative of the final design for Cobbs Creek Dam.

The proposed Cobbs Creek Dam will be a zoned embankment dam about 160 ft (48.8 m) high (Schnabel Engineering 2013a). As a pumped-storage reservoir, the reservoir will experience occasional to regular drawdown as part of its typical operating procedure. A simplified cross-section of the upstream side of the dam is provided in Figure 8-16. The shell will consist primarily of silty and clayey sands from the dam site. The core will be constructed using the lower permeability on-site soils, most of which were classified as elastic silt.

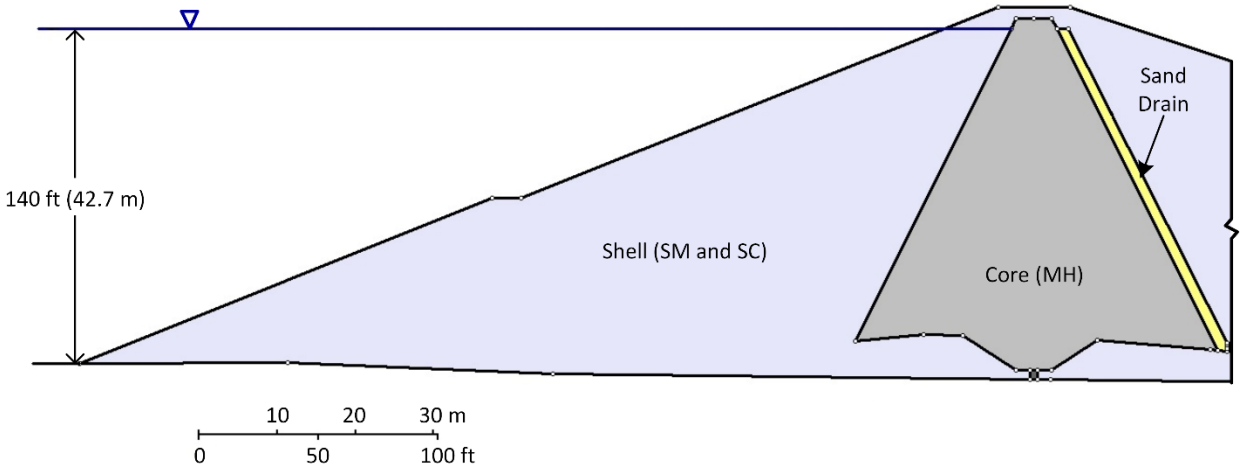

Figure 8-16. Upstream slope of Cobbs Creek Dam

Schnabel Engineering (2013b, c) characterized the undrained strength of the shell and core materials using ICU triaxial compression tests. The tests were performed on specimens compacted to 95% of the Standard Proctor maximum unit weight at water contents about 2% wet of optimum. Three specimens were compacted from each soil sample, and consolidation stresses of 1440, 2880, and 5760 psf (69, 138, and 276 m) were used. Nineteen samples of shell soil were tested for a total of 57 ICU tests on the shell soils. Nine sample of the core soil were tested, resulting in 27 ICU tests on the core soils. Power curves were determined for the mean undrained strength for both soil types. Curved $K_c = 1$ and $K_c = K_f$ envelopes were also determined from the data so that RDD could be evaluated using the Duncan et al. (1990) method.

The power curve parameters for these different interpretations of strength are summarized in Table 8-2. Characterization of the strength of the Cobbs Creek Dam soils is considered in more detail in Chapter 9.

Table 8-2. Power curve parameters for Cobbs Creek Dam soils – mean strength (10% axial strain)

	Shell (SM and SC)			Core (MH)		
	s_u vs. σ'_{1c}	$K_c = 1$	$K_c = K_f$	s_u vs. σ'_{1c}	$K_c = 1$	$K_c = K_f$
a	1.24	0.92	0.71	0.68	0.55	0.69
b	0.40	0.45	1	0.58	0.59	0.89

Limit equilibrium RDD analysis was performed using the Duncan et al. (1990) method and the power curves described in Table 8-2. The power curves were defined in the *Non-linear K_c=1* option in SLIDE by a *Discrete Function* of strengths associated with σ'_{fc} varying between 144 and 7200 psf (6.9 to 345 kPa). The DWW analysis results in a factor of safety of 1.1. The mean undrained strengths result in a SRF_{crit} of 1.56 by the Rational FEA Method described in this chapter. If an adjustment factor of 0.7 is applied, the SRF_{crit} reduces to 1.1, which is the same as the limit equilibrium factor of safety.

The maximum shear strain contours for Cobbs Creek Dam are shown in Figure 8-17 along with the DWW critical failure surface. The two methods predict approximately the same failure mechanism, a deep seated failure mostly in the shell.

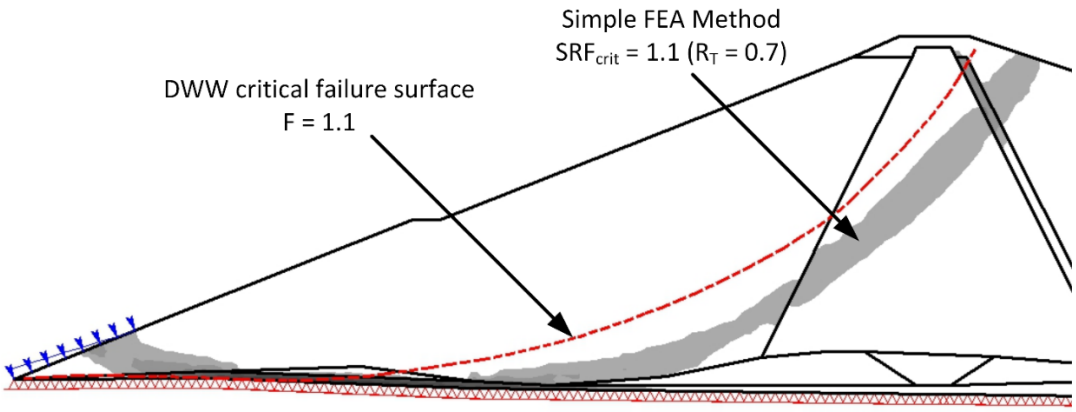

Figure 8-17. Comparison of failure surface predicted by limit equilibrium and FE RDD analyses of Cobbs Creek Dam

Summary of Examples

The four examples of the Rational FEA Method considered in the previous section are summarized in Table 8-3 and compared to the factor of safety from Duncan et al.'s (1990) method. R_T = 0.7 reduces the undrained strengths from ICU triaxial compression in a manner that produces an excellent match with the available case studies and the accepted limit equilibrium method.

Table 8-3. Summary of results for Rational FEA Method

Case Study / Failure criterion	DWW Factor of Safety	Rational FEA Method	
		Reduction Factor, R_T	SRF_{crit}
Pilarcitos / σ_{dmax}	1.05	0.72	1.0
Walter Bouldin / σ_{dmax}	1.04	0.63	1.0
Walter Bouldin / 10% axial strain	1.04	0.71	1.0
Marchand levee / σ_{dmax}	N/A	0.65	1.0
Virginia Dam / 10% axial strain	1.1	0.70	1.1

Detailed FEA Method

A refinement in the results of the FEA rapid drawdown analysis might be expected if the values of R_K and R_ρ are allowed to vary spatially, rather than using a constant value of R_T for the entire embankment. Values of R_K and R_ρ can be predicted at points throughout the embankment based on FE consolidation stress analyses. R_{PS} is assumed to have a constant value of 1.1.

Accounting for Anisotropic Consolidation

The adjustment for anisotropic consolidation, R_K, may vary throughout an embankment as different levels of shear stress are mobilized at consolidation. The variation in R_K with mobilization of shear strength at consolidation measured in the Oak Harbor ACU tests is plotted in Figure 8-18. No ACU tests were performed on Oak Harbor clay with a mobilized consolidation shear stress greater than 45% of the ICU shear strength. Constant R_K at shear stress mobilization over 50% was postulated based the behavior of natural clays presented in Chapter 3. The failure surfaces that will be considered in the following sections have average mobilized consolidation shear stress less than or equal to 50%, so the lack of data at higher shear stresses is less important. The Oak Harbor clay tests (Chapter 6) suggest that R_K may also vary due to the magnitude of the consolidation stress. This effect has not be modeled. Two options for R_K were considered:

- Constant for a given analysis, or
- Variation in R_K according to the trend labeled Model 1 in Figure 8-18

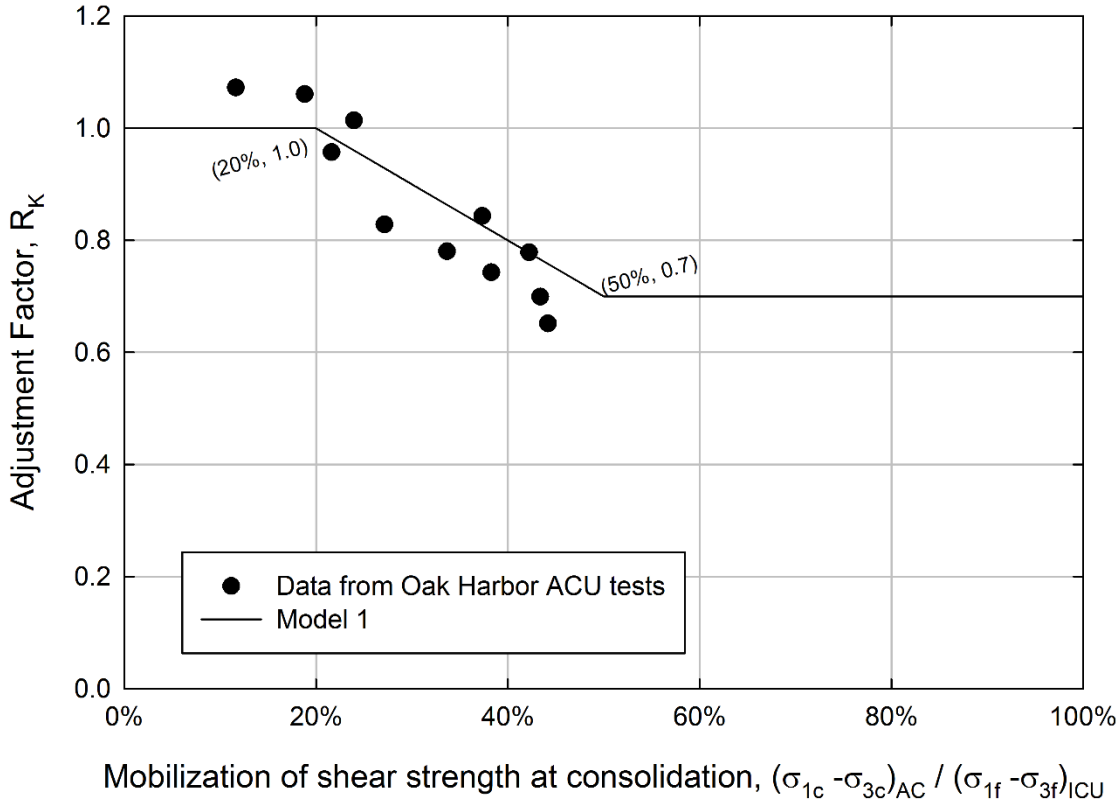

Figure 8-18. R_K Model 1 - Relationship between R_K and mobilized shear strength found for Oak Harbor clay.

Accounting for Stress Rotation

The variation in R_ρ with the stress rotation, ρ, was predicted for the Pilarcitos and Walter Bouldin soils based on their plasticity indices and the correlations developed in Chapter 3. The stress rotation was then considered in two ways: 1) based on the consolidation stress orientation predicted by non-linear FEA and 2) by measuring stress rotation from the vertical. The latter assumption implies that stress rotation effects on undrained strength are related to the soil structure rather than the consolidation stress system.

The amount of stress rotation that occurs from consolidation to failure depends on the orientation of the consolidation stress system and the inclination of the failure surface. Thus, the method of stability analysis must have the ability to consider strength that depends on the failure

surface orientation, which is not possible in Phase^2. Slide, on the other hand, can handle this condition in a piecewise manner.

Limit Equilibrium RDD Analyses with FE-based Strengths

Limit equilibrium analyses were performed in Slide using undrained strengths based on the FEA consolidation stresses. The effects of stress rotation were accounted for using Slide's Generalized Anisotropic (GA) material model, which allows different material types to be assigned to a soil layer depending on the base angle for each slice. Slide allows up to 11 nested soil types for a Generalized Anisotropic material. The effects of stress rotation can be discretized for a soil type in this way. The slice base angles were split into 10° increments for most of the range of possible angles and two larger ranges near -90 and 90° (with respect to horizontal).

The adjusted undrained strength at each interpolation point was calculated as follows:

- Calculate $s_{u\text{-}ICU}$ from σ'_{1c} and ICU power curve
- Apply R_{PS} to account for plane strain,
- Apply R_K as a constant or a function of mobilized shear stress,
- For each range of slice base angle, calculate the typical amount of stress rotation, ρ, and calculate R_ρ based on PI (Figure 3-19), and
- Multiply all the adjustment factors by $s_{u\text{-}ICU}$ for each range of slice base angles.

Each interpolation point will now have eleven associated undrained strengths, one for each range of slice base angle. These sets of strengths were then imported into Slide and assigned to the base angle ranges of the GA material. The factor of safety was calculated by spreadsheet for a few particular surfaces as a check on the limit equilibrium method. The discretized method of handling stress rotation resulted in the same factors of safety compared to the hand calculations.

The advanced FEA Method analyses are summarized for Walter Bouldin and Pilarcitos dams in Table 8-4 and Table 8-5, respectively. The combinations that give the most reasonable results are highlighted with boldface. Neither assumption regarding stress orientation results in a factor of safety close to 1 for the observed failure surfaces.

For both case studies, a factor of safety near 1.0 occurred when undrained strengths were calculated using the following two combinations:

1. R_K and R_ρ are both dependent on the consolidation stress state predicted by the FEA, or
2. R_K is constant and equal to 0.9 (mean value for normally consolidated clay – Chapter 3), and R_ρ is based on the inclination of σ'_1 at failure with respect to *vertical*.

These two case studies do not provide sufficient data to ascertain whether option 1) or 2) above is preferable. Practically speaking, the second option is more desirable because it depends on the FEA only for values of σ'_{1c}. If stress rotation can be measured from vertical, slope stability calculations for CU conditions need only consider the inclination of the failure surface to account for stress rotation.

Table 8-4. Detailed total stress RDD analyses for Walter Bouldin Dam

Effect of Anisotropic Consolidation	Type of Surface	Stress orientation assumption	Factor of Safety
Model 1 (Figure 8-18)	Circular – minimum F	**FEA**	**1.0**
		Vertical	0.83
	Non-circular – Observed failure	FEA	1.4
		Vertical	1.18
R_K = 0.8	Circular – minimum	Vertical	0.92
R_K = 0.9	Circular – minimum	FEA	1.24
	Circular – minimum	**Vertical**	**1.04**

Table 8-5. Detailed total stress RDD analyses for Pilarcitos Dam

Effect of Anisotropic Consolidation	Type of Surface	Stress orientation assumption	Factor of Safety
Model 1 (Figure 8-18)	Circular – minimum F	**FEA**	**1.05**
	Circular – Observed failure	FEA	1.70
R_K = 0.8	Non-circular – minimum F	FEA	1.06
	Circular – minimum F	Vertical	0.90
	Circular – Observed failure	Vertical	1.22
R_K = 0.9	Non-circular – minimum F	FEA	1.19
	Circular – minimum F	**Vertical**	**1.02**
	Circular – Observed failure	Vertical	1.37

It may be completely reasonable for the effects of principal stress rotation to be referenced to the vertical, or some other fixed coordinate system, rather than the stress orientation calculated by the consolidation stress analysis. Compacted soil is placed in horizontal layers similar to natural soil, which is most often horizontally layered. It is not clear in the geotechnical literature whether a change in structure or soil compressibility occurs in response to a rotation of the stress system during long-term consolidation. If these properties do not change as the consolidation stresses rotate in a slope, stress rotation effects on undrained strength should be a function of the rotation with respect to the original state, rather than the consolidation stress state. This observation may also explain why strengths measured in the TC-SR tests on compacted clay were not significantly different from those determined by conventional triaxial compression tests, despite experiencing a 90° stress rotation.

Conclusions

The Rational FEA Method is an easy-to-use means of evaluating embankment stability following rapid drawdown. It produces similar results to the Duncan et al. (1990) method while using a more straightforward interpretation of undrained strength. The Rational FEA Method is summarized for quick reference in Figure 8-3.

Back calculation using RDD failures indicates that an adjustment factor, R_T, of 0.7 should be used to reduce ICU triaxial compression strengths to those appropriate for RDD. The Cobbs Creek Dam example also produced an excellent match with Duncan et al. (1990) with $R_T = 0.7$. The effect of uncertainty in the value of R_T will be considered in the following chapter. The Rational FEA Method should be used in parallel with the Duncan et al. (1990) method until additional experience is gained regarding the relationship between the two analyses for a variety of design conditions.

The Pilarcitos and Walter Bouldin case histories were examined with a more detailed FEA undrained strength rapid drawdown method, which considers the adjustment factors R_K, R_{PS}, and R_ρ separately. R_K and R_ρ were allowed to vary spatially throughout the embankment based on the consolidation stress distribution. In order for R_K and R_ρ to vary spatially, the relationships between these factors, the consolidation stress state, and stress rotation must be defined. These relationships were not available for the case studies and were estimated based on test results on other soils. This type of advanced analysis is not justified unless the variations in R_K and R_ρ have been defined by an extensive program of laboratory testing that may not be practical for routine evaluations of RDD

The Detailed FEA Method was also performed with $R_K = 0.9$, $R_{PS} = 1.1$, and R_ρ based on ρ measured from *vertical*. This procedure produced reasonable factors of safety for both Pilarcitos

and Walter Bouldin Dams. If it is desirable to consider the effects of the various adjustment factors separately, this method is recommended. Like the Rational FEA Method, it relies on the FE consolidation stress analysis only to obtain values of σ'_{1c}..

9. Probabilistic Methods in RDD Analysis

Reliability analyses are becoming more commonplace in geotechnical engineering as a means of assessing the uncertainty associated with a calculated value, such as factor of safety or settlement. Reliability analyses are especially useful to help the engineer decide what factor of safety is appropriate for a particular case, such as rapid drawdown.

Most methods for evaluating reliability require estimates of both the mean, μ, and the standard deviation, σ, for each of the random variables. Variability is often expressed in terms of the coefficient of variation, $COV = \sigma / \mu$. Sleep and Duncan (2014) provide a rough guide for assessing the *COV* based on laboratory data and a summary of typical *COV* values for various parameters. For the purposes of rapid drawdown analysis, the effective stress friction angle, ϕ', and undrained strength ratio, *USR*, are particularly important. In natural clays, the *COV* for ϕ' is often in the range of 2 to 13%, and the *COV* for *USR* is about 5 to 15% (Sleep and Duncan 2014). These values are presented for comparison with the variability in the undrained strength of compacted clays, which will be considered in this chapter.

Reliability analyses use the concept of a performance function, which for rapid drawdown is the relationship between the factor of safety (or critical strength reduction factor) and the random variables. Often the performance function is formulated such that it equals zero at the boundary between satisfactory ($F>1$) and unsatisfactory performance (failure or $F<1$). The likelihood of unsatisfactory performance is often expressed in terms of the reliability index, β, which can be thought of as the number of standard deviations that separate the mean values of the random variables from a critical point on the performance function. The probability that the factor of safety is less than 1.0, $P_{F<1}$, can be determined from β. $P_{F<1}$ depends on the magnitude of the

factor of safety calculated using the most likely (or mean) values, F_{MLV}, and on the standard deviations of the random variables.

Four methods will be used in this chapter to evaluate β and/or $P_{F<1}$:

- Taylor series approximation (e.g. Sleep and Duncan 2014) – First order second moment (FOSM) method that approximates the performance function at the mean values of the variables using a Taylor series expansion. The factor of safety (or other appropriate parameter) is assumed to vary linearly at its mean value, allowing the partial derivatives of the performance function and the variance to be easily estimated. In this case, the performance function does not need to be known explicitly, rather the factor of safety is recalculated while varying each variable above and below the mean by one standard deviation.
- Hasofer-Lind (1974) method – First order reliability method (FORM) that requires the performance function to be explicitly defined in terms of the random variables. This method finds the "design point" on the performance function where the value of β is the same for each the random variable, and β is minimized. Low (1996) noted that combinations of the random variables at any multiple of σ about the mean trace a hyper-ellipse in the original variable space. The ellipse will be skewed if any of the variables are correlated. The dimensions of this ellipse can be varied numerically, keeping the aspect ratio constant until it contacts the performance function. The scaling ratio is equal to the Hasofer-Lind reliability index, and the minimum value of β can be obtained using a spreadsheet. The point at which the expanded ellipse contacts the performance function is referred to as the "design point."

- Simplified Hasofer-Lind method – Filz and Navin (2006) presented a numerical method for determining the Hasofer-Lind β, which does not require an explicit performance function, making it better suited to complex problems like slope stability. Their method determines approximate values for β and the design point. The gradient of the performance function at this point is found by performing additional analyses at slightly different values of the random variables. The value of β is refined using further analyses and the gradient of the performance function.
- Monte Carlo method – Randomly generated realizations of the variables are created based on their probability distributions. The performance function is then used to evaluate whether or not the factor of safety is less than 1. $P_{F<1}$ is calculated directly by comparing the number of instances where F is less than 1 to the number of realizations. A large number of realizations is required to estimate $P_{F<1}$ accurately.

The limit equilibrium and finite element analyses that are used to calculate stability for the performance function assume that the relationship between strength and stress does not vary spatially within a soil layer. In the field, variations in undrained strength tend to be averaged along a failure surface, reducing the effect of the variability of strength on the factor of safety. The effect of this averaging on $P_{F<1}$ will be considered.

Reliability analyses calculate $P_{F<1}$, assuming the rapid drawdown has occurred. The probability of the occurrence of rapid drawdown loading, P_{RDD}, is another essential element that must be included in a comprehensive assessment of the likelihood of rapid drawdown failure.

Quantifying Uncertainty in Strength for RDD

The most important factor influencing slope stability is the soil strength. The variation in strength with confining stress is often expressed using two or more parameters, such as c' and ϕ'

from the Mohr Coulomb failure criterion. However, when representing a data set, it is simpler and often just as appropriate to fix one of the parameters, or the relationship between the two parameters. If the uncertainty in strength, either drained or undrained, can be expressed in terms of a single random variable, the reliability analysis will be simplified.

An example of this concept is given in Figure 9-1 for a hypothetical set of drained strength data. In Figure 9-1(a), *c'* and ϕ' are both considered to be random variables. In this case, the correlation between the two variables would have to be considered in order to perform an accurate reliability analysis. In Figure 9-1(b), the attraction, $a' = c' / \tan \phi'$, has been fixed as suggested by Janbu et al. (1977). This allows the data to be characterized by a single random variable, ϕ'. The value of *c'* would vary as a function of ϕ' rather than as a separate random variable. The range and *COV* of ϕ' as defined in Figure 9-1(b) will be higher than that for ϕ' in Figure 9-1(a) because all of the uncertainty is accounted for in a single parameter.

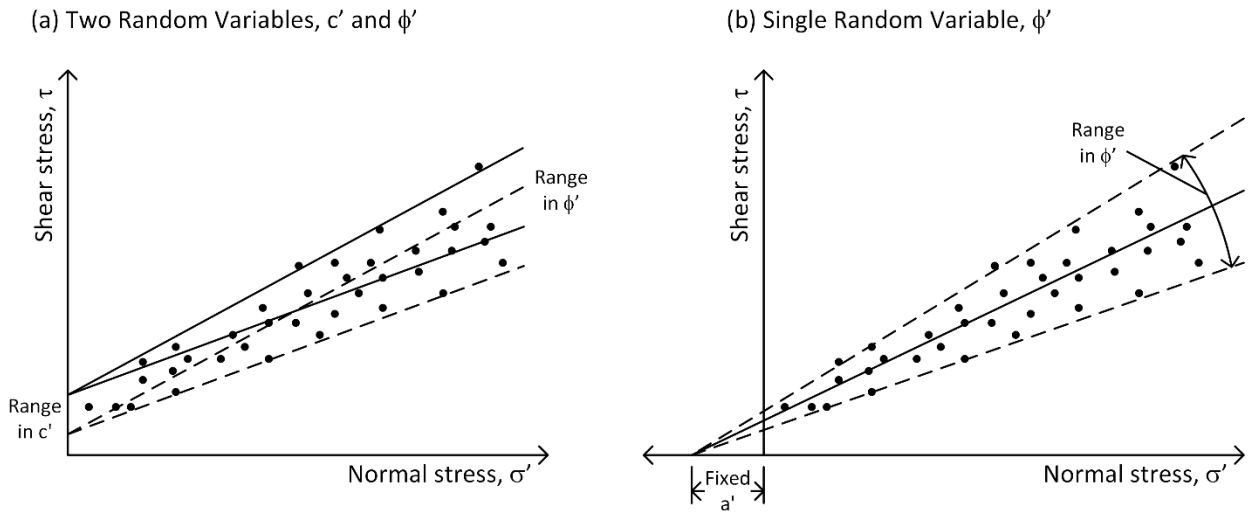

Figure 9-1. Two methods of quantifying the variability in the same set of data using (a) two random variables or (b) a single random variable.

For rapid drawdown, both drained and undrained strength must be considered. Drained strength can affect the consolidation stress state and is used by the DWW method for the K_f

envelope and Stage 3 strengths. Undrained strength is used by both the FE and DWW methods of analyzing RDD. Both drained and undrained strength will be represented by power curves with parameters, *a* and *b*, in this chapter. The power curve parameters are found through transformation to non-dimensional space, and a method for determining these parameters is found in Appendix D.

Review of drained and undrained strength data for compacted Oak Harbor clay and the Cobbs Creek Dam soils (Schnabel 2013a, b, c) suggests that a band of constant slope tends to form in the transformed space as shown in Figure 9-2. The constant slope of the lines is equal to the power curve parameter *b*. The y-intercept of the mean strength line, λ, is the mean value of the natural logarithm of the parameter *a*.

Upper and lower bounds have been drawn parallel to the mean line in Figure 9-2. The bounds were positioned to include about 95% of the data points, which implies that they correspond to two standard deviations above and below the mean if *ln(a)* is normally distributed. The bounds are equally spaced about the mean, corresponding to a normal distribution for *ln(a)* with mean, λ_a, and standard deviation, ζ_a. The parameter *a* is then lognormally distributed with mean, μ_a, and standard deviation, σ_a, which can be calculated from (Baecher and Christian 2003)

$$\mu_a = \exp\left(\lambda_a + 0.5\zeta_a^{\,2}\right) \tag{9-1}$$

and

$$\sigma_a = \sqrt{\mu_a^2\left(\exp\left(\zeta_a^2\right)-1\right)} \tag{9-2}.$$

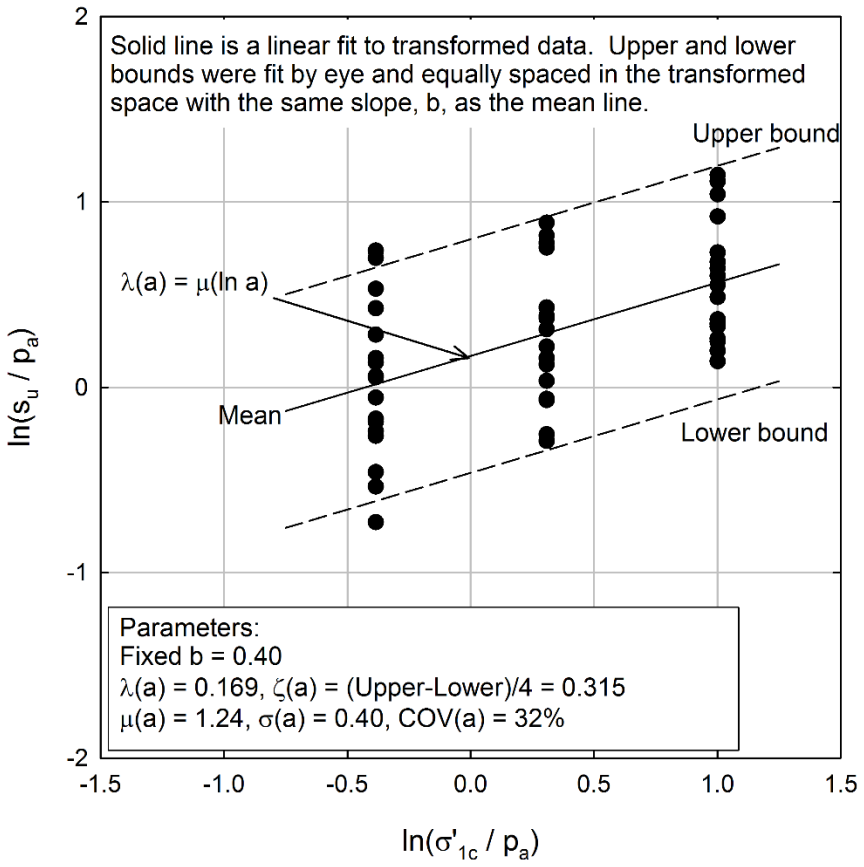

Figure 9-2. Transformed undrained strength data for Cobbs Creek Dam shell material

From μ_a, σ_a, and b, the relationship between undrained strength and the major effective consolidation stress, σ'_{1c}, can be determined at any probabilistic position with respect to the mean. For example, the interpretation in Figure 9-2 results in the undrained strength relationships shown in Figure 9-3. This method results in a simple but useful means of characterizing variability in the undrained strengths.

The method just described considers the relationship between s_u and σ'_{1c}. It can also be used for drained strength by transforming the effective stresses on the failure plane at failure, σ'_{ff} and τ_{ff}. Similarly, the $K_c = 1$ envelope used by the DWW method for rapid drawdown can be represented by power curve by transforming the stresses, σ'_{fc} and τ_{ff}.

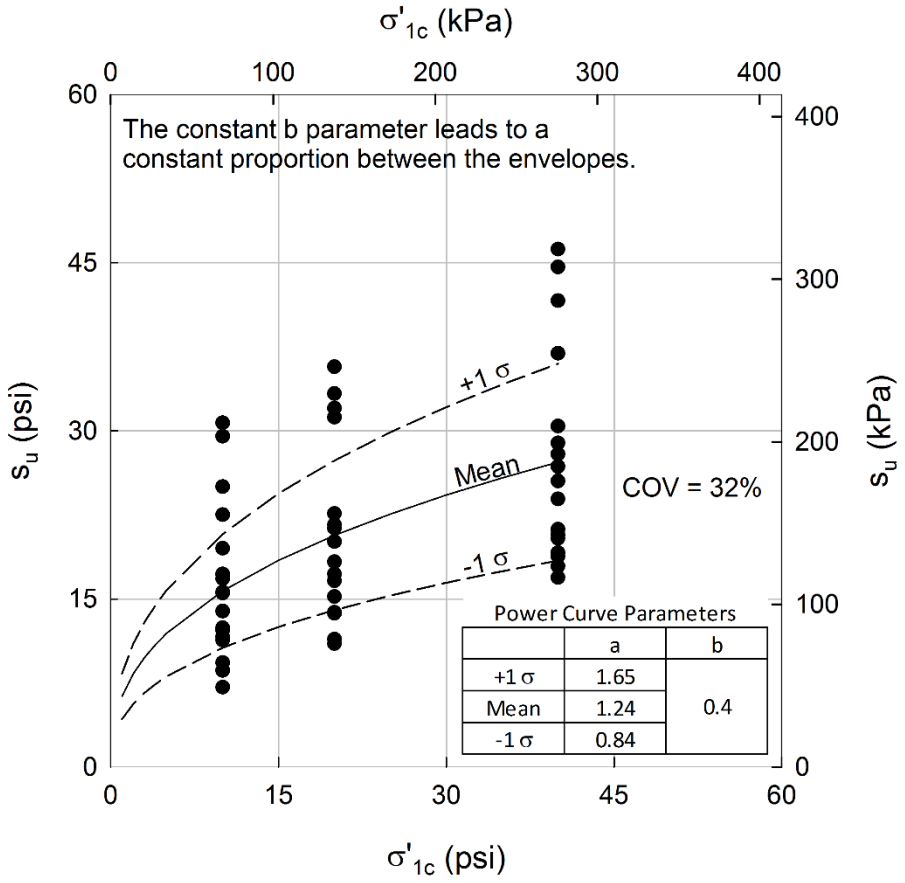

Figure 9-3. Undrained strength relationships for Cobbs Creek Dam shell material.

The parameter *b* controls the shape of the power curve and for shear strength should not exceed 1.0. If *b* is equal to 1.0, the effective stress power curve has a constant slope and passes through the origin, which is equivalent to a constant ϕ' with $c' = 0$. For undrained strengths, *b* equal to 1.0 implies a constant undrained strength ratio, as often occurs in normally consolidated clay.

Oak Harbor Clay

The transformed undrained strengths from ICU triaxial compression tests on Oak Harbor clay are plotted against consolidation stress in Figure 9-4. The mean power curve parameters match those determined in Chapter 6; however the variability is described somewhat differently because the standard deviation was estimated in a different manner.

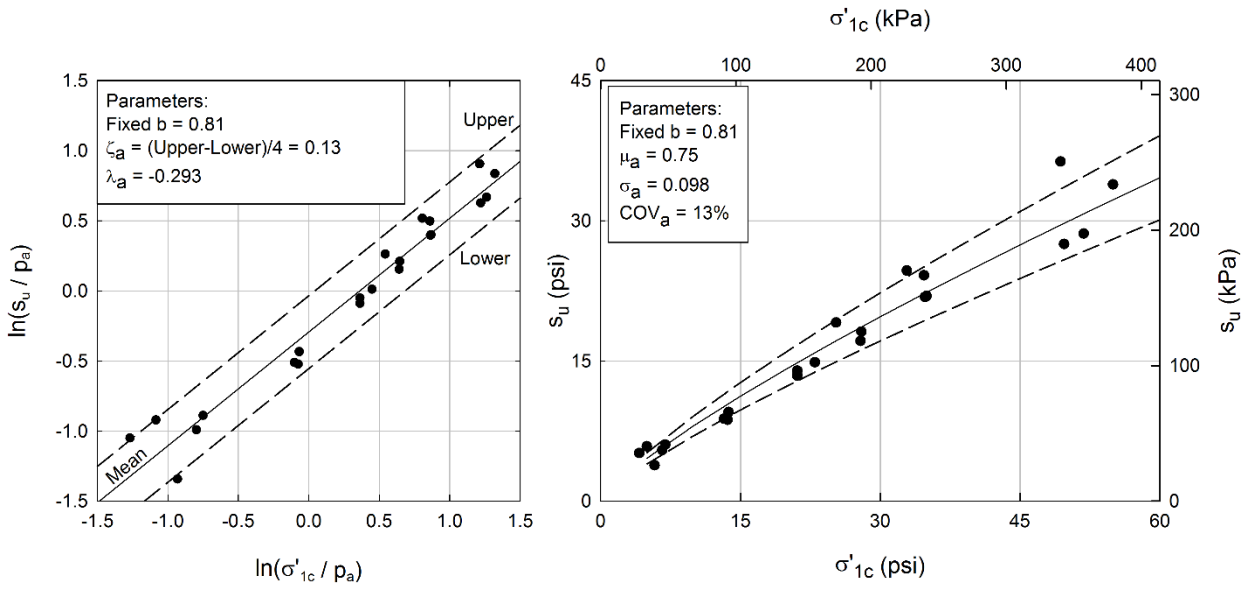

Figure 9-4. Undrained strength relationships for ICU tests on Oak Harbor clay

The Oak Harbor specimens were compacted from a well-mixed, uniform sample and represent little material variability. The variability in undrained strength comes from the testing procedure and, more importantly, the variation in relative compaction. The relative compaction in these tests ranged from 98 to 101% of the Standard Proctor maximum dry unit weight, which means the range of dry unit weight was 3.3 pcf (0.52 kN/m^3). Turnbull et al. (1966) found that well-controlled fills have a standard deviation of about 2 to 2.5 pcf (0.31 to 0.39 kN/m^3). Assuming that range of unit weights is equal to three σ above and below the mean, the range of compacted unit weight expected based on Turnbull et al.'s data is (2)(3)(2 pcf) = 12 pcf (1.89 kN/m^3) to (2)(3)(2.5 pcf) = 15 pcf (2.34 kN/m^3). The range of dry unit weight in the Oak Harbor tests is much lower, so the COV of 13% obtained for the undrained strength parameter, *a*, may be lower than would be expected for most compacted clay fills. Turnbull et al. (1966) also found that compacted water contents tended to vary from 6% above to 6% below optimum. This range is also much greater than the range in water content of 2% used in the Oak Harbor tests, which would likely lead to additional variability in undrained strength. The range of compacted dry

unit weight and water content in engineered fill will also be influenced significantly by factors such as the type of compaction specification and the moisture content of the borrow area.

Cobbs Creek Dam

Shell (SM and SC)

The Cobbs Creek Dam shell materials consisted mostly of silty and clayey sands. The maximum dry unit weight of the soils (ASTM D698) ranged from about 85 to 125 pcf (13.3 to 19.6 kN/m^3). The test specimens were compacted to about 95% relative compaction (ASTM D698). Non-linear DWW envelopes for the shell are given in Figure 9-5 and Figure 9-6. For $K_f = 1$, the parameter b was 1, indicating linear effective stress envelopes with $c' = 0$. A friction angle of 35.2° corresponds to $\mu_a = 0.705$.

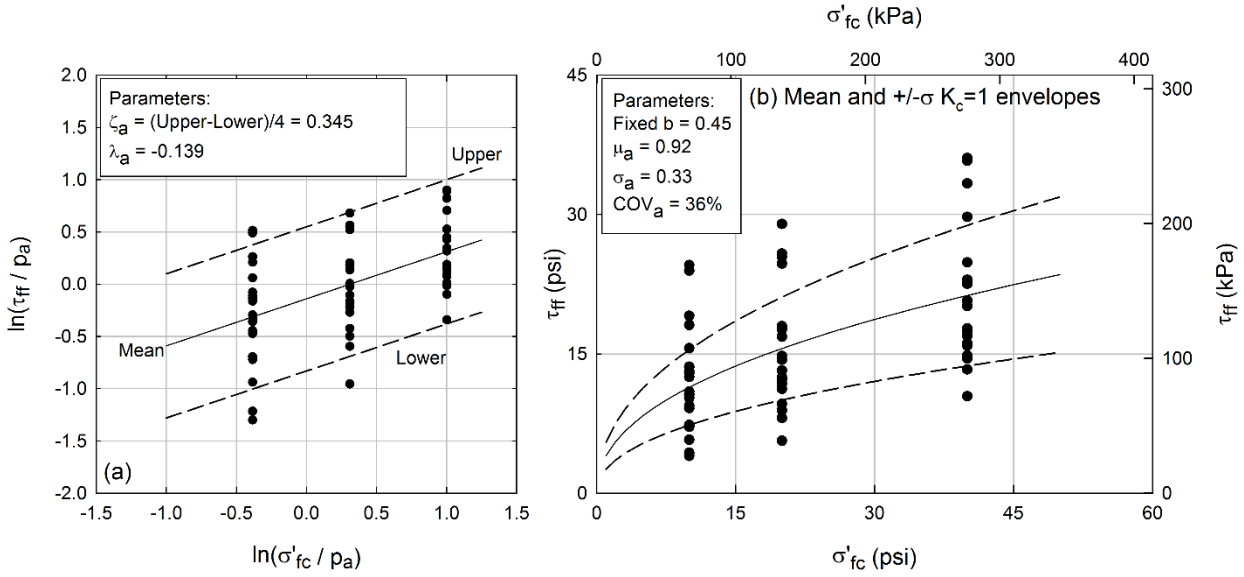

Figure 9-5. $K_c = 1$ envelopes for Cobbs Creek Dam shell soils – (a) transformed variables, (b) shear strength vs. effective consolidation stress

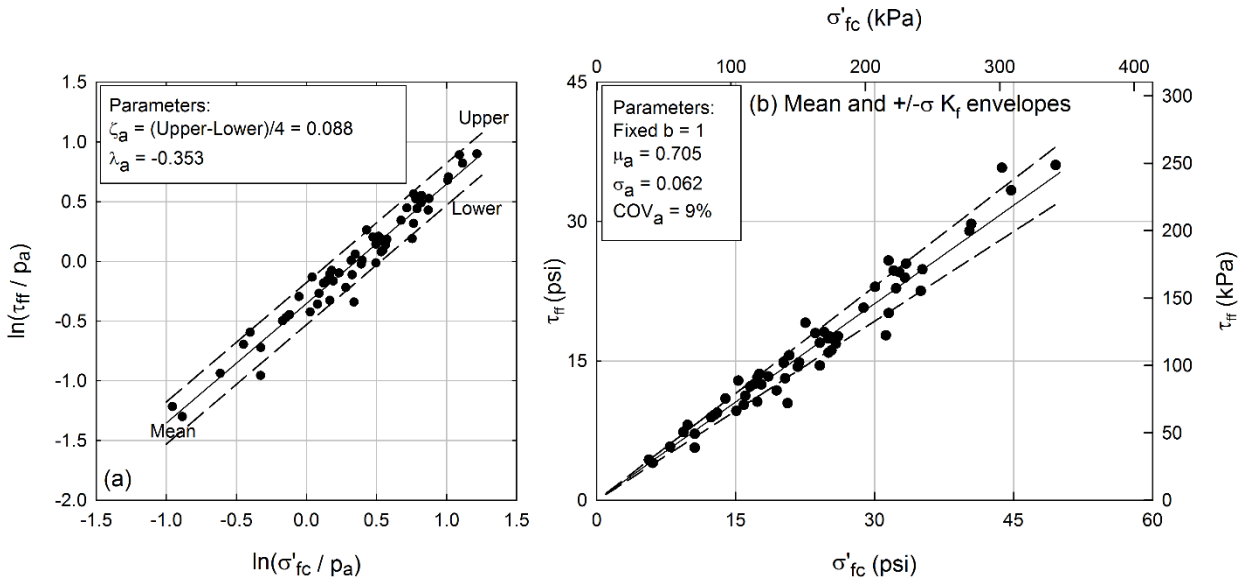

Figure 9-6. $K_c = K_f$ envelopes for Cobbs Creek Dam shell soils– (a) transformed variables, (b) shear strength vs. effective consolidation stress

Core (MH, CL, and CH)

The Cobbs Creek Dam core materials consisted of a mix of elastic silts, lean clays, and fat clays. The maximum dry unit weights based on ASTM D698 ranged from 85 to 111 pcf (13.3 17.4 kN/m^3). The test specimens were prepared at 95% relative compaction (D698). Non-linear DWW envelopes for the core are given in Figure 9-7 and Figure 9-8.

Figure 9-9 presents the results of the analysis of undrained strength, s_u, for the core soils, resulting in a *COV* of 15%. Although both represent undrained strength, the *COV* for s_u and the *COV* for the $K_c = 1$ envelope are slightly different due to the differences in how the strengths were interpreted.

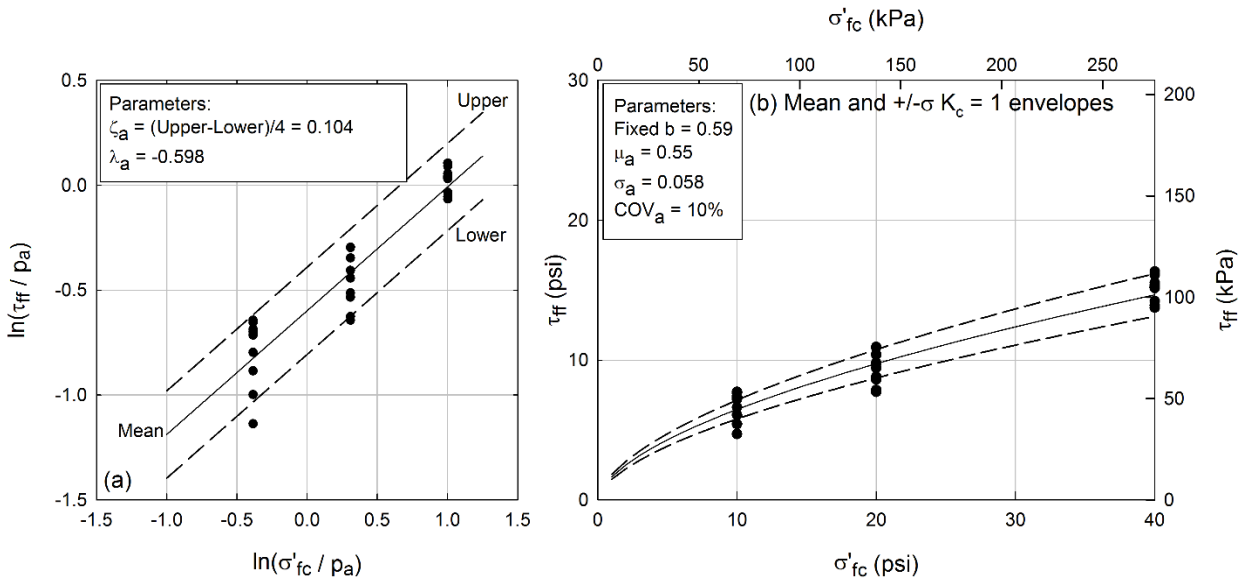

Figure 9-7. $K_c = 1$ envelopes for Cobbs Creek Dam core soils– (a) transformed variables, (b) shear strength vs. effective consolidation stress

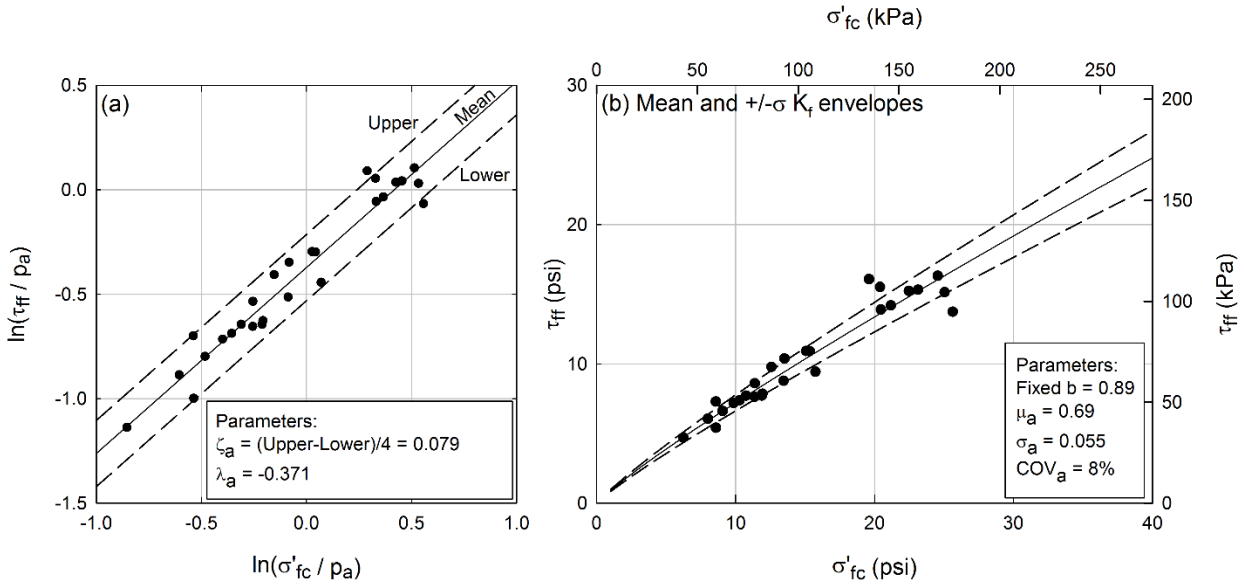

Figure 9-8. $K_c = K_f$ envelopes for Cobbs Creek Dam core soils– (a) transformed variables, (b) shear strength vs. effective consolidation stress

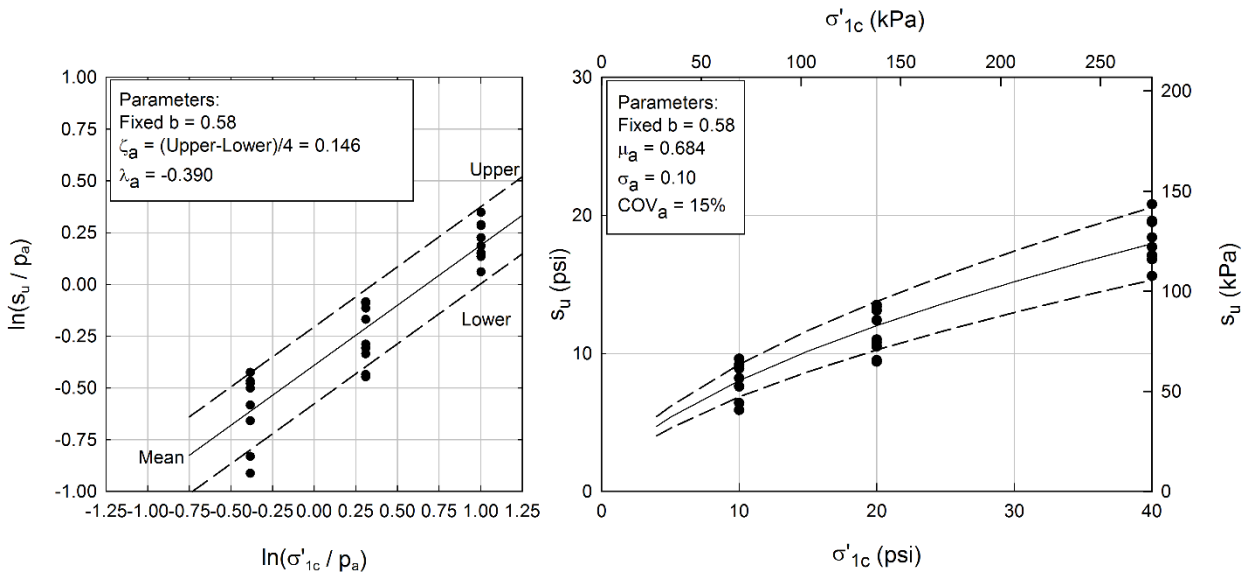

Figure 9-9. Undrained strength variation for Cobbs Creek Dam core soils– (a) transformed variables, (b) shear strength vs. effective consolidation stress

The following analyses of Cobbs Creek Dam assume statistical independence between the drained and undrained power curve parameters for a particular soil, and between the two soil types.

Application to the Limit Equilibrium (DWW) Method

Taylor Series Approximation

Cobbs Creek Dam was analyzed using the DWW method (Duncan et al. 1990) and the non-linear strength envelopes given in Figure 9-5 to Figure 9-8. The factor of safety for the mean or most likely values (MLV) was calculated to be 1.097. The critical failure surface shown in Figure 9-10 is deep-seated and non-circular, passing just above the base of the embankment and through the upper part of the core. In order to assess the reliability of this factor of safety, the Taylor series approximation method presented by Sleep and Duncan (2014) was used. The *a* parameters for each of the four envelopes were varied systematically up and down by one

standard deviation, and the factor of safety was recalculated using the DWW method. The results of these eight stability analyses are summarized in Table 9-1.

The *COV* for the factor of safety was 19%, which corresponds to a reliability index of 0.39, assuming the factor of safety is lognormally distributed. The variation in F is caused mostly by the variability of the shell since most of the failure surface is within the shell. The corresponding probability that $F < 1$ is 35%, which represents uncertainty solely due to the strength parameters.

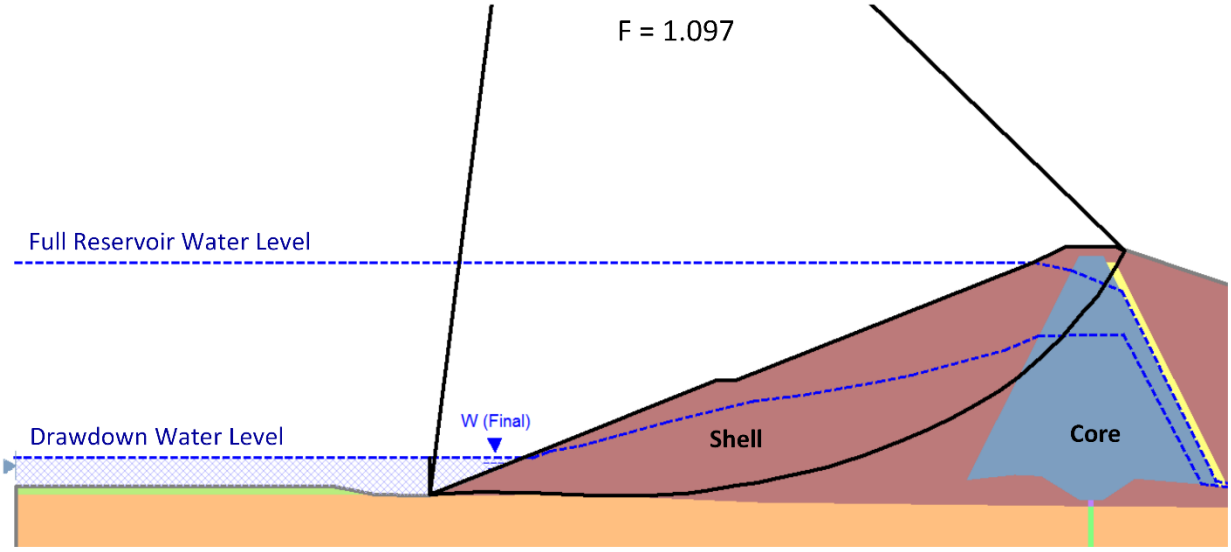

Figure 9-10. DWW critical failure surface for Cobbs Creek Dam

The *COV* for the factor of safety was much lower than the *COV* for the shell $K_c=1$ envelope, which has the most influence on the factor of safety. In order to investigate the source of this lower value for COV_F, the limit equilibrium consolidation stresses were determined along the critical failure surface from the MLV case. The DWW undrained shear strengths were calculated by interpolation for the mean $K_c = 1$ envelope and the +/- one standard deviation envelopes (Cases 1 and 2 in Table 9-1). The envelopes and interpolated strengths are shown in Figure 9-11. It is clear that the interpolation process reduces the variation in undrained strength. In this case, the $K_c=1$ envelopes have a *COV* of 36% but the interpolated strengths only vary up

and down from the mean by 24%. This explains why the *COV* for the DWW factor of safety is significantly lower than that for the shell $K_c=1$ envelope.

Table 9-1. Reliability analysis of the DWW method for Cobbs Creek Dam using Taylor series approximation (boldface indicates parameter varied for each case)

Case	Strength Parameters								Result		
	Shell				Core				F	ΔF	$\left(\frac{\Delta F}{2}\right)^2$
	$K_c = 1$		$K_c = K_f$		$K_c = 1$		$K_c = K_f$				
	a	b	a	b	a	b	a	b			
MLV	0.92	0.45	0.705	1.0	0.55	0.59	0.69	0.89	**1.097**	---	---
COV_a	36%	---	9%	---	10%	---	8%	---			
1	**1.25**	0.45	0.705	1.0	0.55	0.59	0.69	0.89	1.322	0.415	4.3×10^{-2}
2	**0.60**		0.705		0.55		0.69		0.907		
3	0.92		**0.77**		0.55		0.69		1.129	0.069	1.2×10^{-3}
4	0.92		**0.64**		0.55		0.69		1.060		
5	0.92		0.705		**0.61**		0.69		1.105	0.015	5.6×10^{-5}
6	0.92		0.705		**0.50**		0.69		1.090		
7	0.92		0.705		0.55		**0.75**		1.102	0.000	0
8	0.92		0.705		0.55		**0.64**		1.102		

$\sigma_{FS} = (\Sigma(\Delta F/2)^2)^{0.5} =$ 0.21

$COV_F =$ 19%

Reliability Index, $\beta =$ 0.39

Calculated $P(F < 1) =$ **35%**

As shown in Figure 9-11, the undrained strengths used in the DWW calculations do not have the same variability as the measured undrained strengths, as represented by the $K_c=1$ envelopes. This result of the interpolation process will occur any time that K_c is greater than 1.0 for a particular trial surface. Reduced variability in the undrained strength leads to less uncertainty in the factor of safety and a lower $P_{F<1}$.

Chapter 5 evaluated total stress limit equilibrium procedures based on Lowe and Karafiath (1960a, b). The use of τ_{fc} from limit equilibrium and the assumption of no principal stress rotation both lead to significant differences in K_c compared to finite element analysis. The linear interpolation procedure also adds an element of empiricism by reducing the undrained strength more than that caused by anisotropic consolidation. The DWW procedure itself likely adds an unknown amount of systemic uncertainty to the analysis because of these inherent assumptions. There is no clear way to assess the effect of this systemic uncertainty on the results. At the same time, the linear interpolation portion of the DWW procedure systematically reduces variability in a way that is not explicitly evident to the analyst.

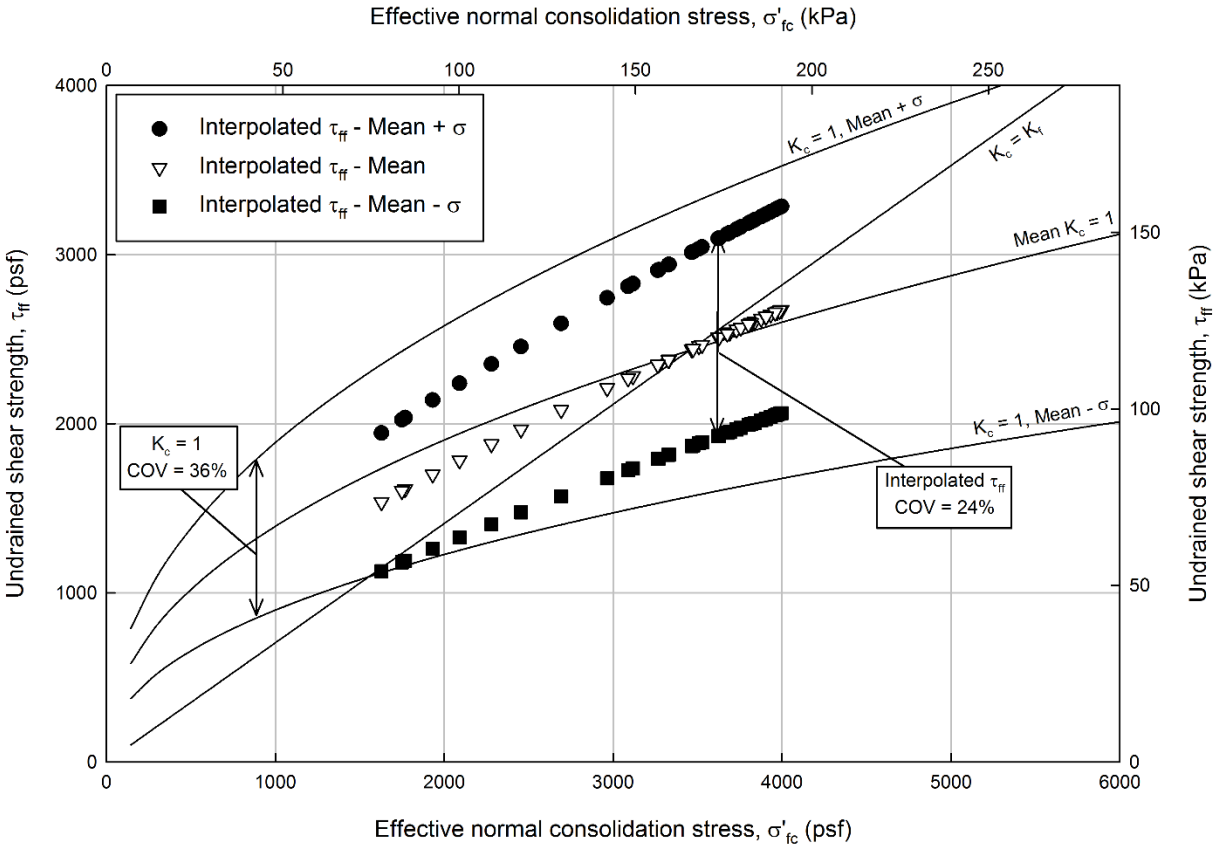

Figure 9-11. Variation in the interpolated undrained strength caused by variation in the K_c=1 envelope for the Cobbs Creek shell soil.

Application to the Rational FEA method

Taylor Series Approximation

The stability of Cobbs Creek Dam was also analyzed using the FEA based method presented in Chapter 8. Using the ICU strength relationships in Figure 9-4 and Figure 9-9 with no reduction factor, the critical *SRF* was 1.56 for Cobbs Creek Dam. Applying the reduction, R_T = 0.7, the *SRF* decreases to 1.1, which is essentially the same as the DWW factor of safety.

The effective stress friction angle for the shell, the *a* parameter of the shell, the *a* parameter of the core, and the reduction factor, R_T, were considered random variables in the Taylor series approximation provided in Table 9-2. A *COV* of 15% was assumed for the adjustment factor, R_T.

For the FE-based RDD method, the overall *COV* of the strength reduction factor was 29%, which is similar to the *COV* for the shell undrained strength. Since R_T is considered to be a random variable, the analysis attempts to assess the systemic variability of the RDD analysis method, not just that due to the strength parameters.

If the uncertainty due to the method is removed from the analysis (i.e., R_T is deterministic), the *COV* of the factor of safety reduces slightly to 25%. This corresponds to $\beta = 0.27$ and $P_{F<1}$ of 39%, assuming a lognormal distribution of *F*. Ignoring the method variability, the reliability index calculated for the FE method is closer to that calculated in Table 9-1 for the DWW method.

Table 9-2. Reliability analysis of the FE rapid drawdown method for Cobbs Creek Dam using Taylor series approximation (boldface indicates the parameter varied for each case)

Case	Strength Parameters							Results		
	Shell			Core			R_T	SRF_{crit}	ΔSRF	$\left(\frac{\Delta SRF}{2}\right)^2$
	ϕ' (deg)	a	b	ϕ' (deg)	a	b				
MLV	35.2	1.24	0.4	34.4	0.68	0.58	0.70	**1.10**	---	---
COV_a	9%	32%	---	---	10%	---	15%			
1	**37.5**	1.24	0.4	34.4	0.68	0.58	0.70	1.10	0	0
2	**32.7**	1.24			0.68		0.70	1.10		
3	35.2	**1.65**			0.68		0.70	1.36	0.54	7.3×10^{-2}
4	35.2	**0.84**			0.68		0.70	0.82		
5	35.2	1.24			**0.78**		0.70	1.14	0.08	1.6×10^{-3}
6	35.2	1.24			**0.58**		0.70	1.06		
7	35.2	1.24			0.68		**0.81**	1.26	0.32	2.6×10^{-2}
8	35.2	1.24			0.68		**0.60**	0.94		

$\sigma_{FS} = (\Sigma(\Delta SRF/2)^2)^{0.5} =$ 0.32

$COV_{SRF} =$ 29%

Reliability Index, $\beta =$ 0.20

Calculated $P(SRF_{crit} < 1) =$ **42%**

Hasofer-Lind Approach with Analytic Performance Function

The Hasofer-Lind (1974) method for determining the reliability index requires an explicit definition of the performance function, $g(x_i)$,or at least a set of points with $g(x_i) = 0$ from which the function can be interpolated. The performance function was approximated for the finite element RDD analysis of Cobbs Creek Dam by repeating the analysis with different combinations of the parameters for the shell and core soils, a_{shell} and a_{core}. The value of a was varied between 0.25 and 2.5 for the shell and from 0.25 to 1 for the core. The critical *SRF* was found for each case. The reduction factor that would cause the *SRF* to be equal to 1.0 was shown in Chapter 8 to be equal to $1 / SRF_{crit}$.

The trend in $1 / SRF_{crit}$ with a_{shell} is plotted in Figure 9-12. In general, power curves with a negative exponent fit the relationship between $1 / SRF_{crit}$ and a_{shell} very well. When a_{shell} was less than a_{core}, the failure zone bypassed the core and deviated from the overall trend. These points were ignored when developing curve fit parameters for each value of a_{core}.

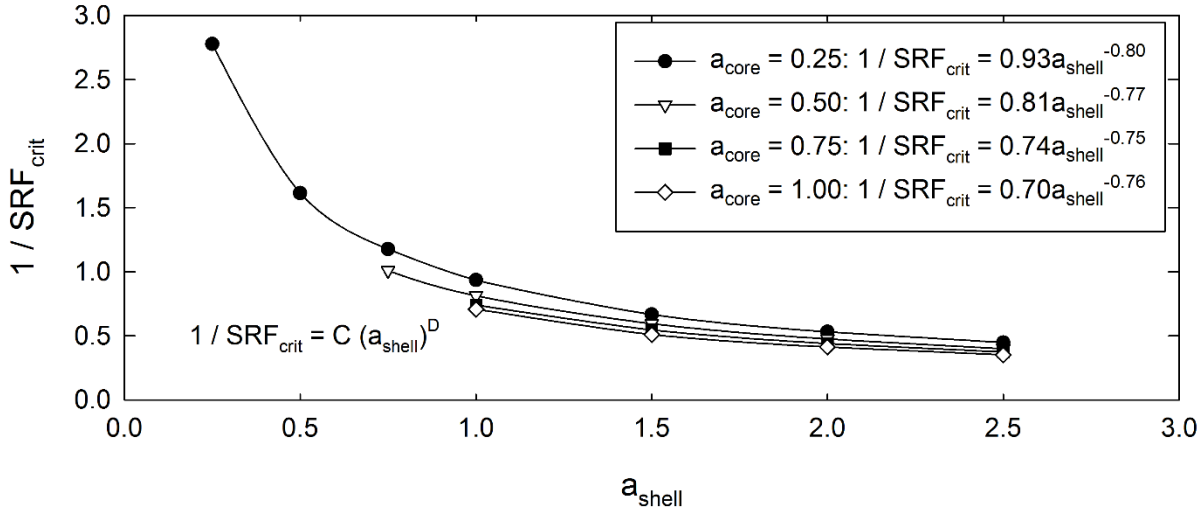

Figure 9-12. Performance function curves for various values of a_{core}

As shown in Figure 9-12, the performance function for a fixed value of a_{core} can be expressed as

$$1/SRF_{crit} = C\left(a_{shell}\right)^{D} \tag{9-3}$$

The particular values of C and D are given in Figure 9-12. These were plotted against the corresponding values of a_{core} in Figure 9-13. The values for C and D were related to a_{core} such that,

$$C = C_0\left(a_{core}\right)^{C_1} \tag{9-4}$$

and

$$D = D_0 + D_1 a_{core} + D_2 \left(a_{core}\right)^2 \tag{9-5}$$

where:

C_0, C_1, D_0, D_1, and D_2 = empirical parameters specific to the Cobbs Creek geometry.

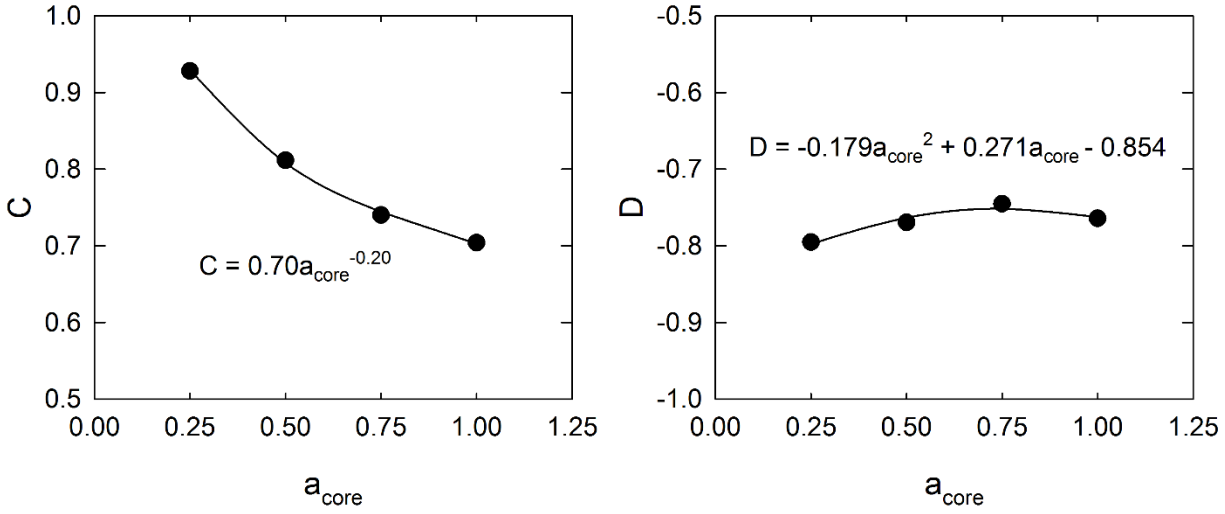

Figure 9-13. Variation of performance function parameters *C* and *D* with a_{core}

Eqn. (3) to (5) were combined to define $g(x_i)$ for the Cobbs Creek Dam with constant *b* parameters for the core and shell, and a constant drained friction angle for the shell,

$$g(a_{core}, a_{shell}, R_T) = R_T - C_0 \left(a_{core}\right)^{C_1} \left(a_{shell}\right)^{D_0 + D_1(a_{core}) + D_2(a_{core})^2} \tag{9-6}$$

The performance function is positive when the critical *SRF* is greater than 1 and negative when the critical *SRF* is less than 1. The performance function should not be used for cases with a_{core} and a_{shell} outside the ranges shown in Figure 9-12 and Figure 9-13.

Eqn. (9-6) was programmed into a spreadsheet following the method described by Low (1996). Table 9-3 summarizes the application of the Hasofer-Lind approach to finite element based RDD analysis. The variables are lognormally distributed, so it was necessary to transform the mean and standard deviation of each variable to equivalent normally distributed variables. The statistical parameters for each variable are provided in the first five rows of Table 9-3.

Table 9-3. Calculation of the RDD reliability index and probability of failure using the Hasofer-Lind method for a performance function based on FEA

		a_{shell}	a_{core}	R_T
Statistical parameters	Mean of variable, $\mu(x_i)$	1.24	0.68	0.70
	COV of variable	0.32	0.15	0.15
	Standard deviation of variable, $\sigma(x_i)$	0.398	0.103	0.105
	Mean of $ln(x_i)$, λ	0.170	-0.391	-0.368
	Standard deviation of $ln(x_i)$, ζ	0.312	0.149	0.149
Hasofer-Lind	Design point variable values, x_i	1.148	0.675	0.686
	Transformed variables, $ln\ x_i$	0.138	-0.393	-0.377
	$\beta_i^2 = ((ln(x_i)-\lambda)/\zeta)^2$	1.05×10^{-2}	1.68×10^{-4}	4.22×10^{-3}

Performance Function Constants	
C_0	0.702
C_1	-0.202
D_0	-0.854
D_1	0.271
D_2	-0.179

Reliability Index, $\beta = (\Sigma\beta_i^2)^{0.5}$	0.122
Performance Function (Eqn. 9-6) , $g(x_i)$ =	0.000
Probability of $F<1$ ($SRF_{crit} < 1$), $P_{F<1}$ =	45%

Note: $P_{F<1}$ assumes $g(x_i)$ is planar

Low's (1996) method for finding the Hasofer-Lind reliability index, β, starts with an estimate of the values, x_i, for each variable. These estimates are varied to find the design point and do not need to initially lie on the $g(x_i) = 0$ surface. Because the variables used in this analysis were lognormally distributed, the variables were first transformed into normal space and then values of β_i^2 are calculated. The overall β was calculated by summing the individual β_i^2 and taking the square root of the sum. At the same time, the performance function (Eqn. 9-6) was calculated from the variables. Using Excel's built-in solver, β was minimized with the constraint that the performance function is equal to zero. This method finds the smallest ellipsoid centered on the mean values of the random variables that is tangent to the performance function. The Hasofer-

Lind method does not require an assumption regarding the distribution of *SRF* (Baecher and Christian 2003) to calculate β.

The probability of $SRF < 1$ was estimated from the minimum value of β by assuming that the performance function is planar (Low 1996). The probability of $SRF < 1$ found using the Hasofer-Lind method was 45%, which is similar to that found by the Taylor Series approximation in Table 9-2.

Simplified Hasofer-Lind Analysis

The Simplified Hasofer-Lind procedure developed by Filz and Navin (2006) and explained in Sleep and Duncan (2014) was also applied to the Cobbs Creek Dam example. This method does not require the performance function to be explicitly defined.

The design point was approximated in the first steps of the procedure by assuming the random variables all impact the *SRF* equally. Strength reduction analyses were repeated for different values of β until $SRF_{crit} \times R_T$ was equal to 1.0. The trial values of the three random variables, a_{shell}, a_{core}, and R_T, for each analysis were found by subtracting β times the standard deviation from the mean for each value, taking into account the lognormal distribution of each. The approximate value of β was found to be 0.12 for this example.

The gradient of the performance function near the approximate design point was found next by perturbing each of the random variables by 10% and observing the change in *SRF*. The relative impact of each variable on the *SRF* was determined using the α factor defined by Filz and Navin (2006). This factor is the ratio of the performance function gradient in the direction of a particular variable to the overall performance function gradient at the approximate design point found at the end of the first step.

The last step refines the design point by including the α factors. Strength reduction analyses were repeated with different values of β until SRF_{crit} was equal to 1.0. In this case, the values of each variable were determined by subtracting $\alpha \times \beta \times \sigma$ from the mean values. This moves the design point to account for differences in the effects of each variable. The final β and corresponding $P_{F<1}$ are given in Table 9-4.

This application of the Simplified Hasofer-Lind method required 13 iterations of strength reduction analysis to perform, starting with an initial estimate of 0.5 for β based on the Taylor Series approximations.

Table 9-4. Summary of Simplified Hasofer-Lind method for rapid drawdown analysis of Cobbs Creek Dam using the Rational FEA method

Initial Estimate for β	Approximate β	Final β	$P_{F<1}$
0.5	0.12	0.15	44%

Monte Carlo Analysis

A spreadsheet Monte Carlo analysis was also performed using on the FEA based performance function for Cobbs Creek Dam (Eqn. 9-6). The spreadsheet was designed to generate 200,000 realizations during one iteration. The lognormal distributions given in Table 9-3 were assumed for the random variables. The probability of $F<1$ was found to be about 45% as shown in Figure 9-14. Additional realizations did not cause substantial change in the value of $P_{F<1}$.

The Monte Carlo method also allows the distribution of the factor of safety to be evaluated. In this case, the factor of safety from each realization can be calculated as R_T / SRF_{crit}. Figure 9-15 shows the frequency of each value of factor of safety for 200,000 realizations. The mean

and standard deviation of F were determined, from which λ_F and ζ_F were determined using Eqn. (9-1) and (9-2). The resulting lognormal distribution fits extremely well to the results of the Monte Carlo analysis. These results confirm that F is lognormally distributed for this problem as assumed to calculate β for the Taylor series approximations.

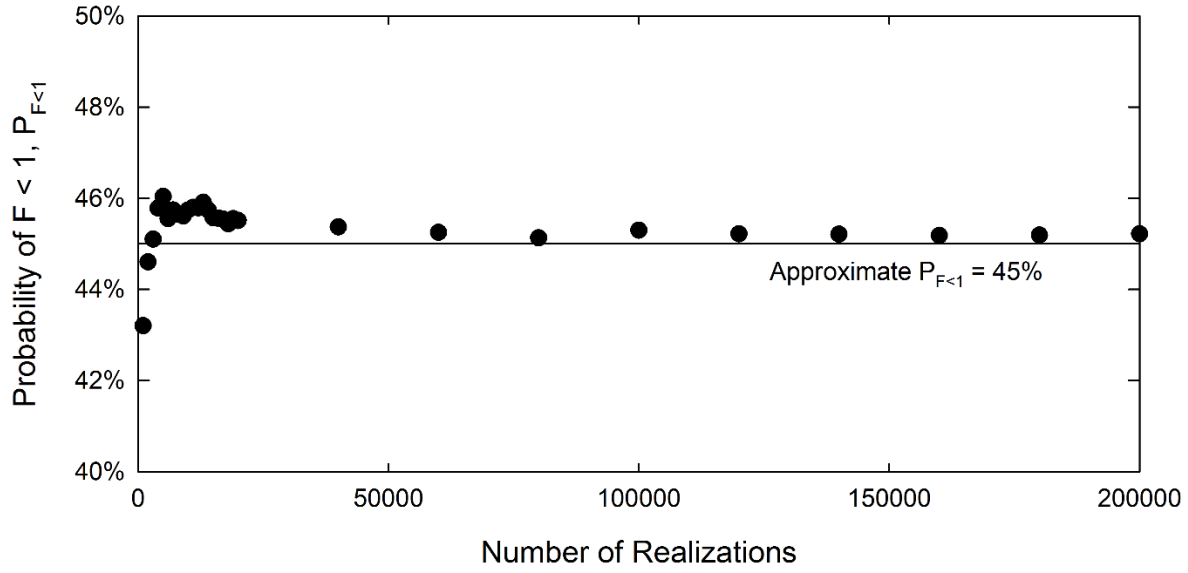

Figure 9-14. Monte Carlo analysis for Cobbs Creek Dam RDD based on Eqn. (9-6)

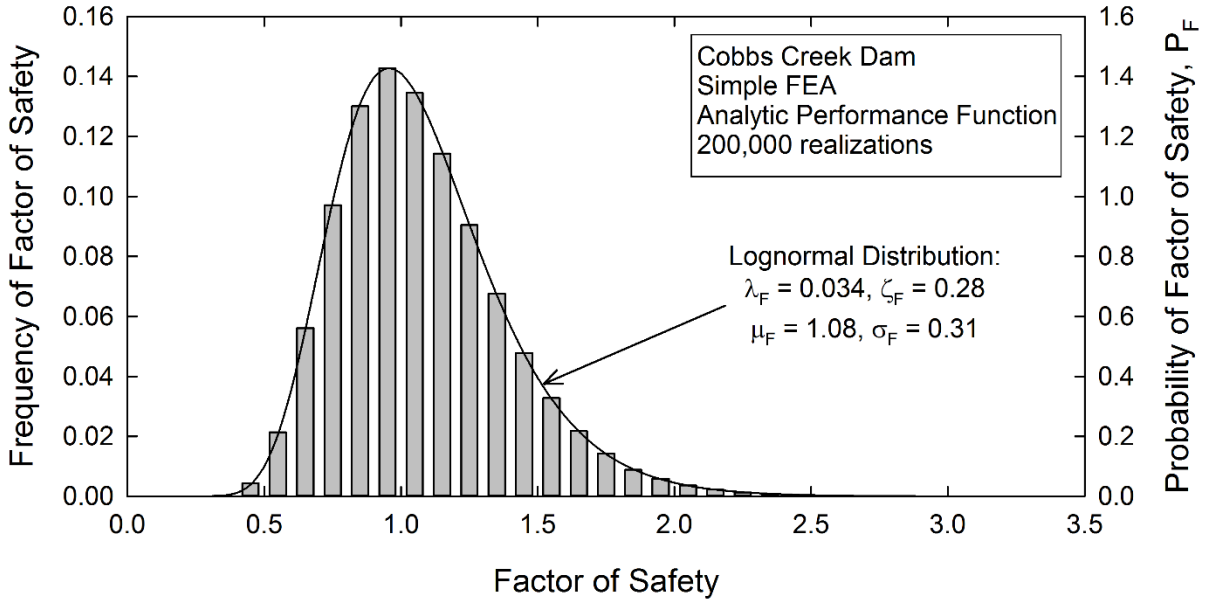

Figure 9-15. Distribution of factor of safety from the Monte Carlo analyses

Comparison of Methods

The various methods for assessing the reliability index and/or $P_{F<1}$ are compared in Table 9-5 for the Cobbs Creek Dam example. The DWW method predicts a lower β than the FEA method regardless of whether the uncertainty in R_T is considered. However, the DWW method likely has an inherent uncertainty that cannot be conveniently determined. In addition, the interpolation procedure was shown to systematically reduce the variability in undrained strength.

Table 9-5. Methods of assessing reliability for rapid drawdown – Cobbs Creek Dam.

	Taylor Series Approximation			Hasofer-Lind Rational FEA (variable R_T)	Simplified Hasofer-Lind Rational FEA (variable R_T)	Monte Carlo Rational FEA (variable R_T)
	DWW	Rational FEA (constant R_T)	Rational FEA (variable R_T)			
F_{MLV}	1.097	1.1	1.1	1.09	1.09	1.09
β	0.39[A]	0.27[A]	0.20[A]	0.12	0.15	---
$P_{F<1}$	35%[B]	39%[B]	42%[B]	45%[B]	44%[B]	45%

[A] Distribution of the factor of safety assumed to be lognormal
[B] Performance function assumed to be planar near the mean values.

The Hasofer-Lind method results in a lower value of β and a correspondingly higher $P_{F<1}$, comparing the FEA analyses with variable R_T. This small difference occurs because the Hasofer-Lind method does not require partial derivatives of the performance function to be approximated by differences about the mean.

The Simplified Hasofer-Lind procedure results in a slightly higher value of β and slightly lower $P_{F<1}$. The Simplified method is likely more accurate than those based on the closed form performance function because that function was itself an approximation. The residuals for the performance function curve fitting had a standard deviation of 0.01. This explains the slight difference between the values of β found by the two Hasofer-Lind methods.

The Simplified Hasofer-Lind method also required only 13 separate strength reduction analyses as opposed to the 28 analyses performed to define the performance function over a broad range of a_{shell} and a_{core} values. For situations where the statistics of the random variables are well-defined, the Simplified method provides an easier to understand and slightly more accurate solution for the Hasofer-Lind reliability index.

The advantage of an explicitly defined performance function is that the impact of changes to the variable statistics (both mean and standard deviation) can be explored more easily. Once the performance function is defined, β can be calculated for any probabilistic condition by changing a few values in the spreadsheet and repeating the Solver routine. Additional stability analyses are not required. The effects of the scale of fluctuation on the COV can also more easily be considered. Explicit definition of the performance function allows Monte Carlo analysis to be implemented to check the Hasofer-Lind solution.

The Taylor series and Hasofer-Lind methods both assume that the performance function varies linearly with respect to the random variables (i.e. the performance function is a planar surface) in order to calculate $P_{F<1}$ from β. While it does not calculate β, the Monte Carlo analysis removes this constraint by directly calculating $P_{F<1}$ for a large number of trials. The performance function is plotted in Figure 9-16 with a_{core} constant at its mean value of 0.68. The design point on the left represents the point where an ellipse defined by the variability of a_{shell} and R_T intersects the performance function. In the region near the mean values, the performance function is almost linear with respect to a_{shell}. For this reason, the methods that assume a planar performance function result in almost the same $P_{F<1}$ as the Monte Carlo method.

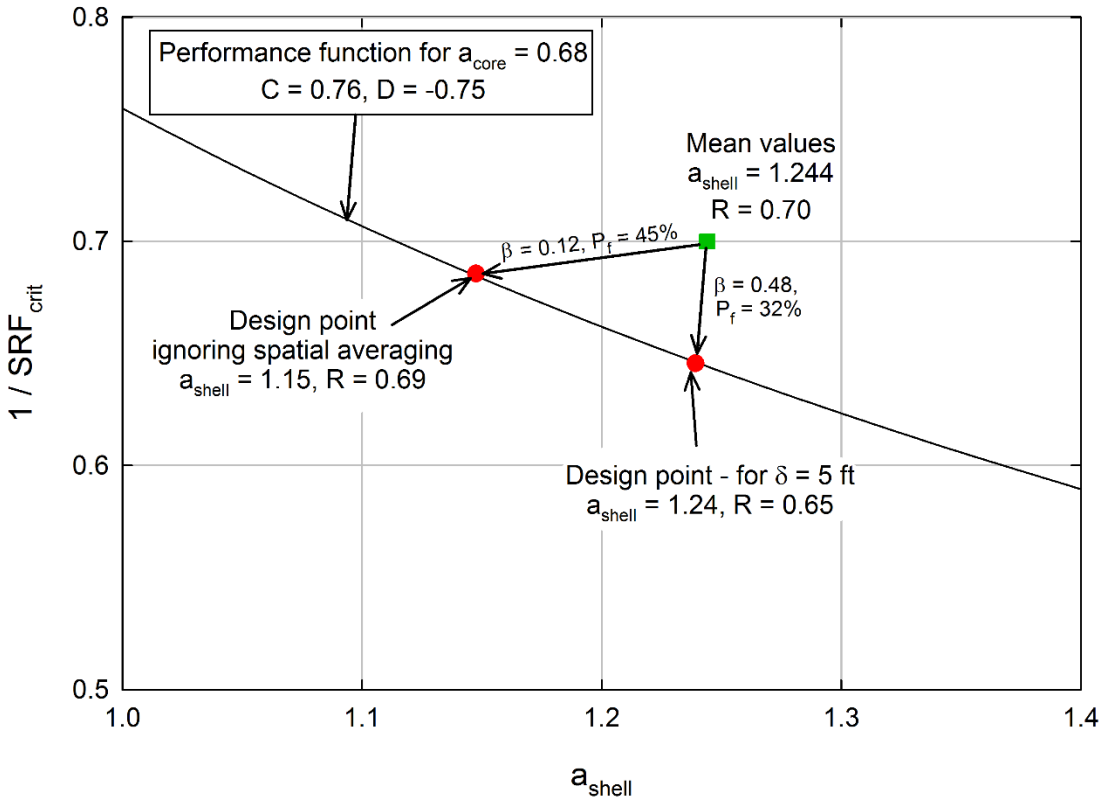

Figure 9-16. Performance function for a_{core} = 0.68 for Cobb's Creek Dam RDD analysis

Effect of Spatial Averaging

The coefficients of variation used in the preceding sections represent uncertainty in the variables but not the spatial variation within the embankment. The strength relationship for each soil layer is assumed to be constant during each analysis case. The relationship varies for other analysis cases as described by the probability distributions. A real failure surface will likely pass through some regions with higher than average strength and other regions that are weaker. High and low strengths will tend to average out along a surface, leading to a reduction in variability and lower standard deviation for the average undrained strength, $\sigma_{su\text{-}average}$. Christian et al.

(1994) state that the reduction in variance for undrained strength along a failure surface of length, L_f, can be approximated by

$$\frac{\left(\sigma_{su-average}\right)^2}{\left(\sigma_{su}\right)^2} \approx \frac{\delta}{L_f} \tag{9-7}$$

where:

σ_{su} = standard deviation of s_u, and

δ = scale of fluctuation.

The spatial correlation of a given variable is often quantified by the scale of fluctuation, δ, which is the typical length of the fluctuations of a random variable about the mean trend. Phoon and Kulhawy (1999) indicate that a typical scale of fluctuation for the vertical direction, δ_z, is about 8 ft (2.5 m) for the undrained strength of natural clay. In compacted fill, δ_z will likely depend on the variability of the borrow materials and differences in compaction between lifts. It is reasonable to assume that δ_z in the vertical direction is on the order of one to two lift thicknesses, or a few feet or less.

Undrained strengths of natural deposits tend to be more closely correlated in the horizontal direction. Modern earthwork procedures will also lead to greater horizontal correlation compared to vertical in compacted fills. Jha and Ching (2013) used horizontal scales of fluctuation, δ_x, ranging from 10 to 40 times δ_z in a study of the effects of spatial variation on undrained slope stability. Using a similar range for compacted fill leads to δ_x in the range of 10 to 80 ft (3 to 24 m), which were judged to be reasonable values for the horizontal scale of fluctuation in compacted fill.

The Hasofer-Lind analysis of RDD variability was repeated three times, accounting for the effects of different degrees of spatial averaging. In order to use the approximation in Eqn. (9-7),

a single value of δ must be selected. A slope failure will not be entirely vertical or horizontal, so δ must be selected between δ_z and δ_x. Three analyses were performed, assuming that δ was 5, 10, and 20 ft (1.5, 3, and 6.1 m), and are summarized in Table 9-6 . The same scale of fluctuation was used for both the core and shell soils. The length of the failure surface in each soil type was determined from the limit equilibrium failure surface determined using the mean values. In each case, a reduced variance was calculated using Eqn. (9-7) for each soil type. The lower variances were then used with the Hasofer-Lind analysis to determine β and $P_{F<1}$.

Table 9-6. Effects of spatial averaging on Hasofer-Lind β and $P_{F<1}$ (Note: the *COV* for a_{shell} and a_{core} are 32% and 15%, respectively)

Scale of fluctuation	δ/L_f		Reduced *COV*		Reliability Index	Probability of failure
δ	Shell	Core	a_{shell}	a_{core}	β	P_f
5	0.013	0.058	3.7%	3.6%	0.48	32%
10	0.026	0.116	5.2%	5.1%	0.46	32%
20	0.053	0.233	7.3%	7.2%	0.44	33%
Spatial averaging ignored (from Table 9-3)					0.12	45%

Consideration of spatial averaging using reasonable values of δ reduced $P_{F<1}$ for Cobb's Creek Dam from 45% to 32%. Reduction in the variation of the soil strength makes the uncertainty in the analysis almost entirely due to the variability in R_T. R_T was not included in the spatial averaging since it is associated with the analysis method rather than the soil properties. The design point for δ = 5 ft is shown in Figure 9-16.

Effect of the Probability of RDD

The probabilities that *F* is less than 1.0 presented in the preceding sections do not consider the prior probability of the occurrence of the rapid drawdown event, P_{RDD} or P(RDD occurs). The value, $P_{F<1}$, could more accurately be referred to as the probability of failure *given* the

occurrence of rapid drawdown, $P_{f \mid RDD}$ or P(RDD failure | RDD occurs). The annual probability of failure due to rapid drawdown, P_f, can be calculated as P(RDD failure) = P(RDD failure | RDD occurs)×P(RDD occurs). This essential detail puts the reliability of earth structures during RDD in the appropriate context.

Earth dams and levees are designed with different purposes and for different operating conditions. For example, the water level in an earth dam in a temperate climate might experience a full drawdown only on rare occasion, possibly a couple of times in its design life. In this case, the annual probability of drawdown might be on the order of 2 / 100 = 0.02. On the other hand, a dam used for water storage in an arid climate might be lowered, on average, every other year, resulting in an annual P_{RDD} of 0.5. A further extreme would be a pumped storage facility where full drawdown might occur multiple times per year with an annual P_{RDD} greater than 1. (One might question whether conventional rapid drawdown analysis is appropriate in the latter two cases because the embankments may never approach a steady state seepage condition.)

Application of this concept is illustrated in Table 9-7 for two hypothetical types of reservoir usage. $P_{f \mid RDD}$ was chosen as 32% based on Table 9-6 and assuming the reliability analysis yields the same result for both reservoir uses. The dam that is usually full has P_f below 1% because drawdown itself is a rare occurrence. The designer might decide that $P_f < 1\%$ is acceptable even though the $P_{f \mid RDD}$ of 32% is initially quite alarming. A low factor of safety for RDD may still be appropriately conservative if viewed in this way. However, for the case where drawdown is a frequent event, the final P_f of 16% is likely unacceptable, and a higher mean factor of safety would probably be required.

Table 9-7. Example calculation of P_f based on probability of RDD occurrence. F_{MLV} is 1.1 for both cases.

Reservoir use	$P_{f \mid RDD} = P_{F<1}$	Approx. P_{RDD}	P_f
Usually full, drawdown rare	32%	2%	(0.32)×(0.02) = 0.6%
Water storage, frequent drawdown	32%	50%	(0.32)×(0.50) = 16%

Summary and Conclusions

Drained and undrained strength for rapid drawdown slope stability analysis can be defined from laboratory test data using power curves with parameters, *a* and *b*. Strength data from compacted specimens suggests that variability in the strength relationships can be quantified by selecting a fixed value of *b* and examining the variability of a single parameter, *a*, for each soil type.

The undrained strength of compacted Oak Harbor clay had a *COV* of 13%. In this case, variation in strength from the trend was mostly the result of differences in the initial dry unit weight. A higher *COV* for undrained strength of compacted fill would be expected in the field because a greater range of compacted dry unit weight and water content would likely occur. In contrast, the Cobb's Creek shell soils had a consistent relative compaction but also a wide range of maximum dry unit weights. This resulted in a *COV* of 32 to 36% for the undrained strength of the compacted shell material. The Cobb's Creek core soils had a smaller range of maximum dry unit weights and a correspondingly lower *COV* of 10 to 15% for undrained strength. The effective stress strength parameters for both soil types had coefficients of variation in the range of 8 to 9%.

The Taylor series method for approximating β and $P_{F<1}$ for the DWW method only considers uncertainty in the soil strength properties. Uncertainty due to the calculation method is not

included and cannot be readily quantified. Linear interpolation was found to damp the effect of strength parameter variations on the factor of safety. For the critical Cobb's Creek Dam surface, the interpolated strengths used for the shell in the DWW Stage 2 calculations had a *COV* of 24% even though the shell $K_c = 1$ envelopes had a *COV* of 36%. This is an effect caused by the calculation method, which may unrealistically reduce the probability of failure.

An explicit performance function was developed for the Cobb's Creek Dam example based on the FEA results, relating the *a* parameters for the core and shell materials and the reduction factor, R_T. The performance function was used to assess reliability by the Hasofer-Lind and Monte Carlo methods. The Hasofer-Lind approach gives a slightly different β than the Taylor series approximation but a similar $P_{F<1}$ because both methods assume that the performance function is planar. The Monte Carlo method also results in a similar $P_{F<1}$ because the performance function is almost planar near the mean values. The simplified Hasofer-Lind procedure (Filz and Navin 2006) produced similar results to the approaches which used the explicit performance function.

The effects of spatial variability were considered by reducing the variance of undrained strength based on estimates of the scale of fluctuation, δ, for compacted soil. The variance of undrained strength reduced considerably in the Cobb's Creek example because the failure surface was deep and relatively long. The *COV* of a_{shell} reduced from 32% to 4% when δ was assumed to be 5 ft. The reduced strength variability caused $P_{F<1}$ to drop from 45% to 32%. The source of uncertainty in the analysis shifts from the material properties to the analysis procedure when spatial averaging is included.

The frequency of drawdown has an important impact on the interpretation of RDD results, for both deterministic and probabilistic assessments. Rapid drawdown analyses will tend to have

low factors of safety and correspondingly high $P_{F<1}$ or $P_{f|RDD}$ unless the embankment design is very conservative. The likelihood of drawdown occurrence must be considered to put a high $P_{f|RDD}$ into the appropriate context. A low F and high $P_{f|RDD}$ may be acceptable when rapid drawdown is a rare event. Embankments that experience frequent drawdown must have low $P_{f|RDD}$ and a correspondingly high factor of safety. The combination of rapid drawdown analysis with reliability analysis and consideration of the probability of drawdown provides a more robust tool for engineering design than deterministic RDD analysis alone.

The reliability analyses presented in this chapter focused on uncertainties in undrained strength, which are not the only variable in a slope stability analysis. For example, weak seams in the embankment or foundation would impact stability and may need to be considered in some situations. For rapid drawdown, it might also be necessary to consider different pore pressures or water levels before drawdown and different amounts of drawdown. The unit weight of the embankment fill will also be variable. In the author's experience, this factor tends to have little impact on stability since the unit weight impacts both the driving and resisting forces in the analysis. A comprehensive reliability analysis should not blindly exclude important sources of uncertainty.

The purpose of Chapter 9 was to illustrate the practical application of probabilistic methods to RDD, not to make judgments regarding the reliability of Cobbs Creek Dam. As stated in Chapter 8, the calculations for Cobbs Creek Dam were based on data from early in the design phase and do not incorporate later improvements to the design. In addition, other factors such as the effects of the distribution of R_T and possible strength gain with time in the compacted soils have not been fully considered. For these reasons, the values of $P_{F<1}$ are not representative of the final design of Cobbs Creek Dam.

10.Major Conclusions and Recommendations for Future Work

Multi-stage methods for evaluating stability with undrained strength rapid drawdown have been studied with particular focus on the application of finite element analysis to rapid drawdown. The following major conclusions have been reached by this research.

Effective Stress Analysis of Rapid Drawdown

- Uncoupled transient seepage ignores changes in pore pressure due to changes in total stress. Uncoupled analysis is inappropriate for RDD and leads to unrealistic pore pressures.
- The numerical modeling requirements to predict realistic pore pressures following RDD or rapid flood loading are exacting and too complicated for standard practice.
- Pilarcitos Dam and a levee example were used to show the impact of compressibility on pore pressures determined using uncoupled transient seepage.

Stress System Effects on Undrained Strength

- Data from the geotechnical literature indicate that anisotropic consolidation tends to cause a reduction in undrained strength compared to isotropic at the same σ'_{1c}. The median adjustment factor, R_K, was found to be 0.9 for undisturbed/remolded soil and 0.94 for compacted clay (based on limited data).
- Laboratory tests on Oak Harbor clay found R_K to be unity (no reduction) at low consolidation stresses and as low as 0.7 for tests with higher σ'_{1c}.
- Plane strain compression tests produce strengths that are on average 10% higher than those from ACU triaxial compression tests, i.e. R_{PS} = 1.1.
- Extension tests were shown to be fraught with difficulties and are not appropriate for slope stability.

- A method for comparing undrained strengths at consistent plane strain conditions was developed. For an average stress rotation, ρ, of 30 to 45° for rapid drawdown, the adjustment factor, R_ρ, should be in the range of 0.6 to 0.8 depending on the soil's plasticity index.
- The empirical adjustment factors can be combined with strengths from ICU triaxial compression tests to obtain the adjusted undrained strength appropriate for rapid drawdown, $s_{u\text{-}ADJ} = R_K \times R_{PS} \times R_\rho \times s_{u\text{-}ICU} \approx 0.6$ to $0.8 \times s_{u\text{-}ICU}$

Finite Element Stress Analysis of Embankments

- A guide for performing finite element stress analysis of embankments was developed, focusing on the use of the non-linear Duncan-Chang hyperbolic model.
- Small elements with a height of 1 ft or 1% of the embankment produce the smoothest contours of stress.
- Embankment elements should be added to the model in stages that are one element high, mimicking construction stages.
- Any boundary water pressures and steady state pore pressures should also be applied in stages.

Evaluation of Limit Equilibrium RDD Procedure

- Limit equilibrium was shown to predict effective normal stresses that are quite close the FEA results while the shear stresses deviate significantly.
- If σ'_{fc} and τ_{fc} are correct, the actual value of K_c at any location is likely to be equal to or greater than the value determined by the limit equilibrium procedure. When K_c is too low, the strength tends to be overestimated at low consolidation stresses and underestimated at high consolidation stresses, relative to the compaction of the soil.

- K_c from FEA was shown to vary from 25% below to 60% above the values estimated by LE.
- The linear interpolation procedure leads to a greater reduction in undrained strength than that caused by anisotropic consolidation alone, based on comparison with laboratory test data. The strengths obtained by linear interpolation are about 60 to 80% of the ICU strength, which is the same range indicated by the analysis of stress system effects on undrained strength performed in Chapter 3.

Undrained Behavior of Compacted Clay

- Guidelines were provided for CU testing of compacted clays, particularly dealing with the intricacies of the saturation process.
- Relative compaction and initial water content were found to have a significant influence on the undrained strength of compacted clays, especially at low consolidation stresses.
- Triaxial tests that induce 90° stress rotation during shear were shown to produce different undrained strengths in compression and extension. Triaxial compression tests with stress rotation produce strengths that correspond well to the other triaxial tests. The triaxial extension tests result in much lower strengths except for σ'_{1c} below 10 psi.
- Strengths measured in the DSS tests on compacted clay were lower than those from triaxial compression and extension. The low strengths were attributed to the difficulty of performing DSS tests on stiff soils like compacted clay with conventional equipment.

Finite Element Methods for RDD Analysis

- The Rational FEA Method of rapid drawdown analysis was developed that uses linear elastic FEA, two stages of finite element calculations, and a constant adjustment factor on undrained strength.
- Based on back analysis, undrained strengths measured by the ICU-TC test must be multiplied by an adjustment factor of 0.7 to obtain the appropriate undrained strength for RDD. This value is in the range expected due to stress system effects and also fits well with the reduction in strength that occurs in the Duncan et al. (1990) limit equilibrium method.
- A Detailed FEA method of rapid drawdown analysis that applies spatially varying adjustments to undrained strength was also developed.

Probabilistic Methods in RDD Analysis

- Undrained strength was represented throughout this probability study using power curves with parameters *a* and *b*. For a given soil, *b* was observed to be relatively constant. This means that the uncertainty in undrained strength can be expressed using *a* as the sole random variable.
- The Cobb's Creek Dam example was used to perform reliability analyses, including Taylor Series approximations, the Hasofer-Lind method, and Monte Carlo Analysis.
- The deterministic factor of safety of 1.1 led to probabilities of a factor of safety less than one ranging from 35% for a Taylor Series approximation based on the Duncan et al. (1990) method to 45% based using Monte Carlo Analysis and the Rational FEA Method.

- The linear interpolation method used by Duncan et al. (1990) implicitly reduces the variability of undrained strength. For this reason, the use of Duncan et al. (1990) method is not recommended for reliability analysis.
- Spatial averaging was used to reduce the *COV* of undrained strength. Uncertainty in the Rational FEA method dominated the analysis when spatial averaging was considered.
- Reliability analyses of RDD should consider the probability of occurrence of the rapid drawdown event, if the probability of failure is to be rightly understood. If rapid drawdown will be a rare occurrence, the probability of failure will be reduced significantly, allowing the use of a lower deterministic F.

Recommendations for Future Work

- Perform more plane strain tests on compacted clays. A few plane strain compression test results on compacted clay are available in the literature. No other stress paths have been considered. Plane strain tests with different amounts of stress rotation on compacted soils with various plasticity indices are needed to improve understanding of compacted soil behavior.
- Compare the effective normal consolidation stress predicted by limit equilibrium to that from FEA for complex geometries or embankments with zones of varying stiffness.
- Improve methods for applying the DSS test to compacted clays. This work would likely require the use of back pressure saturation and platens with pins to accurately measure undrained strength of stiff, initially unsaturated specimens.

- Complete a detailed study of the stress paths followed at various points in an earth dam, starting at construction and proceeding through to steady state seepage. This study would help define the appropriate stress path to follow for the saturation and consolidation of compacted specimens for consolidated undrained triaxial tests.
- Perform a laboratory testing program comparing the effects of the three saturation methods outlined in Chapter 6 on the results of ICU-TC tests.
- Enlarge the RDD case history database. This can be accomplished if new information becomes available for past failures, or if new RDD failures occur and can be thoroughly investigated. Centrifuge testing of RDD should be considered.
- Consider the special cases of RDD for levees and pumped storage facilities, where the seepage conditions at the start of drawdown may deviate significantly from steady state. The profession needs a method to determine what part(s) of the embankment should be considered saturated for rapid drawdown analysis.

References

Akai, K. and Adachi, T. (1965). "Study on the one-dimensional consolidation and the shear strength characteristics of fully saturated clay, in terms of effective stress," *Proceedings of the 6th ICSMFE*, Vol. 1, Montreal, Quebec, 146-150.

Alonso, E. E., Gens, A. and Josa, A. (1990). "A constitutive model for partially saturated soils," *Geotechnique*, 40(3), 405-430.

Alonso, E. E. and Pinyol, N. M. (2011). "Landslides in reservoirs and dam operation," *Proceedings of Dam Maintenance and Rehabilitation II*, Eds. R. Garcia, et al., Taylor & Francis Group, London, 3-27.

Alonso, E. E., Pinyol, N. M., and Gens, A. (2013). "Compacted soil behaviour: initial state, structure and constitutive modelling," *Geotechnique*, 63(6), 463-478.

American Society for Testing and Materials (ASTM) ASTM D422-63 (2007). "Standard Test Method for Particle-Size Analysis of Soils," *Annual Book of ASTM Standards*, ASTM Intl., West Conshohocken, PA, 8 pp.

ASTM D698-12 (2012). "Standard Test Method for Laboratory Compaction Characteristics of Soil Using Standard Effort," *Annual Book of ASTM Standards*, ASTM Intl., West Conshohocken, PA, 13 pp.

ASTM D874-10 (2010). "Standard Test Method for Specific Gravity of Soil Solids by Water Pycnometer," *Annual Book of ASTM Standards*, ASTM Intl., West Conshohocken, PA, 7 pp.

ASTM D1557-12 (2012). "Standard Test Method for Laboratory Compaction Characteristics of Soil Using Modified Effort," *Annual Book of ASTM Standards*, ASTM Intl., West Conshohocken, PA, 14 pp.

ASTM D2435-11 (2011). "Standard Test Methods for One-Dimensional Consolidation Properties of Soils Using Incremental Loading," *Annual Book of ASTM Standards*, ASTM Intl., West Conshohocken, PA, 15 pp.

ASTM D4318-10 (2010). "Standard Test Methods for Liquid Limit, Plastic Limit, and Plasticity Index of Soils," *Annual Book of ASTM Standards*, ASTM Intl., West Conshohocken, PA, 16 pp.

ASTM D4767-11 (2011). "Standard Test Method for Consolidated Undrained Triaxial Compression Test for Cohesive Soils," *Annual Book of ASTM Standards*, ASTM Intl., West Conshohocken, PA, 13 pp.

ASTM D6528-07 (2007). "Standard Test Method for Consolidated Undrained Direct Simple Shear Testing of Cohesive Soils," *Annual Book of ASTM Standards*, ASTM Intl., West Conshohocken, PA, 9 pp.

Barden, L. (1965). "Consolidation of compacted and unsaturated clay," *Geotechnique*, 15(3), 267-286.

Barden, L. (1971). "Examples of clay structure and its influence on engineering behavior," *Stress-strain behavior of soils, Proceedings of the Roscoe Memorial Symposium – Cambridge University*, Ed. R.H.G. Parry, G.T. Foulis & Co. Ltd., Henley-on-Thames, 195-205.

Barden, L. (1974). "Consolidation of clays compacted dry and wet of optimum water content", *Geotechnique*, 24(4), 605-625.

Barrett, J. R. and Moore, P. J. (1975). "Design criteria for rapid drawdown in earth-rock dams," *Criteria and Assumptions for Numerical Analysis of Dams – Proceedings of International Symposium*, Swansea, U.K., Sept. 8-11, 1975, 809-828.

Baecher, G. B. and Christian, J. T. (2003). *Reliability and Statistics in Geotechnical Engineering*, John Wiley & Sons, Inc., Hoboken, NJ, 605 pp.

Balasubramaniam, A. S. and Waheed-Uddin (1977). "Deformation characteristics of weathered Bangkok Clay in triaxial extension," *Geotechnique*, 27(1), 75-92.

Bear, J. (1979). "Chapter six – Flow in the unsaturated zone," *Hydraulics of Groundwater*, McGraw-Hill Publ. Co, New York, NY, 213.

Benson, C. H. and Trast, J. M. (1995). "Hydraulic conductivity of thirteen compacted clays," *Clays and Clay Minerals*, 43(6), 669-681.

Berilgen, M. M. (2007). "Investigation of stability of slopes under drawdown conditions." *Computers and Geotechnics*, 34, 81-91.

Berre, T. (1982). "Triaxial testing at the Norwegian Geotechnical Institute," *Geotechnical Testing Journal*, ASTM, 5(1/2), 3-17.

Bishop, A. W. (1954). "The Use of Pore-Pressure Coefficients in Practice," *Geotechnique*, 4(4), 148-152.

Bishop, A. W. (1966). "The strength of soils as engineering materials", *Geotechnique*, 16(2), 89-130.

Bjerrum, L. and Landva, A. (1966). "Direct simple-shear tests on a Norwegian quick clay," *Geotechnique*, 16(1), 1-20.

Brahma, S. P. and Harr, M. E. (1963). "Transient Development of the Free Surface in a Homogeneous Earth Dam". *Geotechnique*, 12(4), pp. 283-302.

Brandon, T. L.; Martin, L.; Martin, S.; and Xu, G. (2011), "Strength and compressibility correlations for New Orleans area soils," *Report submitted to the US Army Corps of Engineers New Orleans Distric*t, New Orleans, LA, 130 pp.

Broms, B. B. and M. U. Ratnam (1963). "Shear strength of an anisotropically consolidated clay," *Journal of the Soil Mechanics and Foundations Division*, 89(SM6), 1-26.

Broms, B. B. and Casbarian, A. O. (1965). "Effects of rotation of the principal stress axes and of the intermediate principal stress on the shear strength," *Proceedings of the 6th ICSMFE*, Vol. 1, Montreal, Quebec, 179-183.

Browzin, B. S. (1961). "Nonsteady-State Flow in Homogeneous Earth Dams after Rapid Drawdown," *Proceedings of the 5th ICSMFE*, Paris, Vol. 2, 551-554.

Castellanos, B. (2011). Personal communication.

Castellanos, B. (2014). *Use and measurement of fully softened shear strength*, PhD dissertation, Virginia Tech, Blacksburg, VA.

Christian, J. T., Ladd, C. C., and Baecher, G. B. (1994). "Reliability applied to slope stability analysis," *Journal of Geotechnical Engineering*, 120(12), 2180-2206.

Clough, G. W. and Duncan, J. M. (1969). "Finite element analyses of Port Allen and Old River Locks," *Contract Report S-69-6*, USACE WES, 80-92.

Clough, R. W. and Woodward, R. J. (1967). "Analysis of Embankment Stresses and Deformations," *Journal of Soil Mechanics and Foundations Division*, 93(SM4), 529-549.

DeLory, F. A. and Salvas, R. J. (1969). "Some observations on the undrained shearing strength used to analyze a failure," *Canadian Geotechnical Journal*, 6, 97-110.

Desai, C. S. (1972). "Seepage Analysis of Earth Banks Under Drawdown," *Journal of Soil Mechanics and Foundations Division*, 98(SM11), 1143-1162.

Desai, C. S. (1977). "Drawdown Analysis of Slopes by Numerical Method," *Journal of the Geotechnical Engineering Division*, 103(GT7), 667-676.

DiBernardo, A., and C. W. Lovell (1979). *The effect of laboratory compaction on the compressibility of compacted highly plastic clay: Int. Rep., Publ. FHWA/IN/JHRP-79/03*, JHRP, INDOT and Purdue Univ., West Lafayette, IN.

Donaghe, R. T. and Townsend, F. C. (1978)."Effects of anisotropic versus isotropic consolidation in consolidated-undrained triaxial compression tests of cohesive soils," *Geotechnical Testing Journal*, 1(4), 173-189.

Duncan, J. M. and Seed, H. B. (1965). "The effect of anisotropy and reorientation of principal stresses on the shear strength of saturated clay," *Report No. TE 65-3*, Office of Research Services, Univ. of California, Berkeley, CA, 171 pp.

Duncan, J. M. and Seed, H. B. (1966). "Strength variation along failure surfaces in clay," *Journal of the Soil Mechanics and Foundations Division*, 92(SM6), 81-104.

Duncan, J. M. and Dunlop, P. (1969). "Behavior of soils in simple shear tests," *Proceedings of the 7th ICSMFE*, Mexico City, Vol. 1, 101-109.

Duncan, J. M. and Chang, C-Y. (1970). "Nonlinear analysis of stress and strain in soils," *Journal of the Soil Mechanics and Foundations Division*, ASCE, 96(SM5), 1629-1653.

Duncan, J. M., Byrne, P. M., Wong, K. S., and Mabry, P. (1980). "Strength, stress-strain and bulk modulus parameters for finite element analyses of stresses and movements in soil masses," *UCB/GT-80-01*, UC Berkeley.

Duncan, J. M., Wright, S. G., and Wong, K. S. (1990). "Slope stability during rapid drawdown," *Seed Memorial Symposium Proceedings,* Vol. 2, BiTech Publishers, Ltd., Vancouver, B.C., 235-272.

Duncan, J. M., Williams, G. W., Sehn, A. L., and Seed, R. B. (1991). "Estimation earth pressures due to compaction," *Journal of Geotechnical Engineering*, 117(12), 1833-1847.

Duncan, J. M. and Wright, S. G. (2005). "Shear strengths of soil and municipal solid waste," *Soil Strength and Slope Stability*, John Wiley & Sons, Hoboken, NJ, 37-46.

Dyvik, R., Berre, R., Lacasse, S., and Raadim, B. (1987). "Comparison of truly undrained and constant volume direct simple shear tests," *Geotechnique*, 31(1), 3-10.

Filz, G. M. and Navin, M. P. (2006). *Stability of column supported embankments*, Virginia Transportation Research Council, 06-CR13, 73 pp.

Fleming, L.N. and Duncan, J. M. (1990). "Stress-deformation characteristics of Alaskan silt", *Journal of Geotechnical Engineering*, 116(3), 377-393.

France, J. W. and Winckler, C. J. C. (2008). "Rapid Drawdown Analysis – What is an Analyst to Do?" *Proceedings ASDSO – Dam Safety 2008*, Sept. 7-11, 2008, Omnipress.

Fredlund, D. G., Morgenstern, N. R., and Widger, R. A. (1978). "Shear strength of unsaturated soils," *Canadian Geotechnical Journal*, 15(3), 313-321.

Fredlund, M., Lu, H., and Feng T. (2011). "Combined seepage and slope stability analysis of rapid drawdown scenarios for levee design," *Proceedings of GeoFrontiers 2011*, Dallas, TX, 1595-1604.

Frishman, F. (1971). *On the arithmetic means and variances of products and ratios of random variables*, Army Research Office, Durham, NC, 16 pp.

GEO-SLOPE International, Ltd. (2012). *Seepage Modeling with SEEP/W, An Engineering Methodology*, Calgary, Alberta, Canada, 205 pp.

Goodman, L. E. and Brown, C. B. (1963). "Dead Load Stresses and the instability of slopes," *Journal of the Soil Mechanics and Foundations Division*, 89(SM3), 103-134.

Griffiths, D. V. and Lane, P. A. (1999). "Slope stability analysis by finite elements," *Geotechnique*, 49(3), 387-403.

Hambly, E. C. (1972). "Plane strain behavior of remoulded normally consolidated kaolin," *Geotechnique*, 22(2), 201-317.

Hanzawa, H. (1977a). "Geotechnical properties of normally consolidated Fao clay," *Soils and Foundations*, 17(4), 1-15.

Hanzawa, H. (1977b). "Field and laboratory behavior of Khor Al-Zubair clay, Iraq," *Soils and Foundations*, 17(4), 17-30.

Hasofer, A. M. and Lind, N. C. (1974). "An exact and invariant first-order reliability format," *Journal of the Engineering Mechanics Division*, 100(EM1), 111-121.

Hanson, J. Brinch and Gibson, R. E. (1949). "Undrained shear strengths of anisotropically consolidated clays," *Geotechnique*, 1(3), 189-204.

Henkel, D. J. (1960)."The relationships between the effective stresses and water content in saturated clays," *Geotechnique*, 10(2), 41-54.

Henkel, D. J. and Sowa, V. A. (1963). "The influence of stress history on stress paths in undrained triaxial tests on clay," *Laboratory Shear Testing of Soils*, STP No. 361, American Society for Testing and Materials, 280-291.

Henkel, D. J. and Wade, N. H. (1966). "Plane strain tests on a saturated remolded clay," *Journal of the Soil Mechanics and Foundations Division*, 92(SM6), 67-80.

Holtz, R. D. and Krizek, R. J. (1971). "Effects of stress path and overconsolidation ratio on the shear strength of a kaolin clay", *Proceedings of the Fifth Regional Conference for Africa on Soil Mechanics and Foundation Engineering*, Luanda, Angola, Vol. 1, 3-17 to 2-35.

Holtz, R. D. and Kovacs W. D. (1981). "Shear strength of sands and clays," *An Introduction to Geotechnical Engineering*, Prentice Hall, Englewood Cliffs, NJ, 544.

Huang, M. S. and C. Q. Jia (2009). "Strength reduction FEM in stability analysis of soil slopes subjected to transient unsaturated seepage," *Computers and Geotechnics*, 36(2), 93-101.

Jamiolkowski, M., Ladd, C.C., Germaine, J. T., and Lancellotta, R. (1985). "New developments in field and laboratory testing of soils," *Proceedings of the 11th ICSMFE*, San Francisco, Vol. 1, 57-154.

Janbu, N., Kjekstad, O., and Senneset, K. (1977). "Slide in overconsolidated clay below an embankment," *Proceedings of the 9th ICSMFE*, Tokyo, Vol. 2, 95-102.

Jha, S. K. and Ching, J. (2013). "Simplified reliability method for spatially variable undrained engineered slopes," *Soils and Foundations*, 53(5), 708-719.

Johnson, J. M. and Lovell, C. W. (1979). *The effect of laboratory compaction on the shear behavior of a highly plastic clay after saturation and consolidation: Int. Rep., Publ, FHWA/IN/JHRP-79/07*, JHRP, INDOT and Purdue Univ., West Lafayette, IN.

Khera, R. P. and R. J. Krizek (1967). "Strength behavior of an anisotropically consolidated remolded clay," *Highway Research Record 190*, 8-18.

Khera, R. P. and R. J. Krizek (1968). "Effect of principal consolidation stress difference on undrained shear strength," *Soils and Foundations*, 8(1), 1-17.

Kinner, E. B. and C. C. Ladd (1970). *Load-deformation behavior of saturated clay during undrained deformation*, Massachusetts Institute of Technology Soils Publication No. 259.

Koutsoftas, D. C. (1978). "Effect of cyclic loads on undrained strength of two marine clays," *Journal of the Geotechnical Engineering Division*, 104(GT5), 609-620.

Koutsoftas, D. C. (1982). "Discussion to 'Cam-clay prediction,'" *Journal of the Geotechnical Engineering Division*, 108(GT1), 178-181.

Kulhawy, F. H. (1969). *Finite Element Analysis of the Behavior of Embankments*, PhD Dissertation, University of California, Berkeley, CA.

Ladanyi, B. (1967). "Discussion of 'Plane strain tests on a saturated remolded clay," *Journal of the Soil Mechanics and Foundations Division*, 93(SM5).

Ladd, C. C. (1964). "Stress-strain modulus of clay in undrained shear," *Journal of the Soil Mechanics and Foundations Division*, 90(SM5), 103-133.

Ladd, C. C. (1965). "Stress-strain behavior of anisotropically consolidated clays during undrained shear," *Proceedings of the 6th ICSMFE*, Vol. 1, Montreal, Quebec, 282-286.

Ladd, C. C., Bovee, R. B., Edgers, L., and Rixner, J. J. (1971). "Consolidated-undrained plane strain shear tests on Boston Blue Clay," *Research Report R71-13*, No. 273, Dept. of Civil Engineering, MIT, Cambridge, 243 pp.

Ladd, C. C. and Edgers, L. (1972). "Consolidated-Undrained direct simple shear tests on saturated clays," *Research Report R72-82*, No. 284, Dept. of Civil Engineering, MIT, Cambridge, 354 pp.

Ladd, C. C., Foott, R., Ishihara, K., Schlosser, F., and Poulos, H. G. (1977). "Stress-deformation and strength characteristics," *Proceedings of the 9th ICSMGE*, Tokyo, Vol. 2, 421-494.

Ladd, C. C. and DeGroot, D. J. (2003). "Recommended practice for soft ground site characterization," *Proceedings of the 12th Panamerican Conference on Soil Mechanics and Geotechnical Engineering*, Massachusetts Institute of Technology, Cambridge, MA, 55 pp.

Lade, P. V. (2010). "The mechanics of surficial failure in soil slopes," *Engineering Geology*, 114, 57-64.

Lade, P. V., Yamamuro, J. A., and Skyers, B. D. (1996). "Effects of shear band formation in triaxial extension tests," *Geotechnical Testing Journal*, 19(4), 398-410.

Lam, L., Fredlund, D.G., and Barbour, S.L. (1987). "Transient seepage model for saturated–unsaturated soil systems: a geotechnical engineering approach," *Canadian Geotechnical Journal*, 24, 565–580.

Lee, K. L. and Haley, S. C. (1968). "Strength of compacted clay at high pressure," *Journal of the Soil Mechanics and Foundations Division*, 94(SM6), 1303-1332.

Lee, K. L. and Morrison, R. A. (1970). "Strength of anisotropically consolidated compacted clay," *Journal of the Soil Mechanics and Foundations Division*, 96(SM6), 2025-2043.

Lee, K. L. and Shubeck, R. J. (1971). "Plane-strain undrained strength of compacted clay," *Journal of the Soil Mechanics and Foundations Division*, 97(SM1), 219-234.

Li, G. C. and Desai, C. S. (1983). "Stress and Seepage analysis of earth dams," *Journal of Geotechnical Engineering*, 109(7), 946-960.

Long, M. and Menkiti, C. O. (2007). "Geotechnical properties of Dublin Boulder Clay," *Geotechnique*, 57(7), 595-611.

Low, B. K. (1996). "Practical probabilistic approach using spreadsheet," *Uncertainty in the Geologic Environment*, ASCE, Madison, WI, 1284-1302.

Lowe, J. and Karafiath, L. (1960a). "Stability of Earth Dams Upon Drawdown," *Proceedings of the First Panamerican Conference on Soil Mechanics and Foundation Engineering*, Mexico City, Vol. 2, 537-552.

Lowe, J. and Karafiath, L. (1960b). "Effect of anisotropic consolidation on the undrained shear strength of compacted clays," *Research Conference on the Shear Strength of Cohesive Soils*, ASCE, Boulder, CO, 837-858.

Mayne, P. W. (1985a). "Stress anisotropy effects on clay strength," *Journal of Geotechnical Engineering*, 111(3), 356-366.

Mayne, P. W. (1985b). "A review of undrained strength in direct simple shear," *Soils and Foundations*, 25(3), 64-72.

Mitachi, T. and S. Kitago (1976). "Change in undrained shear strength characteristics of saturated remolded clay due to swelling," *Soils and Foundations*, 16(1), 45-58.

Mitachi, T. and Kitago, S. (1979). "The influence of stress history and stress system on the stress-strain-strength properties of saturated clay," *Soils and Foundations*, 19(2), 45-61.

Mitachi, T. and Kitago, S. (1980). "Undrained triaxial and plane strain behavior of saturated remolded clay," *Soils and Foundations*, 20(1), 13-28.

Morgenstern, N. (1963). "Stability charts for earth slopes during rapid drawdown," *Geotechnique*, 13(2), 121-131.

Nakase, A. and Kamei, T. (1983). "Undrained shear strength anisotropy of normally consolidated cohesive soils," *Soils and Foundations*, 23(1), 91-101.

Nian, T., Jiang, J., Wan, S., and Luan, M. (2011). "Strength reduction FE analysis of the stability of bank slopes subjected to transient unsaturated seepage," *Electronic Journal of Geotechnical Engineering*, 16(A), 165-177.

Pariseau, W.G., Schmelter, S.C., and Sheik, A.K. (1997). "Mine slope stability analysis by coupled finite element modeling," *International Journal of Rock Mechanics and Mining Sciences*, 34(3-4), p 520.

Parry, R. H. G. and Nadarajah, V. (1973). "Observations on laboratory prepared, lightly overconsolidated specimens of kaolin," *Geotechnique*, 24(3), 345-358.

Pauls, G. J., Sauer, E. K., Christiansen, E. A., and Widger, R. A. (1999). "A transient analysis of slope stability following drawdown after flooding of a highly plastic clay." *Canadian Geotechnical Journal*, 36, 1151-1171.

Perloff, W. H., Baladi, G. Y. and Harr, M. E. (1967). "Stress distribution within and under long elastic embankments: Research Paper," *Publication FHWA/IN/JHRP-67/14*, JHRP, INDOT and Purdue Univ., West Lafayette, IN.

Pham, H. Q. and Fredlund, D. G. (2011). "Volume-mass unsaturated soil constitutive model for drying-wetting under isotropic loading-unloading," *Canadian Geotechnical Journal*, 48(2), 280-313.

Phoon, K.K. and Kulhawy, F.H. (1999). "Characterization of geotechnical variability," *Canadian Geotechnical Journal*, 36(4), 612-624.

Pinyol, N. M., Alonso, E. E., and Olivella, S. (2008). "Rapid drawdown in slopes and embankments," *Water Resources Research*, 44, W00D03,doi:10.1029/2007 WR006525.

Potts, D. M. and Zdravkovic, L. (1999). *Finite Element Analysis in Geotechnical Engineering: Theory*, Thomas Telford, London, 440 pp.

Potts, D. M. and Zdravkovic, L. (2001). "Embankments," *Finite Element Analysis in Geotechnical Engineering: Application*, Thomas Telford, London, 166-213.

Ramalho-Ortigao, M., Werneck, M. L. G., and Lacerda, W. A. (1983). "Embankment failure on clay near Rio de Janeiro," *Journal of Geotechnical Engineering*, 109(11), 1460-1479.

Rao, R. G., K. K. Rao, and N. S. Murthy (1977). "Construction pore pressures in earth dams," *Proceedings of the 5th Southeast Asian Conference on Soil Engineering*, Bangkok, Thailand, 225-233.

Rocscience (2012). "Transient groundwater analysis with slope stability," *Slide Tutorial #19*, pp. 17.

Rocscience (2014). "Stress analysis settings," <http://www.rocscience.com/help/phase2/webhelp/phase2.htm>, Accessed March 3, 2014.

Rutledge, P. D. (1947). "Cooperative Triaxial Shear Research Program," *Progress Report on Soil Mechanics Fact Finding Survey*, U.S. Army Corps of Engineers Waterways Experiment Station, Vicksburg, MS.

Sanchez, J. M., Sagaseta, C., and Ballester, F. (1979). "Influence of stress history on undrained behaviour of soft clays," *Proceedings 7th European Conference on Soil Mechanics*, Brighton, Vol. 1, 257-261.

Saxena, S. K., Hedberg, J., and Ladd, C. C. (1978). "Geotechnical properties of Hackensack Valley varved clays of New Jersey," *Geotechnical Testing Journal*, ASTM, 1(3), 148-161.

Schnabel Engineering Inc. (2013a). *Calculation Memorandum – Cobbs Creek Rapid Drawdown*, 23 pp.

Schnabel Engineering Inc. (2013b). *CU Test Results, Proposed Embankment Core Material*, Cobbs Creek Dam, 46 pp.

Schnabel Engineering Inc. (2013c). *CU Test Results, Proposed Embankment Shell Material*, Cobbs Creek Dam, 96 pp.

Seed, H. B., Mitchell, J. K., and Chan, C. K. (1960). "The strength of compacted cohesive soils," *Proceedings ASCE Research Conference on the Shear Strength of Cohesive Soils*, ASCE, Boulder, CO, 877-964.

Sherman, W. C. and Clough, G. W. (1968). "Embankment pore pressures during construction," *Journal of the Soil Mechanics and Foundations Division*, 94(SM2), 527-553.

Shibata, T. and Karube, D. (1965). "Influence of the variation of the intermediate principal stress on the mechanical properties of normally consolidated clays," *Proceedings of the 6th ICSMFE*, Vol. 1, Montreal, Quebec, 359-363.

Shibata, T. and Karube, D. (1967). "Discussion of 'Plane strain tests on a saturated remolded clay," *Journal of the Soil Mechanics and Foundations Division*, 93(SM5).

Simons, N. E. (1960). "The effect of overconsolidation on the shear strength characteristics of an undisturbed Oslo clay," *Proceedings ASCE Research Conference on the Shear Strength of Cohesive Soils*, Boulder, CO, 747-763.

Sivakumar, V. and Doran, I. G. (2000). "Yielding characteristics of unsaturated, compacted soils," *Mechanics of Cohesive-Frictional Materials*, 5, 291-303.

Sivakumar, V. and Wheeler, S. J. (2000). "Influence of compaction procedure on the mechanical behavior of an unsaturated compacted clay, Part 1: Wetting and isotropic compression," *Geotechnique*, 50(4), 359-368.

Skempton, A. W. (1954). "The pore pressure coefficients A and B," *Geotechnique*, 4(4), 143-147.

Skempton, A. W. and V. A. Sowa (1963). "The behavior of saturated clays during sampling and testing," *Geotechnique*, 13(4), 269-290.

Sleep, M. D. (2011). *Analysis of transient seepage through levees*, Ph.D. Dissertation, Virginia Tech, Blacksburg, VA, 203 pp.

Sleep, M. D. and Duncan, J. M. (2013). "Effects of initial conditions on the results of transient seepage analyses," *Proceedings of GeoCongress 2013 – Stability and Performance of Slopes and Embankments III*, ASCE, San Diego, CA, 1081-1090.

Sleep, M. D. and Duncan, J. M. (2014). *Manual for Geotechnical Engineering Reliability Calculations*, 2nd Edition, CGPR #76, Virginia Tech, Blacksburg, VA, 75 pp.

Taylor, D. W. (1948). "Chapter 15 – Shearing strength of cohesive soils," *Fundamentals of Soil Mechanics*, John Wiley & Sons, Inc., New York, p. 387.

Terzaghi, K. and Peck, R. B. (1967). "Chapter 5: Plastic equilibrium in soils," *Soil Mechanics in Engineering Practice*, 2nd Edition, John Wiley and Sons, New York, NY, 255-257.

Tinjum, J. M., Benson, C. H., and Blotz, L. R. (1997). "Soil-water characteristic curves for compacted clays," *Journal of Geotechnical and Geoenvironmental Engineering*, 123(11), 1060-1069.

Turnbull, W. J., Compton, J. R., and Ahlvin, R. G. (1966). "Quality control of compacted earthwork," *Journal of the Soil Mechanics and Foundations Division*, 92(SM1), 93-103.

United States Army Corps of Engineers (USACE) (1986). *Seepage Analysis and Control of Dams, Engineer Manual 1110-2-1901*, U.S. Army Corps of Engineers, Washington, DC.

USACE (1984). *Mississippi River Levees Item M-181.1 to 180,2-L Marchand Levee Setback Final Report*, October 1984.

USACE (2003). *Slope stability, Engineer Manual 1110-2-1902*, U.S. Army Corps of Engineers, Washington, D.C. 205 pp.

United States Bureau of Reclamation (USBR) (2011). *Chapter 8: Seepage, Design Standards No. 13 – Embankment Dams*, U.S. Dept. of Interior, 181 pp.

Vaid, Y. P. and Campanella, R. G. (1974). "Triaxial and plane strain behavior of natural clay," *Journal of the Geotechnical Engineering Division*, 100(GT3), 207-224.

van Genuchten, M. Th. (1980). "A closed-form equation for predicting the hydraulic conductivity of unsaturated soils," *Soil Sci. Soc. Amer. J.*, 44, 892-898.

Vanapalli, S. K., Fredlund, D. G. and Pufahl, D. E. (1999). "The influence of soil structure and stress history on the soil-water characteristics of a compacted till," *Geotechnique*, 49(2), 143-159.

Wahler, W. A. and Associates (1970). "Upstream slope drawdown failure investigation and remedial measures, Pilarcitos Dam," *Report to the San Francisco Water Dept.*, as cited in Duncan et al (1990).

Wang, J. L., Vivatrat, V. and Ruser, J. R. (1982). "Geotechnical properties of Alaska OCS marine silts," *Proc. Offshore Tech. Conf.*, Houston, TX, Vol. 4, OTC Paper No. 4412.

Whiteside, S. L. (1976). "A study of the rapid drawdown failure in the Walter Bouldin Dam," *Technical Report CE-211*, Stanford University, August 1976.

Whitman, R. V., Ladd, C. C., and DaCruz, P. (1960). "Discussion to Session 3," *Proceedings ASCE Research Conference on the Shear Strength of Cohesive Soils*, ASCE, Boulder, CO, 1049-1056.

Wong, K. S., Duncan, J. M., and Seed, H. B. (1983). *Comparison of methods of rapid drawdown stability analysis*, Report No. UCB/GT/82-05, University of California, Berkeley, December 1982 – revised July 1983.

Wu, W. and Kolymbas, D. (1991). "On some issues in triaxial extension tests," *Geotechnical Testing Journal*, 14(3), 276-287.

Xu, S.-J., Dang, F.-N., and Qing, H. (2009). "Analysis of stability of dam slope during rapid drawdown of reservoir water level," *Proceedings of 2009 International Conference on Engineering Computation*, Hong Kong, IEEE, 221-224.

Yamamuro, J. A. and Liu, Y. (1995). "Effects of necking and its suppression in axisymmetric extension tests on clay," *Proceedings 16th ICSMGE*, Vol. 2, 633-637.

Yashuhara, K., Yamanoughi, T., and Hirao, K. (1982). "Cyclic strength and deformation of normally consolidated clay," *Soils and Foundations*, 22(3), 78-91.

Appendix A – Derivation of Analytical Method for R_K

A method for estimating $R_K = USR_{ACU} / USR_{ICU}$ was developed based on the assumption made by Taylor (1948). Taylor assumed that an anisotropically consolidated specimen will follow the same stress path as an isotropically consolidated specimen with the same water content. Henkel (1960) noted that lines representing anisotropic consolidation states could be drawn on a plot of axial vs. radial stress, such as the line labeled PSR_c in Figure A-1.

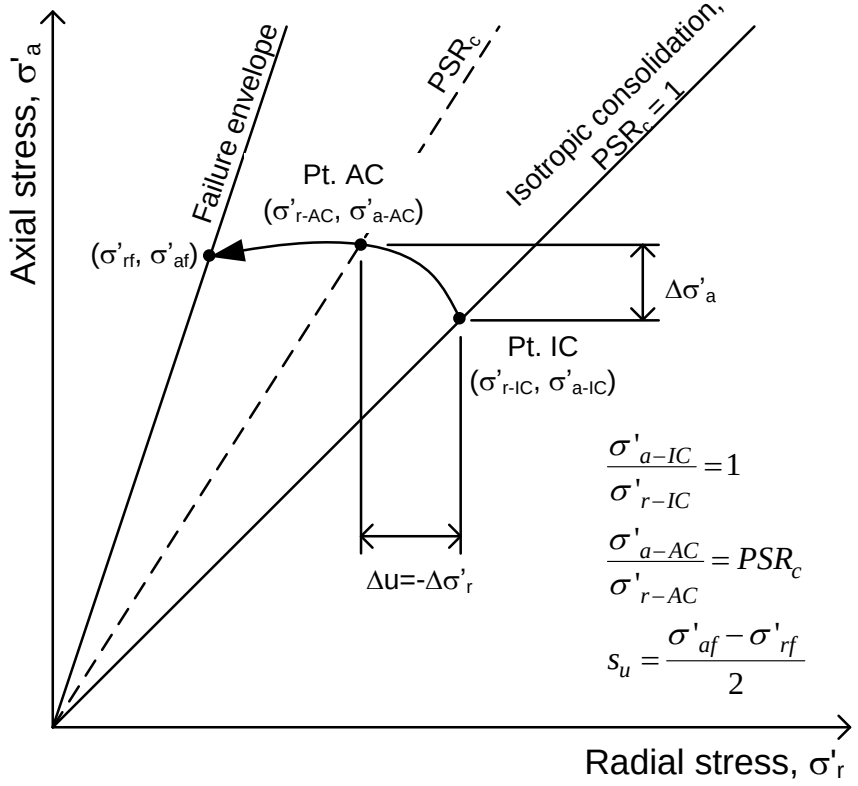

Figure A-1. Undrained effective stress path with both isotropic and anisotropic consolidation

In Figure A-1 isotropic consolidation occurs when the axial and radial stresses are equal at consolidation along the line labeled $PSR_c = 1$. An undrained (constant water content) effective stress path is shown by the curved arrow. Pt. IC represents the start of this stress path at isotropic consolidation line. The point where the dashed PSRc line and the stress path intersect

is labeled Pt. AC. The ratio of σ'_a and σ'_r is equal to PSR_c at this point. Because Pt. AC lies on the same undrained stress path as Pt. IC, Taylor's assumption implies that the undrained strength will be the same for consolidation to either point. Because $\sigma'_{a\text{-}AC}$ is greater than the isotropic value $\sigma'_{a\text{-}IC}$, the undrained strength ratio, *USR*, for anisotropic consolidation will be lower, if they have the same undrained strength.

For normally consolidated Weald clay, Henkel showed that the *USR* for K_0 consolidation is 85% of the value for isotropic consolidation at a consolidated water content of 23%. Similarly, from an undrained test on Boston Blue Clay, Taylor (1948) predicted that the anisotropically USR would be 70 to 90% of the isotropically consolidated value for consolidation stress ratios ranging from 1.5 to 3.6.

Method for Determining R_K

The method starts with Taylor's assumption that effective stress paths are unique for a particular consolidated water content, which allows the effect of anisotropic consolidation on the USR to be quantified. The consolidation stresses for the isotropic ($PSR_c = 1$) and anisotropic ($PSR_c > 1$) states shown in Figure A-1 will be used to derive this method.

The change in effective stress along an ICU triaxial compression stress path with constant cell pressure can be related to the pore pressure response measured in the test. The variation in *PSR* and the pore pressure parameter, *A*, are shown in Figure A-2(a). At a particular value of PSR_c, the corresponding value of A_c can be determined as in Figure A-2(b).

The change in the radial effective stress, $\Delta\sigma'_r$, in an ICU test is the opposite of the change in pore pressure as shown in Figure A-1. Similarly, the change in effective axial stress is equal to the change in the ordinate. From Skempton (1954), the change in pore pressure, Δu, in an ICU triaxial compression test can be expressed as

$$\Delta u = \bar{A}_c \Delta\sigma_1 = \bar{A}_c \Delta\sigma_a \tag{0-1}$$

where $\bar{A}_c$ = the pore pressure parameter corresponding to a particular effective principal stress ratio during undrained shear, PSR_c.

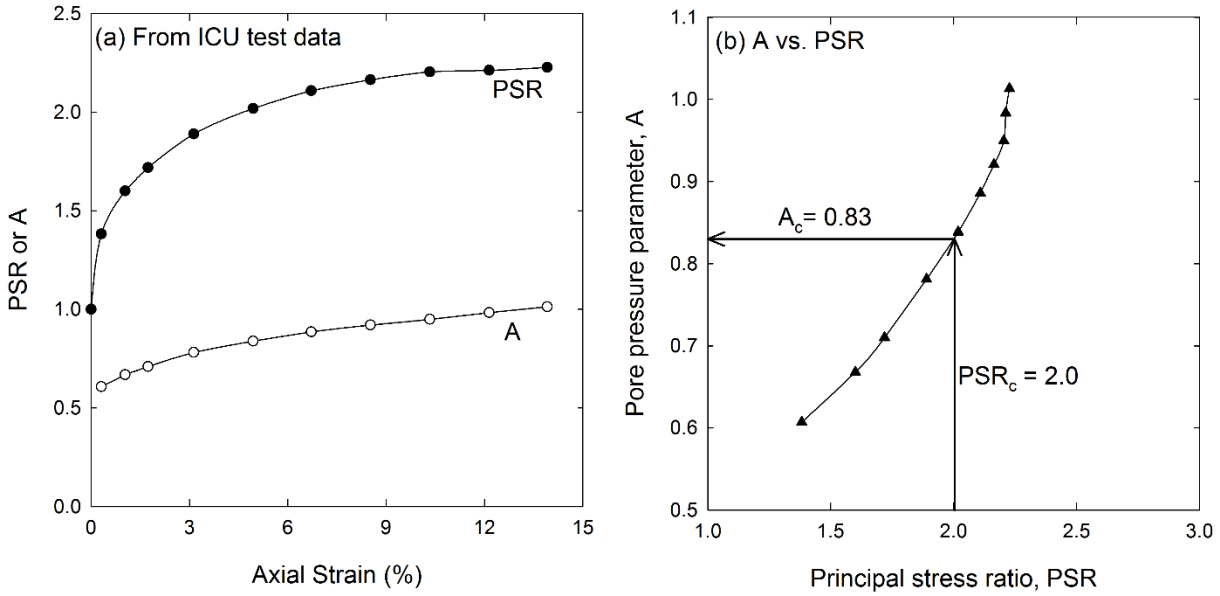

Figure A-2. Relationship between principal stress ratio and pore pressure parameter, $\bar{A}$, during an ICU triaxial test (data from Donaghe and Townsend 1979).

The change in total axial stress can be replaced with the change in effective axial stress plus the change in pore pressure such that

$$\Delta u = \bar{A}_c \left(\Delta\sigma'_a + \Delta u \right) \tag{0-2}$$

The change in pore pressure is the opposite of $\Delta\sigma'_r$. Replacing Δu with $-\Delta\sigma'_r$ and rearranging Eqn. (A-2) yields

$$\frac{\Delta\sigma'_a}{\Delta\sigma'_r} = \frac{\bar{A}_c - 1}{\bar{A}_c} \tag{0-3}$$

The ratio in Eqn. (A-3) is the slope of the line connecting the effective stresses for anisotropic consolidation (Pt. AC) and isotropic consolidation (Pt. IC) at the same consolidated water content. The change in σ'_r for anisotropic consolidation is then simply

$$\Delta\sigma'_r = \frac{\Delta\sigma'_a \bar{A}_c}{\left(\bar{A}_c - 1\right)} \tag{0-4}$$

The effective principal stress ratio can also be used to relate the axial and radial consolidation stresses for any value of PSR_c

$$\sigma'_{a-IC} + \Delta\sigma'_a = PSR_c\left(\sigma'_{a-IC} + \Delta\sigma'_r\right) \tag{0-5}$$

Substituting (A-4) for $\Delta\sigma'_r$ in (A-5) and solving for $\Delta\sigma'_a$,

$$\Delta\sigma'_a = \frac{\left(PSR_c - 1\right)\sigma'_{a-IC}}{1 - \dfrac{PSR_c\bar{A}_c}{\bar{A}_c - 1}} = \frac{\left(\bar{A}_c - 1\right)\left(PSR_c - 1\right)\sigma'_{a-IC}}{\bar{A}_c - 1 - PSR_c\bar{A}_c} \tag{0-6}$$

The effective axial stress for anisotropic consolidation can then be expressed as

$$\sigma'_{a-AC} = \sigma'_{a-IC} + \frac{\left(\bar{A}_c - 1\right)\left(PSR_c - 1\right)\sigma'_{a-IC}}{\bar{A}_c\left(1 - PSR_c\right) - 1} = \sigma'_{a-IC}\left[\frac{PSR_c}{\bar{A}_c\left(PSR_c - 1\right) + 1}\right] \tag{0-7}$$

Assuming the undrained strength for Pt. IC and Pt. AC are identical, the undrained strength ratios for each point are defined using the same s_u as

$$USR_{IC} = \frac{s_u}{\sigma'_{a-IC}} \tag{0-8}$$

and

$$USR_{AC} = \frac{s_u}{\sigma'_{a-AC}} \tag{0-9}$$

The amount of reduction, R_K, in USR resulting from anisotropic consolidation is defined as

$$R_K = \frac{USR_{AC}}{USR_{IC}} = \frac{s_u / \sigma'_{a-AC}}{s_u / \sigma'_{a-IC}} = \frac{\sigma'_{a-IC}}{\sigma'_{a-AC}} \tag{0-10}$$

Inserting Eqn. (A-7), R_K becomes

$$R_K = \frac{\bar{A}_c\left(PSR_c - 1\right) + 1}{PSR_c} \tag{0-11}$$

Eqn. (A-11) can be used to estimate the change in the undrained strength ratio caused by anisotropic consolidation based on the results of an ICU triaxial test using Taylor's assumption. It is evident from Eqn. (A-11) that R_K will be less than 1.0 whenever $\bar{A}_c$ is less than 1.0.

Appendix B – ICU vs. ACU Triaxial Compression Data from Literature

Table B-1. ICU vs. ACU triaxial compression test data for normally consolidated clays

Clay	σ'_{1c} (psi)	Isotropic USR_{IC}	Anisotropic Consolidation PSR_c	%Mob	USR_{AC}	R_K	Specimen type and comments	Reference
Ariake	14	0.649	2.3	44%	0.491	0.76	Remolded, consolidated 1D to 8 psi, stress controlled tests	Yasuhara et al. (1982)
Ariake	28	0.54	2.3	52%	0.455	0.84	Remolded, consolidated 1D to 8 psi, stress controlled tests	Yasuhara et al. (1982)
Ariake	21	0.512	2.3	55%	0.475	0.93	Remolded, consolidated 1D to 8 psi, stress controlled tests	Yasuhara et al. (1982)
Boston Blue	56	0.294	1.92	81%	0.31	1.05	Remolded	Kinner and Ladd (1970)
Boston Blue	84	0.304	2	82%	0.33	1.09	Remolded	Kinner and Ladd (1970)
Boston Blue	57-85	0.303	1.82	74%	0.337	1.11	Remolded, consolidated 1D to 21 psi starting at w% below LL	Ladd (1964)
East Atchafalaya	43	0.318	1.5	52%	0.278	0.87	Remolded, consolidated 1D from slurry to 43 psi	Donaghe and Townsend (1979)
East Atchafalaya	43	0.318	2	79%	0.283	0.89	Remolded, consolidated 1D from slurry to 43 psi	Donaghe and Townsend (1979)
East Atchafalaya	85	0.281	1.5	59%	0.254	0.90	Remolded, consolidated 1D from slurry to 43 psi	Donaghe and Townsend (1979)
Fao clay	31	0.45	2.04	57%	0.38	0.84	Undisturbed, consolidated past σ'_p	Hanzawa (1977a)
Fao clay	89	0.45	2.04	57%	0.38	0.84	Undisturbed, consolidated past σ'_p	Hanzawa (1977a)
Fao clay	116	0.45	2.04	57%	0.38	0.84	Undisturbed, consolidated past σ'_p	Hanzawa (1977a)
Fao clay	28	0.45	2.04	57%	0.39	0.87	Undisturbed, consolidated past σ'_p	Hanzawa (1977a)
Fao clay	7	0.45	2.04	57%	0.41	0.91	Undisturbed, consolidated past σ'_p	Hanzawa (1977a)
Fao clay	49	0.45	2.04	57%	0.41	0.91	Undisturbed, consolidated past σ'_p	Hanzawa (1977a)
Goose Lake	28 to 43	0.361	2	69%	0.292	0.81	Remolded, extruded at LI=0.56, particles possibly oriented parallel to V axis, consolidated to constant mean stresses	Khera and Krizek (1967)
Goose Lake	14 to 21	0.323	1.75	66%	0.327	1.01	Remolded, extruded at LI=0.56, particles possibly oriented parallel to V axis, consolidated to constant mean stresses	Khera and Krizek (1967)
Goose Lake	14 to 21	0.323	1.5	52%	0.329	1.02	Remolded, extruded at LI=0.56, particles possibly oriented parallel to V axis, consolidated to constant mean stresses	Khera and Krizek (1967)
Goose Lake	14 to 21	0.323	2	77%	0.33	1.02	Remolded, extruded at LI=0.56, particles possibly oriented parallel to V axis, consolidated to constant mean stresses	Khera and Krizek (1967)
Goose Lake	14 to 21	0.323	1.25	31%	0.354	1.10	Remolded, extruded at LI=0.56, particles possibly oriented parallel to V axis, consolidated to constant mean stresses	Khera and Krizek (1967)
Grundite	14 - 21	0.389	2	64%	0.285	0.73	Remolded and consolidated to 11 psi in consolidometer	Khera and Krizek (1968)

Table B-1. ICU vs. ACU triaxial compression test data for normally consolidated clays (cont.)

Clay	σ'_{1c} (psi)	Isotropic USR_{IC}	Anisotropic Consolidation PSR_c	%Mob	USR_{AC}	R_K	Specimen type and comments	Reference
Grundite	14 - 21	0.389	1.5	43%	0.303	0.78	Remolded and consolidated to 11 psi in consolidometer	Khera and Krizek (1970)
Guanabara Bay		0.295			0.283	0.96	Undisturbed, SHANSEP procedure	Ramalho-Ortiago et al. (1983)
Hackensack	43	0.219	1.54	80%	0.232	1.06	Undisturbed, varved clay	Saxena, Hedberg, and Ladd (1978)
Hokkaido A - Sample 1	28 to 142	0.42	2.22	65%	0.4	0.95	Remolded, consolidated from slurry to 11 psi	Mitachi and Kitago (1976)
Hokkaido B - Sample 2	28 to 142	0.36	2.22	76%	0.34	0.94	Remolded, consolidated from slurry to 11 psi	Mitachi and Kitago (1976)
Hokkaido C - Sample 3	28 to 142	0.41	2.13	65%	0.36	0.88	Remolded, consolidated from slurry to 11 psi	Mitachi and Kitago (1976)
Kaolin - Hydrite R	500	0.31	2	81%	0.275	0.89	Consolidated from slurry 1D to 492 psi, rebounded and tested	Holtz and Krizek (1971)
Kaolin - Hydrite R	500	0.29	2	86%	0.28	0.97	Consolidated from slurry 1D to 492 psi, rebounded and tested	Holtz and Krizek (1971)
Kawasaki	21-84	0.45	1.92	53%	0.42	0.93	Undisturbed	Ladd (1965)
Kawasaki	43	0.403	2	62%	0.441	1.09	Undisturbed	Ladd (1964)
Kawasaki M10	28-57	0.553	2.38	52%	0.375	0.68	Remolded, consolidated from slurry to 10 psi, number in name refers to approx. PI	Nakase and Kamei (1983)
Kawasaki M15	28-57	0.522	2.50	57%	0.385	0.74	Remolded, consolidated from slurry to 10 psi, number in name refers to approx. PI	Nakase and Kamei (1983)
Kawasaki M20	28-57	0.507	2.44	58%	0.394	0.78	Remolded, consolidated from slurry to 10 psi, number in name refers to approx. PI	Nakase and Kamei (1983)
Kawasaki M30	28-57	0.505	2.44	58%	0.405	0.80	Remolded, consolidated from slurry to 10 psi, number in name refers to approx. PI	Nakase and Kamei (1983)
Khor-Al-Zubair	21-52	0.46	2.02	55%	0.335	0.73	Undisturbed, USR_{IC} is average of three tests, USR_{AC} consolidated past in-situ stress	Hanzawa (1977b)
Kyoto-Sample 2	14	0.43	2.22	64%	0.37	0.86	Remolded at LI=0.65, packed into mold, 1D consol to 7-10 psi, trimmed, A_f = 0.64-0.67 (maybe not completely NC)	Akai and Adachi (1965)
Kyoto-Sample 2	71	0.43	2.22	64%	0.41	0.95	Remolded at LI=0.65, packed into mold, 1D consol to 7-10 psi, trimmed, A_f = 0.64-0.67 (maybe not completely NC)	Akai and Adachi (1965)
Kyoto-Sample 2	43	0.43	2.22	64%	0.42	0.98	Remolded at LI=0.65, packed into mold, 1D consol to 7-10 psi, trimmed, A_f = 0.64-0.67 (maybe not completely NC)	Akai and Adachi (1965)
Mississippi Backswamp	95	0.254	1.74	84%	0.249	0.98	Remolded, consolidated from slurry and trimmed	Whitman, Ladd, and daCruz (1960)
Mississippi Backswamp	43	0.298	1.97	83%	0.298	1.00	Remolded, consolidated from slurry and trimmed	Whitman, Ladd, and daCruz (1960)
Mississippi Backswamp	100	0.286	1.45	54%	0.259	0.91	Remolded, consolidated from slurry and trimmed	Whitman, Ladd, and daCruz (1960)

Table B-1. ICU vs. ACU triaxial compression test data for normally consolidated clays (cont.)

Clay	σ'_{1c} (psi)	Isotropic USR_{IC}	Anisotropic Consolidation PSR_c	%Mob	USR_{AC}	R_K	Specimen type and comments	Reference
Osaka	14	0.473	2	53%	0.401	0.85	Remolded at LI > 1	Shibata and Karube (1967)
Oslo	57	0.36	2	69%	0.32	0.89	Undisturbed, initial w% vary	Simons (1960)
Peerless #1	28	0.469	1.45	33%	0.37	0.79	Remolded, tamped in mold at LI=1, hollow cylinder test	Broms and Ratnam (1963)
Peerless #1	7	0.469	1.45	33%	0.414	0.88	Remolded, tamped in mold at LI=1, hollow cylinder test	Broms and Ratnam (1963)
Peerless #1	26	0.469	1.45	33%	0.436	0.93	Remolded, tamped in mold at LI=1, triaxial	Broms and Ratnam (1963)
Peerless #1	92	0.469	1.45	33%	0.508	1.08	Remolded, tamped in mold at LI=1, hollow cylinder test	Broms and Ratnam (1963)
Peerless #2	7	0.469	1.75	46%	0.425	0.91	Remolded - tamped in mold at LI=1, hollow cylinder, b = 0.5, $PSRc = 2*\sigma'_{1c}/(\sigma'_{2c}+\sigma'_{3c})$	Broms and Ratnam (1963)
Peerless #3	28	0.469	1.75	46%	0.377	0.80	Remolded - tamped in mold at LI=1, hollow cylinder, b = 0.5, $PSRc = 2*\sigma'_{1c}/(\sigma'_{2c}+\sigma'_{3c})$	Broms and Ratnam (1963)
Peerless #4	92	0.469	1.75	46%	0.393	0.84	Remolded - tamped in mold at LI=1, hollow cylinder, b = 0.5, $PSRc = 2*\sigma'_{1c}/(\sigma'_{2c}+\sigma'_{3c})$	Broms and Ratnam (1963)
Plastic Holocene	35	0.324			0.322	0.99	Undisturbed, consolidated to NC, K_0 not given	Koutsoftas (1978,1982)
San Fransisco	29.82	0.33	1.54	53%	0.29	0.88	Undisturbed, TC-SR test	Duncan and Seed (1965)
San Fransisco	41.18	0.33	1.84	69%	0.35	1.06	Undisturbed	Duncan and Seed (1965)
Santander	24	0.215	1.12	26%	0.248	1.15	Remolded, consolidated 1D from LI=2 to 3.5 psi in a split mold, central sand drain, lubricated platens with oil confining, unusual stress-strain curves	Sanchez et al. (1979)
Santander	27	0.215	1.25	47%	0.266	1.24	Remolded, consolidated 1D from LI=2 to 3.5 psi in a split mold, central sand drain, lubricated platens with oil confining, unusual stress-strain curves	Sanchez et al. (1979)
Santander	30	0.215	1.43	70%	0.29	1.35	Remolded, consolidated 1D from LI=2 to 3.5 psi in a split mold, central sand drain, lubricated platens with oil confining, unusual stress-strain curves	Sanchez et al. (1979)
Santander	36	0.215	1.67	93%	0.305	1.42	Remolded, consolidated 1D from LI=2 to 3.5 psi in a split mold, central sand drain, lubricated platens with oil confining, unusual stress-strain curves	Sanchez et al. (1979)
Sapporo	29-86	0.383	1.9	62%	0.301	0.79	Remolded, consolidated 1D	Mitachi and Kitago (1979)
Silty Holocene	35	0.352			0.325	0.92	Undisturbed, consolidated to NC	Koutsoftas (1978,1982)
Skabo	28-84	0.32	2.13	83%	0.32	1.00	Undisturbed, from Landva (1962), no stress paths	Ladd (1965)
Spestone	80	0.211	1.56	85%	0.209	0.99	Remolded, consolidated 1D from slurry to 29 psi, extruded, trimmed, and tested	Parry and Nadarajah (1973)

Table B-1. ICU vs. ACU triaxial compression test data for normally consolidated clays (cont.)

Clay	σ'_{1c} (psi)	Isotropic USR_{IC}	Anisotropic Consolidation PSR_c	%Mob	USR_{AC}	R_K	Specimen type and comments	Reference
VBC	43	0.402	1.5	41%	0.35	0.87	Remolded	Donaghe and Townsend (1979)
VBC	43	0.402	2	62%	0.353	0.88	Remolded	Donaghe and Townsend (1979)
VBC	85	0.335	1.5	50%	0.305	0.91	Remolded	Donaghe and Townsend (1979)
VBC	85	0.335	2	75%	0.321	0.96	Remolded	Donaghe and Townsend (1979)
Vicksburg Buckshot	56 - 84	0.28	1.85	82%	0.28	1.00	Remolded	Ladd (1965)
Wallaceburg		0.32	1.96	77%	0.31	0.97	Undisturbed	Delory and Salvas (1969)
Weald	120-167	0.323	1.68	63%	0.257	0.80	Remolded, formed at an LI of about 0.5	Henkel and Sowa (1963)
Weald	30 - 170	0.319	1.67	63%	0.282	0.88	Remolded, average values for full range of stress	Skempton and Sowa
Whitefish Falls		0.31	2.08	84%	0.33	1.06	Undisturbed	Delory and Salvas (1969)

Table B-2. ICU vs. ACU triaxial compression test data for overconsolidated clays

Clay	σ'_{1c} (psi)	OCR	Isotropic USR_{IC}	Anisotropic Consol. PSR_c	%Mob	USR_{AC}	R_K	Specimen type and comments	Reference
Boston Blue	85	4	0.900	1.00	0%	0.920	1.02	Remolded	Kinner and Ladd (1970)
East Atchafalaya	21	2	0.423	1.50	39%	0.368	0.87	Consolidated from slurry to 43 psi	Donaghe and Townsend (1979)
East Atchafalaya	21	2	0.423	2.00	59%	0.369	0.87	Consolidated from slurry to 43 psi	Donaghe and Townsend (1979)
East Atchafalaya	7	6	0.780	1.50	21%	0.655	0.84	Consolidated from slurry to 43 psi	Donaghe and Townsend (1979)
Guanabara Bay		1.5	0.421			0.321	0.76	SHANSEP, K_0 values not reported, presumed swell at K_0	Ramalho-Ortiago et al. (1983)
Guanabara Bay		2	0.524			0.435	0.83	SHANSEP, K_0 values not reported, presumed swell at K_0	Ramalho-Ortiago et al. (1983)
Guanabara Bay		3	0.708			0.563	0.79	SHANSEP, K_0 values not reported, presumed swell at K_0	Ramalho-Ortiago et al. (1983)
Guanabara Bay		4	0.880			0.690	0.78	SHANSEP, K_0 values not reported, presumed swell at K_0	Ramalho-Ortiago et al. (1983)
Guanabara Bay		8	1.249			0.931	0.75	SHANSEP, K_0 values not reported, presumed swell at K_0	Ramalho-Ortiago et al. (1983)
North Sea	36		0.640	1.80	35%	0.569	0.89	Stress paths appear to fit Taylor hypothesis well	Berre (1982)
North Sea	36		0.640	1.80	35%	0.502	0.78	Stress paths appear to fit Taylor hypothesis well	Berre (1982)

Table B-2. ICU vs. ACU triaxial compression test data for overconsolidated clays (cont.)

Clay	σ'_{1c} (psi)	OCR	Isotropic USR_{IC}	Anisotropic Consol. PSR_c	%Mob	USR_{AC}	R_K	Specimen type and comments	Reference
Oslo	28	6	1.110	2.20	25%	1.170	1.05	AC to 171 psi, rebound AC to lower stress, reconsolidated IC or AC to test stresses	Simons (1960)
Oslo	42	4	0.890	2.08	29%	0.870	0.98	AC to 171 psi, rebound AC to lower stress, reconsolidated IC or AC to test stresses	Simons (1960)
Oslo	14	12	1.750	2.06	15%	1.650	0.94	AC to 171 psi, rebound AC to lower stress, reconsolidated IC or AC to test stresses	Simons (1960)
Oslo	7	24	2.680	2.17	10%	2.970	1.11	AC to 171 psi, rebound AC to lower stress, reconsolidated IC or AC to test stresses	Simons (1960)
Peerless	12	12	1.170	1.45	13%	0.940	0.80	Remolded, hollow cylinder	Broms and Ratnam (1963)
Peerless	12	12	1.170	1.45	13%	1.117	0.95	Remolded, triaxial	Broms and Ratnam (1963)
Peerless	39	3.6	0.704	1.45	22%	0.651	0.92	Remolded, Hollow cylinder	Broms and Ratnam (1963)
Peerless	39	3.6	0.704	1.45	22%	0.609	0.87	Remolded, triaxial	Broms and Ratnam (1963)
Peerless	10	13	1.276	1.75	17%	0.942	0.74	Remolded, hollow cylinder, b = 0.5, $PSR_c = 2*\sigma'_{1c}/(\sigma'_{2c}+\sigma'_{3c})$	Broms and Ratnam (1963)
Peerless	36	3.6	0.732	1.75	29%	0.623	0.85	Remolded, hollow cylinder, b = 0.5, $PSR_c = 2*\sigma'_{1c}/(\sigma'_{2c}+\sigma'_{3c})$	Broms and Ratnam (1963)
Spestone	61	1.3	0.271	1.33	46%	0.276	1.02	Consolidated from slurry to 29 psi, extruded trimmed, consolidated to 80 psi, and swelled slightly all at K_0 conditions	Parry and Nadarajah (1973)
Spestone	50	1.6	0.294	1.19	27%	0.333	1.13	Consolidated from slurry to 29 psi, extruded trimmed, consolidated to 80 psi, and swelled slightly all at K_0 conditions	Parry and Nadarajah (1973)
Spestone	35	2.3	0.771	1.03	2%	0.824	1.07	Consolidated from slurry to 29 psi, extruded trimmed, consolidated to 80 psi, and swelled slightly all at K_0 conditions	Parry and Nadarajah (1973)
VBC	21	2	0.557	1.50	30%	0.527	0.95	Consolidated from slurry to 43 psi	Donaghe and Townsend (1979)
VBC	21	2	0.557	2.00	45%	0.523	0.94	Consolidated from slurry to 43 psi	Donaghe and Townsend (1979)
VBC	7	6	1.230	1.50	14%	1.200	0.98	Consolidated from slurry to 43 psi	Donaghe and Townsend (1979)
VBC	7	6	1.230	2.00	20%	1.160	0.94	Consolidated from slurry to 43 psi	Donaghe and Townsend (1979)
Weald	61-79	2	0.534	1.27	20%	0.457	0.86	Formed at an LI of about 0.5	Henkel and Sowa (1963)
Weald	31-39	4	0.823	1.00	0%	0.799	0.97	Formed at an LI of about 0.5	Henkel and Sowa (1963)
Weald	15-17	8	1.370	1.35	9%	1.151	0.84	Formed at an LI of about 0.5, $K_0>1$, actually TC with SR test	Henkel and Sowa (1963)

Table B-3. ICU vs. ACU triaxial compression test data for compacted clays

Clay	σ'_{1c} (psi)	Isotropic USR_{IC}	Anisotropic Consol. PSR_c	%Mob	USR_{AC}	R_K	Specimen type and comments	Reference
Higgins	118	0.400	2.00	63%	0.360	0.90	Compacted, dry of optimum, USR-IC interpolated	Lee and Morrison (1970)
Higgins	485	0.300	2.00	83%	0.290	0.97	Compacted, dry of optimum, USR-IC interpolated	Lee and Morrison (1970)
Higgins	118	0.470	2.00	53%	0.410	0.87	Compacted, wet of optimum, USR-IC interpolated	Lee and Morrison (1970)
Higgins	490	0.300	2.00	83%	0.310	1.03	Compacted, wet of optimum, USR-IC interpolated	Lee and Morrison (1970)
Monarch	28.5	0.592	2.00	42%	0.770	1.30	Compacted, wet of optimum, USR-IC based on a power curve fit	Lee and Morrison (1970)
Monarch	167	0.441	2.00	57%	0.380	0.86	Compacted, wet of optimum, USR-IC based on a power curve fit	Lee and Morrison (1970)
Monarch	280	0.404	2.00	62%	0.380	0.94	Compacted, wet of optimum, USR-IC based on a power curve fit	Lee and Morrison (1970)
Monarch	493	0.368	2.00	68%	0.310	0.84	Compacted, wet of optimum, USR-IC based on a power curve fit	Lee and Morrison (1970)
Monarch	849	0.336	2.00	74%	0.280	0.83	Compacted, wet of optimum, USR-IC based on a power curve fit	Lee and Morrison (1970)
Monarch	1448	0.307	2.00	81%	0.270	0.88	Compacted, wet of optimum, USR-IC based on a power curve fit	Lee and Morrison (1970)
Monarch	1515	0.305	2.00	82%	0.270	0.89	Compacted, wet of optimum, USR-IC based on a power curve fit	Lee and Morrison (1970)
Monarch	2430	0.282	2.00	89%	0.270	0.96	Compacted, wet of optimum, USR-IC based on a power curve fit	Lee and Morrison (1970)
Monarch	2820	0.275	2.00	91%	0.260	0.95	Compacted, wet of optimum, USR-IC based on a power curve fit	Lee and Morrison (1970)
Monarch	3609	0.264	2.00	95%	0.260	0.98	Compacted, wet of optimum, USR-IC based on a power curve fit	Lee and Morrison (1970)
Monarch	34	0.575	2.25	48%	0.630	1.10	Compacted, wet of optimum, USR-IC based on a power curve fit	Lee and Morrison (1970)
Monarch	182	0.435	2.25	64%	0.350	0.80	Compacted, wet of optimum, USR-IC based on a power curve fit	Lee and Morrison (1970)
Monarch	358	0.388	2.25	72%	0.310	0.80	Compacted, wet of optimum, USR-IC based on a power curve fit	Lee and Morrison (1970)
Monarch	553	0.361	2.25	77%	0.300	0.83	Compacted, wet of optimum, USR-IC based on a power curve fit	Lee and Morrison (1970)
Monarch	250	0.400	2.00	63%	0.400	1.00	Compacted, wet of optimum, USR-AC interpolated	Lee and Morrison (1970)
Monarch	250	0.400	2.21	68%	0.352	0.88	Compacted, wet of optimum, USR-AC interpolated	Lee and Morrison (1970)
Riverview	35	0.982	2.12	27%	0.727	0.74	Compacted about 5% wet of optimum	Castellanos (2011)
Riverview	55	0.649	2.01	39%	0.619	0.95	Compacted about 5% wet of optimum	Castellanos (2011)
St. Croix	15	0.527	1.50	32%	0.612	1.16	Compacted at optimum, low energy, similar ICU and ACU shaped stress paths, USR_{IC} interpolated	Johnson and Lovell (1979)
St. Croix	30	0.407	1.50	41%	0.399	0.98	Compacted at optimum, low energy, similar ICU and ACU shaped stress paths, USR_{IC} interpolated	Johnson and Lovell (1979)
St. Croix	60	0.358	1.50	47%	0.347	0.97	Compacted at optimum, low energy, similar ICU and ACU shaped stress paths, USR_{IC} interpolated	Johnson and Lovell (1979)

Appendix C – Example FEA Embankment Stress Analyses

This appendix contains instructions for two example finite element stress analyses. These examples assume the reader is familiar with Phase^2's terminology and general operation but unfamiliar with the options for initial conditions or the implementation of staged construction in Phase^2.

- Example 1 – illustrates the impact of different initial conditions options on the horizontal stresses calculated for level ground.
- Example 2 – illustrates the process of creating a staged embankment stress model using Phase^2.

Example 1 – Initial Stresses in Level Ground

This example shows how the initial conditions and finite element formulation (effective vs. total stress) affect the simulation of a well-defined geotechnical problem. The goal is to model K_0 stress conditions below level ground shown in Figure C-1. The analysis will use a single stage, i.e. it is a "gravity turn-on" analysis. The method for creating a "Mapped Mesh" in Phase^2 with elements of uniform size and shape is also illustrated.

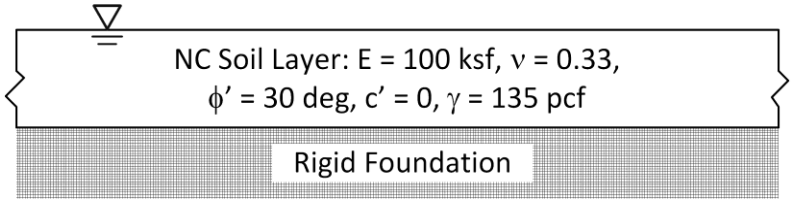

Figure C-1. Soil conditions modeled in Example 1

Analysis Steps

1. Create the FE model
    a. Draw the model shown below in Phase^2 Modeler.

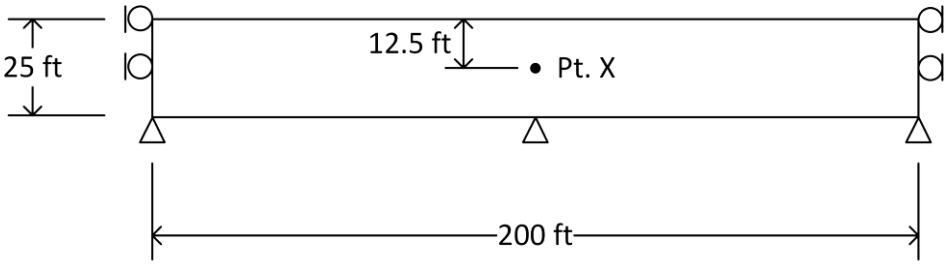

    b. Specify the soil material properties listed below
        i. Linear elastic constitutive model: E = 100,000 psf, ν = 0.33
        ii. Soil strength (a peripheral part of this analysis): ϕ' = 30°, c' = 0 psf
        iii. Soil total unit weight: 135 pcf
        iv. Select "Field Stress & Body Force" from the *Initial Element Loading* drop-down menu.
    c. Draw a *Piezometric Line* coincident with the top boundary of the model.
2. Discretize and Mesh – Uniform element shape or "Mapped Mesh"
    a. Five layers of uniformly shaped 8-node quadrilateral elements will be used for this analysis. Select this element type in the *Mesh Setup* menu.
    b. Discretize the model and then use the *Custom Discretize* tool  to discretize the side boundaries into 5 elements per segment and the bottom and top boundaries into 20 elements per segment.
    c. *Mesh* the model. It will initially consist of irregularly shaped elements.

d. Under *Mesh / Mapped Mesh*, select the *Automatic Mapped Mesh* option. The model should adjust to 100 rectangular elements. If it does not, the discretization must be incorrect.

3. FE Formulation

   a. The type of finite element formulation is changed in the *Project Settings* dialog box under *Analysis*.

   b. Under the *Stress Analysis* settings, make sure the "Use effective stress analysis" box is unchecked to start with a total stress formulation.

4. Initial Element Conditions

   a. Right-click the "Stress block" at the upper right-hand corner of the Modeler window and select "Field Stress…"

   b. In the *Field Stress Type* menu, select "Gravity".

   c. Select "Use the actual ground surface" and make sure the "Use effective stress ratio" box is unchecked to start with a *Total Stress Ratio*.

   d. Enter "0.5" in both of the *Stress Ratio* boxes.

The initial conditions are now set to apply *Body Forces* (self-weight) to the elements when initialized. The *Field Stress* option will apply a stress system that counteracts the *Body Forces* and prevents initial deformation from occurring in the model. The horizontal stress portion of the *Field Stress* will be calculated using a *Total Stress Ratio,* $\sigma_h / \sigma_v = 0.5$. A total stress formulation has been selected that does not take pore pressures into account when solving for equilibrium.

5. Compute the FE model and open the results in the *Interpret* program.

6. Create a query in the middle of the model from (100, 12.5) to (100, 25).

   a. Find the effective vertical and horizontal stresses at (100, 12.5) – Pt. X.

   b. Find the vertical displacement at the ground surface above Pt. X or (100, 25).

7. Repeat the analysis for the following combinations of conditions by changing options in Steps 1.b.iv, 3b, and 4c, respectively:
    a. *Field Stress & Body Forces*, effective stress analysis, and total stress ratio = 0.5
    b. *Field Stress & Body Forces*, total stress analysis, and effective stress ratio = 0.5
    c. *Field Stress & Body Forces*, effective stress analysis, and effective stress ratio = 0.5
    d. *Body Forces Only*, total stress analysis, and field stress ratio not applicable
    e. *Body Forces Only*, effective stress analysis, and field stress ratio not applicable

Discussion of Results

Calculation of the expected σ'_h for K_0 = 0.5 is shown Figure C-2. Since the problem is an existing soil layer with no new loading, no surface displacement is expected. The results of the six trial analyses with different initial stress conditions and finite element formulations are summarized in Table C-1. The *Total Stress Ratio* option for the *Field Stresses* does not give the correct horizontal stress for either type of formulation when the model has pore pressures. The only exception to this would be for cases where K = 1. The *Effective Stress Ratio* results in the correct horizontal stress with either type of FE formulation. All of the analyses with the *Field Stress* option have no displacements at the ground surface. This is a direct result of the field stresses which counteract deformations due to the stresses induced by the body forces.

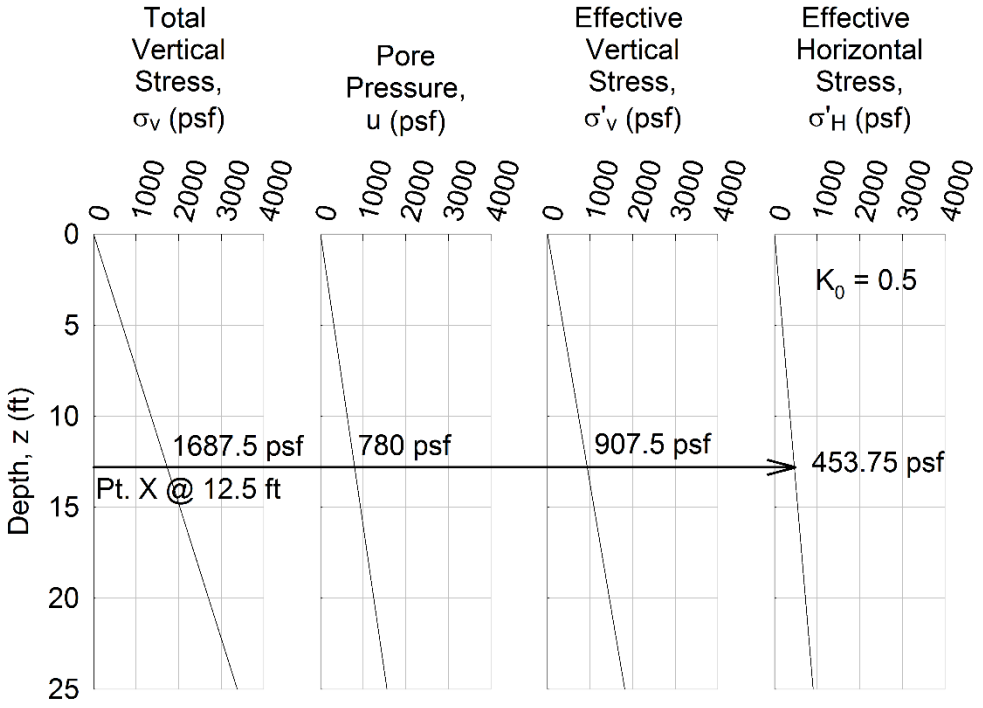

Figure C-2. Calculation of the expected result for the horizontal stress at the middle of the soil layer

Table C-1. Results of Example 1 FE analyses

Initial Element Loading	Field Stress & Body Forces	Field Stress & Body Forces	Body Forces Only
Field Stress Ratio	Total: $K = \sigma_h / \sigma_v$	Total: $K = \sigma'_h / \sigma'_v$	N/A
Total Stress Formulation	σ'_h = 63 psf (Wrong) s = 0 ft (OK)	σ'_h = 454 psf (Right) s = 0 ft (OK)	σ'_h = 51 psf (Wrong) s = 0.3 ft (OK)
Effective Stress Formulation	σ'_h = 63 psf (Wrong) s = 0 ft (OK)	σ'_h = 454 psf (Right) s = 0 ft (OK)	σ'_h = 447 psf (OK) s = 0.15 ft (OK)

The Body Forces Only option does not work with the Total Stress formulation because the program solves for equilibrium based on the total stresses and then subtracts the pore pressures. The effective stress formulation produces a value of σ'_h that is close to correct. The error is due

to the approximation of $\nu = K_0 / (1 + K_0)$. If a value of ν closer to 1/3 is used, the value of σ'_h will approach that calculated in Figure C-2. The Body Forces Only option results in a surface settlement because the weight of the elements induces deformation. These extraneous displacements can be easily zeroed in Phase^2 using the *Displacements / Reset All Displacements…* option.

Example 2 – Staged Construction, Reservoir Loading, and Pore Pressures

This example will step through creating an embankment model in stages, adding a boundary water load in stages, and applying pore pressures in stages. This example focuses on the steps for creating the model, and not the results, so the strengths and material properties are not considered.

Analysis Steps

1. Draw a 25 ft high embankment with 3H:1V slopes and a 25 ft wide crest as shown below.

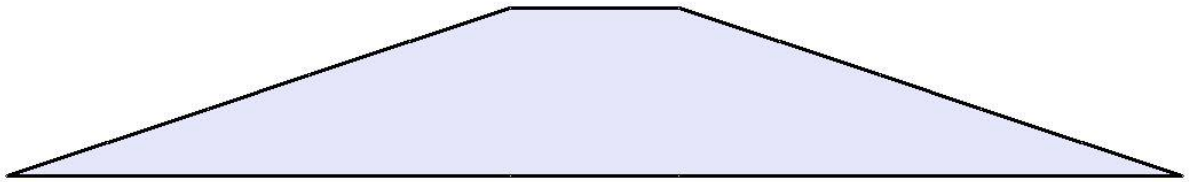

2. Use the *Add Stage* tool  to draw four stage lines at 5 ft increments between the base and the crest. The model should now look like this:

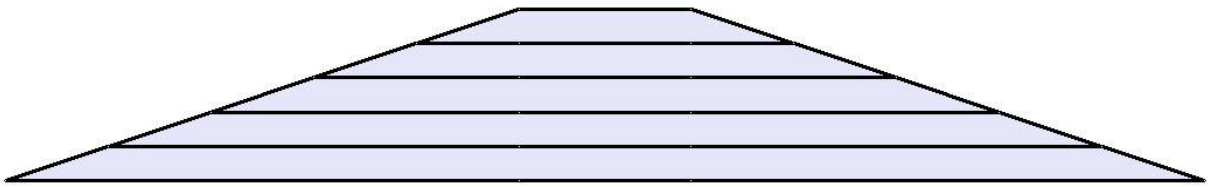

3. Add stages to the model using the *Project Settings* window. Under *Stages*, change the number of stages to 13 (five for the embankment fill, four for the water load, and four for the pore pressures). Stage tabs will appear at the bottom of the Modeler window. These can be renamed for easier reference by right-clicking on the stage tab.
4. Discretize and mesh the model, if this has not yet been performed. The layer staging can be performed before or after the model is meshed. This example will not be concerned with a Mapped Mesh but this could be performed following Example 1, Step 2.
5. Staging the lifts of elements
    a. Select the Stage 1 tab.
    b. Right-click in the gray area of the model and select *Assign Material / More Properties…*
    c. Select *Excavate* at the bottom of the *Assign* window as shown below. As long as this window is open, the elements in a region bounded by a Material or Stage lines can be "excavated" from the model. This means that the elements will not be used for the current stage or any subsequent stages. Mistakes can be corrected by selecting a Material in the *Assign* window and reselecting the portion of the model which was mistakenly excavated.

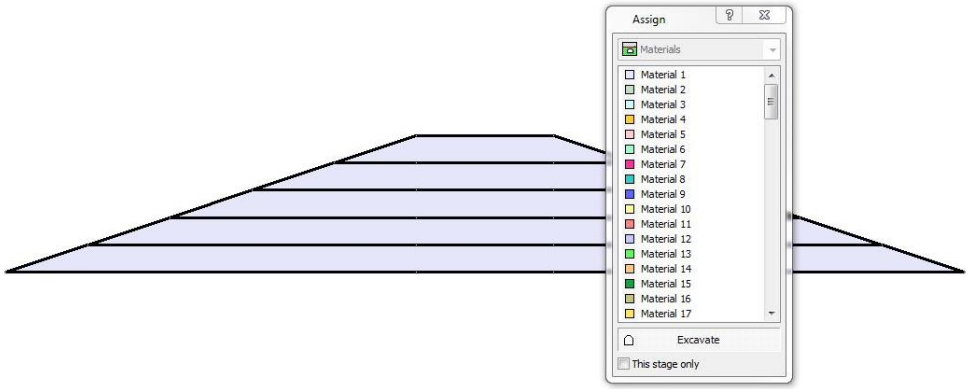

d. With Excavate selected and the model on Stage 1, click on the top four layers of the model. These areas should turn white for this stage and all subsequent stages, indicating that they are excavated. The model should now look like this for all of the stages

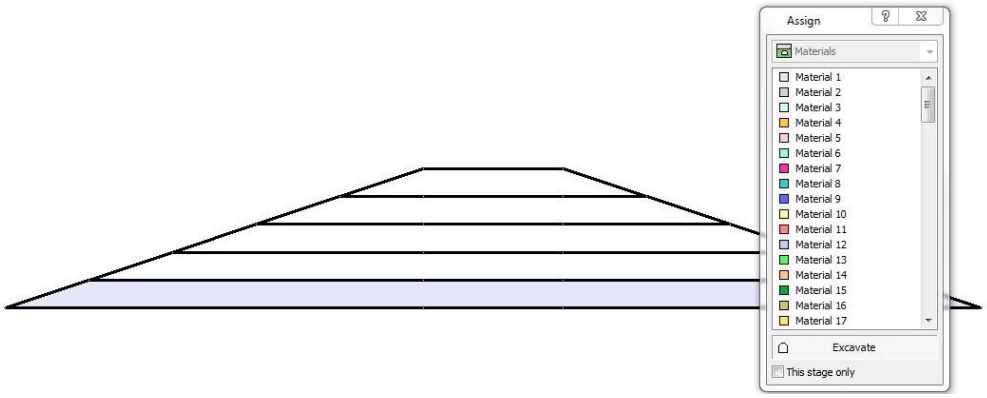

e. The rest of the embankment must now be constructed by adding the elements one lift at a time in Stages 2 to 5. Click on Material 1 in the *Assign* window.

   i. Change to Stage 2 and click in the second layer to turn the elements on.

   ii. Change to Stage 3 and click in the third layer to turn the elements on.

   iii. Repeat through Stage 5.

f. The embankment will now progressively build up in five layers in Stages 1 through 5. The layers will remain in place throughout Stages 6 to 13.

6. Specify *Free* boundary conditions for the nodes on the upper three surfaces and *Fixed* for the base nodes.

7. Add Staged Boundary Water Load

   a. Select *Loading / Distributed Loads / Add Ponded Water Load…*

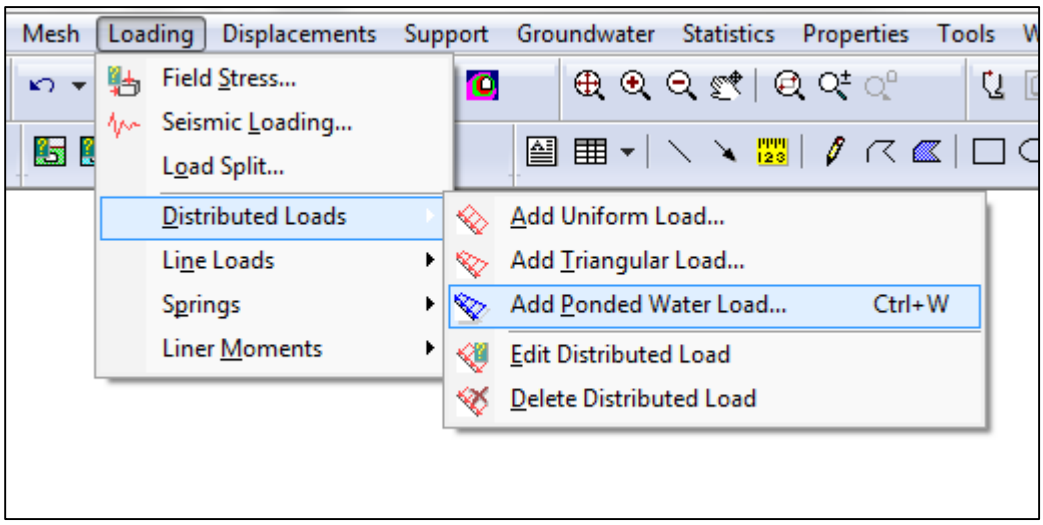

   b. Enter the Total Head in the box. Use 20 ft for this example.

   c. Make sure the *Normal to boundary* radio button is selected.

   d. Select the *Stage Load* checkbox.

   e. Click the *Stage Total Head…* button.

   f. Uncheck the boxes for the first five stages. These correspond to building the embankment.

   g. For Stages 6 to 9, change the Total Head value to 5, 10, 15, and 20, respectively. This will increase the total head boundary water load by five feet in each of these stages.

h. Leave the last four stages at a total head of 20 ft and select OK twice. Select the lower four segments of the slope with the square cursor that appears. Hit enter to apply the Water Load.

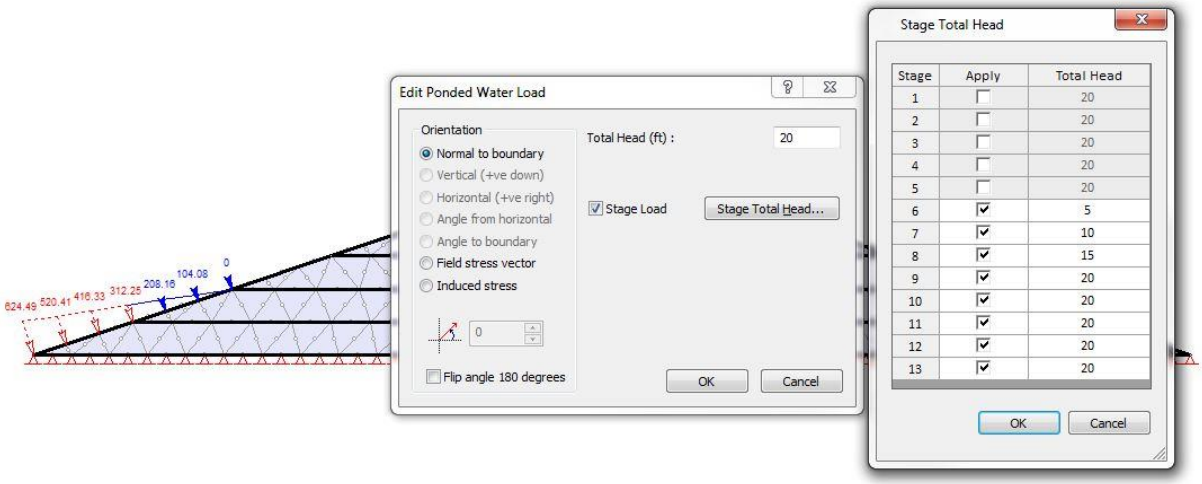

i. Click through Stages 5 through 9. The distributed water load should progressively appear and become larger with each stage.

8. Apply Internal Pore Pressures

a. Calculate the pore pressures corresponding to steady state seepage using a separate Phase^2 model or some other method. Export values of pore pressure for an array of (x, y) coordinates. Calculate the appropriate pore pressures to apply in each step. In this case for four stages, increase the pore pressures by 25% of the steady state values in each stage. For example if the steady state pore pressure is 1000 psf at a point, it will be assigned 250 psf in Stage 10, 500 psf in Stage 11, 750 psf in Stage 12, and 1000 psf in Stage 13.

b. Under *Project Settings / Groundwater*, select *Grid (Pore Pressure)* from the *Method* menu.

c. Select *Groundwater / Water Pressure Grid…*

   i. Paste the (x, y, pore pressure) values for the first PWP stage into the window.

   ii. Use the *Add* button to create space for the other three arrays of pore pressures. Paste each of these as appropriate.

   iii. Rename the Water Pressure Grids for convenient reference.

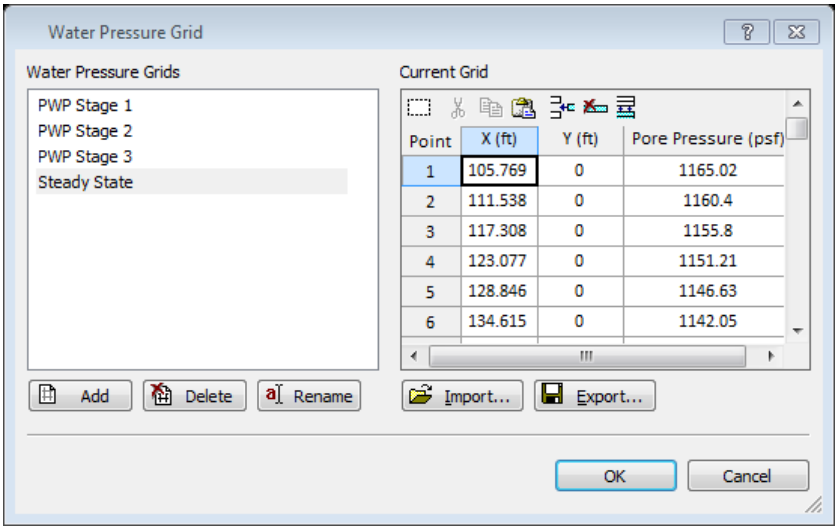

d. Select *Properties / Define Hydraulic…* to assign the water pressure grids to various stages of the model.

   i. Under Material 1, check the *Stage Grids* box.

   ii. Click the *Add Stage* button four times.

   iii. Click on the Grid Name for Stage 1 and select *None*.

iv. Change the next Stage to *10* and select Grid Name *PWP Stage 1*. Repeat for Stages 11 to 13 resulting in the following:

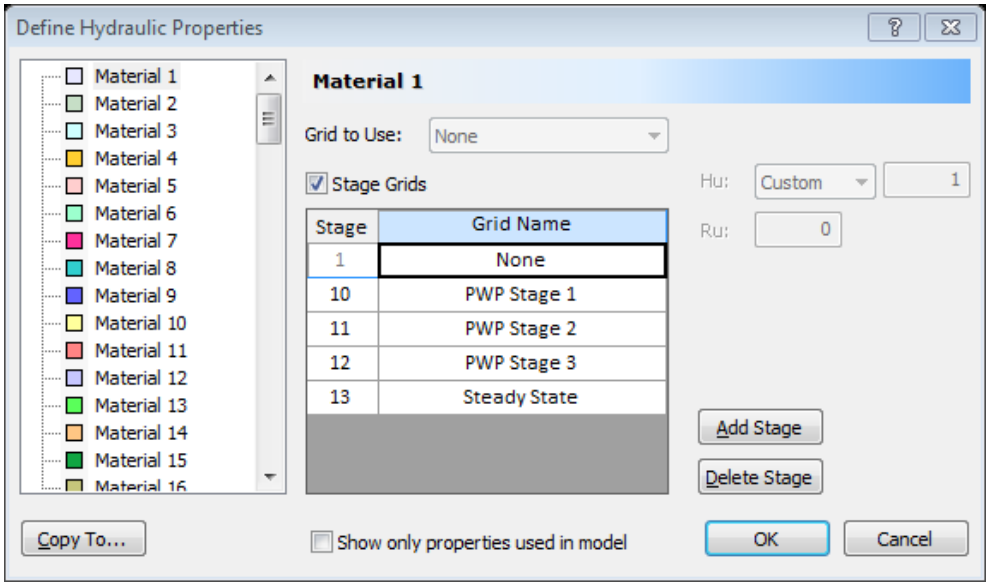

v. This step would have to be repeated for each Material if the model had more than one Material.

vi. An array of symbols (default is blue triangles) will appear for Stages 10 to 13, representing the interpolation points for the pore pressures.

9. At Stage 13, the completed model should look like the one below.

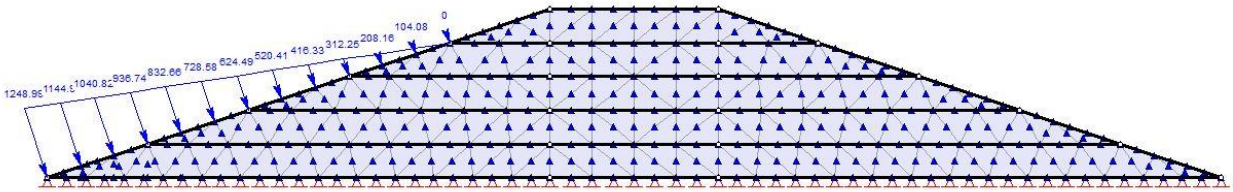

Discussion

This example showed how to implement staged construction in Phase^2 as well as staging of the boundary loads and internal pore pressures. For clarity of explanation, only five stages are used to build the embankment and uniform elements were used. In order to follow the guidelines

of presented in Chapter 4, this example embankment should be built in 25 stages, each 1 ft thick. The use of uniformly shaped and sized quadrilateral elements would also be recommended for an actual stress analysis.

Appendix D – Derivations Related to the Limit Equilibrium RDD Method

The linear interpolation method from Duncan et al. (1990) becomes difficult when $c' > 0$ and the effective normal consolidation stress, σ'_{fc}, is relatively low. Specifically, the following results occur when:

- $\sigma'_{fc} < c' \times \cos \phi'$ – calculated K_f becomes negative because the implied σ'_{3f} is negative. Close to this boundary, K_f is approaches infinity.
- $\sigma'_{fc} < 0$ – calculated K_c becomes negative because the implied σ'_{3c} is negative. Close to this boundary, K_c approaches infinity.

According to Wright (1999), UTEXAS4 does not use interpolation when either of these conditions is encountered (e.g. σ'_{3c} or σ'_{3f} are zero or negative). Instead, the strength corresponding to σ'_{fc} for the lowest of the two envelopes is used by UTEXAS4. Slide v.6.0 also appears to follow this rule.

The effect of non-zero c' on linear interpolation is shown in Figure D-1. The $K_c = 1$ and $K_c = K_f$ envelopes are plotted along with a set of points representing the interpolated strengths along a trial failure surface. At low σ'_{fc}, the interpolated strengths begin to curve toward the $K_c = 1$ envelope. This occurs because K_f becomes large faster than K_c as σ'_{fc} decreases, making K_c closer to 1.0 in a relative sense. It is likely that this curvature in the interpolated strengths is not an intentional part of the interpolation procedure. For this example, one slice has $K_f < 0$ ($\sigma'_{3f} < 0$); therefore the lowest strength envelope is used. As seen in Figure D-1, this creates a discontinuity in the interpolated undrained strengths. Fortunately, this problem occurs at low stresses for which the final strength in the Duncan et al. (1990) method is usually controlled by the Stage 3 drained strength. Even so, it is conceivable that the factor of safety could be unintentionally affected by this problem.

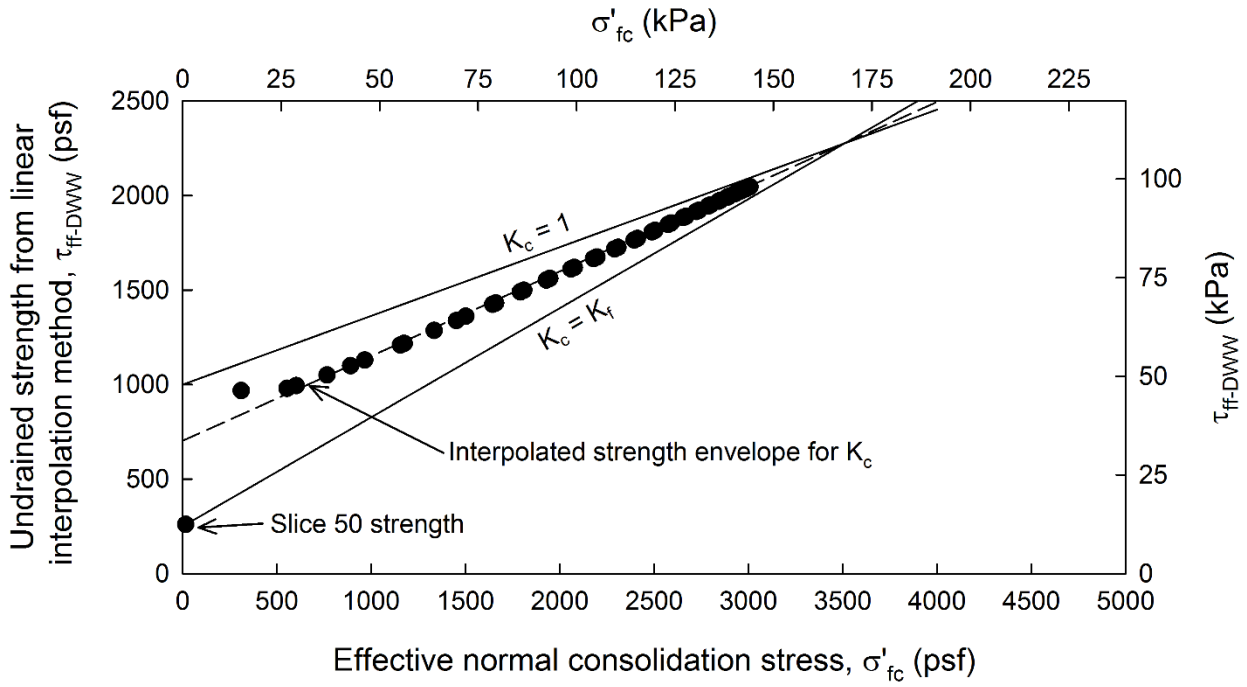

Figure D-1. Strengths from linear interpolation method

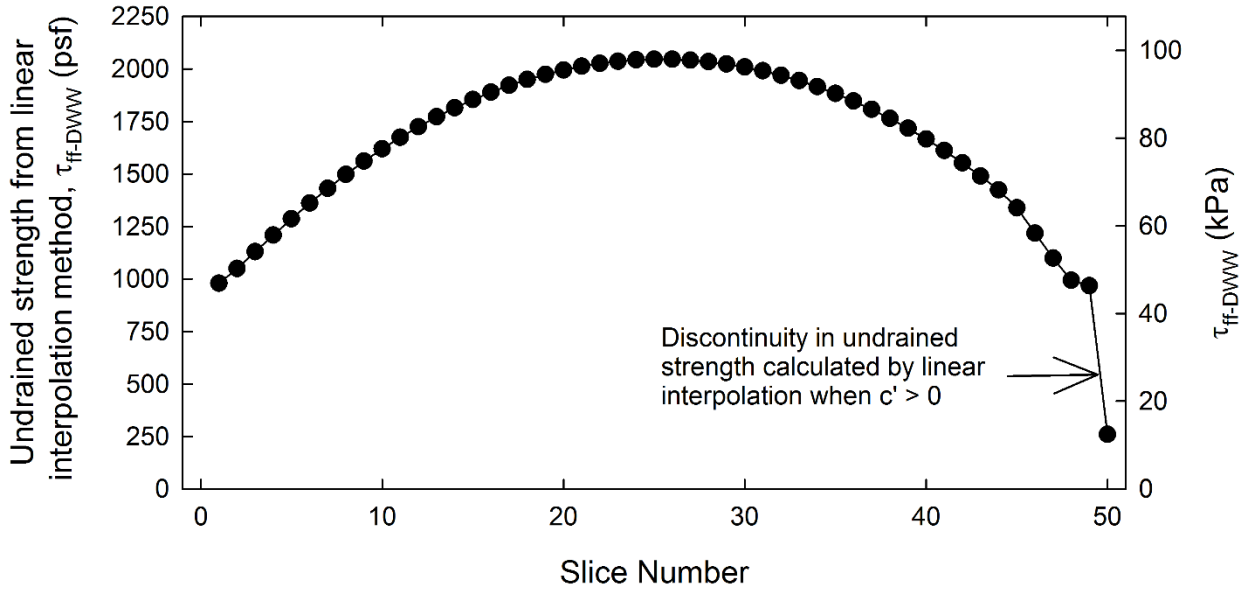

Figure D-2. Undrained strengths determined by linear interpolation along a trial surface

Suggested Modification to the Linear Interpolation Method

The proposed modification to the linear interpolation method interpolates a third linear, undrained strength *envelope* rather than individual strength values as shown in Figure D-3(a). This is accomplished by calculating constant values of K_c and K_f such as those that occur when $c' = 0$. This type of relationship seems to be more consistent with the goal of the interpolation method. Another advantage of this type of relationship is that it can be represented by an intercept, d_{Kc}, and a slope angle, ψ_{Kc}, as shown in Figure D-3(a).

The effective stress failure envelope, or $K_c = K_f$ line, intersects the σ'_{fc} axis at the attraction, $a' = c' / \tan \phi'$. The failure stress ratio, K_f*, for stresses measured with respect to a' is constant for any value of ϕ' and has the value

$$K_f * = \frac{\sigma'_{1f} + a'}{\sigma'_{3f} + a'} = \frac{1 + \sin\phi'}{1 - \sin\phi'} \tag{0-1}$$

The consolidation stress ratio, K_c*, for a given trial surface is also constant if a' is added to the values of σ'_{fc}, such that (USACE 2003)

$$K_c * = \frac{\sigma'_{fc} + a' + \tau_{fc} \dfrac{\sin\phi' + 1}{\cos\phi'}}{\sigma'_{fc} + a' + \tau_{fc} \dfrac{\sin\phi' - 1}{\cos\phi'}} \tag{0-2}$$

Eqn. (5-8) can be used to relate K_c* to the Stage 1 factor of safety, F, by

$$K_c * = \frac{F\cos\phi' + \tan\phi'\left(\sin\phi' + 1\right)}{F\cos\phi' + \tan\phi'\left(\sin\phi' - 1\right)} \tag{0-3}$$

Figure D-3(b) shows how d_{Kc} is found between the known values of c' and $d_{Kc=1}$. The typical interpolation equation (USACE 2003) and the ratios K_c* and K_f* yields

$$d_{Kc} = \frac{d_{Kc=1}\left(K_f * - K_c *\right) + c'\left(K_c * - 1\right)}{\left(K_f * - 1\right)} \tag{0-4}$$

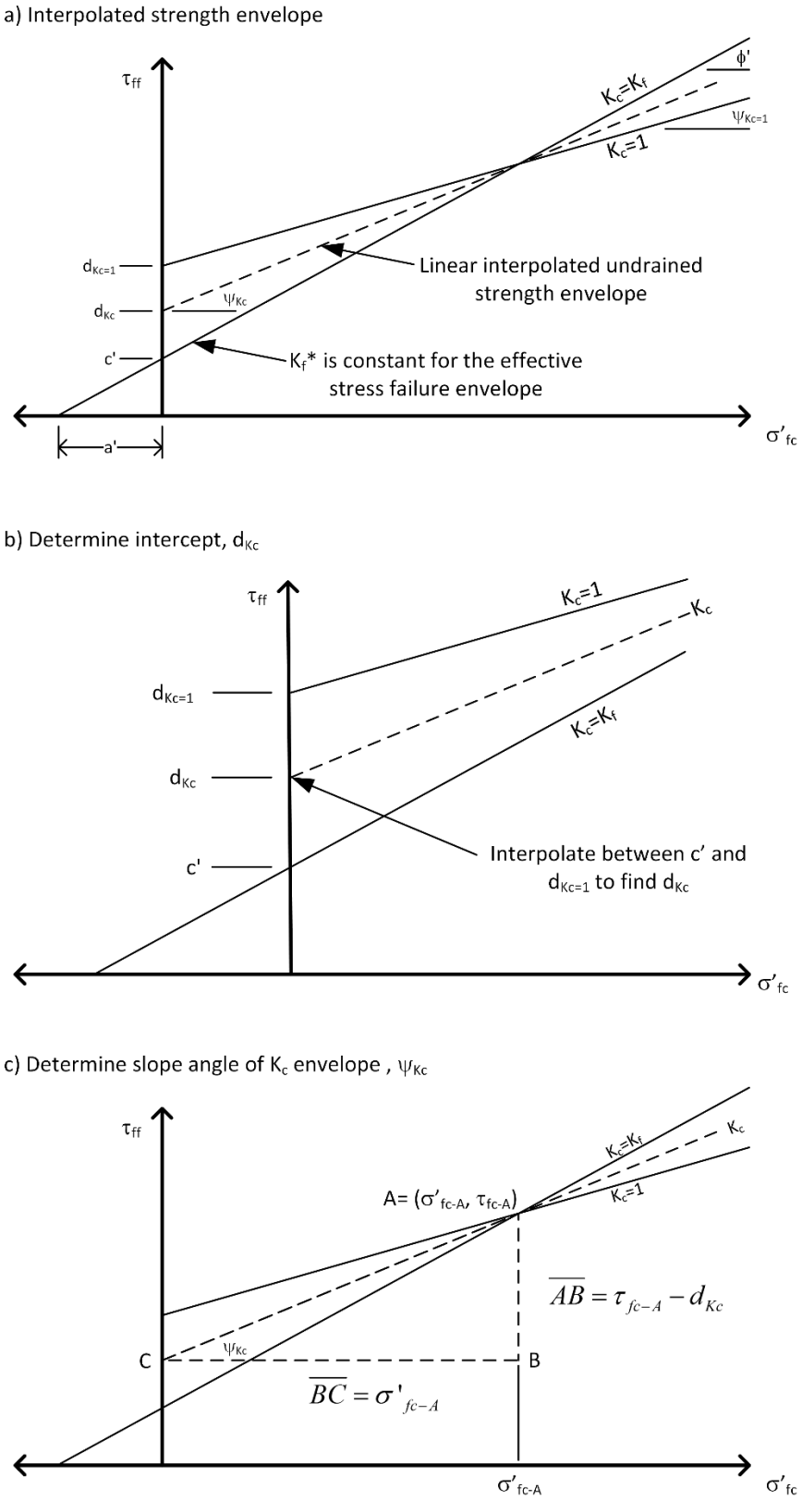

Figure D-3. Linear undrained strength envelope for K_c determined by interpolation

The method for determining the slope angle of the interpolated K_c line is shown in Figure D-3(c). The coordinates of Pt. A are easily found by equating the $K_c=1$ and $K_c=K_f$ shear strengths resulting in

$$\sigma'_{fc-A} = \frac{d_{Kc=1} - c'}{\tan\phi' - \tan\psi_{Kc=1}} \tag{0-5}$$

and

$$\tau_{fc-A} = c' + \sigma'_{fc-A} \tan\phi' \tag{0-6}.$$

Finally, the slope angle of the interpolated line can be determined from the triangle ABC shown in Figure D-3(c)

$$\tan\psi_{Kc} = \frac{\overline{AB}}{\overline{BC}} = \frac{\tau_{fc-A} - d_{Kc}}{\sigma'_{fc-A}} \tag{0-7}.$$

Eqn. (D-4) to Eqn. (D-6) can be inserted into Eqn. (D-7). By rearranging and taking the arctangent, the slope angle is found to be

$$\psi_{Kc} = \tan^{-1}\left[\tan\phi' + \frac{K_f^* - K_c^*}{K_f^* - 1}\left(\tan\psi_{Kc=1} - \tan\phi'\right)\right] \tag{0-8}$$

Eqn. (D-1) and (D-3) are only functions of the strength parameters and the factor of safety for a given surface. This means that Eqn. (D-4) and (D-8) also depend only on the strength parameters and the Stage 1 factor of safety. The values of d_{Kc} and ψ_{Kc} can be calculated directly for each surface after the Stage 1 F is determined. After that, the interpolated shear strength for every slice can be directly calculated as

$$\tau_{ff} = d_{Kc} + \sigma'_{fc} \tan\psi_{Kc} \tag{0-9}$$

This means of calculating the Stage 2 undrained strengths has some computational efficiency compared to conventional interpolation for each slice, regardless of the value of *c'*. The conventional method requires *5N* computations per trial surface for *N* slices. The method

proposed here requires $N+5$ computations per trial surface. This represents a nearly 80% reduction in the number of computations be surface.

This method will produce the exactly same results as "conventional" linear interpolation for cases when c' equals zero. The "correct" method of interpolation for cases with c' greater than zero must be determined based on the philosophical purpose of the linear interpolation method, not mechanics.

It should be noted that the interpolation problems discussion in this appendix can also be avoided if the effective stress strength envelope is represented by a curved envelope that passes through the origin, rather than using c'.

Relationship between $\tau_{ff\text{-}DWW}$ and σ'_{1c}

Start with the following parameters from and ICU-TC test: ϕ', c', $\psi_{Kc=1}$, and $d_{Kc=1}$ and the major effective consolidation stress, σ'_{1c} and conventional consolidation stress ratio, K_c. Consider the following Mohr circle in which

$$q_c = \frac{\sigma'_{1c}}{2}\left(1 - 1/K_c\right) \tag{0-10}$$

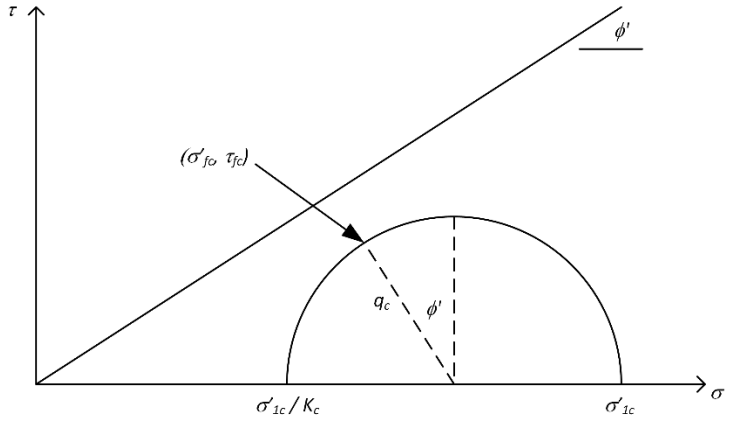

Figure D-4. Mohr circle showing effective consolidation stresses

It is evident that

$$\sigma'_{1c} = \sigma'_{fc} + q_c \sin\phi' + q_c$$
$$\sigma'_{1c} = \sigma'_{fc} + \frac{\sigma'_{1c}}{2}\left(1-1/K_c\right)\sin\phi' + \frac{\sigma'_{1c}}{2}\left(1-1/K_c\right) \quad (0\text{-}11)$$

Solving for σ'_{fc} results in

$$\sigma'_{fc} = \sigma'_{1c} - \frac{\sigma'_{1c}}{2}\left(1-1/K_c\right)\sin\phi' - \frac{\sigma'_{1c}}{2}\left(1-1/K_c\right) \quad (0\text{-}12)$$

Separating out the σ'_{1c} terms and producing a common denominator

$$\sigma'_{fc} = \sigma'_{1c}\left[\frac{2K_c}{2K_c} - \frac{K_c\sin\phi'}{2K_c} + \frac{\sin\phi'}{2K_c} - \frac{K_c}{2K_c} + \frac{1}{2K_c}\right] = \frac{\sigma'_{1c}}{2K_c}\left(K_c + 1 - K_c\sin\phi' + \sin\phi'\right) \quad (0\text{-}13)$$

This equation can be inverted to show that

$$\sigma'_{1c} = \frac{2K_c\sigma'_{fc}}{\left(K_c + 1 - K_c\sin\phi' + \sin\phi'\right)} \quad (0\text{-}14)$$

From the Mohr circle, it is evident that

$$\tau_{fc} = q_c\cos\phi' = \frac{\sigma'_{1c}}{2}\left(1-1/K_c\right)\cos\phi' \quad (0\text{-}15)$$

Combining Eqn. (14) and (15)

$$\tau_{fc} = \frac{\sigma'_{fc}\left(K_c - 1\right)\cos\phi'}{\left(K_c + 1 - K_c\sin\phi' + \sin\phi'\right)} \quad (0\text{-}16)$$

Using Eqn. (D-1) and (D-2), values of K_c* and K_f* can be calculated. These can be used with Eqn. (D-4) to determine the equivalent intercept of the interpolated strength line, d_{Kc}. Likewise, the slope angle of the interpolated line, ψ_{Kc}, can be determined with Eqn. (D-8).

Thus the interpolated undrained shear strength, $\tau_{ff\text{-}DWW}$, becomes

$$\tau_{ff-DWW} = d_{Kc} + \sigma'_{fc}\tan\psi_{Kc} \quad (0\text{-}17)$$

Expanding Eqn. (D-17) results in

$$\tau_{ff-DWW} = \frac{d_{Kc}\left(K_f^* - K_c^*\right) + c'\left(K_c^* - 1\right)}{K_f^* - 1} + \frac{\sigma'_{1c}}{2K_c}\left(1 + \sin\phi' + K_c - K_c \sin\phi'\right)\left[\tan\phi' + \frac{K_f^* - K_c^*}{K_f^* - 1}\left(\tan\psi_{Kc=1} - \tan\phi'\right)\right] \quad \text{(0-18)}$$

Appendix E – Method for Determining Power Curve Parameters

The variation of soil strength with stress is often non-linear, whether it be the variation of undrained strength with effective consolidation stress or shear strength vs. effective normal stress. This curvature can often be described mathematically with good success using a power curve function as suggested by Lade (2010). For example undrained strength, s_u, can be expressed as a function of major effective consolidation stress, σ'_{1c}, as

$$\frac{s_u}{p_a} = a\left(\frac{\sigma'_{1c}}{p_a}\right)^b \tag{0-1}$$

where:

a and b = curve fit parameters based on laboratory test data, and

p_a = atmospheric pressure in the same units as stress

The strength and normal stress have been normalized by atmospheric pressure in Eqn. (E-1). This allows the parameters a and b to be independent of a particular unit system and avoids meaningless units caused by the exponent b.

The parameters a and b can easily be determined by a simple transformation of the data. If the natural logarithm of both sides of Eqn. (E-1) is taken, by the laws of logarithms

$$\ln\left(\frac{s_u}{p_a}\right) = \ln a + b\ln\left(\frac{\sigma'_{1c}}{p_a}\right) \tag{0-2}$$

Eqn. (E-2) describes the equation for a line in terms of the transformed variables. The quantity $ln\ a$ is the y-intercept of this line while the parameter b is the slope. These parameters can thus be determined by the following steps:

1. Normalize the pairs of s_u and σ'_{1c} (or τ_{ff} and σ'_{ff} for drained strength) by p_a.
2. Take the logarithm of the normalized values. The natural logarithm is used herein because it simplifies considerations of probability distribution in Chapter 9. However

the base-10 logarithm is also acceptable, provided later references to *exp(ln a)* are converted to $10^{log\ a}$.

3. Plot the data as the transformed shear strength vs. the transformed consolidation (or normal) stress.
4. Determine the intercept, *ln a*, and slope, *b*, by a curve-fitting procedure or by fitting a line to the data using engineering judgment.
5. Calculate the parameter *a = exp(ln a)*.

The values of *a* and *b* can easily be determined using Microsoft Excel® without graphing. For example, consider the normalized data in rows 3 to 10 of columns A and B in Table E-1. The transformed variables are listed in columns C and D. Using these, Excel's linear regression function, LINEST, can be used to directly calculate *ln a* and *b*. LINEST returns an array of two values in which the slope and intercept of the best-fit line are the first and second values in the array, respectively. The following formulae are used:

Cell F4: "=INDEX(LINEST(D3:D10,C3:C10),2)"

Cell F5: "=EXP(F4)"

Cell F6: "=LINEST(D3:D10,C3:C10)

Table E-1. Finding power curve coefficients in Excel

	A	B	C	D	E	F
1						
2	σ'_{1c} / p_a	s_u / p_a	$\ln(\sigma'_{1c}/p_a)$	$\ln(s_u/p_a)$		
3	0.25	0.28	-1.39	-1.27		
4	0.5	0.54	-0.69	-0.62	ln a =	-0.103
5	0.75	0.72	-0.29	-0.33	a =	0.902
6	1.0	0.92	0.00	-0.083	b =	0.813
7	1.5	1.22	0.41	0.20		
8	2.0	1.57	0.69	0.45		
9	2.5	2.0	0.92	0.69		
10	3.0	2.1	1.10	0.74		

Power curves for Overconsolidated Soils

The undrained strength ratio of over-consolidated clays is sometimes described using the following equation (Jamiolkowski et al. 1985)

$$USR_{OC} = \left(\frac{s_u}{\sigma'_{vc}}\right)_{OC} = S\left(\frac{\sigma'_p}{\sigma'_{vc}}\right)^m = \left(\frac{s_u}{\sigma'_{vc}}\right)_{NC} OCR^m \qquad (0\text{-}3)$$

where:

S = undrained strength ratio for the normally consolidated condition,

σ'_p = preconsolidation stress,

OCR = overconsolidation ratio,

σ'_{vc} = current vertical effective consolidation stress,

m = parameter that controls the increase in USR_{OC} with increased OCR, which is related to the compressibility of the soil.

Eqn. (E-3) can be rearranged such that

$$s_{u-OC} = S\left(\sigma'_{vc}\right)^{1-m}\left(\sigma'_p\right)^m \qquad (0\text{-}4)$$

Dividing both sides of the equation by p_a and multiplying the right side by $(p_a/p_a)^m$, yields

$$\frac{s_{u-OC}}{p_a} = S\left(\sigma'_{vc}\right)^{1-m}\left(\sigma'_{p}\right)^{m} p_a^{-1}\left(\frac{p_a}{p_a}\right)^{m} \quad (0\text{-}5)$$

Rearranging terms

$$\frac{s_{u-OC}}{p_a} = S\left(\frac{\sigma'_{p}}{p_a}\right)^{m}\left(\frac{\sigma'_{vc}}{p_a}\right)^{1-m} \quad (0\text{-}6)$$

When σ'_{vc} is the major effective stress, Eqn. (E-6) has the same form as Eqn. (E-1) such that

$$a = S\left(\frac{\sigma'_{p}}{p_a}\right)^{m} \quad (0\text{-}7)$$

and

$$b = 1 - m \quad (0\text{-}8).$$

Ladd and DeGroot (2003) state that *m* is usually between 0.7 and 0.9 for cohesive soils. From Eqn. (E-8), the power curve parameter *b* would be expected to be in the range of 0.1 to 0.3 for overconsolidated clay.